Far-Infrared Spectral Radiance Studies: Application to Water Vapour and Cirrus

Cathryn Fox

Thesis presented for the degree of

Doctor of Philosophy of Imperial College London

and the

Diploma of Imperial College

Space and Atmospheric Physics Group

Department of Physics

Imperial College London

March 2015

Declaration of Originality

The work presented in this thesis is that of the author, and any information, data or figures taken from other sources has been referenced accordingly.

Cathryn Fox, 31st March 2015

Copyright Declaration

The copyright of this thesis rests with the author and is made available under a Creative Commons Attribution Non-Commercial No Derivatives licence. Researchers are free to copy, distribute or transmit the thesis on the condition that they attribute it, that they do not use it for commercial purposes and that they do not alter, transform or build upon it. For any reuse or redistribution, researchers must make clear to others the licence terms of this work.

Abstract

This thesis presents the analysis of high-resolution spectral radiances recorded using the Imperial College Tropospheric Airborne Fourier Transform Spectrometer (TAFTS) instrument, which uniquely has the ability to record high resolution in-situ measurements, both up-welling and down-welling, in the far-infrared spectral region 80-800cm^{-1}. The TAFTS data used in this work has been recorded during two diverse field campaigns, one ground-based, and one onboard the Facility for Airborne Atmospheric Measurements (FAAM) BAe-146 research aircraft.

The far-infrared spectral region has been shown to have a dominant contribution to the radiative cooling of the planet to space. Atmospheric water vapour is known to absorb radiation in a pure rotation band in the far-infrared, and also exhibits a background slowly-varying absorption known as the water vapour continuum. Observations of far-infrared radiances made by TAFTS during the Radiative Heating in Underexplored Bands Campaign (RHUBC) in Barrow, Alaska, are compared to simulations using line-by-line radiative transfer models in order to validate the current water vapour continuum parameterisation. Results presented here show that the current MT-CKD v2.5 parameterisation is accurately representing the water vapour continuum at wavenumbers between 350-500 cm^{-1}.

This thesis also considers the radiative effect of cirrus clouds in the far-infrared. These clouds have an important influence on current climate, and are known to scatter and absorb radiation in the infrared, however currently there have been relatively few measurements of the cirrus radiative effect in the far-infrared spectral region. Presented here are mid- and far-infrared observations of the radiative signature of cirrus recorded using the TAFTS and the UK Met Office Airborne Research Interferometer Evaluation System (ARIES) instruments, during the first phase of the aircraft-based Cirrus Coupled Cloud-Radiation Experiment (CIRCCREX), which flew out of Prestwick, Scotland in November 2013. These spectral measurements were compared to simulations using the LBLDIS model, which utilises cirrus scattering databases developed by Baum et al. at the SSEC, University of Wisconsin-Madison. This work represents the first time that the consistency of these databases have been tested across the entire infrared region. It was found that the model was underestimating brightness temperatures in the region 330-600 cm^{-1}, and that further work is required in this region.

Acknowledgements

The work presented in this thesis would not have been possible without the help and support of many individuals. Firstly, thanks go to my supervisor Dr Juliet Pickering, for her advice, support and encouragement over the course of my PhD. A huge thank you to Dr Jon Murray, who has been a constant source of knowledge and advice, and thanks also to the other members of the TAFTS team past and present, namely Paul Green, Ralph Beeby, Neil Humpage and Alan Last.

I am also grateful to our collaborators on CIRCCREX: the UK Met Office, FAAM, the University of Manchester, and the University of Hertfordshire. Thanks to the instrument operators, engineers and staff of the FAAM BAe-146 for their expertise, for providing data used in this thesis, and for help carrying TAFTS. Thanks to the RHUBC principal investigator Dave Turner for supporting our participation in the campaign, for providing the corrected AERI-ER spectra, and for helpful comments. I also appreciate help given by Bryan Baum and Aronne Merelli at the SSEC, University of Wisconsin-Madison.

The Space and Atmospheric Physics Group at Imperial has been a constant source of ideas, discussions, and advice, as well as a lot of cake. My thanks to you all.

Lastly I must thank my family, who have supported me throughout my PhD, and even made admirable attempts to understand what I actually do all day.

This PhD was funded by NERC. The FAAM BAe-146 is jointly funded by NERC and the UK Met Office. Data from the AERI-ER and other instruments during RHUBC were provided by the U.S. Department of Energy as part of the Atmospheric Radiation Measurement Program. The REFIR-PAD data was kindly provided by the authors of Liuzzi et al. [2014].

Contents

Abstract 3
Acknowledgements 4
List of Figures 8
List of Tables 15
List of Acronyms 16
1 Introduction 19
2 Background and current research areas 22
2.1 Radiative balance of the Earth 22
2.1.1 The role of the atmosphere 22
2.1.2 The Earth's radiative energy budget 25
2.1.3 The importance of the far-infrared region 29
2.2 Atmospheric water vapour 31
2.2.1 Introduction 31
2.2.2 The water vapour continuum 32
2.2.3 Recent water vapour continuum studies 36
2.3 Radiative properties of cirrus 37
2.3.1 The radiative effect of cirrus 38
2.3.2 Cirrus properties 40
2.3.3 Observation of cirrus 44
2.4 Summary 48
3 Fourier Transform Spectroscopy: theory and instrumentation 49
3.1 Introduction 49
3.1.1 The Michelson interferometer 50
3.1.2 The Martin-Puplett interferometer 53
3.1.3 Advantages of Fourier transform spectroscopy 55
3.2 TAFTS 56
3.2.1 Pointing optics box 57
3.2.2 Interferometer 58
3.2.3 Cryostat and detectors 60
3.2.4 Electronics 61
3.2.5 TAFTS data acquisition and processing 62
3.3 AERI and AERI-ER 79

3.4 ARIES 79
3.5 Summary 80
4 Radiative transfer: Theory and simulation 81
4.1 Radiative transfer in a non-scattering atmosphere 81
4.2 Spectral lines 83
4.3 Line-by-line radiative transfer codes 85
4.4 Radiative transfer in a cloudy atmosphere 87
4.5 Line-by-line discrete ordinates method for radiative transfer in a scattering atmosphere 89
4.6 Scattering databases 90
4.6.1 Microphysical data 91
4.6.2 Ice particle habits and surface roughness 92
4.6.3 Single scattering properties 93
5 Ground-based observations of the far-infrared water vapour foreign continuum during RHUBC 96
5.1 Introduction 96
5.2 The Radiative Heating in Underexplored Bands Campaign 97
5.2.1 Field campaign description 97
5.2.2 Instrumentation 99
5.3 Cross-comparison of TAFTS and AERI-ER observed FIR spectral radiances 100
5.3.1 Data selection 100
5.3.2 Radiance comparison 101
5.4 Water vapour continuum simulations and measurements 104
5.4.1 Simulated radiances 104
5.4.2 Comparison of observed and simulated radiances 106
5.4.3 Discussion and comparison with previous studies 109
5.5 Summary and conclusions 113
6 Studies of the sensitivity of cirrus scattering models to changes in cloud properties 114
6.1.1 ARIES LW channel (550-1400 cm^{-1}) 123
6.1.2 ARIES SW channel (1800-2300 cm^{-1}) 123
6.1.3 TAFTS LW channel (100-320 cm^{-1}) 123
6.1.4 TAFTS SW channel (320-580 cm^{-1}) 124
6.2 Summary and conclusions 126

7 Aircraft-based observations of cirrus mid- and far-infrared radiative signatures during CIRCCREX-I 127
7.1 Introduction 127
7.2 Spectral radiance measurements 134
7.2.1 Tri-spectral algorithm analysis of ARIES spectra 134
7.2.2 MIR and FIR spectra recorded in the presence of cirrus 138
7.3 Auxiliary measurements 143
7.3.1 Atmospheric profiling 143
7.3.2 Cloud physics 146
7.4 Determination of cirrus properties 147
7.4.1 In-situ measurements of properties 148
7.4.2 Retrieval of properties from ARIES spectra 152
7.5 Results of modelling across the MIR and FIR 156
7.6 Summary & conclusions 163
8 Conclusions and future work 164
8.1 Summary of results from ground-based arctic study 164
8.1.1 MT-CKD v2.5 validation 164
8.1.2 TAFTS/AERI-ER comparison 164
8.2 Results of sensitivity studies to changes in cloud properties 165
8.3 Summary of results from airborne cirrus study 165
8.3.1 Simultaneous FIR and MIR spectra recorded above cirrus 165
8.3.2 Determination of cirrus properties 166
8.3.3 First test of Baum scattering models in FIR region 166
8.4 Future Work 166
8.4.1 Improved and extended cirrus datasets 166
8.4.2 Testing and validation of alternative cirrus scattering models 167
8.4.3 Measurements of FIR surface emissivity 168
8.4.4 FIR space-based observations 168
8.4.5 Implications for GCMs and NWP 168
References 170

List of Figures

Figure 2.1*: Schematic showing the calculation of the amount of solar energy intercepted by the Earth. The parallel arrows represent solar radiation, the radial arrows outgoing thermal radiation.* 23

Figure 2.2: *A simple model of the greenhouse effect.* 24

Figure 2.3: *Estimate of the Earth's annual and global mean energy budget, all units are in* Wm^{-2}*. From Kiehl and Trenberth* [1997]. 26

Figure 2.4: *Spectrum of OLR at TOA for five standard atmospheres, indicating the principal greenhouse gases in each spectral region.* 28

Figure 2.5: *Greenhouse parameter (solid lines) as a function of wavenumber for five standard atmospheres, with surface temperature emission (dashed lines)* 28

Figure 2.6: *Cooling rate from the Earth's surface to TOA for (a) tropical and (b) subarctic winter standard atmospheres with no clouds present. From Brindley and Harries [1998]* 30

Figure 2.7: *Illustration of the water cycle and its interaction with the greenhouse effect. The insert (upper-left) shows how the amount of atmospheric water vapour would increase with an increase in temperature. From IPCC* [2013]. 32

Figure 2.8: *LBLRTM simulations of TOA upwelling radiances using a mid-latitude winter standard profile. The spectrum in blue includes the MT-CKD v2.5 continuum model, the spectrum in black does not.* 35

Figure 2.9: *Mean 2006-2011 cloud cover from CloudSat/CALIPSO [IPCC, 2013]* 38

Figure 2.10: *The habits of ice crystals as a function of both ambient temperature and ice supersaturation (IWC)* [*Emersic*, 2012] 42

Figure 2.11: *In situ particle size distributions measured above optically thin and thick cirrus. From Cox et al. [2010]* 44

Figure 3.1: *Schematic of a Michelson interferometer. Incoming light enters at* $I1$ *and is split at the beamsplitter* BS*. Half the signal is reflected to mirror* $M1$*, and the other half to mirror* $M2$*. Moving* $M2$ *along the distance* $x2$ *creates a difference in path length of* x*, resulting in interference when the beams recombine at* BS*. The beam is output to the detector at* $O2$*.* 51

Figure 3.2: *Schematic of a Martin-Puplett interferometer. The two inputs* $I1$ *and* $I2$ *are directed into the system by polariser* $P1$*, before being divided by polarisation at*

polariser $P2$*. The two divided signals are reflected by rooftop mirrors* $RM1$ *and* $RM2$*, one of which can be moved along distance* x *to create a path difference between the two signals. They are recombined when they return to* $P2$*, at which point they interfere according to the path difference. Finally the signal is divided again at polariser* $P3$ *and directed to two sets of detectors at the outputs* $O1$ *and* $O2$*.* 54

Figure 3.3: *The TAFTS instrument. The two aluminium sections are the pointing optics box and main interferometer chamber, the blue cylinder is the cryostat.* 56

Figure 3.4: *A schematic of the optical elements inside the TAFTS POB, from Green [2003]. The four internal blackbodies are labelled* $BBdh$*,* $BBdc$*,* $BBuh$ *and* $BBuc$ *where the subscripts denote whether the black body is hot (h) or cold (c) and whether it is located in the upwelling (u) or downwelling (d) arm. DW radiation enters through the DW aperture and is directed by mirrors A, B and D through window C. UW radiation enters through the UW aperture and is directed by mirrors E, F and G through window H.* ...58

Figure 3.5: *A schematic of the optics layout inside the TAFTS interferometer chamber* 59

Figure 3.6: *Schematic of the optics and detectors inside the TAFTS cryostat. Radiation from the interferometer is directed onto two dichroic filters DF1 and DF2, where it is split into LW and SW beams and directed onto the relevant detector.* 61

Figure 3.7: *Raw interferograms recorded during flight B818. The view configuration is* $h_n z_z$*. Left shows the two LW channels, right the two SW channels. Complementary channel signals shown in black (ch0) and blue (ch1).* 62

Figure 3.8: *The differenced interferograms from the complementary channels shown in Figure 3.7*.....63

Figure 3.9: *FFTs of raw interferograms of (a) SW ch0; and (b) SW ch1. Spikes are due to power supply pickup.* 64

Figure 3.10: *FFT of the differenced interferograms shown in Figure 3.9*.....64

Figure 3.11: *Upper panels – TAFTS laser fringe timings for operation in (a) laboratory conditions; (c) aircraft conditions. Lower panels – corresponding Fourier analysis of the above fringe timings, showing low frequency components associated with the scan gearing mechanism, and a sharp peak at 200 Hz associated with the stepper motor driving the roof-top mirror. The Fourier analysis of the aircraft measurements (d) shows the low frequency and 200 Hz components, as in the lab based measurements (b). However, there are now many broad high frequency components. These new components are associated with vibrations in the beamsplitter.* 66

Figure 3.12: *TAFTS raw spectral scans for the calibration viewing configurations (a) h_nc_z; (b) c_nh_z; (c) h_nh_z; (d) c_nc_z; and differential spectra (e) h_nc_z-c_nc_z; (f) c_nh_z-h_nh_z.. The colours represent the scan cycle number progressing sequentially from black to red. The blue trace represents the imaginary part of the signal.* 72

Figure 3.13: *(a) the residual between the two differential spectra, attributed to the instrument self-emission; (b) and (c) the differential spectra with the emission term removed*.....73

Figure 3.14: *(a) The variation in h_nc_z-c_nc_z (black) and h_nh_z-c_nh_z (red) blackbody temperature differences in the nadir arm, for 6 sequential TAFTS scans; (b) The maximum uncertainty associated with the blackbody PRT sensors; (c) The nadir response functions for the 6 scans once the blackbody emission and self-emission terms have been removed.*.....74

Figure 3.15: *Calibrated nadir view TAFTS SW radiances (upper) and brightness temperatures (lower) for the B818 measurements (black-red), with their uncertainties (blue-green).*.....78

Figure 4.1: *Schematic showing $I\upsilon$ travelling through an absorbing material*.....81

Figure 4.2: *Flowchart showing the inputs and outputs of LBLRTM* 87

Figure 4.3: *Flowchart showing the inputs and outputs of LBLDIS* 90

Figure 4.4: *Ice-particle volume as a function of habit and maximum dimension $Dmax$ for (a) $Dmax \leq 1000\ \mu m$ (small-to moderately sized particles) and (b) $Dmax > 1000\ \mu m$ (moderate to large particles). From Baum et al. [2011].*.....92

Figure 5.1: *LBLRTM simulations of down-welling spectral radiance performed using a US standard atmosphere (PWV = 13.5 mm) and a sub-arctic winter atmosphere observed during RHUBC (PWV = 1.4 mm).* 98

Figure 5.2: *The guest instrument facility at the ACRF-NSA, where the TAFTS instrument was housed during RHUBC. Photo credit: ARM.*.....99

Figure 5.3: *(a) Comparison of AERI-ER (black) and TAFTS (red) radiance spectra; (b) their residual (black) and combined instrumental uncertainty (blue) for the dataset recorded on the 10th March 2007. The TAFTS spectra have been filtered to match the resolution of the AERI-ER.*.....103

Figure 5.4: *The final composite temperature (a) and relative humidity (b) atmospheric profiles used in the analysis, with the combined uncertainty values shown in blue.*.....105

Figure 5.5: *Comparison of the TAFTS and simulated radiances. (a) A section of the TAFTS data measured during the 1333 radiosonde launch (black), with the corresponding*

simulated radiance (red). The window regions are indicated in purple. (b) Observation - simulation residual (black), cumulative uncertainties (blue). The red stars in each microwindow are the magnitude of the residual between the simulation when using adjusted model continuum coefficients, and the original simulation. 107

Figure 5.6: *Sources of uncertainty in the radiance simulation. All panels; the observed-simulated residual (black). (a) The equivalent radiance uncertainty due to the T and RH uncertainties in the LBLRTM profile (red). (b) The TAFTS radiometric calibration uncertainty (blue). (c) and (d) Uncertainty due to a 5% perturbation in the AER v3.2 water vapour line intensity and width respectively, where the coloured lines represent the original simulation minus the perturbed simulation.*.....108

Figure 5.7: *Percentage adjustments to the continuum model as calculated from TAFTS radiances recorded during the 1333 UTC radiosonde launch. The dashed red line through these points is a linear fit to these data, weighted for the uncertainties.* 109

Figure 5.8: *A comparison of the MT-CKD continuum model with the results of studies by Green et al. [2012], Liuzzi et al. 2014] and this study.* 112

Figure 6.1: *ARIES LW channel simulations of varying cloud optical thickness performed using the (a) GHM; (b) ASC; (c) SC scattering database. The cloud particle effective radius is held fixed at 35 μm for all simulations.*.....115

Figure 6.2: *ARIES LW channel simulations of varying cloud particle effective radius performed using the (a) GHM; (b) ASC; (c) SC scattering database. The cloud optical thickness is held fixed at 4 for all simulations.* 116

Figure 6.3: *ARIES SW channel simulations of varying cloud optical thickness performed using the (a) GHM; (b) ASC; (c) SC scattering database. The cloud particle effective radius is held fixed at 35 μm for all simulations.*.....117

Figure 6.4: *ARIES SW channel simulations of varying cloud particle effective radius performed using the (a) GHM; (b) ASC; (c) SC scattering database. The cloud optical thickness is held fixed at 4 for all simulations.* 118

Figure 6.5: *TAFTS LW channel simulations of varying cloud optical thickness performed using the (a) GHM; (b) ASC; (c) SC scattering database. The cloud particle effective radius is held fixed at 35 μm for all simulations.*.....119

Figure 6.6: *TAFTS LW channel simulations of varying cloud particle effective radius performed using the (a) GHM; (b) ASC; (c) SC scattering database. The cloud optical thickness is held fixed at 4 for all simulations.* 120

Figure 6.7: *TAFTS SW channel simulations of varying cloud optical thickness performed using the (a) GHM; (b) ASC; (c) SC scattering database. The cloud particle effective radius is held fixed at 35 μm for all simulations.*.....121

Figure 6.8: *TAFTS SW channel simulations of varying cloud particle effective radius performed using the (a) GHM; (b) ASC; (c) SC scattering database. The cloud optical thickness is held fixed at 4 for all simulations.* 122

Figure 6.9: *The variation of the asymmetry parameter g with wavenumber for the (a) GHM; (c) ASC; and (e) SC databases, and the variation of the single scattering albedo* ω0 *with wavenumber for the (b) GHM; (d) ASC; and (f) SC databases. The dashed line is to allow easier comparison.* 125

Figure 7.1: *A plot of the flight track of the FAAM aircraft during B818 on the 29th November* 131

Figure 7.2: *UKMO cloud forecast model for 1200 UTC on the 29th November 2013. Cirrus is indicated in turquoise, and cirrus with underlying low cloud in green. Image courtesy UKMO.*.....131

Figure 7.3: *10.8 μm inverted BT scale images from SEVIRI taken at (a) 1130 UTC; (b) 1145 UTC; (c) 1200 UTC; (d) 1215 UTC showing the band of cirrus cloud that was sampled during flight B818. The red dot shows the location of the aircraft in each image.* 132

Figure 7.4: *MODIS level 1b scene from the MODIS Terra overpass, 1200 UTC, 29/11/13, showing the cirrus conditions in the measurement area. Source: NASA* [2014].....133

Figure 7.5: *The Lidar observations for the B818 flight, showing the position of clouds. Cirrus can be seen above approx. 7000m, with underlying low cloud at around 2000m. Image courtesy F. Marenco, UKMO.* 133

Figure 7.6: *The (a) real; and (b) imaginary component of the complex index of refraction for ice and water. The windows used in the tri-spectral analysis are indicated by blue and purple lines.*.....135

Figure 7.7: *B818 ARIES UW tri-spectral differences. Points that meet the cirrus threshold of BTD(8.3-11μm) > 0.4K are shown in red.*.....136

Figure 7.8: *B818 BTD(8.3-11μm) against time, showing where in the flight cirrus was encountered. Points meeting the cirrus threshold are shown in red. The aircraft OAT is overplotted in orange*.....137

Figure 7.9: *ARIES LW individual spectra recorded during the three time periods of coincidental TAFTS and ARIES views, showing the variation in brightness temperatures over the measurement time.* 139

Figure 7.10: *The measured B818 ARIES (a) LW and (b) SW spectra for time 11:39:16-11:39:45 UTC. The spectra are averaged over 2K brightness temperature bins in the window region 8.3-8.4 μm / 1190-1205 cm^{-1}* 141

Figure 7.11: *The measured B818 TAFTS (a) LW and (b) SW spectra, that coincide with the 2K averaged ARIES spectra plotted in Figure 7.10* 142

Figure 7.12: *Sources of the atmospheric (a) temperature and (b) humidity profile used for simulating flight B818 atmospheric radiances; the final composite (c) temperature and (d) humidity profiles. The uncertainties on the composite temperature and humidity profiles are ±0.3 K and ±2 % respectively from the instrumentation.*.....145

Figure 7.13: *A view of the cloud probe pylons attached to the underside of the aircraft wings* 146

Figure 7.14: *(a) Original CIP tip design, showing how particles can shatter and 'bounce' into the sample volume; (b) Modified 'Korolev tips' which deflect shattered fragments away from the sample volume. Image credit: Droplet Measurement Technologies [2014].* 147

Figure 7.15: *PSDs of ice particles observed by the SID2, 2DC, and 2DS instruments, along with a composite PSD constructed by interpolation throughout the three instruments measurement ranges. Measurements were averaged along three level runs within the cirrus. The uncertainties shown on the composite profile are calculated from the uncertainties on the individual cloud probes.*.....150

Figure 7.16: *Lidar backscatter signal (top panel) and relative depolarisation ratio (lower panel) for the B818 cirrus section.* 151

Figure 7.17: *Bi-spectral plots for the three Baum scattering databases showing how BTD vary with varying particle effective radius (r_eff) and cloud optical depth (τ). The bispectral values of the individual B818 ARIES spectra are overplotted as stars, where the colour black-red denotes sequential scans (as in Figure 7.9 (a)) The 2K averaged ARIES spectra are overplotted as red triangles.* 154

Figure 7.18: *MODIS Level 2 cloud product – (a) particle effective radius and (b) cloud optical thickness, from the MODIS Terra overpass, 1200 UTC, 29/11/13. Source: NASA* [2014].....155

Figure 7.19: *The B818 spectral average ARIES_0 LW spectra (black), alongside simulations using the three scattering databases GHM, ASC, and SC (coloured lines). Also plotted are the observation-simulation residuals and the uncertainties due to the*

instrumentation (orange) and the atmospheric profile used in the simulation (purple). 158

Figure 7.20: *The B818 spectral average ARIES_0 SW spectra (black), alongside simulations using the three scattering databases GHM, ASC, and SC (coloured lines). Also plotted are the observation-simulation residuals and the uncertainties due to the instrumentation (orange) and the atmospheric profile used in the simulation (purple).* 159

Figure 7.21: *The B818 spectral average TAFTS_0 LW spectra (black), alongside simulations using the three scattering databases GHM, ASC, and SC (coloured lines). Also plotted are the observation-simulation residuals, and the uncertainties due to the instrumentation (orange) and the atmospheric profile used in the simulation (purple).* 160

Figure 7.22: *The B818 spectral average TAFTS_0 SW spectra (black), alongside simulations using the three scattering databases GHM, ASC, and SC (coloured lines). Also plotted are the observation-simulation residuals, and the uncertainties due to the instrumentation (orange) and the atmospheric profile used in the simulation (purple).* 161

List of Tables

Table 2.1: *Ice crystal habits observed in cirrus clouds* [*Heymsfield and Platt*, 1984].....43

Table 5.1: *Continuum strengths for each micro-window alongside the associated uncertainty as derived in this study*.....110

Table 7.1: *Information on the spectra included in each ARIES 2K average*.....140

Table 7.2: *Cloud characterisation at each in-situ measurement height*.....149

Table 7.3: *Cirrus properties from the three B818 ARIES spectral averages, retrieved using a RT model and the three different scattering databases of Baum et al.* [2014] 153

List of Acronyms

2DC	2-Dimensional Particle Size Spectrometer
2DP	2-Dimensional Particle Size Spectrometer
2DS	2-Dimensional Stereo Probe
3V-CPI	3-View Cloud Particle Imager
ACRF-NSA	Atmospheric Radiation Measurement Climate Research Facility - North Slope of Alaska
AER	Atmospheric and Environmental Research Inc.
AERI	Atmospheric Emitted Radiance Interferometer
AERI-ER	Atmospheric Emitted Radiance Interferometer – Extended Range
AIRS	Atmospheric Infrared Sounder
ARIES	Airborne Research Interferometer Evaluation System
ARM	Atmospheric Radiation Measurement Program
ASC	Aggregate Solid Columns
AVAPS	Airborne Vertical Atmospheric Profiling System
CAESER	Cirrus and Anvils: European Satellite and Airborne Radiative measurement project
CALIPSO	Cloud/Aerosol Lidar and Infrared Pathfinder Satellite Observation
CAVIAR	Continuum Absorption by Visible and IR radiation and its Atmospheric Relevance campaign
CDP	Cloud Droplet Probe
CERES	Clouds and the Earth's Radiant Energy System
CFC	Chlorofluorocarbon
CIP	Cloud Imaging Probe
CIRCCREX	Cirrus Coupled Cloud-Radiation Experiment
CKD	Clough-Kneizys-Davies
DISORT	DIScrete Ordinate Radiative Transfer code
DW	Down-Welling
FAAM	Facility for Airborne Atmospheric Measurements
FFT	Fast Fourier Transform
FIR	Far-InfraRed
FIRST	Far-Infrared Spectroscopy of the Troposphere instrument
FTS	Fourier Transform Spectrometer

GCM	General Circulation Model
GenLn2	General Line-by-Line Atmospheric Transmittance and Radiance Model
GHM	General Habit Mixture
GVR	G-band water-Vapour Radiometer
HITRAN	High Resolution Transmission
HWHM	Half-Width at Half-Maximum
IASI	Infrared Atmospheric Sounding Interferometer
IPCC	Intergovernmental Panel on Climate Change
ISCPP	The International Satellite Cloud Climatology Project
IWC	Ice Water Content
LBLDIS	Line-By-Line DISORT model
LBLRTM	Line-By-Line Radiative Transfer Model
LW	Longwave
MIR	Mid-InfraRed
MODIS	The Moderate Resolution Imaging Spectro-radiometer
MT-CKD	Mlawer-Tobin-Clough-Kneizys-Davies
NWP	Numerical Weather Prediction
OLR	Outgoing Longwave Radiation
POB	Pointing Optics Box
PRT	Platinum Resistance Thermistor
PSD	Particle Size Distribution
PWV	Precipitable Water Vapour
REFIR-PAD	Radiation Explorer in the Far InfraRed – Prototype for Applications and Development
RH	Relative Humidity
RHUBC	Radiative Heating in Underexplored Bands Campaign
RTM	Roof Top Mirror
RU	Radiance Unit (1 RU = 1 $mW/(m^2.sr.cm^{-1})$)
SC	Solid Columns
SEVIRI	Spinning Enhanced Visible and Infrared Imager
SHEBA	Surface Heating Budget of the Arctic Ocean campaign
SID	Small Ice Detector
SLR	Straight and Level Run

SSP	Single Scattering Parameters
SW	Shortwave
TAFTS	Tropospheric Airborne Fourier Transform Spectrometer
TOA	Top Of Atmosphere
UKMO	United Kingdom Meteorological Office
UoM	University of Manchester
UV	Ultra-Violet
UW	Up-Welling
WINTEX	WINTer EXperiment

1 Introduction

It is well documented that the Earth's climate is changing, and the emission of anthropogenic greenhouse gases has been identified as one of the major contributors to this. Carbon dioxide is usually regarded as the most important anthropogenic greenhouse gas, and there has been an 80% increase in its emission from anthropogenic sources between 1970 and 2004 [*IPCC*, 2007]. However, it is also clear that water vapour plays an important role in the climate, even though direct emission by human activity is negligible. Where water vapour becomes important is in the hydrological cycle, as the temperature of the Earth affects the amount of water vapour in the atmosphere (a feedback effect). Therefore it is vitally important that this gas be well understood. Water vapour contributes to the greenhouse effect in three major spectral bands: the υ_2 vibration-rotation band (centred at 1600 cm^{-1}), the atmospheric window region (800-1250 cm^{-1}), and the far-infrared pure rotation band (below 500 cm^{-1}) [*Sinha and Harries*, 1995]. The first two of these bands are well understood, but the effect of water vapour in the far-infrared region of the spectrum has not been extensively studied. This is due to technological limitations of available instrumentation and the opacity of the atmosphere in the lower troposphere when observed from ground level.

The Imperial College Tropospheric Airborne Fourier Transform Spectrometer (TAFTS) [*Canas et al.*, 1997], used in this work, was developed in order to address this lack of FIR measurements. TAFTS has a spectral range of 80-800 cm^{-1} and a resolution of 0.12 cm^{-1}, and thus allows high-resolution measurements to be taken that extend into the far-infrared. TAFTS has been deployed on several data campaigns, both airborne and ground-based, and it is the analysis of data from these campaigns, and the use of these to validate simulations performed by radiative transfer models that is presented in this thesis.

Another topic of research interest in the FIR is the radiative effect of Cirrus (ice crystal) clouds. These clouds have an important influence on current climate, and any changes to their characteristics as a result of climate change will have a substantial feedback impact. TAFTS has been used to study the effect of cirrus cloud in the FIR, a topic that although recognised as significant, is currently poorly understood. The radiative properties of cirrus have not been fully determined, limiting the accuracy to which they can be described in GCMs. To improve this situation, this thesis examines radiance measurements taken using TAFTS alongside measurements of the clouds' physical properties (ice crystal size, shape etc.) with the aim to

provide a better understanding of scattering of FIR radiation by cirrus, which in turn can improve the representation of cirrus in models.

The remainder of this thesis is organised as follows:

Chapter 2 provides a detailed description of the radiative effect of both water vapour and cirrus in the atmosphere, and the motivation behind the observations which are presented in this thesis. In addition, methods of measurement and past studies of water vapour and cirrus are discussed.

Chapter 3 gives a description of Fourier Transform Spectroscopy (FTS) theory, both as a general technique and then as specifically applied to the TAFTS instrument. The chapter continues with a description of the instrument, the sampling system and calibration procedure, and then closes with a short description of other FTS instruments used in this work.

Chapter 4 goes into detail of the processes of radiative transfer, through both a non-scattering (clear sky) and scattering (cloudy) atmosphere. The radiative transfer models LBLRTM [*Clough et al.*, 2005] and LBLDIS [*Turner*, 2005], used in this work to simulate radiances, are described. When simulating scattering of radiation by cirrus, databases of single scattering parameters are employed to represent the range of shapes and sizes of ice crystals in the cloud. This chapter closes with a description of these parameters, and three newly-developed databases from Baum et al. [2014], which are used in this work.

Chapter 5 presents measurements taken using the TAFTS instrument during the Radiative Heating in Underexplored Bands Campaign (RHUBC) [*Turner and Mlawer*, 2010], which took place in Barrow, Alaska, in February and March 2007. The TAFTS measurements are used first in a cross-comparison study with another interferometer of a different design, the Atmospheric Emitted Radiance Interferometer – Extended Range (AERI-ER) instrument. TAFTS observations are then compared to simulated radiances produced by a radiative transfer model in order to test the performance of the model, and in particular to validate the latest version of the water vapour continuum parameterisation, the MT-CKD v2.5. The work presented in this chapter has been published in the paper by Fox et al. [2015].

Chapter 6 describes a series of sensitivity studies of the changes in the simulated radiances of MIR and FIR spectra in the presence of cirrus, given changes in the underlying cloud properties. These simulations are performed using the cirrus scattering databases described in Chapter 4, and allow an investigation into the link between the microphysical properties of the cloud and the macrophysical radiative signature.

Chapter 7 presents observations of cirrus cloud during the first flight campaign of the Cirrus Coupled Cloud-Radiation Experiment (CIRCCREX), which took place in Prestwick, Scotland, during November and December 2013. The author was a participant in this aircraft campaign, and was responsible for the pre-flight preparation and in-flight operation of the TAFTS instrument. The recorded radiance measurements are compared to simulations, which are made using the cirrus scattering and radiative transfer models described in Chapter 4. This work represents the first time that these scattering databases have been tested in the FIR spectral region.

Finally, Chapter 8 concludes and summarises all the work presented herein, and suggests possible improvements and future work.

2 Background and current research areas

This chapter provides an introduction to the atmospheric physics relevant to the work presented in this thesis, and a summary of the research that has currently been carried out in this field. Firstly the radiative balance of the Earth is discussed, with an explanation of the greenhouse effect and the role of atmospheric gases. The significance of the far-infrared (FIR) spectral region is then outlined. The importance of water vapour in the climate system is then discussed, detailing how it contributes to the greenhouse effect, and its behaviour under climate change. The continuum contribution to water vapour absorption is introduced, and previous studies are discussed. Cirrus clouds and their role in the atmosphere are then introduced, including a description of their physical and radiative properties, and a review of observation techniques and recent research.

2.1 Radiative balance of the Earth

This section provides an overview of the importance of atmospheric gases in regard to the Earth's climate, leading into a discussion of the radiation budget of the Earth. The significance of the far-infrared spectral region is then shown, as the majority of radiation from the Earth's surface is emitted at wavelengths in this region.

2.1.1 The role of the atmosphere

The Earth's atmosphere is composed of a mixture of gases, predominantly nitrogen and oxygen, but with minor constituents carbon dioxide, water vapour and ozone playing important roles. The atmosphere is constantly bombarded by photons from the sun at all wavelengths. These photons can either be scattered by atmospheric gases or aerosol, reflected back to space by clouds or the Earth's surface, absorbed by atmospheric gases or aerosol (leading to heating of the atmosphere) or they may reach the Earth's surface, causing warming. The Earth and atmosphere may then emit photons at infrared wavelengths, which in turn can be absorbed, scattered etc. These radiative-transfer processes are the major methods in which heat is transferred from one region of the system to another. Following the method in Andrews [2010], the effect of the atmosphere can be investigated by considering two simple models; the first of the Earth with no atmosphere, and the second taking the effect of the atmosphere into account.

2.1.1.1 A simple radiative model with no atmosphere

The solar constant (total irradiance emitted from the sun) at the Earth's mean distance is $F_S = 1370\ Wm^{-2}$. However not all of this power is available to heat the Earth's surface - the amount intercepted by the Earth is contained in a tube of cross-sectional area πa^2 where a is the radius of the Earth (see Figure 2.1). Therefore, the total solar energy received by the Earth from the sun is $F_s \pi a^2$.

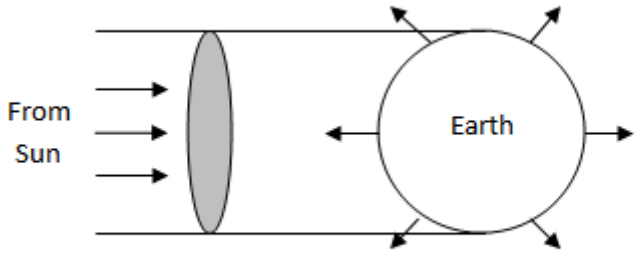


Figure 2.1*: Schematic showing the calculation of the amount of solar energy intercepted by the Earth. The parallel arrows represent solar radiation, the radial arrows outgoing thermal radiation.*

The albedo A of the Earth is 0.3 i.e. 30% of incoming shortwave radiation is reflected back to space. Total absorbed solar energy is therefore $(1 - A)F_S \pi a^2$. Assuming the Earth emits as a black body, then the power emitted can be described by the Stefan-Boltzmann equation:

$$Power\ emitted\ per\ unit\ area = \sigma T^4 \qquad 2.1$$

where σ is the Stefan-Boltzmann constant. An equilibrium expression can be therefore written as

$$(1 - A)F_S \pi a^2 = 4\pi a^2 \sigma T^4 \qquad 2.2$$

This gives the temperature of the Earth as $T \approx 255\ K$, which is much lower than the observed mean surface temperature of $T = 288\ K$. This difference must therefore be accounted for by the presence of the atmosphere, which can now be considered.

2.1.1.2 A simple radiative model including an atmosphere

Consider adding a layer of atmosphere of temperature T_a to the model described above. The solar flux at the top of the atmosphere, taking into account albedo and the intercepted area, is

$$F = \frac{1}{4}(1 - A)F_S \approx 240\ Wm^{-2}$$

2.3

Of this, a fraction $\tau_{SW}F$ is absorbed by the ground and therefore $(1 - \tau_{SW})F$ is absorbed by the atmosphere, where τ_{SW} is the fraction of shortwave radiation transmitted by the atmosphere. Assuming the surface emits as a black body, then from equation 2.1 the emitted flux from the surface is $F_g = \sigma T_g^4$. The longwave transmittance of the atmosphere is τ_{LW} and therefore the fraction of surface radiation reaching the top of the atmosphere is $\tau_{LW}F_g$. The remainder is absorbed by the gases in the atmosphere, which in turn emits as a black body, emitting a flux of $F_a = (1 - \tau_{LW})\sigma T_a^4$ both upwards and downwards. These processes are summarised in Figure 2.2.

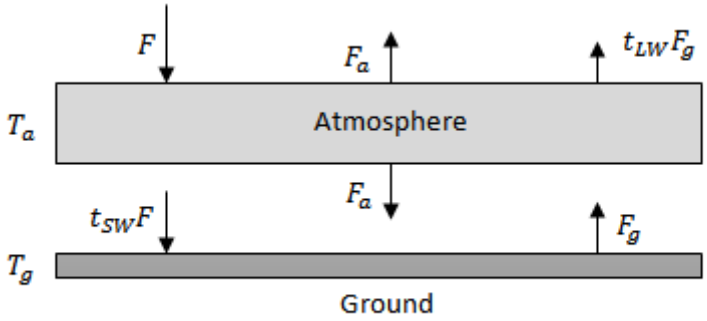


Figure 2.2: *A simple model of the greenhouse effect.*

If the system is in radiative equilibrium, then the fluxes can be equated as

$$F = F_a + \tau_{LW}F_g$$

2.4

above the atmosphere and

$$F_g = F_a + \tau_{SW}F$$

2.5

below the atmosphere.

Rearranging and eliminating F_a gives

$$F_g = \sigma T_g^4 = F\frac{1+\tau_{SW}}{1+\tau_{LW}} \qquad 2.6$$

Approximate values for τ_{SW} and τ_{LW} in the Earth's atmosphere are 0.9 and 0.2 respectively, giving a temperature for the Earth's surface of $T_g \approx 286\,K$, a much closer value to the observed mean temperature.

This is a simple model of the greenhouse effect, a natural phenomenon that accounts for the difference between the external radiative temperature of the planet, and the warmer surface temperature - a difference that allows life to flourish. The effect arises due to the fact that most incident shortwave radiation from the sun is transmitted to the ground (i.e. passes easily through the atmosphere) while most outgoing longwave radiation emitted from the Earth's surface is absorbed by gases within the atmosphere, resulting in 'trapping' of the heat. Gases that contribute strongly to this effect by allowing solar radiation to be transmitted but absorbing and emitting longwave radiation are known as greenhouse gases [*Andrews*, 2010].

If there are clouds present, the effect on the system is less well understood, and this is an active research area. However, it can be said that the presence of clouds has a two-fold effect: Firstly, clouds can reflect the incoming solar radiation back to space, resulting in a cooling effect. Secondly, they can absorb upwelling longwave radiation from the Earth, thereby causing warming. Which of these two effects is dominant depends on the microphysical properties of the clouds e.g. particle composition, size, shape and concentration, cloud altitude and temperature [*Harries*, 2000]. This is further discussed in §2.3.

2.1.2 The Earth's radiative energy budget

The amount of energy provided to the Earth-Atmosphere system from the Sun is known as the radiative energy budget, as shown in Figure 2.3. On the left-hand side of Figure 2.3 incoming shortwave radiation is shown to take part in four main processes; it may be reflected back to space by clouds, aerosols and atmospheric gases, or by the Earth's surface, or it can be absorbed by the surface or by gases in the atmosphere. The right-hand side of Figure 2.3 shows the processes that occur when longwave radiation is emitted from the Earth. It can be seen that apart from a small amount that emits straight to space in the atmospheric window region (described further below) all of the emitted LW radiation is absorbed by clouds or by greenhouse gases in the atmosphere. These then re-emit radiation to space (the OLR) or back down to the surface. The method by which greenhouse gases absorb longwave

radiation is through the gas molecules being excited by the available energy, causing translational, vibrational or rotational movements. Since these vibrational, rotational and transitional energy levels are quantized, energy exchanges can only occur at discrete energies. Energy is proportional to frequency ($E = hf$), and therefore the atmosphere will only absorb and emit radiation at certain frequencies.

Radiation in the atmosphere is described by various parameters including frequency f, wavelength λ or wavenumber υ, all of which are related by the speed of light c as shown in equations 2.7 and 2.8 below.

$$c = f\lambda \tag{2.7}$$

$$\upsilon = \frac{1}{\lambda} = \frac{f}{c} \tag{2.8}$$

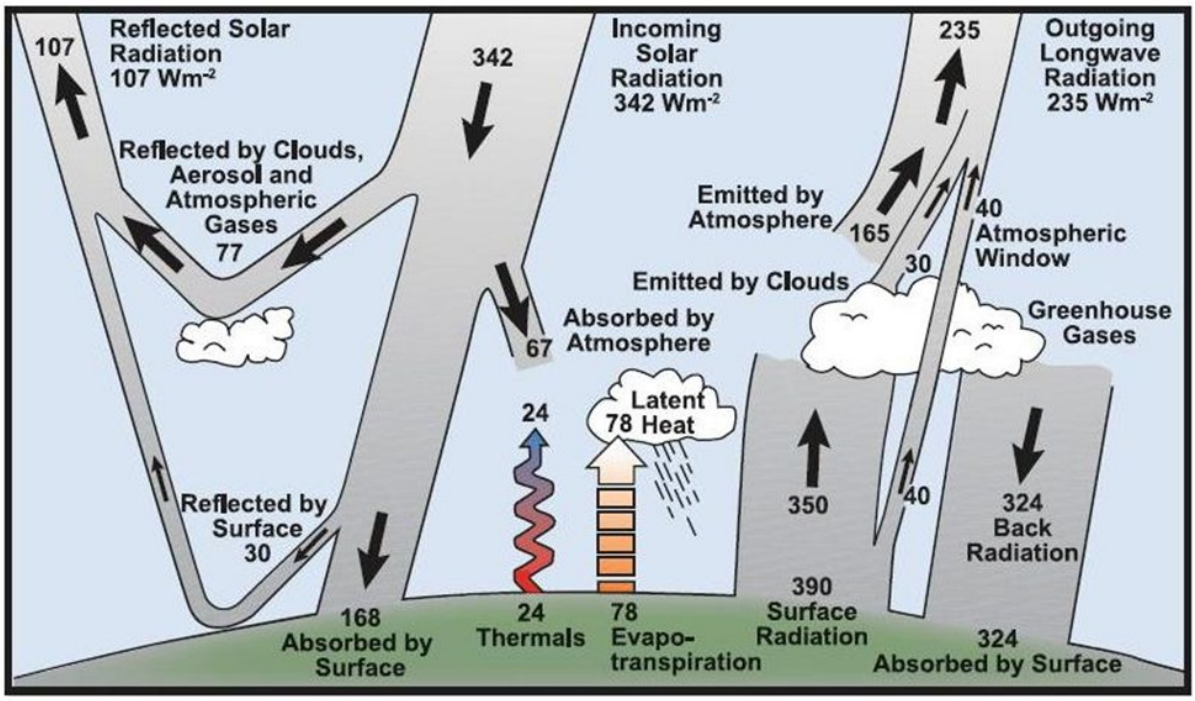


Figure 2.3: *Estimate of the Earth's annual and global mean energy budget, all units are in* Wm^{-2}. *From Kiehl and Trenberth* [1997].

The main greenhouse gases in the atmosphere and the wavenumbers at which they absorb can be seen in Figure 2.4, which shows the spectral Outgoing Longwave Radiation (OLR) at the Top of the Atmosphere (TOA) for five different standard atmospheres. If no gases were

present, the spectrum would be a smooth Planck radiation curve; however absorption lines at the wavenumbers of the molecular energy states can be seen. The five different atmospheres for which spectra are shown are tropical (blue), mid-latitude summer (green), sub-arctic summer (red), mid-latitude winter (yellow) and sub-arctic winter (purple). Figure 2.4 shows that the colder atmospheres (i.e. the winter ones) emit lower radiances due to the colder temperature of the Earth's surface.

The differences between a Planck radiation curve at the Earth's surface temperature and the OLR at TOA is known as the greenhouse parameter G_υ, which can be calculated from equation 2.9, where σ is the Stefan-Boltzmann constant, T_s is the surface temperature, and $T_{e,\upsilon}$ is the effective temperature of the emitted radiation at wavenumber υ.

$$G_\upsilon = \sigma\left(T_s^4 - T_{e,\upsilon}^4\right) \qquad 2.9$$

G_υ is plotted for five standard atmospheres in Figure 2.5, along with the Planck radiation curves for emission at the surface temperature of each atmosphere. Figure 2.5 clearly shows that the large CO_2 absorption band centred at 667 cm^{-1} is responsible for the largest values of G_υ, however the absorption caused by water vapour spreads over a much larger range of wavenumbers. In the longwave FIR region water vapour is the dominant absorbing species, and this region provides a high fraction of the total OLR absorbed by the atmosphere (see §2.1.3). Also visible in the diagram is the atmospheric window region 800-1250 cm^{-1}, where values of G_υ are close to zero; this spectral region is relatively transparent as there are few absorbing species.

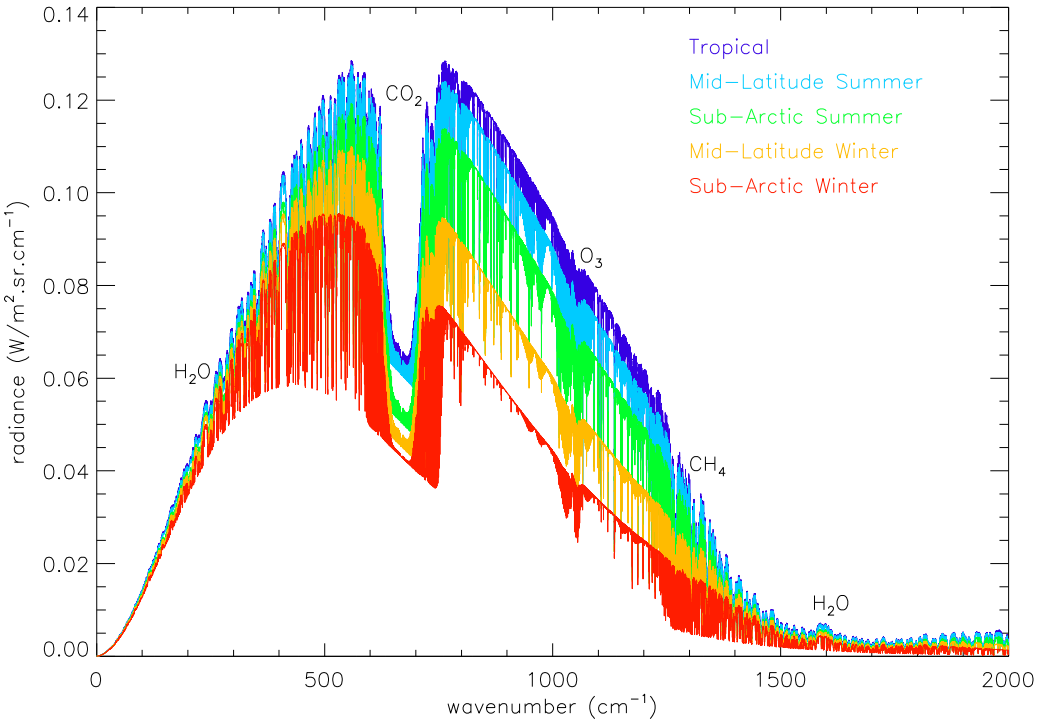


Figure 2.4: *Spectrum of OLR at TOA for five standard atmospheres, indicating the principal greenhouse gases in each spectral region.*

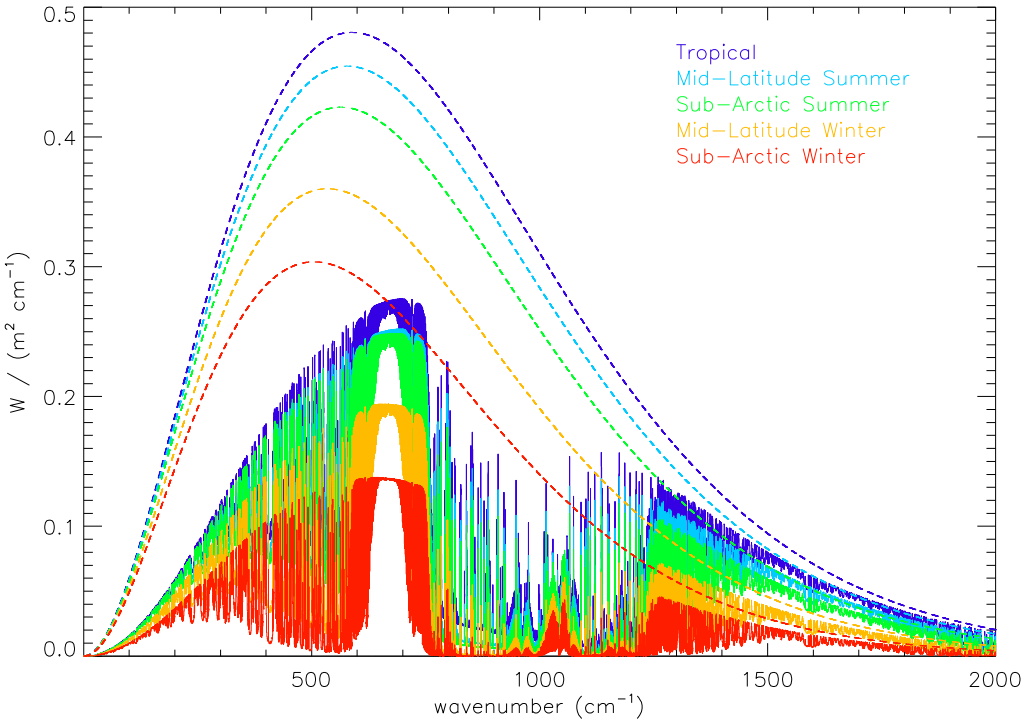


Figure 2.5: *Greenhouse parameter (solid lines) as a function of wavenumber for five standard atmospheres, with surface temperature emission (dashed lines)*

2.1.3 The importance of the far-infrared region

When viewed from space, the Earth may be described as an infrared object, as it emits radiation in the longwave part of the electromagnetic spectrum from wavelengths of around 1 mm to 4 μm (10-2500 cm^{-1}). This includes the regions known as the far-infrared (FIR) and the mid-infrared (MIR). There is no formal definition of where the boundary of the FIR occurs, but it is generally accepted to be wavelengths greater than about 15 μm, or wavenumbers below 667cm^{-1} [*Harries et al.*, 2008]. The effective surface emitting temperature of the Earth is ≈ 288 K as discussed in §2.1.1, and at this temperature the Planck curve peaks at around 500 cm^{-1}, meaning that the majority of OLR from the Earth is indeed in the FIR region. If it is taken into account that the Earth's upper troposphere falls to temperatures as low as 230 K (and therefore would emit radiation at longer wavelengths), it has been found that (depending on the latitude and humidity) between 27 and 35 % of the total energy escaping to space is of wavenumbers below 500 cm^{-1} [*Sinha and Harries*, 1995], and up to 45 % is below the FIR 'boundary' of 667 cm^{-1} [*Harries et al.*, 2008].

Figure 2.6 shows the radiative cooling rates for a clear sky (i.e. cloud free) tropical and a subarctic winter standard atmosphere as calculated by Brindley and Harries [1998]. A radiative cooling (or heating) rate may be defined as the rate of energy loss (or gain) of a volume of the atmosphere, $dQ/dt = Q$, where Q is heat energy. It can be evaluated as a function of altitude z and spectral wave number υ, thus identifying those regions of the atmosphere which contribute the most to emission of radiation to space. The cooling rate is equal to the vertical gradient of the net radiative flux F_N, (where net radiative flux = downwelling flux - upwelling flux, or $F_N = F^{\downarrow} - F^{\uparrow}$ [*Andrews*, 2010]) and is usually expressed as a rate of change of temperature for the volume of air concerned. The total radiative cooling rate may be found by integrating equation 2.10 over υ and z [*Harries et al.*, 2008].

$$h_{\upsilon}(z) = \frac{dT_{\upsilon}(z)}{dt} = \frac{Q_{\upsilon}}{\rho(z)c_p} = \frac{1}{\rho(z)c_p}\frac{dF_{N,\upsilon}(z)}{dz} \qquad 2.10$$

In Figure 2.6 the radiative cooling rates for both (a) tropical and (b) subarctic winter standard atmospheres is shown to be high at wavenumbers in the FIR below 667 cm^{-1}. This reinforces the importance of the FIR to the radiative balance of the Earth, as one third and one quarter of the total greenhouse forcing occurs in this region for the subarctic and tropical atmospheres respectively [*Brindley and Harries*, 1998]. Additionally, Figure 2.6 shows that radiative

cooling rates are high at pressures of 200-800 mb, i.e. in the mid-to upper troposphere where clouds are likely to be located.

As discussed in §2.1.2, the main absorbing atmospheric gas in the FIR is water vapour. In addition, there is absorption and scattering of radiation at these wavelengths by clouds, particularly cirrus, which is composed of ice crystals. The remainder of this chapter goes on to describe the effects of water vapour and cirrus in the atmosphere.

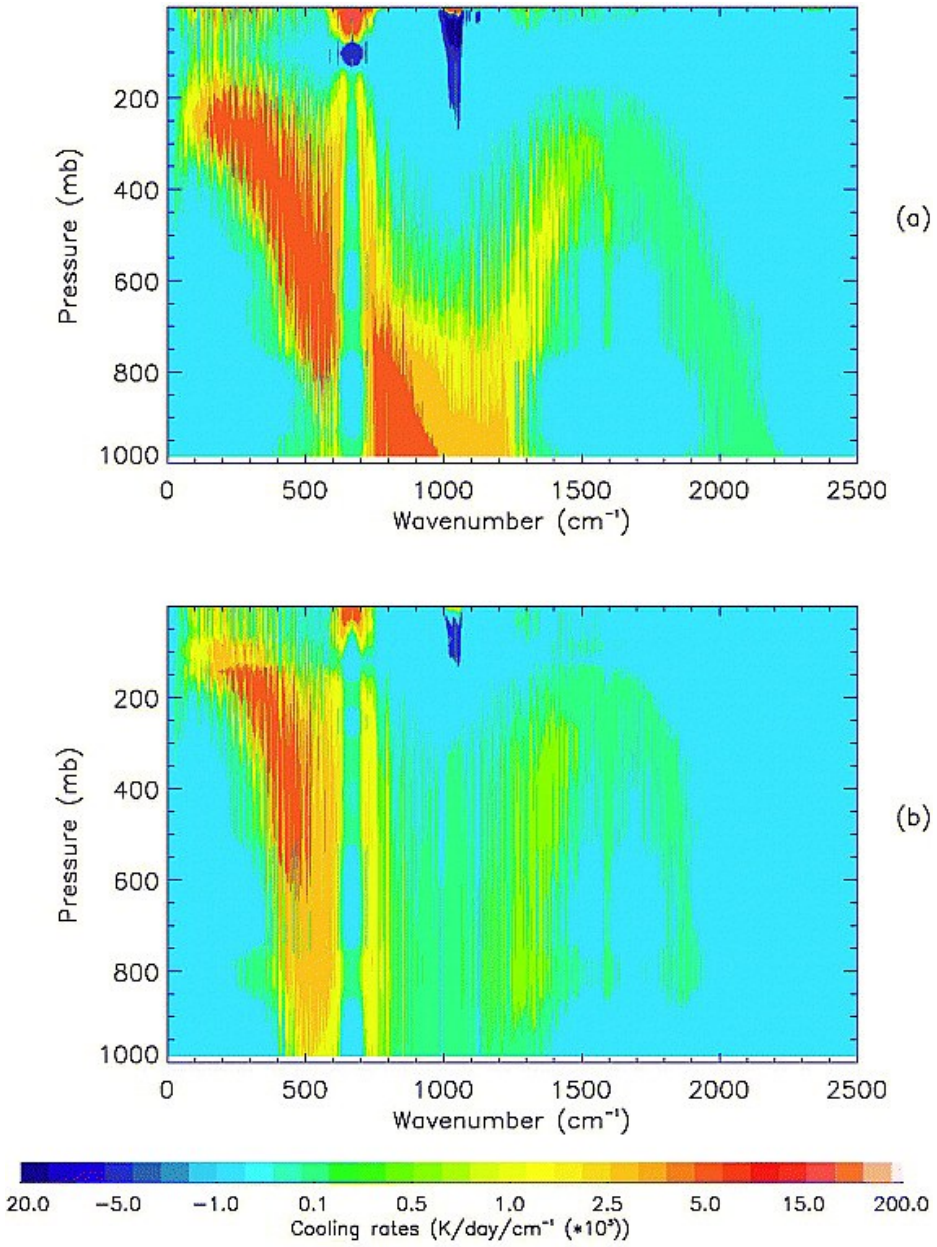


Figure 2.6: *Cooling rate from the Earth's surface to TOA for (a) tropical and (b) subarctic winter standard atmospheres with no clouds present. From Brindley and Harries [1998]*

2.2 Atmospheric water vapour

2.2.1 Introduction

The importance of water vapour as a greenhouse gas was first identified by John Tyndall in 1861. From his laboratory experiments, he determined that the dominant trapping of heat in the atmosphere was primarily due to the trace gases water vapour and carbon dioxide, which constitute less than 1% of the atmospheric mass [*Tyndall*, 1861]. As described in §2.1, atmospheric water vapour absorbs strongly in the infrared in the spectral region 0-800 cm^{-1} and is the most significant absorber of atmospheric radiation below 600 cm^{-1}. It is therefore important that its spectrum is accurately defined if the Earth's energy balance is to be understood.

Discussions on climate change often focus on increased concentrations of CO_2 caused by anthropogenic activity and the resultant rise in global temperatures as the increased CO_2 levels absorb a higher fraction of radiation. In comparison, water vapour may not appear to contribute significantly to climate change, as human activity does not directly increase its levels in the atmosphere by any great amount. However, it still has a critical effect, and this can be explained by examining the two main processes behind changes in climate - forcings and feedbacks. Forcings can be broadly defined as direct changes due to an external input i.e. the global temperature changes directly caused by an increase in solar irradiance, or increased CO_2 levels, or an increase in atmospheric aerosol caused by volcanic activity. Feedbacks on the other hand, are the changes in the climate which occur in response to forcings. Research has shown that the recent increases in CO_2 (a forcing) will cause higher surface temperatures, which in turn will lead to increased evaporation from the oceans and a higher concentration of atmospheric water vapour. This would create further surface warming due to the increased absorption of radiation, and therefore further evaporation and so on. Figure 2.7 shows this cycle, with the white curls indicating evaporation, which is balanced by precipitation. The red arrows demonstrate the outgoing infrared radiation, which is partially absorbed by water vapour and other greenhouse gases. The upper-left insert in Figure 2.7 shows how the amount of atmospheric water vapour changes with a change in temperature; this is roughly equal to a 7% change in water vapour with every degree change in temperature [*IPCC*, 2013].

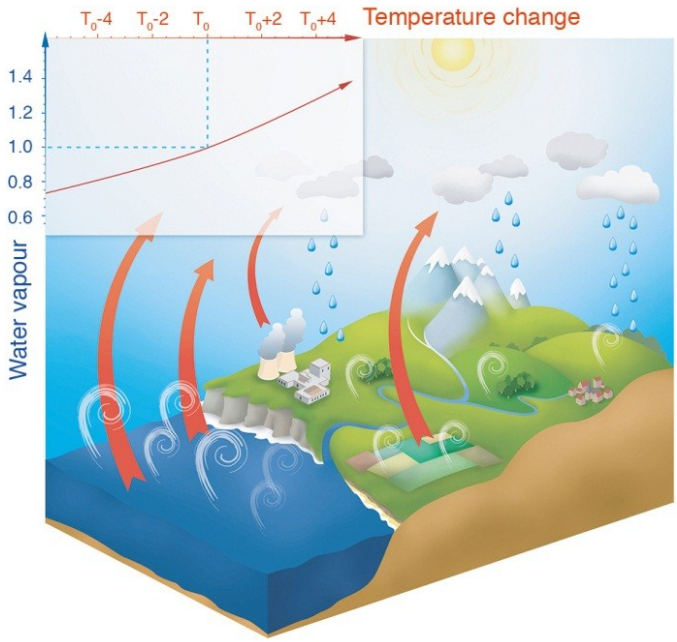


Figure 2.7: *Illustration of the water cycle and its interaction with the greenhouse effect. The insert (upper-left) shows how the amount of atmospheric water vapour would increase with an increase in temperature. From IPCC* [2013].

It is through this feedback process that water vapour makes a significant contribution to the enhanced greenhouse effect [*Harries*, 2000; *IPCC*, 2013]. This is described as a positive feedback, as the effect of warming the climate is to produce more warming. Conversely, a negative feedback would be one in which warming the climate creates a cooling effect in response.

If these effects are to be parameterised in a model, the absorption and emission spectra of water vapour must be known accurately, particularly in the far-infrared at wavenumbers below 667 cm^{-1} [*Harries et al.*, 2008]. Absorption by water vapour has a notable feature; the water vapour continuum, which is discussed in the following section.

2.2.2 The water vapour continuum

As discussed in §2.1.2, absorption and emission of radiation by atmospheric gases is caused by excitations or de-excitation of electrons between levels, or by vibrational or rotational movements of the molecules. These energy changes are discrete, and thus result in well-defined spectral lines at known wavelengths. However, in addition to the absorption from individual spectral lines, water vapour exhibits an underlying slowly varying component known as the continuum, which can be observed in the microwindows between lines [*Shine et al.*, 2012].

A cause of the continuum absorption was first put forward by Elsasser [1938a, 1938b], who after noticing that the absorption was not at wavelengths where water vapour has vibrational or rotational bands, theorised that the absorption was caused by the 'far wings' of strong water monomer lines. These far wings are due to broadening of spectral lines, which changes the wavelengths of allowed transitions slightly, and photons of slightly greater or smaller wavelengths may be absorbed or emitted. The result of this is that instead of being thin and well defined, single spectral lines typically have a bell curve shape, the peak and HWHM of which depends on temperature and pressure [*Harries et al.*, 2008]. This broadening is caused by several processes including the Doppler Effect, collisions with other molecules or effects of neighbouring molecules, and is discussed further in §4.2.

A different explanation for continuum absorption in the microwave region was given by Viktorova and Zhevakin [1967], who suggested that the water dimer rotational spectrum was causing the additional absorption. Penner and Varanasi [1967] then also proposed that the absorption was due to 'intermolecular coupling' rather than the water monomer. The water dimer $(H_2O)_2$ is caused by water molecules forming temporary bonds when they collide in the atmosphere. Water vapour is especially prone to this, as it is a strongly polar molecule i.e. it has an unbalanced distribution of electrons between the oxygen and hydrogen ions. This results in a negative charge around the oxygen ion and a positive charge around the hydrogen ions, allowing the molecule to make asymmetric vibrations and rotations. Two water molecules are able to form a bond through their opposing positive and negative charges, making a water dimer [*Shine et al.*, 2012]. These dimers are thought to contribute to the absorption spectrum of water vapour by the interaction of the dipoles changing the wavelengths of the vibrational and rotational states in the molecule [*Ptashnik*, 2008]. Water vapour may also form similar bonds with molecules of other atmospheric components such as N_2 and O_2. Again, this alters the distribution of charges and perturbs the vibrational and rotational states, contributing to the absorption spectrum [*Rowe and Walden*, 2009]. These two sets of interactions, water-water and water-air, are known as the self-broadened and foreign-broadened continuum respectively [*Held and Soden*, 2000].

The true cause of the continuum has not yet been resolved, however in order to determine how the water vapour continuum affects the Earth's energy budget, it is necessary to be able to represent its absorption accurately in radiative transfer models. In the FIR region of the spectrum, the shape of the water vapour absorption lines can be described by a Voigt lineshape. However, in the 'wings' extending either side of the absorption lines, there is a deviation from this model. The width and intensity of these wings depends on wavenumber,

temperature, pressure and interactions with other molecules. An early model of the continuum was formulated by Clough, Kneizys and Davies (CKD) [*Clough et al.*, 1989], and was adopted by many atmospheric radiative transfer models including the General Line-by-Line Atmospheric Transmittance and Radiance Model (GenLn2) [*Edwards*, 1992] and the Line By Line Radiative Transfer Model (LBLRTM) [*Clough et al.*, 2005], both of which have been used in many studies of water vapour absorption. The CKD model has undergone frequent updates since it was originally developed, as more data has become available. It is a semi-empirical model, based on a theoretical framework that is adjusted to fit new observations.

The CKD model assumes that all absorption within ±25 cm^{-1} of the line centre is the principal line, and all absorption beyond this is due to the continuum. The lineshape function used is the Lorentz function

$$L(\nu \pm \nu_i) = \frac{1}{\pi} \frac{\alpha_i}{(\nu \pm \nu_i)^2 + \alpha_i^2} \qquad 2.11$$

where ν is wavenumber relative to a line centre at wavenumber ν_{i_i}, with line half-width α_i. The continuum is incorporated through two functions $\chi(\nu)$, one for each of the foreign- and self- continua, which are multiplied by the line function given in equation 2.11 to give the line strength including the continuum contribution.

The foreign- and self-broadened continuum coefficients can therefore be defined as

$$C(\nu) = \sum_i S_i[L(\nu - \nu_i)\chi(\nu - \nu_i) + L(\nu + \nu_i)\chi(\nu + \nu_i)] \qquad 2.12$$

where the sum is performed over all water vapour lines and S_i is the intensity of the transition at wavenumber ν_{i_i}, with line half-width α_i [*Mlawer et al.*, 2012].

The most major update to the CKD model was in 2003, when it was replaced in the majority of radiative transfer models by the Mlawer-Tobin-CKD (MT-CKD) version [*Mlawer et al.*, 2003]. This newer formulation retains much of the original but has an updated set of functions to account for continuum measurements. It assumes that both far wings of lineshapes and collisional broadening (both self- and foreign-broadened components) contribute to continuum absorption, based on measurements of downwelling infrared radiances made by Turner et al. [2004]. It was also found that the collision induced

absorption is the dominant contributing factor within water vapour absorption bands, while far wings contribute more strongly in between these bands [*Mlawer et al.*, 2003]. Figure 2.8 shows TOA simulated radiances produced using the radiative transfer model LBLRTM, using a standard mid-latitude winter profile. One simulation includes the most recent MT-CKD v2.5 model and one has no contribution from continuum absorption. Figure 2.8 shows that the effect of the continuum is visible in the microwindow regions in between the spectral lines, where the spectrum including the continuum has lower radiances due to the increased absorption. This is because the continuum effect is a weak background absorption, and as such only has a significant contribution in those spectral regions where there is little absorption by spectral lines.

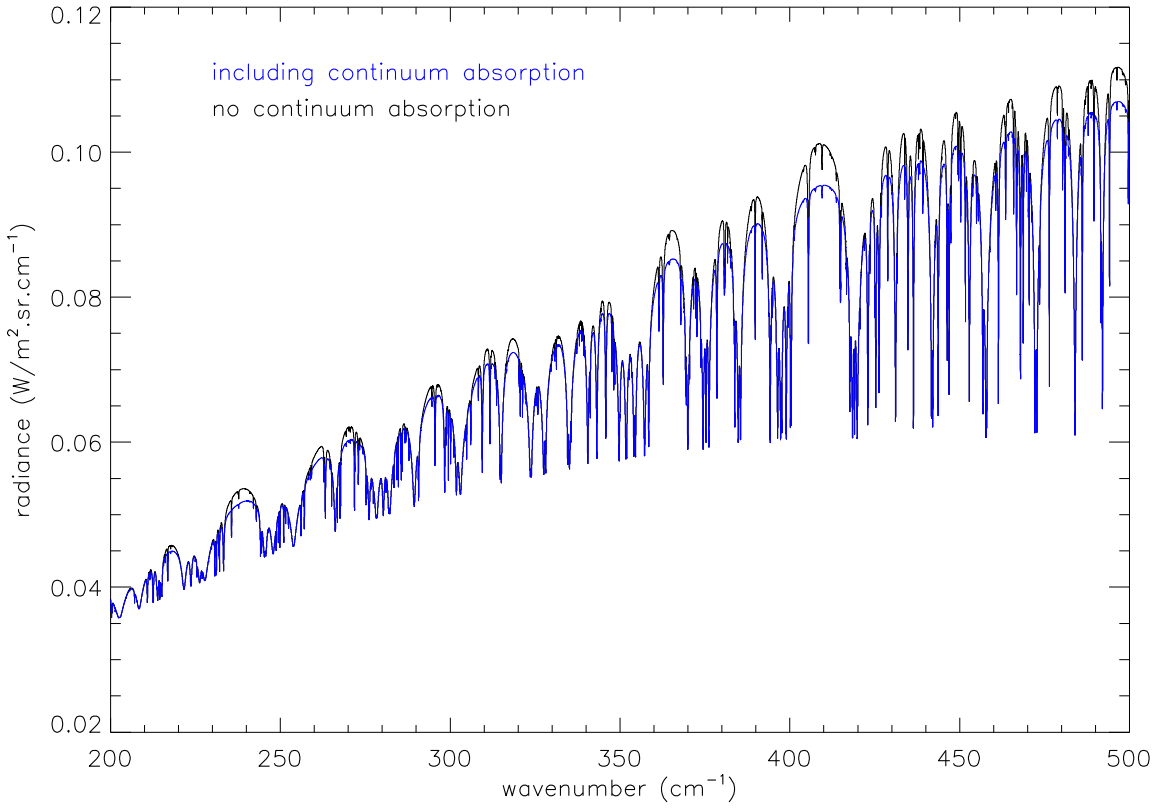


Figure 2.8: *LBLRTM simulations of TOA upwelling radiances using a mid-latitude winter standard profile. The spectrum in blue includes the MT-CKD v2.5 continuum model, the spectrum in black does not.*

2.2.3 Recent water vapour continuum studies

There have been recent studies to improve the water vapour continuum formulation in the far-infrared, a region of the spectrum that has not formerly been extensively studied, due to limitations in instrumentation.

Work by Green et al. during the Continuum Absorption by Visible and IR radiation and its Atmospheric Relevance (CAVIAR) airborne campaign over the Swiss Alps validated the current model parameterisation (MT-CKD 2.5) at wavenumbers above 300 cm^{-1} but recommended it be strengthened in the FIR by up to 50% below 100 cm^{-1} [*Green et al.*, 2012].

The Radiative Heating in Underexplored Bands Campaign (RHUBC) [*Turner and Mlawer*, 2010] at the Atmospheric Radiation Measurement (ARM) site in Barrow, Alaska, used two radiometers, AERI-ER (range 520-3020 cm^{-1}) and TAFTS (range 350-500 cm^{-1}), to take ground-based measurements of clear-sky downwelling radiances which were identified as being particularly good for investigating the water vapour continuum. The data recorded by AERI-ER resulted in a major update to the continuum parameterisation (MT-CKD 2.4) in the FIR range 400-600 cm^{-1} [*Delamere et al.*, 2010], and it is the analysis of the TAFTS measurements from this campaign [*Fox et al.*, 2015] that forms part of the work presented here (see §5).

The second phase of RHUBC took place in the Atacama Desert, Chile, in 2009 [*Turner and Mlawer*, 2010] and during this study three radiometers were deployed simultaneously: the Far-Infrared Spectroscopy of the Troposphere instrument (FIRST, [*Mlynczak et al.*, 2006]), the Radiation Explorer in the Far InfraRed (REFIR, [*Palchetti et al.*, 2005]) and an AERI [*Knuteson et al.*, 2004a]. Radiances from the three instruments were compared and found to agree within their overlap ranges, and data from FIRST (measurement range 100-1000 cm^{-1}) was used to validate the MT-CKD v2.1 and v2.4 continuum models. It was found that the models were not accurately representing the observations in the region 200-300 cm^{-1} [*Cageao et al.*, 2010].

Downwelling spectral radiances in the range 180-1100 cm^{-1} were recorded at the Dome-C site in Antarctica using the Radiation Explorer in the Far InfraRed – Prototype for Applications and Development (REFIR-PAD) instrument [*Bianchini and Palchetti*, 2008], and analysed by Liuzzi et al. [2014]. Their findings show good consistency between the current MK-CKD 2.5 model and observations, extending validation of this model much further into the FIR region. However this study highlighted discrepancies between

measurements and model simulations of >10 % at wavenumbers below 350 cm^{-1}, and concludes that water vapour absorptive line strengths may need to be adjusted [*Liuzzi et al.*, 2014].

2.3 Radiative properties of cirrus

Cirrus clouds are high, icy clouds that often have a tenuous or ghostly appearance to the observer. However, their importance in the radiation budget and hydrological cycle of the Earth should not be underestimated. This section highlights the microphysical and macrophysical properties of cirrus, its bulk scattering properties, and the impact of these properties on a global climate model.

Cirrus is a cold cloud consisting of ice particles. For these to form, temperatures must be low and therefore altitudes must be high; usually at least 6 km, with pure ice clouds existing at temperatures lower than 230K [*Guignard et al.*, 2012]. Cirrus is ubiquitous over the globe, present at all latitudes and relatively stable and long-lived, but because of its height in the atmosphere has not been extensively studied. Space-based satellite measurements reveal that about 30% of the Earth is covered by cirrus at any one time, with 60-80% coverage in the tropics [*Wylie et al.*, 1994; *Stubenrauch et al.*, 2006; *Nazaryan et al.*, 2008; *Lee et al.*, 2009; *Guignard et al.*, 2012]. Infrared satellite measurements show that semi-transparent cirrus make up 25% of all high clouds [*Guignard et al.*, 2012], and satellites operating in the visible region record that tropical daytime cirrus occurs about 40% of the time during January-July [*Heidinger and Pavolonis*, 2005].

Figure 2.9 shows the globally distributed fraction of high, middle, and low cloud in December-February and June-August, and from panels (a) and (e) illustrates that much of the high cirrus is located over the tropical zones between 60°N and 60°S.These wide-ranging spatial and temporal distributions indicate that cirrus is an important cloud type in its significance to the Earth's climate system. The most recent fifth assessment report of the Intergovernmental Panel on Climate Change [*IPCC*, 2013] identified the role of cirrus as a major source of uncertainty; cirrus has poor representation in GCMs [*Eliasson et al.*, 2011] and uncertainties are particularly large concerning microphysical processes affecting both cirrus amount and cloud opacity.

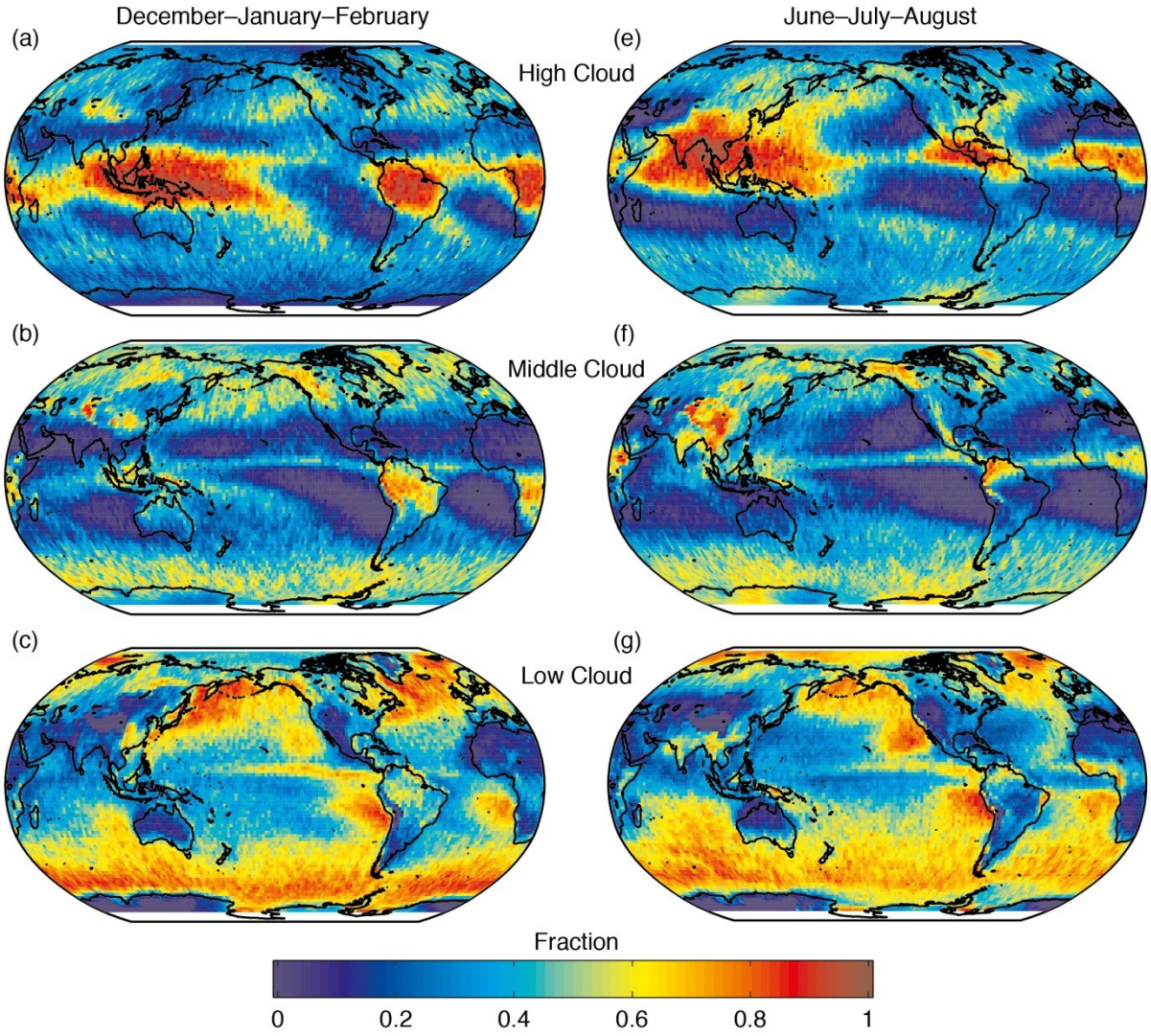


Figure 2.9: *Mean 2006-2011 cloud cover from CloudSat/CALIPSO [IPCC, 2013]*

2.3.1 The radiative effect of cirrus

The effect that cirrus has upon the radiation balance of the atmosphere can be summarised as the sum of the shortwave radiative effect and the longwave radiative effect, which are the differences between the cirrus reflected flux and the clear-sky reflected flux in the shortwave and longwave regions respectively. The balance between these greenhouse and albedo effects determines the net impact of cirrus on the climate system [*Lynch et al.*, 2002]. It has been shown that which process dominates is sensitive to the microphysical and macrophysical properties of the cloud, which in turn depend on their composition and location [*Stephens et al.*, 1990].

In general, the shortwave radiative effect is negative (i.e. cirrus has a cooling effect on the Earth's surface) as the presence of cirrus cloud acts to reflect a greater portion of the

incoming solar shortwave radiation back to space, preventing it from reaching the Earth or being absorbed by the atmosphere. Conversely the longwave radiative effect is generally positive (i.e. cirrus has a warming effect) as cirrus traps the emitted longwave radiation from the Earth, leading to greater absorption in the atmosphere. The net radiative effect of cirrus can therefore be positive, negative, or neutral [*Baran*, 2012].

The net radiative effect of cirrus is dependent upon a number of parameters including the cloud altitude and geometric size, the particle size distribution (PSD) and habit (shape) of the ice crystals that make up the cirrus, and the mass of ice contained within the cloud (the ice water content, IWC). The optical depth of the cloud, τ, which can be defined as the approximate ratio between the column integrated IWC and the ice crystal effective dimension (the longest axis of the crystal shape), is very important in determining how much radiation is transmitted or reflected. However, these properties are all highly variable and therefore difficult to parameterise in GCMs, leading to large uncertainties in studies investigating the effect that cirrus has on the Earth-atmosphere radiation [*Ringer et al.*, 2006; *Edwards et al.*, 2007; *Gu et al.*, 2011].

In order to reduce these uncertainties in the cirrus radiative effect, space-based measurements of the warming or cooling of cirrus have been recorded by satellite instruments. Choi and Ho [2006] examined six years (2000-2005) of cirrus observations from the MODIS and CERES instruments and found that the optical depth of tropical cirrus greatly affects the radiative effect: an optical depth of $\tau < 10$ gives a warming effect, and an optical depth of $\tau > 10$ gives a cooling effect. Additionally, they found that over 60% of tropical cirrus is optically thin, leading to an overall warming between 25°N-25°S, as the abundance of thinner cloud dominates over the cooling effect of the thicker clouds [*Choi and Ho*, 2006].

Other studies have shown the importance of ice crystal size and shape to the overall radiative effect of cirrus. Zhang et al. [1999] demonstrated that changing crystal size and keeping all other parameters constant (IWC, cloud vertical extent, crystal shape) resulted in a change in the flux at the Earth's surface from a cooling of -40 Wm^{-2} with small crystals, to a warming of 20 Wm^{-2} with larger ice particles. Additionally, a study by Fu [2007] found that for a cirrus cloud of optical depth $\tau = 4$, a change in the aspect ratio (i.e. ratio of length to diameter) of pristine hexagonal ice crystals from 1.0 to 0.1 would result in a change in shortwave radiative cooling from -30 Wm^{-2} to -70 Wm^{-2} respectively. Another parameter that has been found to affect the scattering of ice crystals is surface roughness. Laboratory studies

by Ulanowski et al. [2006] showed that ice crystals whose surfaces were roughened could reflect almost twice as much incident solar radiation back to space than smooth crystals, implying that cirrus made up of rougher crystals would have a much greater cooling effect.

These studies show that not only is cirrus cloud an important factor in the radiative balance of the Earth, but that its radiative effect is strongly dependent upon microphysical and macrophysical properties. Therefore, in order to improve the representation of cirrus in GCMs, and assess how this may change under the effect of climate change, a better understanding of these underlying properties is essential.

2.3.2 Cirrus properties

The properties of cirrus clouds are highly variable from cloud to cloud, and it is therefore difficult to assign a single set of values by which to characterise them in GCMs [*Dowling and Radke*, 1990]. This is particularly important when considering the radiative impact of cirrus on climate, as their infrared radiative properties are intrinsically linked to their physical properties [*Stephens et al.*, 1990]. Macrophysical properties are those which refer to the bulk physical properties of a whole cirrus cloud layer, while microphysical properties describe the properties of individual ice crystals that make up the cloud.

2.3.2.1 Macrophysical properties

Cirrus clouds are composed predominantly of ice, and it is this property that distinguishes them from the majority of other cloud types, which are composed of water droplets or a mixture of both ice and liquid water. Cirrus range in altitude from 4-20 km depending on latitude and season and have thickness varying between 0.1-8 km. Their IWC ranges between 0.0001-1.2 gm^{-3} and their visible optical thickness can vary from sub visual to opaque. This significant variation in properties results in many uncertainties when modelling the effect of cirrus on climate [*Lynch et al.*, 2002].

It is also uncertain how the properties of cirrus will change with changes in climate. In model studies, an increase in CO_2 causes increased cloudiness around the tropopause and reduced cloudiness in the upper troposphere, thus increasing the height of the cloud layer. This height increase has a two-fold effect: firstly, a higher cloud top has a lower temperature, thus reducing the upward radiation from the top of the atmosphere [*Wetherald and Manabe*, 1988]. Secondly, an increase in height changes the microphysical properties of the cloud. Studies show that increasing height clearly corresponds with increasing ice particle number density, decreasing effective radius, decreasing ice content and increasing net radiative

forcing [*Jensen et al.*, 1994]. Thus, the increase in CO_2 has a warming effect on the climate. An increased cloud height would also increase the amount of infrared radiation absorbed, as studies have shown that maximum absorption occurs in higher clouds, and least absorption in lower cloud. Again this would give a positive climate feedback from cirrus [*Maestri and Rizzi*, 2003]. However, it has also been shown that for cirrus clouds with an optical depth greater than $\tau = 0.8$, the increase in scattering and reflection of incoming solar radiation by ice crystals may outweigh the warming effect and overall be a negative feedback [*Ou and Liou*, 1984]. Thus the impact of climate change on cirrus is complicated, and even more so when microphysical properties are taken into account.

2.3.2.2 Microphysical properties

Cirrus clouds are composed predominantly of ice crystals, which vary in size from <10μm to many thousands of microns, and form a great variety of different shapes [*Heymsfield and Miloshevich*, 2003; *Field et al.*, 2007]. The amount of solar radiation transmitted and reflected from the clouds is determined by how light is scattered by these crystals. Climate models parameterise this scattering using the asymmetry parameter g, which represents the amount that light is scattered in the direction of the incident beam, and the optical depth τ, which gives the vertically integrated extinction of radiation entering the cloud [*Garrett*, 2003]. Using these two values, the fraction of solar radiation reflected by a cirrus cloud (the albedo) is approximately given by

$$A \approx \frac{\tau'}{1+\tau'} \qquad 2.13$$

where

$$\tau' = \sqrt{\frac{3}{2}(1-g)\tau} \qquad 2.14$$

However, for cirrus, the parameters g and τ are not well defined [*Meador and Weaver*, 1980]. The asymmetry term g is dependent on ice crystal shape and size, but as this is highly variable throughout cirrus, climate models often assume a single habit for all crystals, or an idealised mix of habits is used [*Baran*, 2005; *Baran and Labonnote*, 2007; *Baum et al.*, 2014]

In reality, ice crystals have irregular shapes that are not consistent through the extent of the cloud, giving a range of values for g; measurements in extra-tropical ice clouds generally show values for g of 0.73-0.78 [*Garrett et al.*, 2001]. The shape or 'habit' of the ice crystals has been found to be dependent on temperature and relative humidity as well as collision and coalescence processes in the clouds [*Liou*, 2002]. Ice crystal habits are generally classified using the scheme developed by Magono and Lee [1966], with examples shown in Figure 2.10.

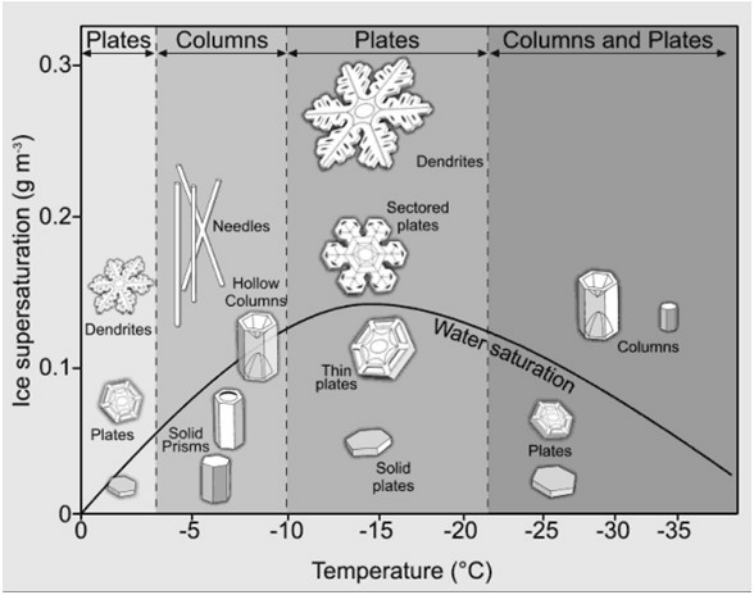


Figure 2.10: *The habits of ice crystals as a function of both ambient temperature and ice supersaturation (IWC)* [*Emersic*, 2012]

The relationship between crystal habit and temperature is summarised in Table 2.1, which shows hollow columns and hexagonal plates being dominant near the cloud top, spatial crystals such as bullet rosettes the most abundant above temperatures around -40°C and hollow or solid crystals dominating below about -50°C [*Heymsfield and Platt*, 1984].

Table 2.1: *Ice crystal habits observed in cirrus clouds* [*Heymsfield and Platt*, 1984]

Temperature	**Within main portions of cloud**		**Near cloud top**
	Convective clouds	**Stable clouds**	
Above -40°C	Spatial crystal forms Some columns, plates, bullets		Hollow columns, hexagonal plates
-40°C to -50°C	Predominantly spatial crystal forms	Predominantly hollow columns	Hollow columns, hexagonal plates
Below -50°C	Predominantly hollow or solid columns, some hexagonal plates	Predominantly hollow or solid columns, thick hexagonal plates	Hollow or solid columns, some hexagonal plates

The crystals at the top of the cloud are likely to be smaller because cirrus growth is proportional to vapour pressure. As vapour pressure is lower at higher altitudes, hence the crystals are smaller [*Lynch et al.*, 2002]. The distance from the top of the cloud has been found to be proportional to crystal size i.e. larger crystals are more likely to be found at the base of the cloud [*Heymsfield et al.*, 1990]. This is due to crystals falling through the cloud with gravity, giving them more time to grow and collide, forming large, irregularly shaped, aggregate crystals [*Heymsfield et al.*, 2002]. Thus a single cloud can contain a range of particle sizes, from small single ice crystals at cloud top, to aggregated crystals several cm in size at cloud base. The number density of ice particle sizes is known as the particle size distribution (PSD) [*Field et al.*, 2005, 2007]. An example of several PSDs measured by the 2DC cloud probe during the airborne WINter EXperiment (WINTEX) campaign [*Cox et al.*, 2010] is shown in Figure 2.11. The measurements are taken within cirrus of visible optical thicknesses $\tau = 0.3$ and $\tau = 0.1$, at four different altitudes. It can be seen that the maximum size of the PSD increases with decreasing height, this is due to large aggregate particles forming as crystals fall through the cloud as discussed above. Figure 2.11 also indicates a higher number of particles in the optically thicker cirrus than the optically thin.

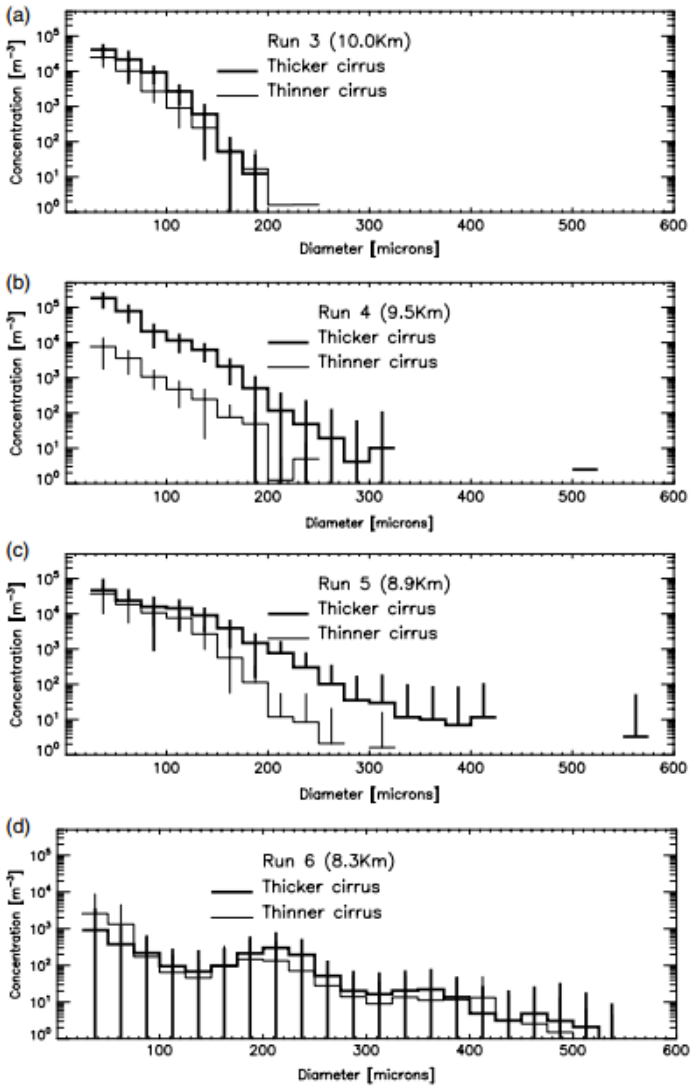


Figure 2.11: *In situ particle size distributions measured above optically thin and thick cirrus. From Cox et al. [2010]*

2.3.3 Observation of cirrus

Modern research into cirrus properties employs the use of many instruments: aircraft probes, airborne and ground-based remote sensing using lidar and radar, and radiometric probing by satellite. Information about cirrus optical properties can be retrieved from radiometric observations if it is known how these properties vary with wavenumber and how they are related to the physical properties of cirrus.

Studies indicate the importance of cirrus in the FIR region 100-500 cm^{-1} [*Maestri and Rizzi*, 2003], and as scattering by ice crystals reaches a local maximum at around 40-500 cm^{-1} (see Figure 7.6), cirrus properties at these wavenumbers are uniquely interesting [*Edwards and Slingo*, 1996]. Up to the present there have been relatively few measurements taken in these

spectral regions and FIR properties are mostly defined using modelling studies - an unsatisfactory situation given the inconsistencies found between cirrus observational data and models. Thus it is clear that further studies in the FIR are required to adequately describe this cloud type.

2.3.3.1 Space-based observations

There are a number of instruments currently in operation that have the ability to retrieve cirrus cloud properties in a range of different spectral bands. The International Satellite Cloud Climatology Project (ISCPP) uses a group of satellites that measure emitted infrared and reflected visible radiances. These can detect cloud presence and optical depth by comparison of the measured radiances with calculated expected radiances from models [*Rossow and Schiffer*, 1999]. The Moderate Resolution Imaging Spectro-radiometer (MODIS) [*Platnick et al.*, 2003], which flies on board the NASA Aqua and Terra satellites, measures reflected radiances in specifically chosen radiance bands (spectral range 0.4 to 14.4 μm), compares them to cirrus and surface reflectances and infers cirrus optical depth, ice water content and effective radius on a global scale [*Rolland et al.*, 2000; *Lee et al.*, 2009]. High resolution infrared spectrometers such as the Atmospheric Infrared Sounder (AIRS) [*Aumann et al.*, 2003] and the Infrared Atmospheric Sounding Interferometer (IASI) [*Blumstein et al.*, 2004], are able to simultaneously retrieve information about cirrus ice crystal effective particle size and optical depth by exploiting the sensitivity of mid-infrared spectral radiances to ice properties [*Yang et al.*, 2001]. The main active remote sensing techniques are radar and lidar, which emit radio waves and visible radiation respectively. Instruments utilising these techniques include the Cloud Profiling Radar on board the NASA CloudSat satellite, which provides estimates of global ice water paths [*Stephens et al.*, 2008] and the Cloud/Aerosol Lidar and Infrared Pathfinder Satellite Observation (CALIPSO) which carries a three channel elastic backscatter lidar [*Hunt et al.*, 2009].

2.3.3.2 Ground-based observations

The TAFTS instrument was deployed at the ground-based RHUBC campaign in 2007, as described in §2.2.3, and one of the aims of this campaign was to observe the spectral signature of cirrus. This was the first time that TAFTS had been used in its zenith-viewing geometry from a ground-based site. Results from this experiment showed that the fraction of ice water content attributed to small ice crystals in the cirrus PSD needed to be increased in order to gain the best agreement between observations and simulations. This study was

limited by a lack of in-situ measurements of cirrus ice particle size, and thus relied upon parameterised PSDs from other studies [*Humpage*, 2010].

Work by Maestri et al. [2014] analysed downwelling FIR spectral radiance measurements recorded by the REFIR-PAD instrument in the presence of cirrus. These observations took place at a ground-based site at 3500 m above sea level at the Testa Grigia station in Italy. Cloud properties were retrieved using radiosondes, a millimetre-wave spectrometer and a Raman lidar system. These properties were then used to simulate radiances in the region 250-1100 cm^{-1}, resulting in excellent observation-simulation agreement in the mid-infrared window, but large residuals in the FIR. This study concluded that ground-based studies of cirrus are prone to uncertainties in retrieved cloud properties and an incomplete knowledge of the atmospheric state, and that these uncertainties could be much reduced using a down-looking (satellite or aircraft) experimental configuration [*Maestri et al.*, 2014].

2.3.3.3 Airborne observations

Aircraft-based campaigns to study effects of cirrus in the far-infrared require several types of instrumentation. In addition to a radiometer such as TAFTS to take radiance measurements, the physical properties (ice crystal size and shape, optical thickness, particle size distribution etc.) of the cloud must be detected and recorded by auxiliary ice probes. These are required to allow simulation of spectra using radiative transfer models (see §4) for comparison with in-situ observations.

The TAFTS instrument, used in this work, has been previously deployed in airborne campaigns to measure properties of cirrus. In 2002, TAFTS recorded FIR spectral radiance observations of tropical convective outflow cirrus during the second phase of the Egrett Microphysics Experiment with Radiation, Lidar and Dynamics (EMERALD-II), which took place off the north coast of Australia. Simulations were performed using in-situ measurements of atmospheric state and cloud particle PSDs, and it was found that these simulations predicted a cirrus layer that was far more opaque than the one observed. Results from this experiment showed that small ice crystals were not being correctly counted during in-situ measurements, and that in order to gain the best agreement between observations and simulations, the small crystal concentrations in the measured PSD needed to be reduced by 66% [*Humpage*, 2010].

During the WINter EXperiment (WINTEX) campaign [*Cox et al.*, 2010], a series of UK Met Office winter experiments flown from Cranfield, UK, between October 2004 and February

2005, the TAFTS (FIR) and ARIES (MIR) radiometers were simultaneously flown on-board the FAAM aircraft to sample cirrus over the North Sea. Pressure, temperature and dew point temperature were recorded throughout the flight by core instrumentation on-board FAAM, and cloud microphysical measurements were taken using a 2-dimensional cloud probe (2DC) and a 2-dimensional precipitation probe (2DP) [*Knollenberg*, 1970], which sampled particle size and concentration. However, it was found that the cloud needed to be more thoroughly sampled in order to fully characterise the radiative effect of the cirrus, as the measured PSDs required scaling of the small crystal contribution in order to produce simulated radiances in agreement with observations.

The Cirrus and Anvils: European Satellite and Airborne Radiative measurement project (CAESAR) took place in the UK in four phases between November 2005 and July 2007. One of the scientific aims of CAESAR was to relate the cirrus microphysics to remote sensing data across the visible, thermal infrared, FIR and microwave regions of the electromagnetic spectrum. Again, the TAFTS and ARIES instruments were simultaneously flown on-board the FAAM aircraft, along with the 2DC and 2DP cloud probes. The data from this campaign proved to be problematic to analyse, due to noise issues caused by vibration of the beamsplitter inside the TAFTS instrument. Another problem that was identified was the shattering of large ice crystals on the inlets of the cloud probes, leading to a miscounting of particle sizes. This problem of shattering is well-known, and methods of identifying and filtering spurious particles using interarrival times [*Field et al.*, 2006] have now been developed and incorporated into the processing of data from cloud probes [*Baran*, 2012; *Cotton et al.*, 2013; *Baran et al.*, 2014].

These previous campaigns highlight the difficulty in studying cirrus radiative effect in the FIR region, and provide experience and knowledge that can be taken forward to new campaigns. One such campaign is the Cirrus Coupled Cloud-Radiation Experiment (CIRCCREX), the first stage of which took place in November 2013. Data from this campaign includes high-resolution radiative measurements over the entire infrared spectral range 100-3000 cm^{-1}, as well as detailed observations of the atmospheric state (e.g. temperature and relative humidity) and in situ cloud particle measurements from several state-of-the-art cloud probes. The analysis of these data forms part of the work presented in this thesis (see §7).

2.4 Summary

This chapter has used a simple model of the equilibrium balance of the Earth-Atmosphere system to demonstrate the role of gases in the atmosphere, and how changes in the concentration of these gases may affect this balance. There then followed a section on the importance of water vapour in the climate system, including further detail on the climate forcings and feedbacks associated with water vapour, and then focusing on the underlying continuum contribution to water vapour absorption. Section 2.3 described the physical and radiative properties of cirrus clouds and their role in the atmosphere, a description of how their macro- and micro-physical properties are linked, and a review of observation techniques and recent research.

3 Fourier Transform Spectroscopy: theory and instrumentation

This section describes Fourier Transform Spectroscopy (FTS), and how it can be used to determine how gases absorb and emit radiation in the atmosphere. Following this are descriptions of the three instruments used in this work to record infrared radiance measurements for comparison with simulations. These instruments: TAFTS, AERI-ER and ARIES, are all Fourier Transform spectro-radiometers, and thus this section includes an introduction to Fourier transform spectroscopy via the Michelson interferometer, and then goes on to describe a variation on this, the Martin-Puplett interferometer, on which TAFTS is based.

3.1 Introduction

Fourier transform spectroscopy (FTS) is a technique used to obtain a spectrum by applying a Fourier transformation to the output of a two-beam interferometer. It makes use of Fourier theory - the mathematical method of decomposing any continuous function into components of sine and cosine waves. The FTS theory is briefly described here, but much more detailed explanations are widely available e.g. [*Chamberlain*, 1979; *Thorne*, 1988; *Davis et al.*, 2001].

The basis of the FTS method is that any given function, $f(x)$ can be decomposed into its component sine and cosine functions. This means that a function $f(x)$ varying in the spatial domain x may be transformed using a Fourier transform equation to give a function in the frequency domain $F(\sigma)$. The converse transformation is also possible. The equations, or Fourier pairs, required to do these transformations are given in complex notation in equations 3.1 and 3.2.

$$f(x) = \int_{-\infty}^{\infty} F(\sigma) e^{+2i\pi\sigma x}\, d\sigma \qquad 3.1$$

$$F(\sigma) = \int_{-\infty}^{\infty} f(x) e^{-2i\pi\sigma x}\, dx \qquad 3.2$$

FTS can be used in situations where two beams of radiation interfere. The power in the interference pattern caused by these beams (the interferogram), which is measured as a function of distance, can be transformed into a frequency spectrum, made up of the power at all frequencies of each of the constituent waves. For example, a measured interferogram $I(x)$ can be related to its power spectrum $B(\sigma)$ using the complex form relations in equations 3.3 and 3.4.

$$I(x) = \int_{-\infty}^{\infty} B(\sigma) e^{+2i\pi\sigma x}\, d\sigma \qquad 3.3$$

$$B(\sigma) = \int_{-\infty}^{\infty} I(x) e^{-2i\pi\sigma x}\, dx \qquad 3.4$$

These relations can be written in terms of their sine and cosine functions, where the even cosine function comprises the real part and the odd sine function the imaginary part, as in equations 3.5 and 3.6.

$$I(x) = \int_{-\infty}^{\infty} B(\sigma)\cos(2\pi\sigma x)\; d\sigma + i\int_{-\infty}^{\infty} B(\sigma)\sin(2\pi\sigma x)\; d\sigma \qquad 3.5$$

$$B(\sigma) = \int_{-\infty}^{\infty} I(x)\cos(2\pi\sigma x)\; dx + i\int_{-\infty}^{\infty} I(x)\sin(2\pi\sigma x)\; dx \qquad 3.6$$

The use of FTS theory in the interpretation of output from a basic Michelson interferometer and then a Martin-Puplett interferometer, such as the one used in TAFTS, are described below.

3.1.1 The Michelson interferometer

In a Michelson interferometer [*Michelson*, 1890] (shown in a schematic in Figure 3.1), an incoming beam of light at input I_1 is divided into two beams of equal intensity and amplitude using a beamsplitter BS. These two resulting beams are then directed towards mirrors $M1$ and $M2$, where they are reflected back to the beamsplitter to be first recombined and then

divided a second time. This secondary pair of beams is then directed out of the interferometer, one via the same port as I_1, and the other out of the output port O_2, which may also be used as a secondary input. A detector is placed at one or both of the output ports.

When both mirrors are equidistant from the beamsplitter, the path difference is $x = 0$. The two beams are perfectly in phase, so when they are recombined they undergo constructive interference, resulting in all the input power exiting at O_2 and none being sent back to the source at O_1. If mirror M_2 is displaced one quarter wavelength $\lambda/4$, the path difference is now $\lambda/2$ and the beams interfere destructively when recombined, with all the power now going to O_1 and none to O_2. A further increase in path difference to $x = \lambda$ results in constructive interference, and further increases give a periodic sequence of maxima and minima at the detector at O_2. Maxima occur when the path difference is equal to $m\lambda$, and minima when it is equal to $m\lambda + \lambda/2$.

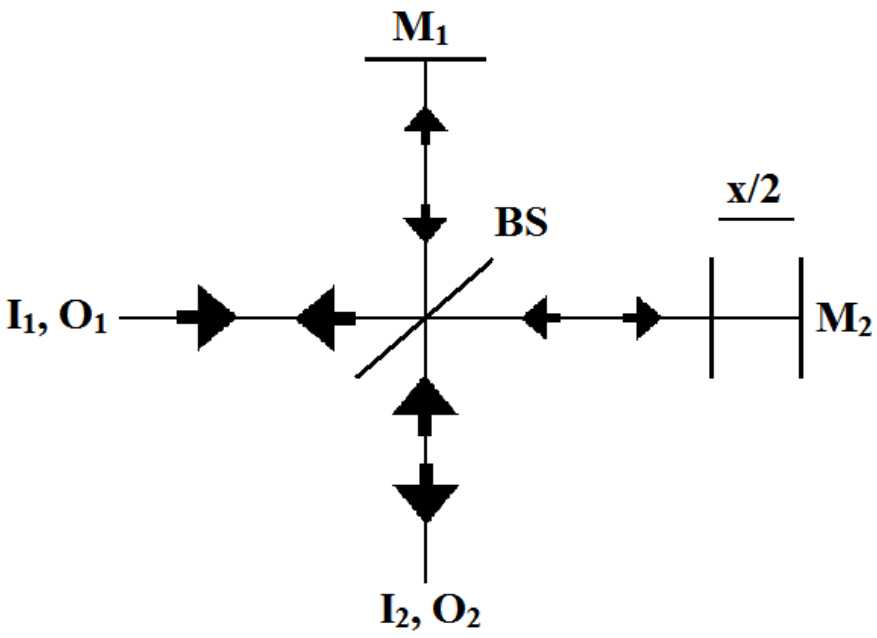


Figure 3.1: *Schematic of a Michelson interferometer. Incoming light enters at I_1 and is split at the beamsplitter BS. Half the signal is reflected to mirror M_1, and the other half to mirror M_2. Moving M_2 along the distance $x/2$ creates a difference in path length of x, resulting in interference when the beams recombine at BS. The beam is output to the detector at O_2.*

The intensity of the output beam at O_2 is

$$I_\sigma(x) = \bar{I}_\sigma(1 + \cos(2\pi\sigma x))$$

3.7

where σ is the wavenumber of the source radiation and $\bar{I}$ is the mean interferogram value. This output signal is a constant modulated by a cosine term - it is this cosine term that contains the spectral information on the measured radiation.

For a broadband source whose intensity is defined as $B(\sigma)$, the interferogram $I_0(x)$ can be written as an integral of all the individual monochromatic interferograms from each wavenumber component:

$$I_0(x) = \int_{-\infty}^{\infty} B(\sigma)(1 + \cos(2\pi\sigma x))\, d\sigma$$

$$= \int_{-\infty}^{\infty} B(\sigma) d\sigma + \int_{-\infty}^{\infty} B(\sigma)\cos(2\pi\sigma x)\, d\sigma$$

$$= \bar{I} + \int_{-\infty}^{\infty} B(\sigma)\cos(2\pi\sigma x)\, d\sigma$$

3.8

The modulated second term of equation 3.8 is the cosine Fourier transform of $B(\sigma)$, and therefore by performing the inverse cosine transform on the interferogram, the source intensity $B(\sigma)$ can be found [*Thorne*, 1988]. This gives the transform pair,

$$I(x) = \int_{-\infty}^{\infty} B(\sigma)\cos(2\pi\sigma x)\ d\sigma$$

3.9

$$B(\sigma) = \int_{-\infty}^{\infty} I(x)\cos(2\pi\sigma x)\ dx$$

3.10

FTS theory as utilized in the TAFTS instrument can now be considered, through the description of the Martin-Puplett interferometer.

3.1.2 The Martin-Puplett interferometer

The TAFTS instrument uses a Martin-Puplett interferometer [*Martin and Puplett*, 1969] which is similar in design to the Michelson interferometer, but with several distinct differences which give it an advantage at longer wavelengths in the far-infrared. The main difference between the two is that the Martin-Puplett splits the incoming beam by polarisation, rather than by amplitude. As well as being more efficient at longer wavelengths, this allows each input signal to remain distinct throughout its path through the interferometer, and therefore all four ports can be more easily used (two inputs and two outputs) without the signals becoming confused. In the case of TAFTS, this allows the instrument to sample both up-welling and down-welling radiation.

Figure 3.2 shows a schematic of a typical Martin-Puplett interferometer. It uses three plane wire grid polarisers $P1$, $P2$ & $P3$ which all effectively transmit one polarisation and reflect the orthogonal polarisation. It also uses two triangular rooftop mirrors $RM1$ and $RM2$. Here, perfect optical behaviour is assumed i.e. no losses at the components. Unpolarised radiation from two input ports I_1 and I_2 is incident upon polariser $P1$, which transmits parallel polarised light and reflects perpendicular polarised light. Half the power from each beam is lost, and the other half, which contains a combined signal made up of components from both inputs polarised orthogonally to each other, is directed into the rest of the interferometer. The polariser $P1$ can be referred to as a beam combiner.

The second polariser $P2$ acts as the beam splitter, as its grid is oriented at 45º with respect to rays emerging from $P1$. Polariser $P2$ divides the beam by polarisation, as half the beam will have parallel polarisation and will be transmitted, whereas half will have perpendicular polarisation and will be reflected. The resultant two beams are directed towards rooftop mirrors $RM1$ and $RM2$, which are designed to rotate the angle of polarised light by 90º. Thus when the beams are returned to $P2$ the half that originally was reflected will now be transmitted and vice versa, and so the beams will be recombined. However, one rooftop mirror can be moved in the direction of the beam distance $x/2$, and therefore a path difference x can be introduced, resulting in interference of the beams when they are recombined. The recombined beam is now directed towards the third polariser $P3$ which is

polarised at the same angle as $P1$, therefore splitting the beam into two outputs $O1$ and $O2$. These outputs both contain components of the original two inputs $I1$ and $I2$.

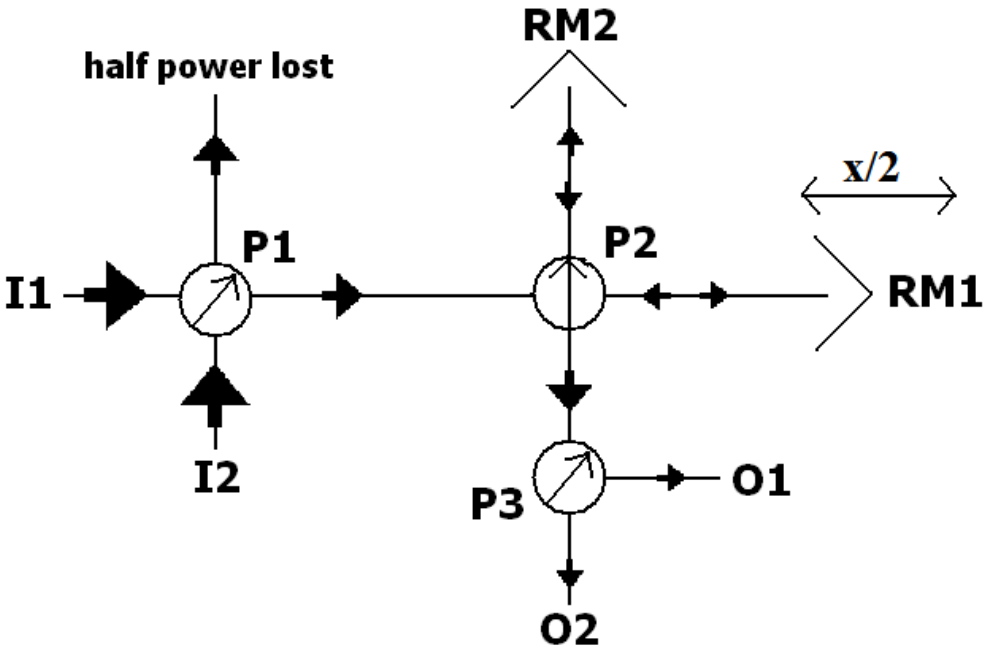


Figure 3.2: *Schematic of a Martin-Puplett interferometer. The two inputs $I1$ and $I2$ are directed into the system by polariser $P1$, before being divided by polarisation at polariser $P2$. The two divided signals are reflected by rooftop mirrors $RM1$ and $RM2$, one of which can be moved along distance x to create a path difference between the two signals. They are recombined when they return to $P2$, at which point they interfere according to the path difference. Finally the signal is divided again at polariser $P3$ and directed to two sets of detectors at the outputs $O1$ and $O2$.*

If the intensity of the two input sources are I_1 and I_2, and f_1 and f_2 are the fractions of these initial intensities that are measured at the output ports $O1$ and $O2$, a detector at either output will register the total power from both inputs, given by equation 3.11. The contribution of each input source that is detected at the outputs is dependent on the path difference x and the wavenumber σ [*Martin and Puplett*, 1969].

$$f_1 I_1 + f_2 I_2 = \frac{1}{2}(I_1 + I_2) \pm \frac{1}{2}(I_1 - I_2)\cos\left(\frac{2\pi\sigma x}{\lambda}\right) \qquad 3.11$$

The second term in equation 3.11 gives the modulated part of the measured radiation at each output, and is the difference in intensity of the original two inputs. This is the source of the differential measurement made by TAFTS and is exploited when both calibrating and measuring net radiation in the atmosphere.

Overall, the Martin-Puplett interferometer has several advantages for measuring low intensity radiance in the far-infrared, including greater efficiency in the beamsplitters and the ability to measure two sources simultaneously. These were some of the reasons that this design was selected for use in the TAFTS instrument. The reasoning behind the use of an FTS for the atmospheric measurements taken by TAFTS, as opposed to a different design of spectrometer, is explained below.

3.1.3 Advantages of Fourier transform spectroscopy

An FTS has several advantages over other designs such as a grating spectrometer, the main one being its ability to measure a wide range of wavelengths simultaneously with a small number of detectors. This is known as the multiplex or Fellgett advantage, and greatly reduces the time required to observe many frequencies - a grating spectrometer would need to scan each frequency separately [*Davis et al.*, 2001]. This is particularly useful in situations where the FTS is constantly moving i.e. on an aircraft platform, as the full range of necessary frequencies can be recorded for each instantaneous optical view. Multiplexing also allows the FTS to have a single set of detectors, reducing the cost, or increasing the spectral coverage by allowing detectors of greater sensitivity to be used at lower expense. The single set of detectors also decreases the size of the instrument, making it easier to build and transport.

Another advantage of the FTS is that it can operate using a larger aperture than other spectrometers, increasing the amount of radiation input to the system and allowing a greater signal-to-noise ratio. This is called the throughput or Jacquinot advantage. The resolving power of a spectrometer is inversely proportional to aperture size, as the interferogram is multiplied by a sinc function related to the aperture width. However, this effect is dependent on wavenumber and is minimal in the longer wavelengths of the far-infrared [*Thorne*, 1988].

The following sections go into detail of the design of the three radiometers used to record measurements for this work. The TAFTS instrument is described in most detail, as the author both operated the instrument during the CIRCCREX campaign (see §7), and calibrated and analysed the data recorded. Data from the other two radiometers described were recorded and processed by other groups.

3.2 TAFTS

The TAFTS instrument [*Canas et al.*, 1997], pictured in Figure 3.3, is a polarising Martin-Puplett interferometer as described in §3.1.2. It was designed and built at Imperial College London and has been utilised in several science campaigns, both ground-based and airborne. TAFTS is uniquely capable of recording high resolution (0.12 cm^{-1}) in-situ FIR (80-600 cm^{-1}) radiance measurements in both the nadir and zenith directions. The spectral range of the instrument covers the majority of the water vapour pure rotation band. During the design of TAFTS, several challenges resulting from the aircraft environments in which the instrument would be operating needed to be considered. The instrument needed to be as compact and light as possible, while being sturdy enough to withstand flight conditions. The instrument also encounters aircraft vibrations, rapidly changing scenes and changes in temperature and pressure, and therefore efforts needed to be made to minimise any effect these may have on the data that is recorded. TAFTS is made up of four main sections; the pointing optics box (which directs incident radiation into the instrument and also contains four calibration black bodies), the interferometer chamber, the cryostat (containing liquid helium cooled detectors) and the instrument electronics. The first three of these are bolted together in the main bulk of the instrument (as shown in Figure 3.3); the electronics are housed separately. Each of these components will now be discussed in order to give a full overview and understanding of the instrument and the data which it records.



Figure 3.3: *The TAFTS instrument. The two aluminium sections are the pointing optics box and main interferometer chamber, the blue cylinder is the cryostat.*

3.2.1 Pointing optics box

An advantage of TAFTS is its ability to simultaneously record up- and down-welling radiances. This is one of the reasons that a Martin-Puplett design was chosen - the two input ports allow one port to sample in the nadir direction and one in the zenith. This results in the Pointing Optics Box (POB) comprising two 'arms', one nadir and one zenith, containing steerable gold plated mirrors which control the radiation being viewed by the instrument. The POB also contains four black body calibration targets ($BBh_z, BBc_n, BBh_z, BBc_n$), where the acronym denotes whether the black body is hot (h, approximately 50ºC) or cold (c, ambient outside air temperature, maintained above 0ºC by heaters) and whether it is located in the nadir (n) or zenith (z) arm. The temperature of each of the blackbodies is measured by a Platinum Resistance Thermistor (PRT) located inside the blackbody cavity.

The layout of the POB is shown schematically in Figure 3.4. Radiation enters the POB through the portholes in the top and bottom of the box (DW and UW apertures), allowing both nadir (UW) and zenith (DW) scene views. The steerable mirrors A and E can be adjusted to swap between scene views and views of the black bodies in the two arms of the instrument, giving rise to nine possible configurations viewing either the hot (h) or cold (c) black bodies in one or both arms, or the scene views (z or n) in one or both arms. By convention, these configurations are noted with nadir input view first, and the zenith input second i.e. c_nh_z, h_nc_z, c_nc_z, h_nh_z, n_nc_z, n_nh_z, c_nz_z, h_nz_z, and n_nz_z, where the subscripts denote the nadir (n) and zenith (z) arm of the instrument. For example, for the configuration h_nz_z, the nadir arm is viewing the hot blackbody, while the zenith arm is viewing the zenith scene view i.e. the down-welling radiation.

Fixed mirrors B & D, and F & G direct the radiation from the downwelling and upwelling arms respectively into the main interferometer through two vacuum windows C and H. These windows are made from 40 μm thick polypropylene, which has high transmission in the FIR. The viewports on the POB (labelled DW and UW apertures in Figure 3.4) that allow scene view radiation to enter do not have any windows (this is so that scene view and black body radiation travels along the same optical path) and so the POB must be kept in good condition to prevent degradation of the optical components by any grease, dirt, water etc. that enters from the outside air. This also introduces a problem with residual water vapour inside the POB absorbing radiation and producing extra spectral lines. A small temperature probe is also located inside the POB to allow monitoring of the internal temperature.

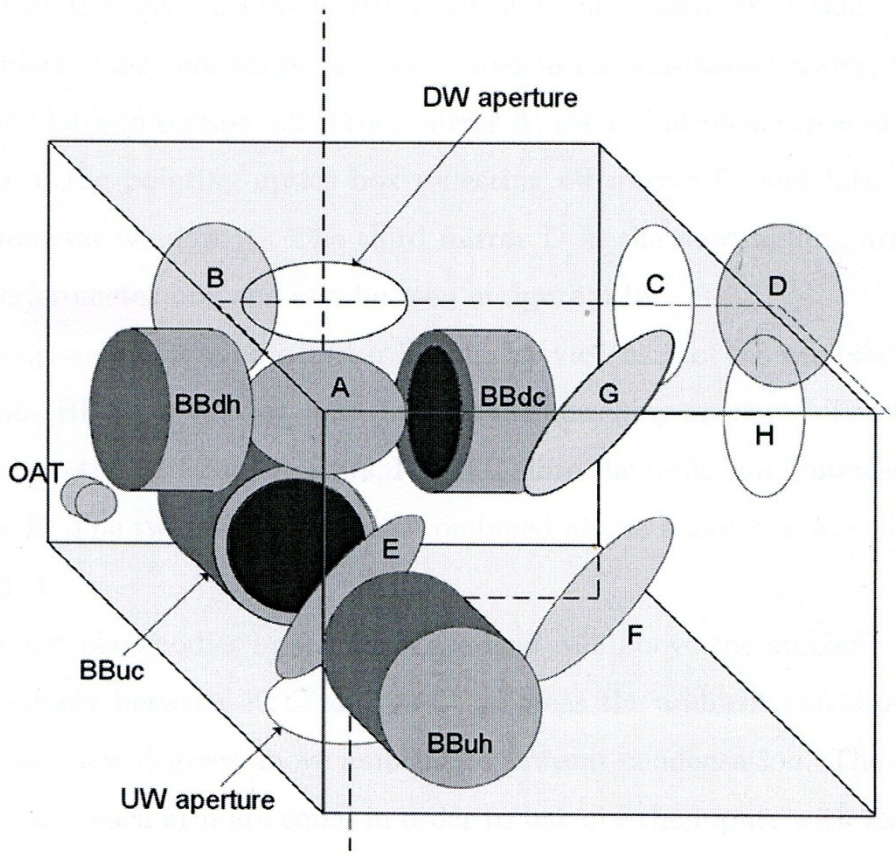


Figure 3.4: *A schematic of the optical elements inside the TAFTS POB, from Green [2003]. The four internal blackbodies are labelled* BB_{dh}, BB_{dc}, BB_{uh} *and* BB_{uc} *where the subscripts denote whether the black body is hot (h) or cold (c) and whether it is located in the upwelling (u) or downwelling (d) arm. DW radiation enters through the DW aperture and is directed by mirrors A, B and D through window C. UW radiation enters through the UW aperture and is directed by mirrors E, F and G through window H.*

3.2.2 Interferometer

The TAFTS interferometer is contained in an evacuated aluminium box. It is evacuated in order to reduce vibrations on the beamsplitter which cause noise on the spectra, and also to eliminate residual water vapour causing path dependent absorption within the interferometer. As discussed, the interferometer is of the Martin-Puplett type, and a schematic of the particular optical configuration is shown in Figure 3.5.

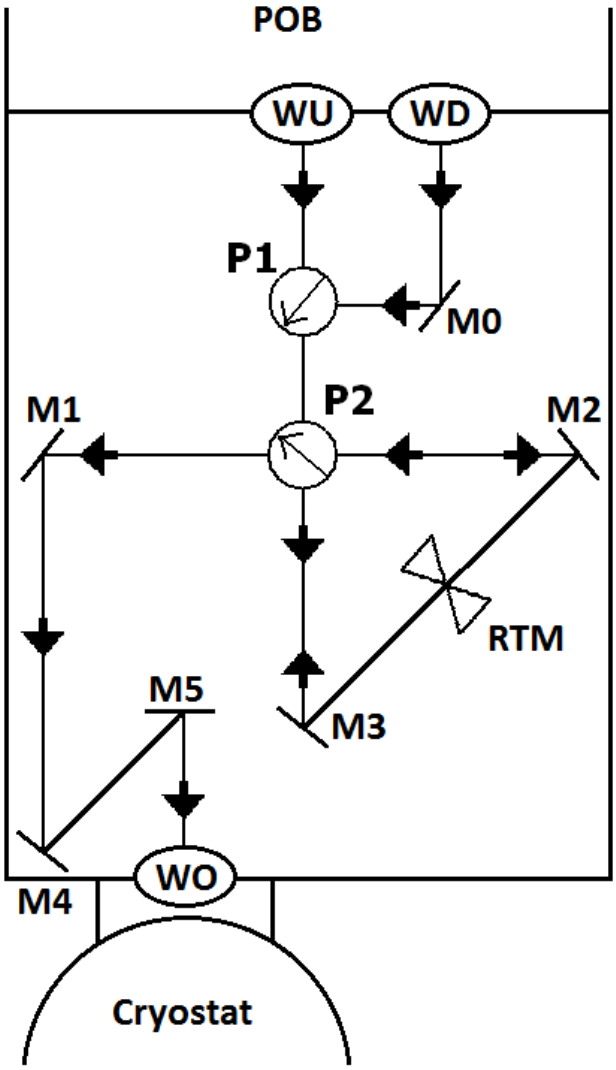


Figure 3.5: *A schematic of the optics layout inside the TAFTS interferometer chamber*

The two beams of radiation enter the interferometer through windows WU and WD. The polarisers $P1$ and $P2$ consist of mylar substrates of thickness 1.5 μm and diameter 65 mm, onto which a 40 mm wide strip of copper wire grid (1 μm width and 2 μm pitch) is lithographically attached. $P2$ splits the radiation by polarisation and directs it, via $M2$ and $M3$, to a back-to-back rooftop mirror RTM. Although interferometers of this type usually only have one moving mirror, the back-to-back design used in TAFTS allows an extra two-fold increase in optical path difference for the same physical distance that the mirror has to travel [*Green*, 2003]. The RTM can be driven back and forth over a distance of 25 mm, producing an optical path difference of 100 mm between the two beams. The movement of RTM is controlled with a motor and gears, with the mirror itself being set into three V-grooves containing ball bearings, ensuring a smooth movement. After passing through the

optics, the recombined radiation beam is directed into the cryostat section of the instrument through another polypropane window WO.

Also contained within the interferometer is a He:Ne metrology laser, the beam of which is sent through the optical system physically offset from the FIR radiation. This is used for sampling purposes and is discussed further in §3.2.5. The laser beam is split by intensity by polariser $P2$, which has a semi-silvered surface above and below the polariser for this reason.

3.2.3 Cryostat and detectors

The third section of the TAFTS instrument is a cryostat container which houses the detectors and several other optical devices, as shown in Figure 3.6. The measured radiation enters the cryostat through window WO, is passed through two 12 μm limit long-pass filters F (eliminating very short wave radiation) and is directed by two mirrors onto an analyser $P3$ which again splits the beam by polarisation, isolating the complementary outputs of the interferometer. The resultant two polarisation coded beams pass through two dichroic filters, $DF1$ and $DF2$, which split the radiation into two waveband regions: longwave (LW, 80-320 cm^{-1}) and shortwave (SW, 320-600 cm^{-1}). These are then directed to one of the four photoconductor detectors used in TAFTS; two shortwave Si:Sb detectors and two longwave Ge:Ga detectors. There is a LW and a SW detector placed at each of the analyser outputs so that the dichroic filters can direct radiation to the relevant detector.

The detectors operate at a temperature of around 6K. This temperature is maintained in the cryostat by evacuated layers of insulation and two cryogen tanks, the inner tank containing liquid helium (4.2K) and the outer tank containing liquid nitrogen (77K).

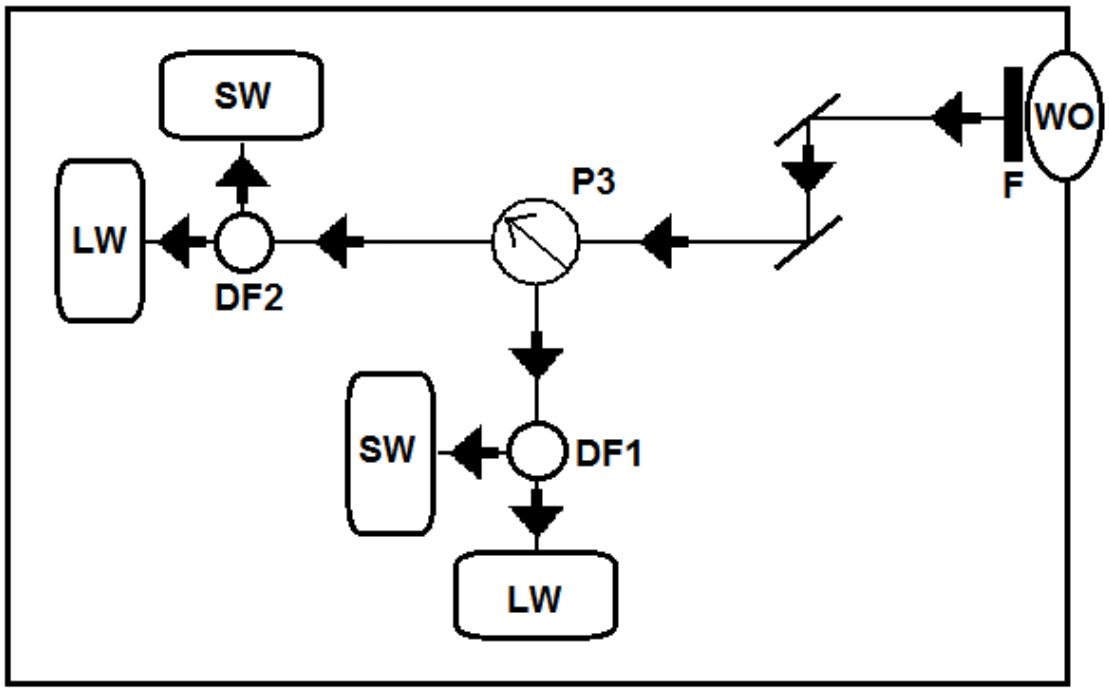


Figure 3.6: *Schematic of the optics and detectors inside the TAFTS cryostat. Radiation from the interferometer is directed onto two dichroic filters DF1 and DF2, where it is split into LW and SW beams and directed onto the relevant detector.*

3.2.4 Electronics

The electronics component of TAFTS is housed in a box that is separate from the rest of the instrument. This is so that it can be placed inside the aircraft during a flight campaign. The signal from the detectors is converted using an analogue to digital converter, having first been amplified using DC-coupled differential amplifiers. The digitised signal is then transmitted to the electronics box inside the aircraft. The data that is stored by the electronics comprises four sets of digitised data from the four detectors, the laser fringe timings, and housekeeping data such as black body temperatures and the time the data was recorded. Each scan is stored separately on disk to be downloaded and analysed later.

3.2.5 TAFTS data acquisition and processing

The processing of data recorded by the TAFTS instrument may be thought of in four stages; differencing of raw interferograms, sampling interferograms, performing the Fourier transform, and calibration.

Differencing of outputs

The data recorded by TAFTS includes four interferograms per scan – two from the LW detectors (known as LW channels 0 and 1), and similarly two from the SW detectors (known as SW channels 0 and 1). This allows a differencing of the complementary outputs, which is useful for reducing the noise on the interferograms as will now be discussed. Figure 3.7 shows raw TAFTS interferograms recorded during flight B818 (described further in §7). The view configuration is set to the nadir hot black body and zenith external views. The raw interferograms for the two LW channels are shown on the left, and similarly the two SW channels on the right. The complementary signals are shown in black for channel 0, and blue for channel 1. The raw interferograms shown in Figure 3.7 are distorted by various effects, which can be reduced by differencing of the outputs as will now be explained.

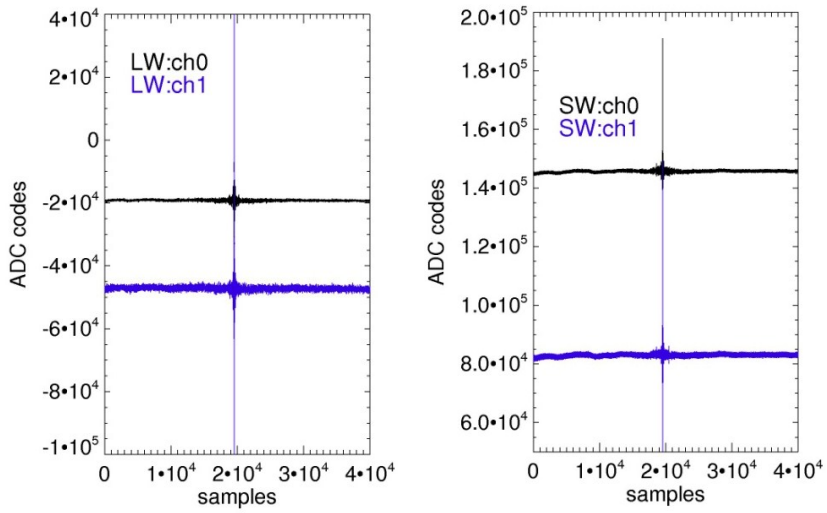


Figure 3.7: *Raw interferograms recorded during flight B818. The view configuration is $h_n z_z$. Left shows the two LW channels, right the two SW channels. Complementary channel signals shown in black (ch0) and blue (ch1).*

The distortion on the raw interferograms seen in Figure 3.7 is caused by two separate effects:

1. Excessive noise on the LW ch1 due to a poor connection during the flight.
2. External scene variation causing slow variation on all channels (most apparent in the 0–10,000 sample region). This has a greater effect on the SW channels as the atmospheric opacity over the shortwave spectral range of TAFTS is significantly less than that of the longwave.

Differencing of the complementary channels alleviates both of these effects, as can be seen in the differenced interferograms in Figure 3.8, where the noise on the interferograms is much reduced and the variation on the SW channel has been removed.

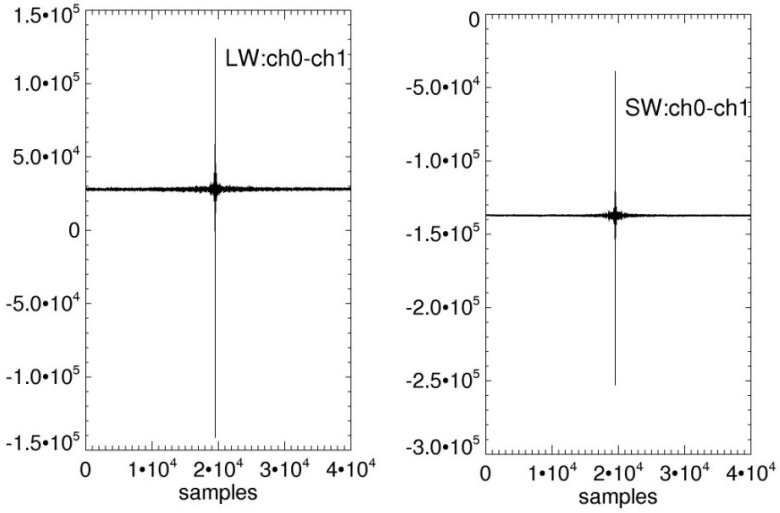


Figure 3.8: *The differenced interferograms from the complementary channels shown in Figure 3.7*

An additional effect that is not readily apparent in Figure 3.7 is that of power supply pickup. This significantly affects the shortwave channels, and when a transform of the raw interferograms is performed, several clear spikes are visible in the spectrum as shown in Figure 3.9. These spikes are related to the power supply frequency (400 Hz).

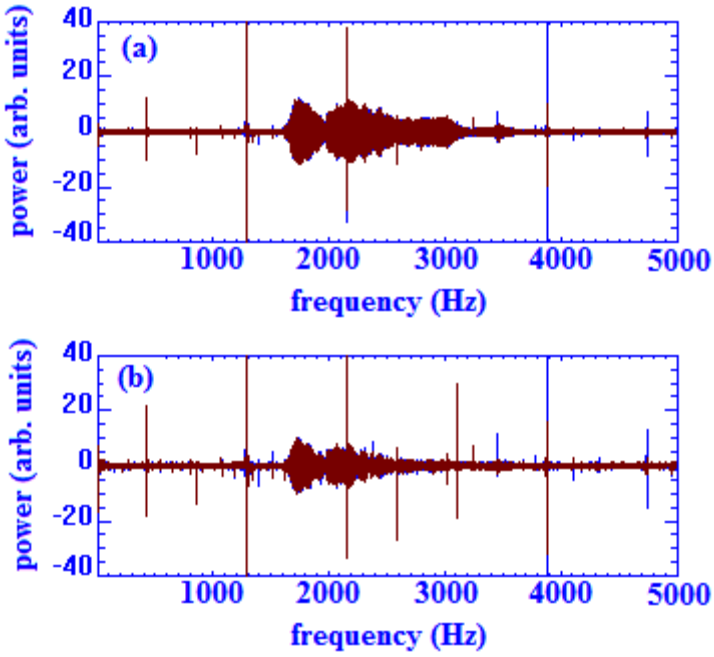


Figure 3.9: *FFTs of raw interferograms of (a) SW ch0; and (b) SW ch1. Spikes are due to power supply pickup.*

This effect can also be removed by differencing of the complementary channels, after factoring in the gain difference between the two detectors. The FFT of the differenced interferograms is shown in Figure 3.10, where it can be seen that all but one spike has been removed. This remaining spike was only apparent in SW ch1 and appeared randomly in the data. Where this was present it was manually removed by interpolation.

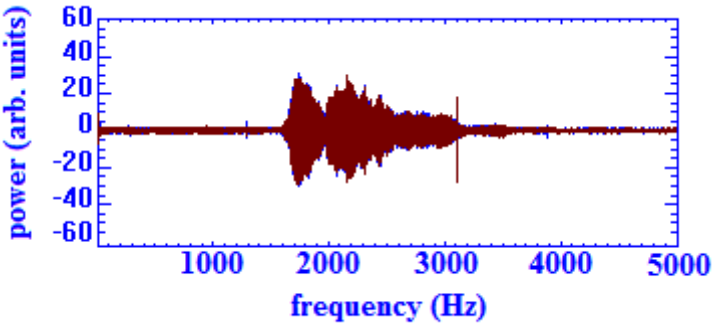


Figure 3.10: *FFT of the differenced interferograms shown in Figure 3.9*

The Brault resampling scheme

The interferograms cannot be continuously sampled, but instead must be sampled at a spatial interval that is dependent on the highest frequency that is measured. In order to fully resolve the frequencies contained in the interferogram, the sampling frequency must be at least twice the maximum frequency σ_{max} measured; this sampling frequency is known as the Nyquist frequency. Expressing this in the spatial domain, the minimum spatial sampling Δx must be at least half the wavelength of the lowest wavelength λ_{min} measured i.e.

$$\Delta x = \frac{\lambda_{min}}{2} = \frac{1}{2\sigma_{max}} \qquad 3.12$$

For TAFTS, a maximum measured wavenumber of 1000 cm^{-1} would result in a minimum sampling interval of 5 μm. For TAFTS, the interferogram is oversampled with a sampling frequency interval of 20 kHz. However, this method of sampling is not ideal as the mirror velocity is not constant. This is due to slight variations in the power of the motor powering the mirror movement, variation in tension of the motor drive wire, and vibrations caused by the aircraft. Thus an alternative sampling method developed by Brault [1996] is used.

The Brault technique uses a similar approach to that described above, except it samples in intervals of constant time which, using the laser in the interferogram system, can be converted into constant spatial intervals, thus compensating for the uneven movement of the mirror. The He:Ne laser, which has a wavelength of 633 nm, is sent through the optical system slightly offset from the measured FIR beam. It therefore produces its own interference pattern which varies sinusoidally in intensity. This interference pattern is used to infer the distance travelled by the mirror, since a transition from a bright to a dark laser fringe corresponds to a path difference of $m\lambda + {}^{\lambda}/_{2}$ of the laser light. The rate of the variation of the laser fringes is around 80 kHz, and therefore for the desired sampling frequency of 20 kHz, the sampling must take place every four laser fringe crossings. Using a detector, the time taken for four laser fringes is recorded, and even if this time varies, the distance the mirror has moved in the interval is always equal to 4λ. Thus the interferograms recorded by TAFTS, which have been sampled at uniform time intervals, are resampled onto a uniform spatial grid using the laser fringe timings to ensure the spatial sampling interval is constant.

Correction for in-flight vibration

When TAFTS is operated onboard an aircraft platform, the additional vibrations caused by the aircraft cause significant effects on the timings of the laser fringes, and therefore on the recorded interferograms. This can be observed in the upper panels of Figure 3.11, which shows recorded laser-fringe timings for an individual scan in (a) laboratory conditions and (b) flight conditions. The lower panels show the corresponding Fourier analysis of these laser timings.

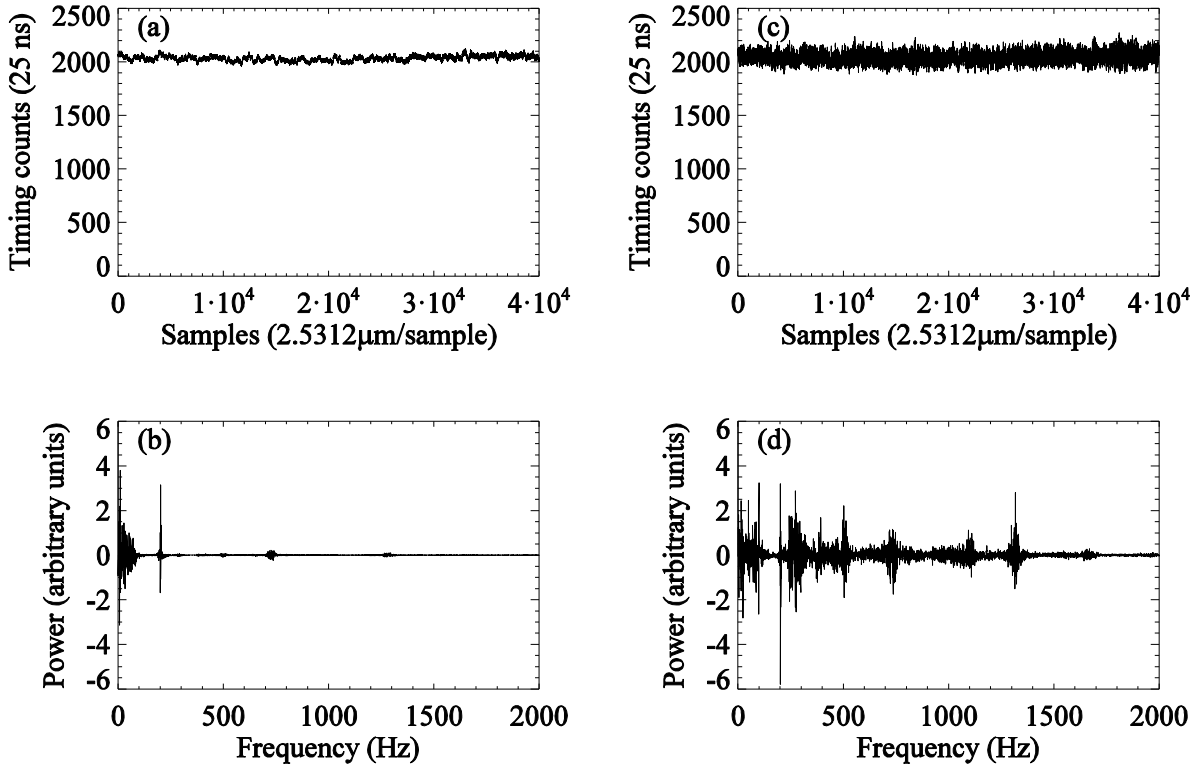


Figure 3.11: *Upper panels – TAFTS laser fringe timings for operation in (a) laboratory conditions; (c) aircraft conditions. Lower panels – corresponding Fourier analysis of the above fringe timings, showing low frequency components associated with the scan gearing mechanism, and a sharp peak at 200 Hz associated with the stepper motor driving the roof-top mirror. The Fourier analysis of the aircraft measurements (d) shows the low frequency and 200 Hz components, as in the lab based measurements (b). However, there are now many broad high frequency components. These new components are associated with vibrations in the beamsplitter.*

The laboratory frequency analysis shows well-defined frequency periodicities, which are caused by the stepper motor and gearing mechanism used to drive the mirror. In the frequency analysis of the flight conditions, an increase in the velocity variation is shown.

This is due to vibrations on the beamsplitter itself. Although the interferometer is housed in a vacuum and anti-vibration mounts are used to isolate the system, enough vibration is transmitted through the casing to cause resonant vibrations in the thin (1.5 μm) Mylar substrate that makes up the beamsplitter. As described above, the Brault resampling method will account for small variations caused by the mirror scan mechanism, however it will not unambiguously correct for the vibrations of the beamsplitter.

If a constant frequency motion is applied to the beamsplitter, the (0, 0) vibration mode will result in a large amplitude variation in the centre of the Mylar, with a decreasing amplitude to zero at the fixed edges. This translates to a proportional variation in velocity across the beamsplitter substrate, depending on which part of the beamsplitter the radiation passes through. As described above, the laser passes through the interferometer system at an offset to the measured FIR radiation, and travels through the beamsplitter approximately 22.5 mm above the centre, whereas the FIR radiation passes nominally through the central 40 mm. This means that the fringe timings that are derived from the laser will underestimate the velocity variations at the centre of the beamsplitter substrate, i.e. those experienced by the FIR radiation.

To understand how the vibration affects the recorded spectrum, consider a simple interferogram of the form

$$I(x) = B(\sigma)\cos(2\pi\sigma x)$$

3.13

where $B(\sigma)$ is the spectral signature under investigation. If there are periodic errors in the sampling interval, then the path difference x' at the sampling position can be written in terms of the ideal path difference x, by

$$x' = x + \beta\sin(2\pi\varepsilon + \varphi)$$

3.14

where β is the amplitude, ε the spatial frequency of the error, and φ the phase between the sampling and the vibration.

For $\beta \ll {}^{\lambda}/_{4}$, the resulting interferogram can be written

$$I(x') = B(\sigma)\cos(2\pi\sigma x) - \pi\sigma\beta\cos\big(2\pi x(\sigma \pm \varepsilon)\big) \quad for\ \varphi = 0$$

3.15

or

$$I(x') = B(\sigma)\cos(2\pi\sigma x) - \pi\sigma\beta\sin\big(2\pi x(\sigma \pm \varepsilon)\big) \quad for\ \varphi = {}^{\pi}/_{2}$$

3.16

The resultant spectrum $B(\sigma)$ will contain the spectral peak plus two satellite peaks of amplitude $B(\sigma)(\pi\sigma\beta)$ at spectral position $(\sigma \pm \varepsilon)$. These additional peaks are known as 'ghosts', and appear as distinct features, adding to and distorting the spectrum of interest. This distortion is seen in TAFTS aircraft data, and exhibits a scan to scan variation which is assumed to be due to the relative phase between the vibration and interferogram sample at zero path difference for each scan. The magnitude of the ghost is dependent on the optical frequency, and is calculated to be about 10 % from a signal at 300 cm^{-1}.

By making assumptions concerning how the amplitude and phase vary across the beamsplitter substrate surface, a correction can be applied by manipulating the analysis of the fringe timings i.e. the velocity variation seen in the laser fringes is multiplied in an iterative manner in order to find the velocity variation in the interferogram. When transformed back to the timing domain and applied to the resampling scheme, this correction can reduce the continuum ghost considerably [J.E. Murray, personal communication, January 2015]. In practise, data with significant ghosting is excluded from further analysis.

Fourier transformation of interferograms to raw spectra

Once the interferograms have been sampled on a uniform grid, they have an apodisation and phase correction applied before an FFT is performed to transfer them into wavenumber space and produce the raw spectra. The apodisation is needed because the distance over which the interferogram is measured is equal to the maximum path difference $\pm L$, meaning the far ends are cut off (an ideal interferogram has infinite extent). The spectrum can therefore be written as in equation 3.17. This has the same effect as multiplying the interferogram by a box function of width $2L$, which when Fourier transformed becomes a sinc function. To reduce

this effect, the interferogram is apodised using a function that slowly reduces the intensity to zero. For TAFTS, a Kaiser-Bessel function is used.

$$B(\sigma) = \int_{-L}^{L} I(x) e^{-2i\pi\sigma x}\, dx$$

3.17

An ideal interferogram would be centred on the point of zero path difference $\Delta x = 0$. However, due to the finite sampling interval, the point sampled closest to the interferogram centre is likely to be offset from the point $\Delta x = 0$ by some increment ϵ, so that the interferogram takes the form

$$I(x) = \int_{-\infty}^{\infty} B(\sigma) \cos\big(2\pi\sigma(x-\epsilon)\big)\, d\sigma + i \int_{-\infty}^{\infty} B(\sigma) \sin\big(2\pi\sigma(x-\epsilon)\big)\, d\sigma$$

3.18

Once transformed, this offset takes the form of a wavenumber dependent phase lag ϕ such that the spectrum may be written

$$B(\sigma) = \int_{-\infty}^{\infty} I(x) \cos(2\pi(\sigma+\phi)x)\, dx + i \int_{-\infty}^{\infty} I(x) \sin(2\pi(\sigma+\phi)x)\, dx$$

3.19

If the phase ϕ between the real and imaginary components of the power spectrum were zero, all the power would be present in the real part of the spectrum. However, if it is non-zero, some of the power is rotated into the imaginary part and the spectrum needs to be corrected. This is done by calculating the phase between the real and imaginary parts as in equation 3.20.

$$\phi = \tan^{-1} \frac{B_r(\sigma)}{B_i(\sigma)}$$

3.20

The calculated phase angle is then used to correct the spectrum according to the equation

$$B(\sigma) = B_r(\sigma)\cos\phi(\sigma) + B_i(\sigma)\sin\phi(\sigma)$$

3.21

Each individual spectrum is phase-corrected in this way before they are co-averaged.

TAFTS calibration algorithm

The TAFTS calibration procedure is based on the algorithm developed by Revercomb et al. [1988], with some additional elements particular to the Martin-Puplett layout, and is briefly described here.

All spectrometers have an instrument response function $R(\sigma)$ which represents the relationship between the measured spectrum $S_m(\sigma)$, and the true spectrum $S_T(\sigma)$, as given in equation 3.22.

$$S_T(\sigma) = \frac{S_m(\sigma)}{R(\sigma)}$$

3.22

For TAFTS, the response function is calculated by recording measurements of the black body targets, which have known temperature and emissivity (from laboratory experiments). These calibration measurements are performed in cycles interspersed with measurements of the atmospheric state, allowing a true picture of the response function and its changes throughout the operation period to be recorded. As discussed in §3.2.1, the black bodies are either hot (h) or cold (c), and two may be viewed at a time through the two input ports in the nadir and zenith arms. The available calibration viewing configurations are therefore c_nh_z, h_nc_z, c_nc_z, and h_nh_z, where the subscripts denote the view in the nadir (n) or zenith (z) arm. Figure 3.12 shows TAFTS differential shortwave spectra recorded during flight B818 for a series of sequential scan cycles. Panels (a) and (b) show the h_nc_z and c_nh_z calibration spectra, where cycle number denoted by a colour bar that varies black to red temporally. Panels (c) and (d) are the h_nh_z and c_nc_z spectra, for these the differential signal is very small as the temperatures of the blackbody views are very similar. Hence the signal-to-noise was very poor and so all cycles were averaged.

From Revercomb et al. [1988], an instrumental response function $R(\sigma)$ may be calculated from two measured calibration spectra as in equation 3.23, where $S_h(\sigma)$ and $S_c(\sigma)$ are the measured spectra, $\varepsilon_h(\sigma)$ and $\varepsilon_c(\sigma)$ are the emissivity of the blackbodies and $B(\sigma, T_h)$ and $B(\sigma, T_c)$ are the Planck function at the temperature of the blackbodies.

$$R(\sigma) = \frac{S_h(\sigma) - S_c(\sigma)}{|\varepsilon_h(\sigma)\ B(\sigma, T_h) - \ \varepsilon_c(\sigma)\, B(\sigma, T_c)|}$$

3.23

Applying this to the TAFTS B818 spectra, the response function for the nadir scene view can be calculated from calibration spectra which contain the same view in the zenith arm, e.g. the two configurations $h_n c_z$ and $c_n c_z$, which are both viewing the zenith cold blackbody. By differencing these spectra, the common view cancels. TAFTS viewing configurations give two of these differential spectra for the nadir view, i.e.

$$(h_n c_z - c_n c_z) = (h_n - c_n)$$

$$(c_n h_z - h_n h_z) = (c_n - h_n)$$

These differential spectra are shown in panels (e) and (f) Figure 3.12. Ideally these two sets of differential spectra should be equal and opposite, but in practise this is not the case, as shown in panel (a) of Figure 3.13, which is the sum of the two spectra shown in panels (e) and (f) of Figure 3.12. This residual between the two differential signals is attributed to the instrument blackbody self-emission, and is removed from the raw data as in equation 3.24. The two differential spectra with the emission term removed are shown in panels (b) and (c) of Figure 3.13, where they are now equal and opposite.

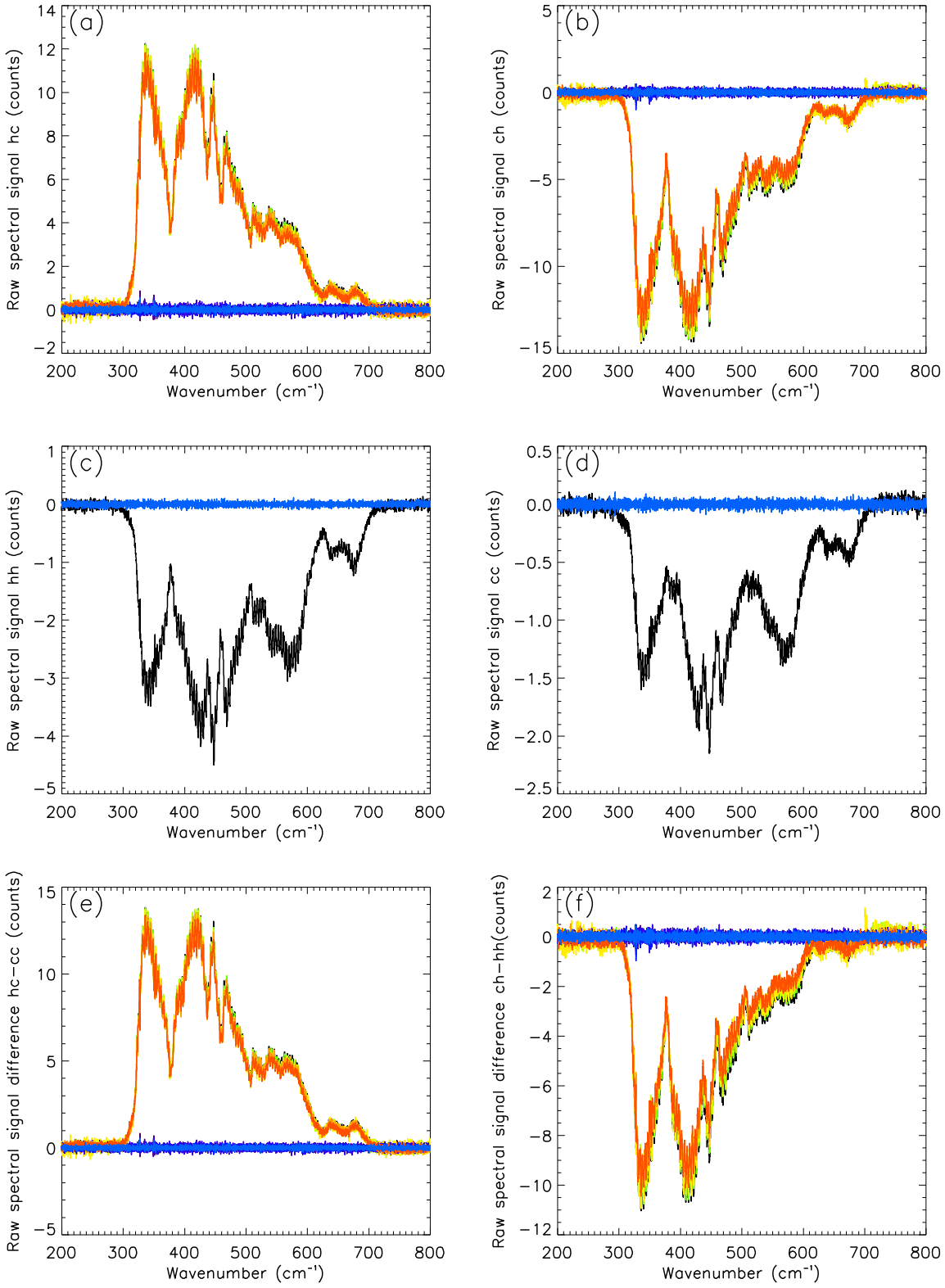


Figure 3.12: *TAFTS raw spectral scans for the calibration viewing configurations (a) h_nc_z; (b) c_nh_z; (c) h_nh_z; (d) c_nc_z; and differential spectra (e) h_nc_z-c_nc_z; (f) c_nh_z-h_nh_z.. The colours represent the scan cycle number progressing sequentially from black to red. The blue trace represents the imaginary part of the signal.*

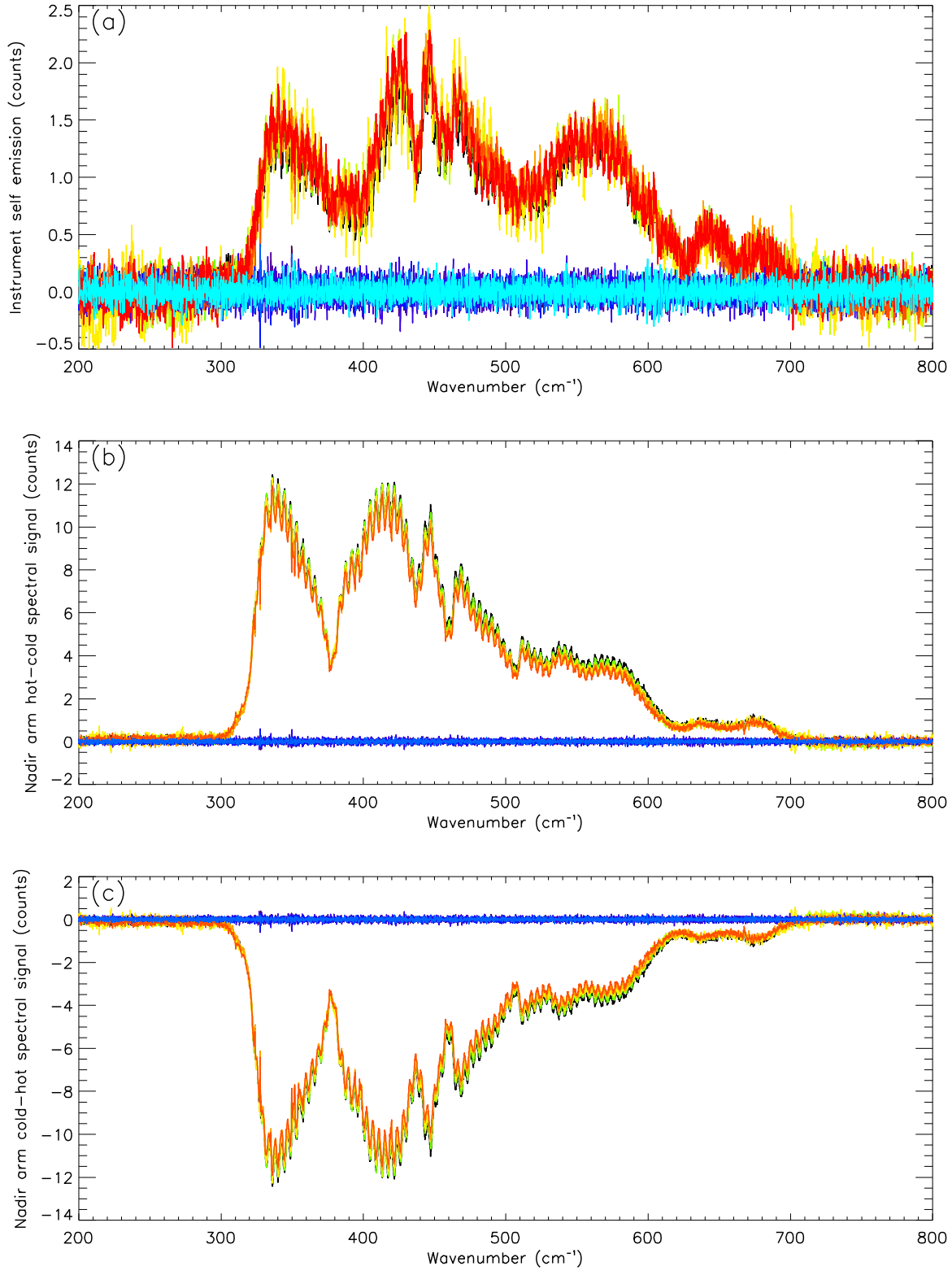


Figure 3.13: *(a) the residual between the two differential spectra, attributed to the instrument self-emission; (b) and (c) the differential spectra with the emission term removed*

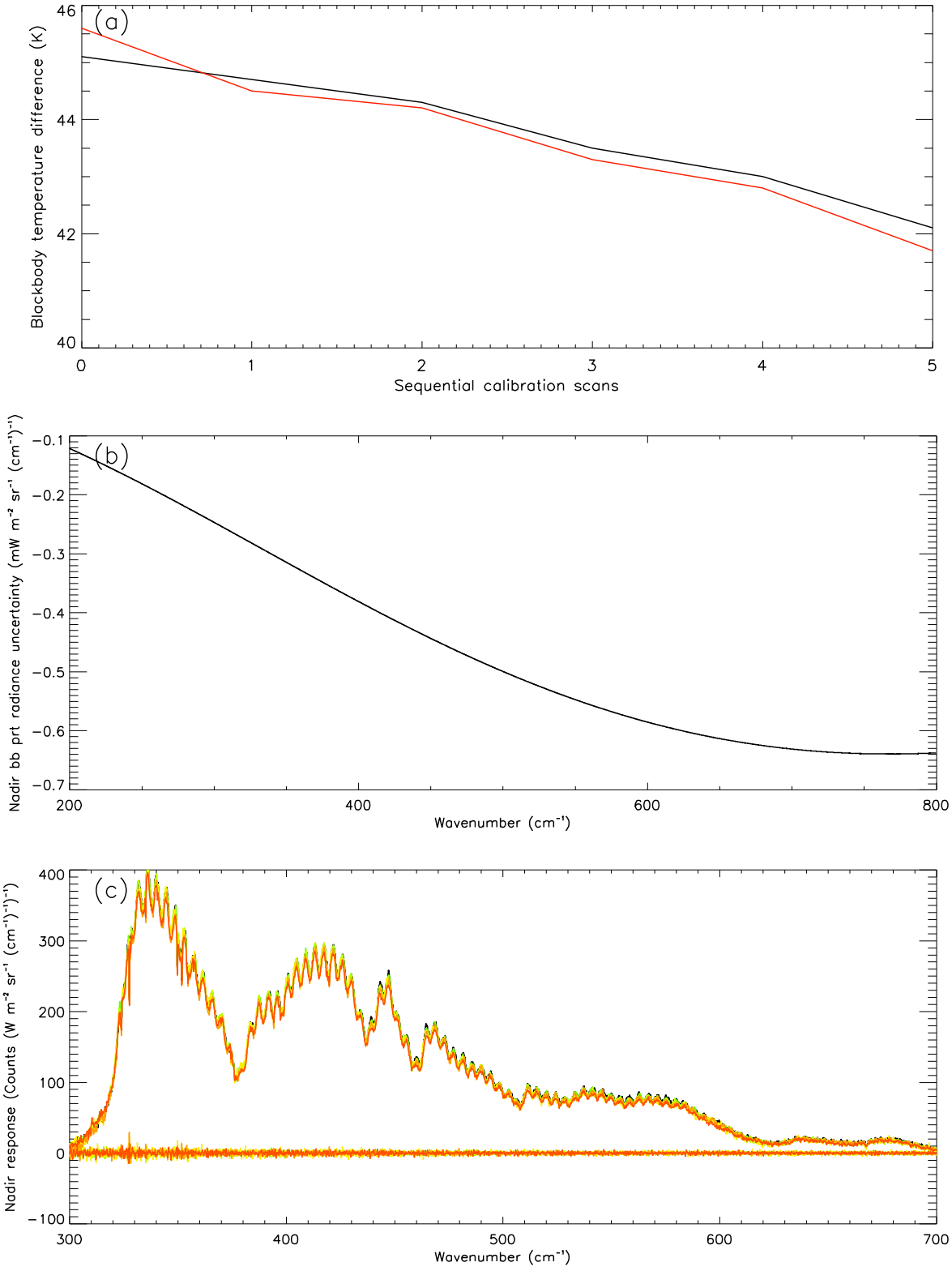


Figure 3.14: *(a) The variation in h_nc_z-c_nc_z (black) and h_nh_z-c_nh_z (red) blackbody temperature differences in the nadir arm, for 6 sequential TAFTS scans; (b) The maximum uncertainty associated with the blackbody PRT sensors; (c) The nadir response functions for the 6 scans once the blackbody emission and self-emission terms have been removed.*

The emission of the blackbodies is dependent on their temperature, which is not constant over the measurement time. Panel (a) of Figure 3.14 shows the variation in the temperature of the blackbodies in the nadir arm over 6 sequential TAFTS scans, as measured by the PRT sensors. The h_nc_z-c_nc_z difference is plotted in black, and the h_nh_z-c_nh_z in red. Panel (b) shows the blackbody temperature uncertainty, which is associated with the accuracy of the PRT sensor (±0.2 K). It is plotted at the maximum uncertainty, which for the nadir (h_n-c_n) view, is equal to $(T_{hot} + 0.2K) - (T_{cold} - 0.2K)$. Panel (c) shows the final nadir response functions for the TAFTS nadir view, once the blackbody emission and self-emission terms have been removed. The response function is given as

$$R_n(\sigma) = \frac{(h_n - c_n) - (self\ emission)}{|\varepsilon_h(\sigma)\ B(\sigma, T_h) - \ \varepsilon_c(\sigma)\, B(\sigma, T_c)|}$$

3.24

Once the nadir response function has been found, it can be used to calculate the true spectrum of the atmospheric state $S_n(\sigma)$ (i.e. the sky view of up-welling radiation measured in the nadir arm), by dividing the measured spectrum by the response function $R_n(\sigma)$ as in equation 3.22. Again, a differential spectrum has to be found by differencing common views in the zenith arm, in this case the differential spectrum is

$$(n_n h_z - h_n h_z) = (n_n - h_n) - (self\ emission)$$

3.25

Equation 3.22 can be therefore be rewritten as in equation 3.26, where the Planck function and emissivity for the hot blackbody is added to account for the offset that is introduced by subtracting the hot blackbody spectrum from the nadir sky-view spectrum.

$$S_n(\sigma) = \frac{n_n(\sigma) - h_n(\sigma) - (self\ emission)}{R_n(\sigma)} + \varepsilon_h(\sigma)\, B(\sigma, T_h)$$

3.26

Substituting in the expression for $R_n(\sigma)$ in equation 3.24 gives the calibrated nadir scene view radiances as:

$$S_n\,(\sigma) = \frac{n_n(\sigma) - h_n(\sigma) - (self\ emission)}{(h_n - c_n)}\left[\varepsilon_h(\sigma)\,B(\sigma, T_h) - \varepsilon_c(\sigma)\,B(\sigma, T_c)\right] + \varepsilon_h(\sigma)\;B(\sigma, T_h)$$

3.27

TAFTS uncertainty sources

The TAFTS combined radiance uncertainty is calculated from a number of sources including the response function, which are all incorporated into a single uncertainty on the calibrated spectra. The individual uncertainties are combined in quadrature, whereby a total uncertainty σ associated with a quantity f is found by combining the uncertainties in x, y, z etc., according to the equation

$$\sigma_f^2 = \frac{\delta f^2}{\delta x}\sigma_x^2 + \frac{\delta f^2}{\delta y}\sigma_y^2 + \frac{\delta f^2}{\delta z}\sigma_z^2 + \cdots$$

3.28

The calibrated TAFTS spectra have four sources of uncertainty: two associated with the blackbody temperatures, one from the sky-view spectra, and one from the response function. The temperature of each of the blackbodies is measured by the PRTs inside the blackbody cavities. These PRTs measure to a precision of

$$\sigma_{Tpres} = \pm\, 0.0005\, T$$

3.29

and have an accuracy of

$$\sigma_{Tacc} = 0.03\ \pm\ 0.0005\, T$$

3.30

for temperatures in °C, as quoted by the manufacturers.

The uncertainty due to noise from the sky view spectra is calculated from the standard deviation of the imaginary part of each raw spectrum i.e.

$$\sigma_{sv} = \sqrt{\frac{\sum_{i=1}^{N}(x_{sv} - \mu_{sv})^2}{N}}$$

3.31

where x_{sv} is each individual sky view spectrum, μ_{sv} is the mean of the sky view spectra, and N is the total number of sky view spectra.

The uncertainty from the response function is also made up of uncertainties from the blackbody temperatures and the noise on the calibration spectra (σ_{cal}, calculated in the same way as σ_{sv} in equation 3.31 above). These are combined to give a total uncertainty for the response function of

$$\sigma_R^2 = \left(\frac{dR}{dS_{cal}}\right)^2 \sigma_{cal}^2 + \left(\frac{dR}{dT_{pres}}\right)^2 \sigma_{Tpres}^2 + \left(\frac{dR}{dT_{acc}}\right)^2 \sigma_{Tacc}^2$$

3.32

All of the uncertainties for the calibrated spectra can now be combined as one single uncertainty σ_S^2 as in equation 3.33.

$$\sigma_S^2 = \left(\frac{dS}{dS_{sv}}\right)^2 \sigma_{sv}^2 + \left(\frac{dS}{dT_{pres}}\right)^2 \sigma_{Tpres}^2 + \left(\frac{dS}{dT_{acc}}\right)^2 \sigma_{Tacc}^2 + \left(\frac{dS}{dR}\right)^2 \sigma_R^2$$

3.33

Typical random uncertainty in Radiance Units (RU) for the TAFTS SW measurements are 0.7 RU at 330 cm^{-1}, rising to 2.0 RU at 450 cm^{-1} and 4.0 RU at 550 cm^{-1}, where 1 RU is 1 $mW/(m^2.sr.cm^{-1})$.

The final calibrated nadir view radiances and brightness temperatures for the TAFTS B818 measurements in the example above are shown in Figure 3.15, with their respective uncertainties as calculated above.

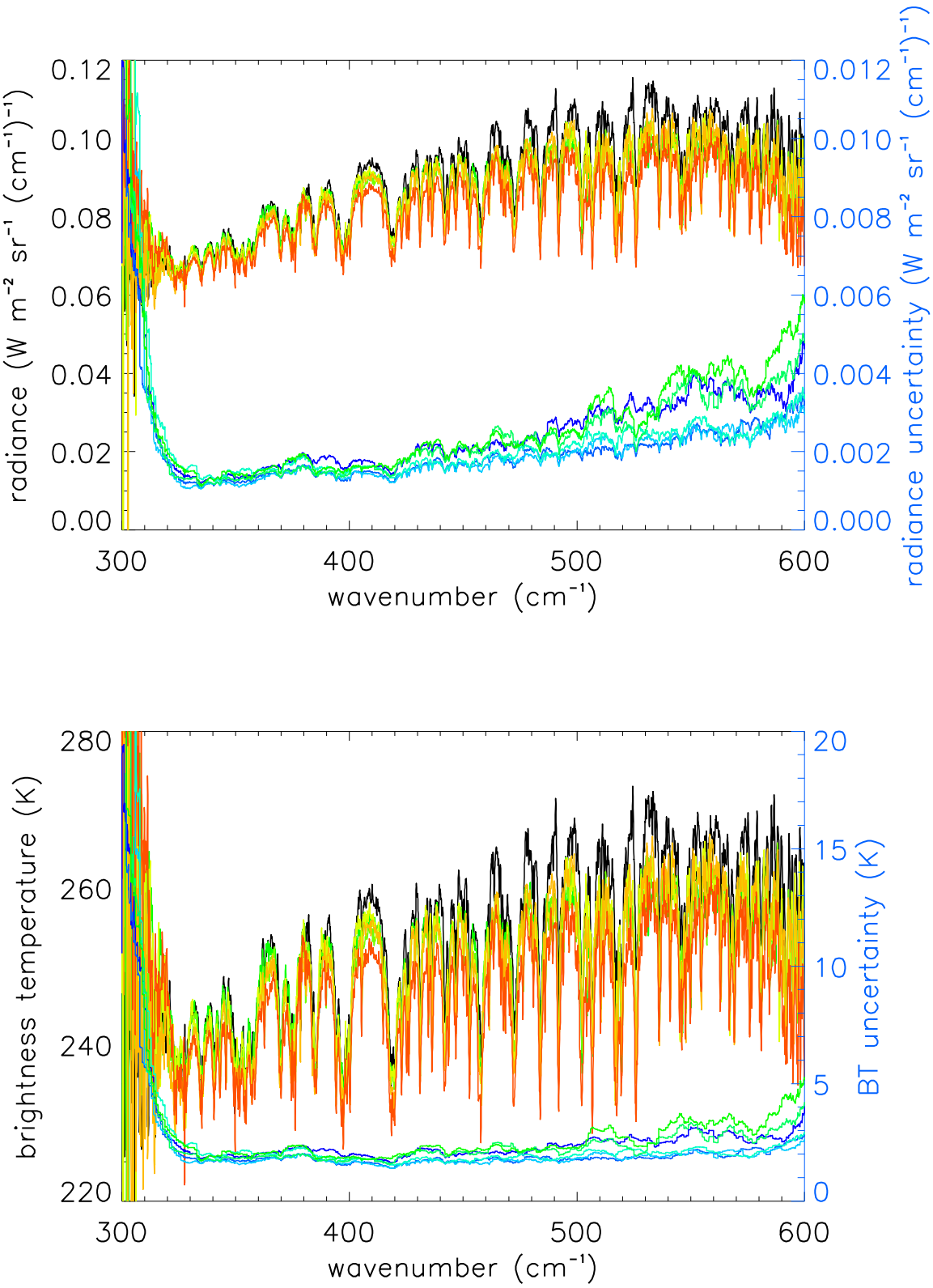


Figure 3.15: *Calibrated nadir view TAFTS SW radiances (upper) and brightness temperatures (lower) for the B818 measurements (black-red), with their uncertainties (blue-green).*

3.3 AERI and AERI-ER

The Atmospheric Emitted Radiance Interferometer (AERI) is a ground-based FTS that measures down-welling atmospheric radiances [*Knuteson et al.*, 2004a, 2004b] from 520-3020 cm^{-1} (3.3-19 mm) at 0.5 cm^{-1} resolution with a calibration accuracy of < 1% of the ambient radiance [*Delamere et al.*, 2010]. The AERI was developed by the University of Wisconsin Space Science and Engineering Center for use within the ARM program, resulting in the deployment of an AERI instrument at each of the ARM climate research facilities and mobile facilities. An extended range (380-3020 cm^{-1} / 3.3-26 μm) version of the instrument was developed (AERI-ER) specifically to cover the water vapour rotational band.

The AERI-ER is a Michelson design interferometer, whose output is directed to two cryogenically cooled detectors: a longwave Hg:Cd:Te detector with range 380-1800 cm^{-1} and a shortwave In:Sb detector with range 1800-3020 cm^{-1}. Two high-emissivity calibration blackbodies are used; one at 60 °C (hot) and one at ambient temperature, and the total random radiometric uncertainty is less than 0.05 RU across the spectrum. For further details on the AERI-ER see Knuteson et al. [2004a, 2004b].

The AERI-ER has been used to investigate the foreign-broadened water vapour continuum in the Surface Heating Budget of the Arctic Ocean (SHEBA) campaign, which resulted in a revision of the CKD continuum model at FIR wavelengths [*Tobin et al.*, 1999], and in the RHUBC campaign, which resulted in a major update to the MT-CKD continuum model in the FIR region 400-600 cm^{-1} [*Delamere et al.*, 2010].

3.4 ARIES

The Airborne Research Interferometer Evaluation System (ARIES) [*Wilson et al.*, 1999], is an airborne interferometer developed by the United Kingdom Meteorological Office (UKMO) capable of making measurements of up- and down-welling infrared radiation in the range 550-3000 cm^{-1} (3.3-18 μm) at a resolution of 1 cm^{-1}. ARIES is flown alongside TAFTS on the FAAM aircraft, and has been deployed in numerous campaigns including those to investigate the water vapour continuum (e.g. Taylor et al. [2003]; Green et al. [2012]) and cirrus radiative properties (e.g. Baran and Francis [2004]; Maestri [2005]; Cox et al. [2010]; Baran et al. [2014]).

ARIES is a Michelson-type interferometer with a maximum path difference of ±1.037 cm. It uses two onboard temperature-stabilised blackbody targets, and has two sets of detectors; a Hg:Cd:Te detector covering the longer-wave 550-1800 cm^{-1} region and a In:Sb detector

covering the shorter-wave 1700-3000 cm^{-1}. The detectors are cooled to approximately 80K. ARIES is fitted with a He-Ne laser for sampling purposes and is capable of recording two full scans per second.

Instrument uncertainty is < 0.2K viewing a 280K target at 1000 cm^{-1} for one minute, and co-addition of scans adds an additional uncertainty equal to the standard deviation of the spectra. However this co-addition also reduces the random noise by a factor of $1/\sqrt{N}$ where N is the number of averaged scans. The calibration procedure used for ARIES scans is similar to that described in Revercomb et al. [1988].

3.5 Summary

This chapter has described how Fourier Transform Spectroscopy is used to obtain a spectrum of atmospheric radiation from the output of an interferometer instrument, via the explanation of different variations of spectrometer design. The three main instruments that were used in this thesis to record spectroscopic measurements: TAFTS, AERI-ER and ARIES were then introduced. Further detail on the design, data processing and calibration of the TAFTS instrument were given, as this was directly worked on by the author.

4 Radiative transfer: Theory and simulation

The physics of radiative transfer theory in atmospheres both with and without cloud cover is discussed in this chapter, followed by a description of the models used to simulate FIR spectra in this work.

4.1 Radiative transfer in a non-scattering atmosphere

The Beer-Bouguer-Lambert Law states that the fractional decrease in radiance along a path is proportional to the mass of absorbing material it encounters along the path. Hence for a beam of radiation of radiance I_υ at wavenumber υ, travelling along a path of length ds, in a unit volume containing a density ρ_a of radiatively active gas (as shown in Figure 4.1), the fractional decrease in radiance due to absorption by the gas can be written as:

$$dI_\upsilon = -k_\upsilon \rho_a I_\upsilon ds \tag{4.1}$$

where k_υ is the mass extinction coefficient of the gas. This has contributions from both the mass absorption coefficient k_a and the mass scattering coefficient k_s as

$$k_\upsilon = k_a + k_s \tag{4.2}$$

Initially, the atmosphere can be assumed to be non-scattering, and therefore only the contribution k_a should be considered.

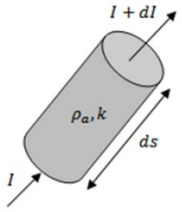


Figure 4.1: *Schematic showing I_υ travelling through an absorbing material*

The material through which the radiation is travelling contains particles which also emit radiation and therefore equation 4.1 can be modified to include this additional energy. If the

radiation from the material is modelled as a source function S_υ, which is proportional to $k_\upsilon\ \rho_a\ ds$, the radiative transfer equation can now be written

$$\frac{dI_\upsilon}{ds} = -k_\upsilon\ \rho_a\ (I_\upsilon - S_\upsilon)$$

4.3

which is also known as Schwarzschild's equation. Several simplifications can be used when this is applied to radiative transfer in the atmosphere. The first is known as the plane parallel approximation, and assumes that the intensity of the radiance only varies along the z coordinate, and not along the x or y. This is a fair approximation on a local scale, although in reality radiation travels in all directions and should be described using spherical polar coordinates. The second assumption is that the atmosphere is in local thermodynamic equilibrium. This is valid for a localised volume in which the radiation can be considered to be isotropic, and where collision induced radiation events are more frequent than radiative transitions (below around 70 km in altitude in the atmosphere).

Kirchhoff's law states that emissivity is equal to absorptivity, and assuming that the material emits as a black body, the source function S_υ can be replaced by the Planck radiation function B_υ. Using this and the assumptions outlined above, equation 4.3 can be rewritten as

$$\mu\ \frac{dI_\upsilon(z,\mu)}{dz} = -k_\upsilon\ \rho_a[I_\upsilon(z,\mu) - B_\upsilon(z)\ ]$$

4.4

where μ is the cosine of the viewing zenith angle θ, and $B_\upsilon(z)$ is the Planck function at an altitude z where the temperature is $T(z)$. A positive value of μ denotes upwelling radiances, while a negative value implies downwelling radiances.

The z dependence in equation 4.4 can be replaced with the optical depth τ, a dimensionless quantity. The differential form of the optical depth can be defined as

$$d\tau = -k_\upsilon(z)\rho_a(z)dz$$

4.5

Using this, equation 4.4 can be re-written as in equation 4.6, which is Schwarzschild's equation for a non-scattering atmosphere:

$$\frac{dI_\upsilon(\tau,\mu)}{d\tau} = I_\upsilon(\tau,\mu) - B_\upsilon(\tau)$$

4.6

4.6 is a first-order differential equation, and in order to solve it for both upwelling and downwelling radiances, two sets of boundary conditions must be introduced. One boundary can be taken as the emitted flux from the surface, defined by the Planck function $B_\upsilon(\tau)$ at the temperature of the surface. The second boundary is taken as the top of the atmosphere, where the emitted radiance may be approximated as zero.

4.2 Spectral lines

The absorption and emission of thermal photons by gases in the atmosphere is dependent on the energy differences between the vibrationally or rotationally excited states of the molecules in the gases [*Andrews*, 2010]. The energy differences are quantised, meaning that they may only take certain discrete values determined by quantum mechanical selection rules. This requires that photons in the atmosphere can only be absorbed and emitted at certain discrete frequencies which correspond to the energies of the levels, governed by the equation $E = hf$, where h is Planck's constant. The energy of a photon may thus be quantified either by its wavelength λ, where $\lambda = c/f$, or by its wavenumber ν, where $\nu = f/c = 1/\lambda$.

The atmosphere's extinction coefficient k_ν, a constant of proportionality that determines the fractional decreases in the spectral radiance of a beam as it passes through an absorbing material would be zero at all wavenumbers except for those values at which transitions between energy levels occur. At these wavenumbers k_ν is large - these spikes in the extinction coefficient are known as spectral lines. The extinction coefficient may be expressed as a sum of these spectral lines i.e.

$$k_\nu = \sum_n S_n \delta(\nu - \nu_n)$$

4.7

where S_n are constants representing the line strengths, and $\delta(\nu - \nu_n)$ is the Dirac delta function; an idealised function that is zero everywhere except at the line, and has an integral

of one over the line i.e. the line is infinitely thin [*Dirac*, 1958]. In practice, physical effects lead to broadening of the lines, requiring the Dirac delta function in equation 4.7 to be replaced by line-shape functions f_n as follows:

$$k_\nu = \sum_n S_n f_n(\nu - \nu_n)$$

4.8

The line-shape functions f_n are normalised, so that the integral over all wavenumbers is equal to one. The broadening of atmospheric spectral lines is caused by three main physical processes: natural broadening, collisional broadening, and Doppler broadening.

Natural broadening, or natural line width, arises from the uncertainty in the energy of the states involves in the transition (due to Heisenberg's Uncertainty Principle), thus widening the energy values at which the extinction coefficient peaks. Collisional broadening happens when the molecule in question collides with other molecules in the atmosphere, interrupting the emission process. This results in the transition between states having a finite collisional lifetime τ_c , meaning that the energy levels are no longer precisely defined but instead have a spread of values. This spread is described by the Lorentz lineshape

$$f_L(\nu - \nu_n) = \left(\frac{\gamma L}{\pi c}\right) \frac{1}{(\nu - \nu_n)^2 + \gamma_L^2}$$

4.9

The line width at half maximum is given by $\gamma_L = (2\pi\tau_c)^{-1}$, and using kinetic theory [*Goody and Yung*, 1989] the pressure and temperature dependence of γ_L can be written as

$$\gamma_L \propto pT^{-\frac{1}{2}}$$

4.10

The electromagnetic radiation emitted from a moving particle will undergo the Doppler Effect; a shift in frequency of the radiation emitted. If the particle is moving away from the observer at velocity u, the Doppler shift $(\nu - \nu_0)$ of a spectral line at wavenumber ν_0 is given by $(\nu - \nu_0) = \frac{u}{c}\nu_0$, with the condition that $u \ll c$. For a large number of particles, the velocities can be described using the Maxwell-Boltzmann distribution, which states that the probability of a particle having a velocity between u and $u + du$ is $P(u)du$, given that

$$P(u) = \left(\frac{m}{2\pi k_B T}\right)^{\frac{1}{2}} exp\left(-\frac{mu^2}{2k_B T}\right)$$

4.11

where k_B is the Boltzmann constant and m is the mass of the particle. The range of velocities of the particles leads to a variation in spectral shifts, and it is this that results in Doppler broadening of a spectral line. The spectral line shape for a Doppler broadened line is obtained by convolving $P(u)$ with a Dirac delta function, giving

$$f_D(\nu - \nu_n) = \frac{1}{\gamma_D\sqrt{\pi c}} exp\left(-\frac{(\nu - \nu_n)^2}{\gamma_D^2}\right) \quad 4.12$$

where

$$\gamma_D = \frac{\nu_n}{c}\left(\frac{2k_B T}{m}\right)^{\frac{1}{2}} \quad 4.13$$

The Doppler line shape is a Gaussian distribution with a Half-Width at Half-Maximum (HWHM) of $\gamma_D(ln2)^{\frac{1}{2}}$. As can be seen in equation 4.13, γ_D is proportional to $T^{\frac{1}{2}}$ but independent of p.

This means that at low altitudes and therefore higher pressures, collisional broadening dominates (since γ_L is proportional to p), whereas Doppler broadening becomes more significant at higher altitudes. Also, Doppler broadening has a greater effect on spectral lines in the visible and ultraviolet regions than in the infrared due to its dependence on wavenumber.

Both collisional and Doppler broadening effects can be taken into account by convolving the Lorentz and Doppler lineshape functions, resulting in a function known as the Voigt lineshape. This is used throughout this work for the simulation of spectral radiances.

4.3 Line-by-line radiative transfer codes

Line-by-line radiative transfer models are able to calculate the radiance at every spectral line within a chosen wavenumber range at a given resolution. This is achieved by solving of the radiative transfer equation computationally at each layer in the atmosphere to give the radiance expected at a given height, either upwelling or downwelling.

The model used in this work is the Line By Line Radiative Transfer Model (LBLRTM) version 12.2 [*Clough et al.*, 2005]. LBLRTM is regularly updated with new line strength measurements, incorporates the MT-CKD water vapour continuum parameterisation (again

with updates), and can be combined with scattering models to simulate atmospheres containing clouds (see §7).

The main features of LBLRTM are given in Clough et al. [2005], and can be summarised as follows:

- Line strengths are taken from the HITRAN 2008 database [*Gordon et al.*, 2007], a collection of molecular absorption information for many different molecules. This information is used to calculate the absorption of radiation as it passes through the atmosphere.
- The water vapour continuum is modelled using the MT-CKD parameterisation, which includes both the self- and foreign-broadened contributions (see §2.2.2).
- Lines are simulated using a Voigt line shape, which takes into account broadening of spectral lines by collision and Doppler broadening
- Simulations can be tailored to match observations by a Fourier Transform Spectrometer such as TAFTS. This is done by choosing an instrument function that matches the apodisation function of the preferred instrument, i.e. for TAFTS, a Kaiser-Bessel function would be used (see §3.2).

LBLRTM uses a variety of inputs to produce the simulated radiances. This is summarised in the flowchart in Figure 4.2. A file containing information about the line strengths from HITRAN is produced to be read into the main program. This file is known as a 'TAPE 3'. A second file, called a 'TAPE5', contains information about the atmosphere that is to be simulated. This includes the altitude of the observer, the view angle, and the altitude of the boundary (either surface or TOA). An atmospheric profile is also needed, which should contain the temperature, pressure and atmospheric gas concentrations at each layer height at which the radiance is to be calculated. This profile can be created by the user for specific atmospheric conditions, or one of six standard profiles can be used. The calculated radiances from the main LBLRTM program are output into two files, one binary (TAPE 11) and one in ASCII format (TAPE 27).

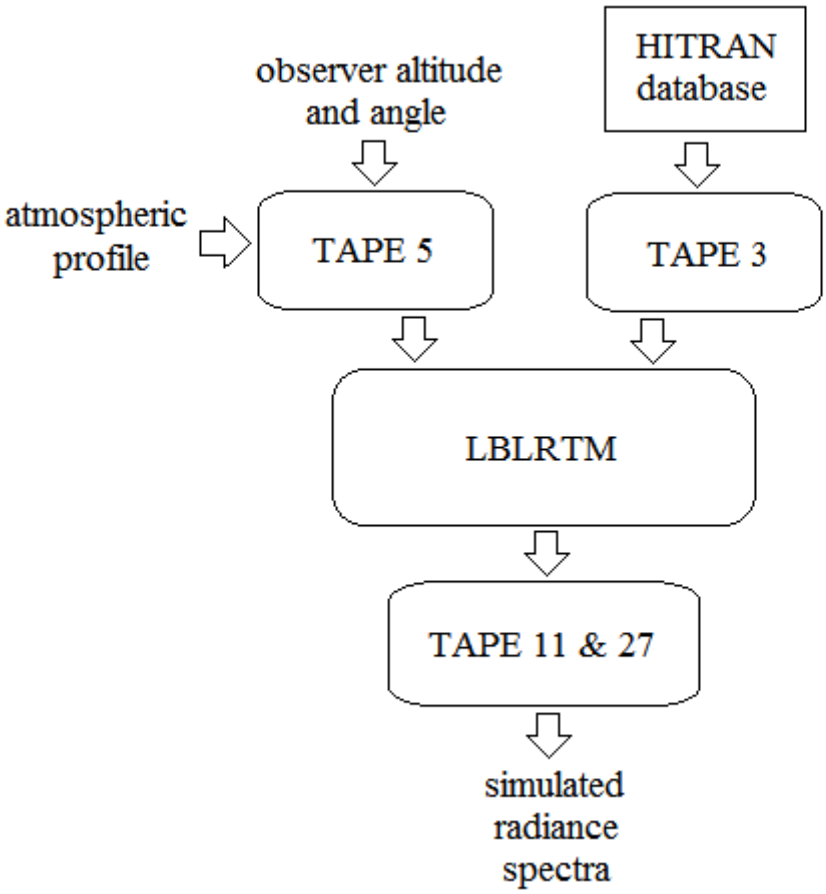


Figure 4.2: *Flowchart showing the inputs and outputs of LBLRTM*

LBLRTM also has the ability to output brightness temperatures, or optical depths for each profile layer. The latter of these can be used with scattering models to simulate cloudy atmospheres, which will now be discussed.

4.4 Radiative transfer in a cloudy atmosphere

Clouds in the atmosphere contain particles which scatter thermal radiation, therefore this scattering must be considered in addition to absorption as contributing to the total extinction of radiation. Hence a term representing the source of radiation associated with this scattering must be added to the radiative transfer equation. If β_a is the absorption coefficient of the absorbing gases and cloud particles, and β_s is the scattering coefficient of the cloud particles, the extinction coefficient is

$$\beta_v = \beta_a + \beta_s \qquad 4.14$$

The total source function for the atmosphere may now be written as

$$S_\upsilon = \frac{\beta_a B_\upsilon + \beta_s J_\upsilon}{\beta_\upsilon}$$

4.15

where J_υ is the source function associated with scattering and B_υ is the Planck function.

Inputting this into the radiative transfer equation gives

$$\mu \frac{dI_\upsilon}{dz} = -\beta_a(I_\upsilon - B_\upsilon) = -\beta_s(I_\upsilon - J_\upsilon) = -\beta_\upsilon(I_\upsilon - S_\upsilon)$$

4.16

The single scattering albedo ω_0 of the cloud particles is defined as the ratio of the scattering to extinction coefficients:

$$\omega_0 = \frac{\beta_s}{\beta_\upsilon}$$

4.17

Combining equations 4.15 and 4.17 gives the source function for scattering in the form:

$$S_\upsilon = (1 - \omega_0)B_\upsilon + \omega_0 J_\upsilon$$

4.18

When radiation is scattered by a particle in the atmosphere, it is scattered in all directions. The amount of energy scattered in each direction is determined by the wavelength of the incident radiation, and by the shape, size, composition and orientation of the particle. This means that scattering is not isotropic, and therefore a scattering phase function $P(\theta)$, where θ is the scattering angle, is defined to describe the distribution of the scattered energies. When $P(\theta)$ is integrated over a sphere (such as in equation 4.19 where θ and ϕ are the zenith and azimuthal angles respectively), it is normalised to unity.

$$\int_0^{2\pi} \int_0^{\pi} \frac{P(\theta)}{4\pi} \, sin\theta \, d\theta \, d\phi = 1$$

4.19

Considering radiative transfer in a plane-parallel atmosphere only (i.e. with no azimuthal dependence), the phase function can be rewritten as

$$P(\theta) = \frac{1}{2}\int_0^{\pi} P(\theta)\, d\theta$$

4.20

The azimuth-independent scattering source function can therefore be defined as

$$J_\upsilon = \frac{1}{2}\int_{-1}^{1} P(\theta)\, I_\upsilon(\tau,\theta)\, d\theta$$

4.21

Combining equations 4.16, 4.18 and 4.21 gives the radiative transfer equation for thermal radiation in a scattering atmosphere:

$$\mu\frac{dI_\upsilon(\tau,\mu)}{d\tau} = I_\upsilon(\tau,\mu) - (1-\omega_0)B_\upsilon(\tau) - \frac{\omega_0}{2}\int_{-1}^{1} P(\mu,\theta)\, I_\upsilon(\tau,\theta)\, d\theta$$

4.22

4.5 Line-by-line discrete ordinates method for radiative transfer in a scattering atmosphere

When simulating radiances in a cloudy atmosphere such as the one described above, this work uses a model that combines optical depth outputs from LBLRTM with a cloud particle scattering model: The DIScrete Ordinate Radiative Transfer code (DISORT) [*Stamnes et al.*, 1988]. The combination of these two components results in a model known as LBLDIS [*Turner*,2005].

The DISORT code solves the radiative transfer equation for a cloudy atmosphere, along with a set of first order differential equations. The atmosphere is split into a number of layers, each of which have constant ω_0, $P(\theta)$ and τ. DISORT then sets the boundary conditions (TOA or surface), along with the condition that upward and downward intensities must be continuous at each layer boundary, thus generating a set of differential equations with coefficients that can be solved.

The method by which LBLDIS is operated is summarised in a flowchart in Figure 4.3. Firstly, a number of atmospheric layers are defined in LBLRTM (taken from the input

atmospheric profile). Optical depths for each of these layers are calculated by LBLRTM and these, along with layer temperature and altitude, are passed to LBLDIS. Two further input files are required; a parameter file in which the user specifies information about the cloud layer (height, optical depth etc.), and a scattering database which includes the scattering properties (g, ω_0, β_v etc.) for the cloud layer as a function of wavenumber. The cloud is assumed to be homogenous in each layer.

LBLDIS combines the optical depths from LBLRTM with those of the cloud to produce total optical depths for each layer, which are then used to calculate the radiative transfer. An output file is produced containing the simulated radiance spectrum.

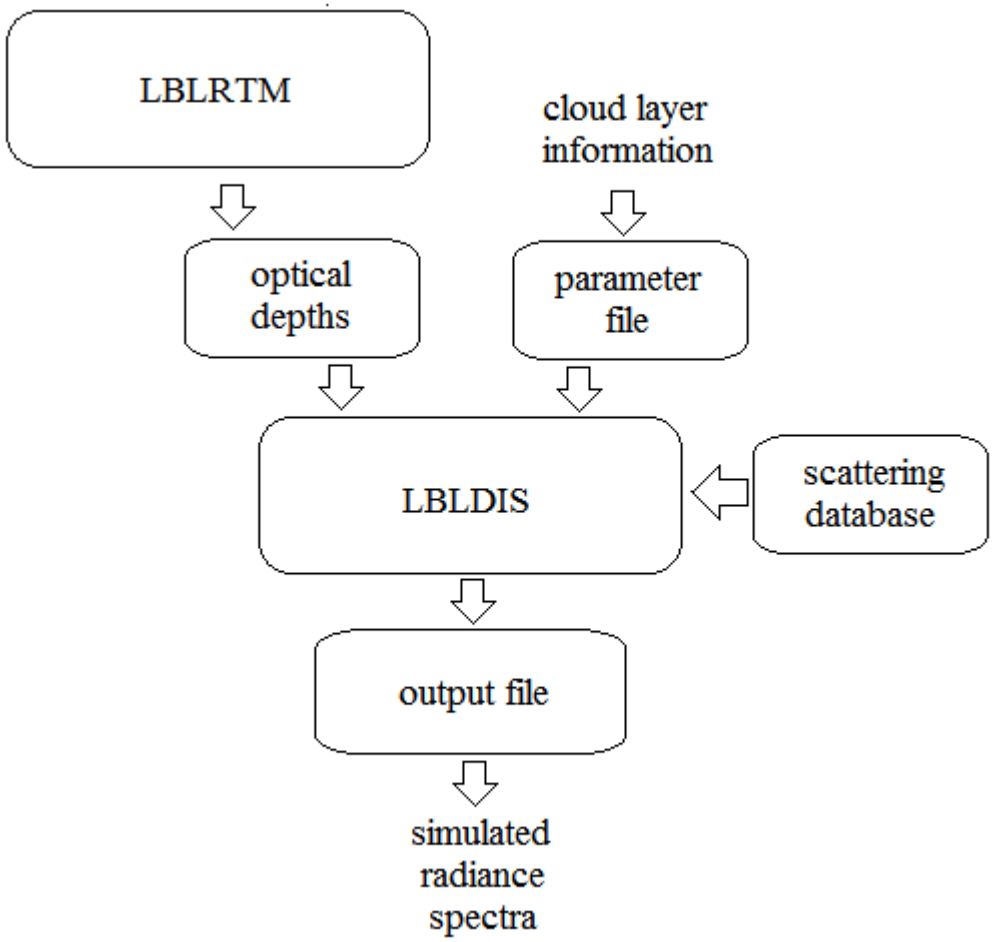


Figure 4.3: *Flowchart showing the inputs and outputs of LBLDIS*

4.6 Scattering databases

The ability of the LBLDIS model to accurately simulate the cloud radiances relies heavily upon the scattering database used. The databases used in this work were developed by Baum et al. at the Space Science and Engineering Center of the University of Wisconsin-Madison [*Baum et al.*, 2014]. They consist of sets of single scattering properties (SSPs), including the

single scattering albedo ω_0, extinction coefficient β_v, and scattering phase function $P(\theta)$ for a wide wavelength range spanning the ultraviolet (UV) to the FIR.

The scattering parameterisation developed by Baum et al. is based on bulk ice-cloud properties, and incorporates microphysical data from a variety of field campaigns [*Baum et al.*, 2005a] as well as ice-particle SSPs developed from several different numerical light-scattering models. The method by which the bulk ice-cloud scattering and absorption models were built is reported in Baum et al. [2005a, 2005b, 2007], and is briefly described below.

4.6.1 Microphysical data

The field campaigns which obtained the microphysical data used to develop the cirrus scattering and absorption models used here [*Baum et al.*, 2014] took place over both hemispheres, in midlatitude and tropical climates. A total of 12815 individual PSDs were recorded, which have particle number densities from 10 to >6000 μm. Also recorded for each PSD was the cloud temperature, the IWC (range 10^{-6} to 10^{0} g m^{-3}) and the median mass particle diameter D_m. The PSDs were filtered to only include those recorded at ≤ - 40°C, in order to ensure measurements were taken within clouds composed of ice. The effective diameter D_e for the PSDs tended to increase monotonically with IWC [*Baum et al.*, 2005a], and the range of D_e calculated was 10 to 180 μm.

The effective diameter is calculated from the PSDs using

$$D_e = \frac{3}{2}\,\frac{\sum_{h=1}^{M}\int_{D_{min}}^{D_{max}} V_h(D)\,f_h(D)\,n(D)\,dD}{\sum_{h=1}^{M}\int_{D_{min}}^{D_{max}} A_h(D)\,f_h(D)\,n(D)\,dD} = \frac{3}{2}\,\frac{V_{tot}}{A_{tot}}$$

4.23

where D_{max} and D_{min} are the maximum and minimum particle sizes in the distribution, $f_h(D)$ is the ice particle habit fraction of habit h for size D, $n(D)$ is the number distribution for size D, and $V_h(D)$ and $A_h(D)$ are the projected volume and area of a specific particle of habit h for size D, respectively. The habit fraction is defined so that for each size bin

$$\sum_{h=1}^{M} f_h(D) = 1$$

4.24

where M is the total number of habits.

The IWC for a given PSD is calculated using

$$IWC = \rho_{ice} \sum_{h=1}^{M} \int_{D_{min}}^{D_{max}} V_h(D)\, f_h(D)\, n(D)\, dD \qquad 4.25$$

where $\rho_{ice} = 0.917\ g\ cm^{-3}$ and is the density of ice [*Baum et al.*, 2014].

The PSDs were measured primarily using 2D imaging probes (see §7.3.2), and thus were affected by the issue of shattering of large ice crystals on the probe inlets, resulting in an overly large concentration of small particles, and an under-counting of large particles. The PSDs used by Baum et al. have been reprocessed to account for this effect using the method described by Field et al. [2006], which uses particle inter-arrival times to estimate the fraction of particles affected and corrects the size concentrations accordingly.

4.6.2 Ice particle habits and surface roughness

The Baum et al. [2014] databases are based on a library of SSPs developed for habits including plates, droxtals, hollow and solid columns, hollow and solid bullet rosettes, an aggregate of solid columns and a small/large aggregate of plates. Three SSPS databases are available that assume the use of solid columns only (SC), an aggregate of solid columns only (ASC), and a general habit mixture that incorporates all the habits (GHM). Further details on the geometries of these habits is given in Baum et al. [2011], and the ice-particle volume for each habit as a function of maximum particle dimension D_{max} is given in Figure 4.4.

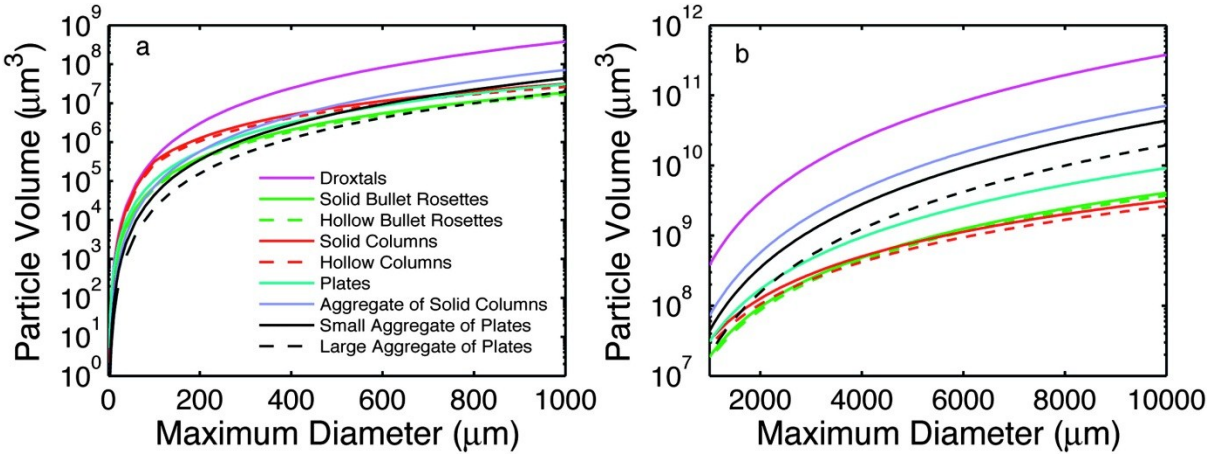


Figure 4.4: *Ice-particle volume as a function of habit and maximum dimension D_{max} for (a) $D_{max} \leq 1000\ \mu m$ (small-to moderately sized particles) and (b) $D_{max} > 1000\ \mu m$ (moderate to large particles). From Baum et al. [2011].*

Studies have shown that the surface roughness of ice particles has an important effect on the scattering properties of ice crystals. Ulanowski et al. [2006] used laboratory-grown roughened ice crystals in light scattering experiments, and found that particles with rough surfaces have qualitatively different phase functions to those with smooth surfaces, with the roughened particles having increased side and back scattering. The asymmetry parameter g is typically about 0.8±0.04 and 0.63±0.05 for smooth and rough crystals respectively. Further work by Ulanowski et al. [2014] used in situ measurements of ice particle roughness taken using the Small Ice Detector 3 (SID-3) during flights in mid-latitude cirrus clouds. They compared the retrieved roughness to those obtained to the lab-grown ice crystals, and found that the in situ roughness corresponded to the roughest subset of lab particles, and in some cases even extends beyond the most extreme lab values.

The SSPs used in the databases of Baum et al. [2014] assume that the ice crystals are severely roughened, and account for this roughness using the ray-tracing method of Yang et al. [2008].

4.6.3 Single scattering properties

The SSPs provided in the databases of Baum et al. [2014] are the single scattering albedo, asymmetry parameter, extinction coefficient, extinction efficiency, total projected particle area, and full phase matrix. These are all given as functions of the effective diameter that ranges from 10 to 120 μm in increments of 5 μm for a total of 23 individual $D_e$values. The SSPs are given for 445 discrete wavelengths between 0.2 and 100 μm. The equations for calculating the SSPs are taken from Appendix B of [*Baum et al.*, 2011] and Appendix A of [*Baum et al.*, 2014], and are reproduced below.

The mean scattering cross section $\bar{\sigma}_{sca}$ at a specific wavenumber λ is given by

$$\bar{\sigma}_{sca}(\lambda) = \frac{\int_{D_{min}}^{D_{max}} \left[\sum_{h=1}^{M} \sigma_{sca,h}(D,\lambda)\, f_h(D)\right] n(D)\, dD}{\int_{D_{min}}^{D_{max}} [\sum_{h=1}^{M} f_h(D)] n(D)\, dD} \qquad 4.26$$

where $\sigma_{sca,h}(D,\lambda)$ is the scattering cross section at particle size D, for wavenumber λ and habit h.

Similarly, the mean extinction cross section $\bar{\sigma}_{ext}$ is given by

$$\bar{\sigma}_{ext}(\lambda) = \frac{\int_{D_{min}}^{D_{max}} \left[\sum_{h=1}^{M} \sigma_{ext,h}(D,\lambda)\, f_h(D)\right] n(D)\, dD}{\int_{D_{min}}^{D_{max}} [\sum_{h=1}^{M} f_h(D)] n(D)\, dD}$$

4.27

The mean single scattering albedo $\bar{\omega}_0$ is determined by the ratio of the mean scattering and extinction cross sections:

$$\bar{\omega}_0(\lambda) = \frac{\bar{\sigma}_{sca}(\lambda)}{\bar{\sigma}_{ext}(\lambda)}$$

4.28

The extinction efficiency Q_{ext} for a given particle size is the extinction cross section divided by the total projected area, and the mean extinction efficiency $\bar{Q}_{ext}$ is the extinction cross section divided by the total projected area for a given PSD:

$$\bar{Q}_{ext}(\lambda) = \frac{\int_{D_{min}}^{D_{max}} \left[\sum_{h=1}^{M} Q_{ext,h}(D)\, A_h(D)\, f_h(D)\right] n(D)\, dD}{\int_{D_{min}}^{D_{max}} [\sum_{h=1}^{M} A_h(D)\, f_h(D)] n(D)\, dD}$$

4.29

The bulk extinction coefficient $\bar{\beta}_{ext}$ is defined as

$$\bar{\beta}_{ext}(\lambda) = \int_{D_{min}}^{D_{max}} \left[\sum_{h=1}^{M} Q_{ext,h}(D)\, A_h(D)\, f_h(D)\right] n(D)\, dD$$

4.30

The scattering phase function $\overline{P}(\theta)$, where θ is the scattering angle, is given by

$$\overline{P}(\theta,\lambda) = \frac{\int_{D_{min}}^{D_{max}} \left[\sum_{h=1}^{M} P_h(\theta,D,\lambda)\, \sigma_{sca,h}(D,\lambda)\, f_h(D)\right] n(D)\, dD}{\int_{D_{min}}^{D_{max}} \left[\sum_{h=1}^{M} \sigma_{sca,h}(D,\lambda)\, f_h(D)\right] n(D)\, dD}$$

4.31

The asymmetry factor $\bar{g}$ is given by

$$\overline{g}(\lambda) = \frac{\int_{D_{min}}^{D_{max}} \left[\sum_{h=1}^{M} g_h(D,\lambda)\, \sigma_{sca,h}(D,\lambda)\, f_h(D)\right] n(D)\, dD}{\int_{D_{min}}^{D_{max}} \left[\sum_{h=1}^{M} \sigma_{sca,h}(D,\lambda)\, f_h(D)\right] n(D)\, dD}$$

4.32

and defines the amount of radiation that is scattered in the forward direction i.e. for $g = 1$ all radiation is scattered forwards, for $g = -1$ all radiation is back-scattered, and for $g = 0$, the radiation is scattered isotropically.

The choice of which habit database (SC, ASC, GHM) to use in simulating recorded spectral measurements is an important one. Although the GHM database best represents the complexity of natural ice clouds compared to using a single habit model, it is more important that the habit choice is sufficient in reproducing in situ measurements for the specific application for which they are to be used.

Studies investigating the consistency of the three habit databases when compared to in situ measurements indicate that the comparisons from the SC model provide the best match to values of both IWC and median particle diameter (D_{mm}) from field campaigns. The ASC model tended to underestimate the IWC and overestimate D_{mm}, whilst the GHM model performed well at reproducing the IWC, but tended to overestimate the D_{mm} at values above 400 μm [*Baum et al.*, 2014].

A second study evaluating the ability of the three databases to reproduce polarized reflectivities found that the GHM model with severe particle roughening provided the closest values, although single habit models were also able to simulate the reflectivities [*Cole et al.*, 2013].

A final study by Baum et al. [2014] used retrievals of cloud optical thickness (τ) in the solar (0.86-2.13 μm) and MIR (8.5-12 μm) spectral regions to test the consistency of the databases across the spectrum. They found that in the MIR the difference in τ was very small, indicating little sensitivity to habit in this region. The solar region is much more sensitive, and it was found that the ASC model performed the best at representing τ in this region.

5 Ground-based observations of the far-infrared water vapour foreign continuum during RHUBC

This chapter reports the results of a case study using TAFTS to take FIR clear-sky measurements in order to study the water vapour continuum. These measurements were recorded while TAFTS was deployed during the Radiative Heating in Underexplored Bands Campaign (RHUBC). The chapter begins with an introduction to the campaign, its aims, and the range of instrumentation used in this work. The focus of the analysis is on a single case of measurements, made in clear sky conditions, at 1333 UTC on the 10th March 2007. These recorded TAFTS spectra are used in a cross-comparison with the AERI-ER instrument present during the campaign, and then used in a validation study of the most recent iteration of the MT-CKD water vapour continuum parameterisation, the MT-CKD v2.5.

5.1 Introduction

The Radiative Heating in Underexplored Bands Campaign (RHUBC) took place in Barrow, Alaska, in February and March 2007. During RHUBC, high resolution far-infrared spectra were measured simultaneously and independently by two different spectrometers - the Imperial College Tropospheric Airborne Fourier Transform Spectrometer (TAFTS) and the Atmospheric Radiation Measurement program (ARM) Atmospheric Emitted Radiance Interferometer - Extended Range (AERI-ER).

As outlined in §2.2, water vapour is responsible for over half of the natural greenhouse effect of the Earth, and the majority of the absorption of solar radiation by the atmosphere [*Kiehl and Trenberth*, 1997], resulting in it being the most important radiatively active atmospheric gas [*Harries*, 1996]. A key region is the far-infrared (FIR) pure rotation band (50-650 cm^{-1} / 15.4-200 μm), from which up to 35 % of outgoing longwave radiation originates [*Clough et al.*, 1992; *Sinha and Harries*, 1995]. Measurements presented here focus on the water vapour continuum absorption (see §2.2.2). Theories as to the cause of the continuum focus on absorption by the far-wings of vibration-rotation transitions [*Elasser*, 1938; *Clough et al.*, 1989] or by weakly bound pairs of water molecules, the water dimer [*Baranov and Lafferty*, 2012]. The semi-empirical Mlawer-Tobin-Clough-Kneizys-Davies (MT-CKD) continuum model [*Mlawer et al.*, 2003; *Clough et al.*, 2005], widely used in radiative transfer simulations by the atmospheric science community, has been developed and continually updated as new measurement data has become available. The latest iteration, the MT-CKD

version 2.5 [*Mlawer et al.*, 2012] was used in this work. In the spectral range 400-600 cm^{-1}, a major update to the parameterisation (MT-CKD 2.4) resulted from analysis by Delamere et al. [2010] of data recorded by the Atmospheric Emitted Radiance Interferometer - Extended Range (AERI-ER, see §3.3)) instrument during the Radiative Heating in Underexplored Bands Campaign (RHUBC) [*Turner and Mlawer*, 2010].

In this study, measurements from the AERI-ER are compared to those recorded by the Imperial College TAFTS instrument (see §3.2) recorded during the same campaign, allowing a direct comparison between the two instruments for the first time. The TAFTS measurements presented here cover parts (350-550 cm^{-1}) of the FIR water vapour spectrum at a higher spectral resolution than has previously been reported by studies using alternative instrumentation [*Cageao et al.*, 2010; *Delamere et al.*, 2010; *Liuzzi et al.*, 2014]. The water vapour continuum is a low resolution absorption, however higher resolution measurements allow more accurate rendering of the absorption lines, and easier separation of the line and continuum contributions. This study evaluates the current continuum model at FIR wavelengths, complementing previous studies from other locations and atmospheric conditions. These results, although from a single case, suggest that current model parameters are accurately representing the water vapour continuum across the entire spectrum.

5.2 The Radiative Heating in Underexplored Bands Campaign

5.2.1 Field campaign description

RHUBC [*Turner and Mlawer*, 2010] was a ground-based study which took place at the Atmospheric Radiation Measurement Climate Research Facility - North Slope of Alaska (ACRF-NSA) site from 22 February to 14 March 2007.

RHUBC had three main objectives:

1. To record clear-sky radiative measurements to be used to reduce uncertainties in water vapour spectroscopy, particularly concerning the water vapour continuum and water vapour absorption line parameters.
2. To cross-calibrate the TAFTS instrument with the AERI-ER instrument. An inter-comparison study between the two FIR spectrometers allows higher confidence in results from both instruments.

3. To investigate the radiative properties of sub-arctic cirrus using measurements from both TAFTS and AERI-ER. This has allowed a high-resolution study spanning the mid- and far-infrared [*Humpage*, 2010], and is not addressed here.

Across the majority of surface locations on Earth, the FIR spectral region is saturated by strong absorption in the high pressure and humidity of the near surface, rendering its spectroscopic features unobservable. There are three options to overcome this near surface opacity; observations from space (via satellite), from aircraft, or from cold and dry surface locations such as high mountain tops or arid arctic regions. The timing and location for RHUBC was chosen to exploit this last scenario, as the relative transparency of the atmosphere, dry climate and low occurrence of optically thick low clouds during the winter at the ACRF-NSA site makes it ideal to conduct studies of this nature [*Turner and Mlawer*, 2010]. The typical transparency of the atmosphere for RHUBC is demonstrated in Figure 5.1 by the contrast between the simulated sea-level infrared radiance spectrum for a US standard atmosphere (PWV = 13.5 mm) and the much drier (PWV = 1.4 mm) sub-arctic winter atmosphere observed during RHUBC at ACRF-NSA. FIR (50-650 cm^{-1}) radiances are much reduced for the sub-arctic case due to the much colder temperatures in the arctic atmosphere lowering the overall radiance curve, but also the greater atmospheric transparency in this region, represented by the visible deepening of the microwindows between the water vapour absorption lines.

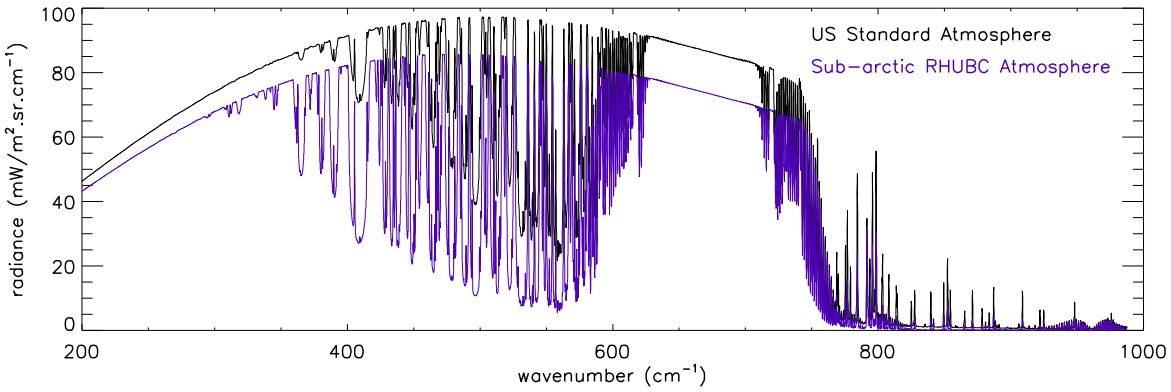


Figure 5.1: *LBLRTM simulations of down-welling spectral radiance performed using a US standard atmosphere (PWV = 13.5 mm) and a sub-arctic winter atmosphere observed during RHUBC (PWV = 1.4 mm).*

5.2.2 Instrumentation

The ACRF-NSA was established to address the need for long term monitoring of the atmosphere in the arctic, a region particularly sensitive to changes in global climate. A large number of the instruments present at the facility have been continuously recording data since July 1997, giving an overview of long-term changes in atmospheric conditions as well as cloud and radiative processes taking place in the high latitude climate. For RHUBC, in addition to the two FIR interferometers (TAFTS and AERI-ER, described fully in §3.2 and §3.3), three millimeter-wave radiometers, a cloud-sensitive lidar and a radiosonde sounding station were employed (additional details given in Turner and Mlawer [2010]).

Most of the instruments were located on two trailer platforms. TAFTS was housed in the guest instrument facility shown in Figure 5.2, where a steel cylinder was installed to connect the TAFTS down-welling viewing port to a hole in the roof of the trailer. This minimised any contamination of the field of view from within the trailer. A pump was used to move air from outside into the TAFTS instrument, ensuring that the sampled air was as similar as possible in temperature and water content to the air outside the trailer.



Figure 5.2: *The guest instrument facility at the ACRF-NSA, where the TAFTS instrument was housed during RHUBC. Photo credit: ARM.*

Routine radiosonde launches are performed twice daily at the ACRF-NSA site, and for the duration of RHUBC additional launches took place, making a total of 92 (32 in clear sky conditions) over the three week field campaign. Radiosondes are battery-powered meteorological instrument packages that are carried into the atmosphere by weather balloons.

They measure atmospheric parameters including pressure, altitude, latitude and longitude, temperature and relative humidity. These measurements are then transmitted to ground by radio signals. The radiosondes deployed during RHUBC were the Vaisala RS-92, which have a temperature (T) and relative humidity (RH) measurement uncertainty of ±0.5 °C and ±5 %RH respectively [*Vaisala*, 2010b]. Mirroring the procedure used by Delamere et al. [2010], the radiosonde data have been corrected using the Miloshevich et al. [2009] clear-sky scheme, to minimize profile bias. This correction was derived using comparisons of radiosonde data with measurements from instruments of known accuracy, and is valid in clear or near-clear sky conditions. RS-92 radiosondes have also been found to exhibit sonde-to-sonde variability in the calibration of their water vapour sensors [*Cady-Pereira et al.*, 2008; *Miloshevich et al.*, 2009], and therefore each water vapour profile measured by RHUBC radiosondes has been scaled to match the PWV retrievals measured coincidentally by the G-band water-Vapour Radiometer (GVR) present at ACRF-NSA [*Cadeddu et al.*, 2007; *Cimini et al.*, 2009]. The GVR PWV uncertainty is approximately 2% and this error has been incorporated into the RH uncertainties of the profile measurements in this analysis.

5.3 Cross-comparison of TAFTS and AERI-ER observed FIR spectral radiances

In 2004, Turner et al. compared the observed radiance measured by two AERI-ER present at the NSA site and found that the two instruments agreed within measurement uncertainties [*Turner et al.*, 2004b]. Additionally, an AERI instrument (without extended range) was compared to the Far-Infrared Spectroscopy of the Troposphere (FIRST) radiometer (measurement range 50-2000 cm^{-1}) [*Mlynczak et al.*, 2006] in 2009 during the second phase of RHUBC in Cerro Toco, Chile, with differences in measurements between the two instruments found to be of the order 2-3 % of radiance within their overlap range (500-800 cm^{-1}) [*Cageao et al.*, 2010]. However the AERI-ER, with ability to take measurements further into the FIR portion of the spectrum than the AERI, has not previously been compared with a different design of interferometer such as TAFTS.

5.3.1 Data selection

TAFTS was deployed during RHUBC from 3rd-12th March 2007. Due to intermittent cabling and alignment issues, it was only possible to record data on the 4th, 5th, 9th and 10th March. The optimal weather conditions for studies of the water vapour continuum occurred on the 10th March, and the dataset from this day was therefore used for this analysis. March 10th had stable clear sky conditions combined with low PWV of 1.0 mm rising to 1.6 mm over the course of the day, allowing the far-IR spectral region to be observed. The TAFTS

data consists of 81 spectral scans averaged over the 20 minutes of measurement time. The standard deviation of the spectra is taken as a calibration uncertainty, in combination with the measurement uncertainty of the TAFTS instrument (see §3.2). Only TAFTS data at wavenumbers greater than 350 cm^{-1} has been used here, as the opacity of the atmosphere did not allow observation of the longer wavelength region (see §5.2.1).

The AERI-ER data used here consisted of 26 spectral scans recorded over the same time period as the analysed TAFTS measurements. The data recorded by AERI-ER during RHUBC has been post-processed to reduce uncorrelated errors [*Turner et al.*, 2006], account for an improved blackbody emissivity model [*Turner*, 2003], and correct for oscillations around 400 cm^{-1} [*Delamere et al.*, 2010]. Due to noise and calibration considerations, AERI-ER measurements from RHUBC are limited to those at wavenumbers above 400 cm^{-1}.

The spectral range over which the AERI-ER and TAFTS data overlapped was 400-550 cm^{-1}. As the TAFTS radiance spectra have a resolution of 0.12 cm^{-1}, the data was filtered to match the resolution of AERI-ER (0.5 cm^{-1}). This was achieved by multiplying the TAFTS interferogram by the Fourier transform of the AERI-ER instrument response function. The response function is a sinc function [*Knuteson et al.*, 2004a, 2004b], and therefore its Fourier transform is a boxcar function of width twice the AERI-ER optical path length (1.037 cm). A reverse Fourier transform was then performed on the newly-apodised TAFTS interferogram to return it to wavenumber space, allowing it to now be compared to the AERI-ER radiances at the same spectral resolution.

5.3.2 Radiance comparison

The observed radiances from the two instruments are shown in Figure 5.3 (a), with the difference between them plotted in Figure 5.3 (b). The combined uncertainty of the two instruments (both from radiative calibration and the standard deviation of the averaged spectra) is plotted in blue to give a comparison with the residual.

Figure 5.3 shows good agreement between the two instruments, with an average bias of 0.42 RU (where 1 RU is 1 $mW/(m^2.sr.cm^{-1})$) i.e. TAFTS consistently records slightly lower radiances than AERI-ER. The standard deviation of the residuals is 2.21 RU, and the maximum deviation of the residual from zero is 6.27 RU, which is within three standard deviations. The average combined instrumental uncertainty is 2.27 RU, and 68 % of the residual data lies within the uncertainty boundaries. Figure 5.3 shows that several of the residual features that lie outside the range of the uncertainties occur at the peaks of absorption

lines (e.g. 442, 457, 484, 518, 526 cm^{-1}). This could be attributed to additional emission by water vapour within the TAFTS instrument, resulting in increased differences at the strong line centres.

The strong agreement between the TAFTS and AERI-ER measurements gives confidence in the ability of both instruments to accurately represent the far-infrared down-welling radiances, given their differences in interferometer and detector design. Data from the AERI-ER at RHUBC has been used to develop the MT-CKD 2.4 continuum parameterization [*Delamere et al.*, 2010], and therefore the agreement between the two instruments indicates that the data obtained from TAFTS at RHUBC can be used to study the foreign-broadened water vapour continuum the lower wavenumbers to which the TAFTS measurement range extends.

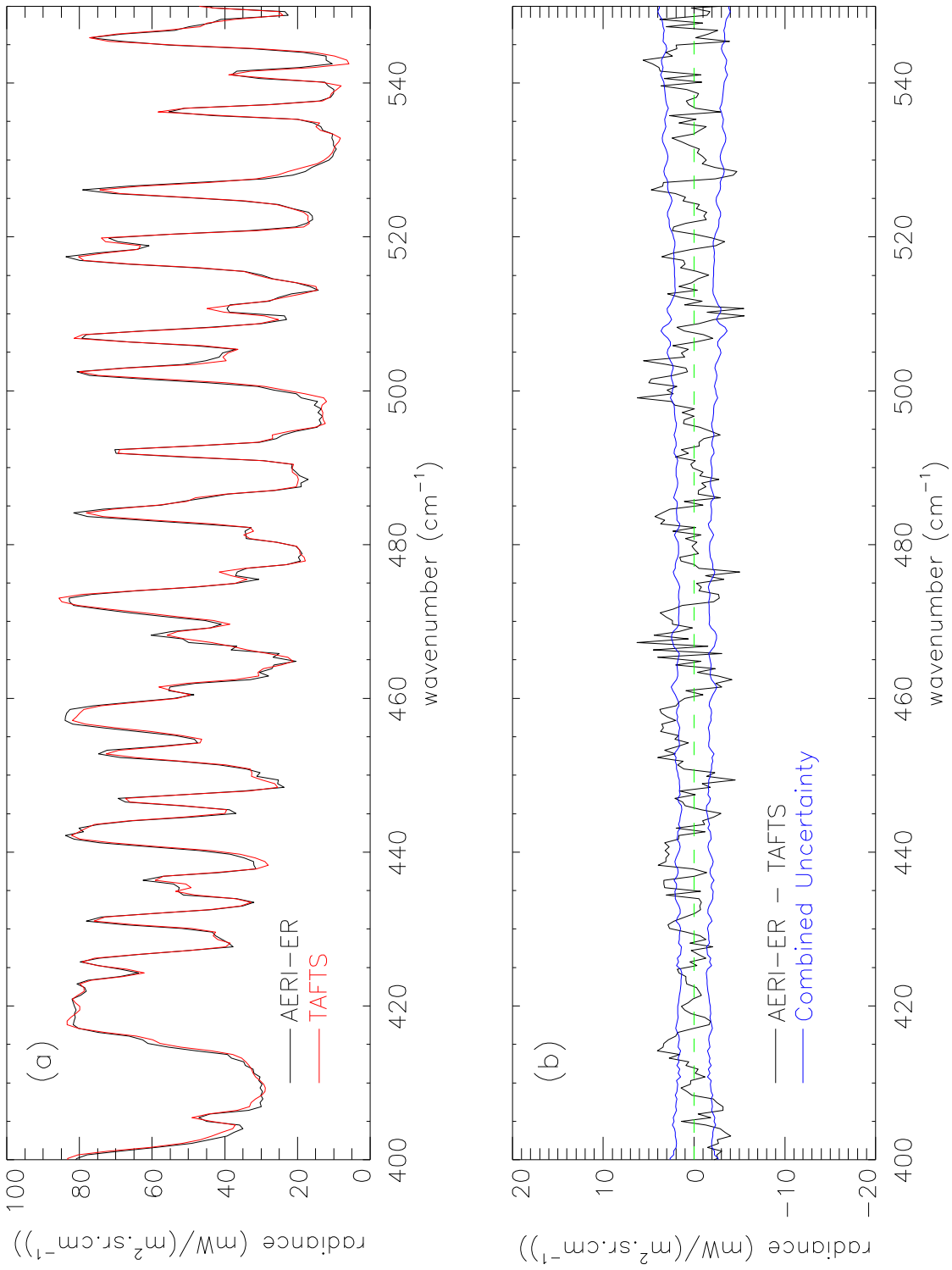


Figure 5.3: *(a) Comparison of AERI-ER (black) and TAFTS (red) radiance spectra; (b) their residual (black) and combined instrumental uncertainty (blue) for the dataset recorded on the 10th March 2007. The TAFTS spectra have been filtered to match the resolution of the AERI-ER.*

5.4 Water vapour continuum simulations and measurements

The TAFTS FIR spectra recorded on the 10th March 2007 were compared to simulated spectra for the observed conditions, generated using the Line By Line Radiative Transfer Model (LBLRTM) [*Clough et al.*, 2005]. This comparison was used to evaluate the ability of the model to correctly simulate the water vapour continuum as observed in this case study. The effect of the continuum can be observed in the spectral micro-windows i.e. those regions in between the spectral absorption lines, and therefore any differences between measured and simulated radiances due to continuum effects are expected to be observed in these micro-windows.

5.4.1 Simulated radiances

The LBLRTM requires an accurate profile of atmospheric conditions in order to simulate the expected radiances. The primary source of atmospheric profile T and RH information was from the 1333 UTC radiosonde release, which was corrected according to the procedure used by Delamere et al. [2010] as outlined in §5.2.2. In addition, measurements from the 40 m observation tower at the site were used to construct the profile close to the surface. Above the tropopause, a sub-arctic winter standard atmospheric profile [*McClatchey et al.*, 1972] was used. The final composite T and RH atmospheric profiles for the duration of the 1333 sonde, where these data have been combined and smoothed, along with their uncertainties, are shown in Figure 5.4. The smoothing gives representative values at the profile levels input into LBLRTM and avoids any problems due to random noise fluctuations. The profile has 150 fixed pressure levels; 100 levels in the troposphere (1038-100 hPa) and 50 levels between 100 and 10 hPa.

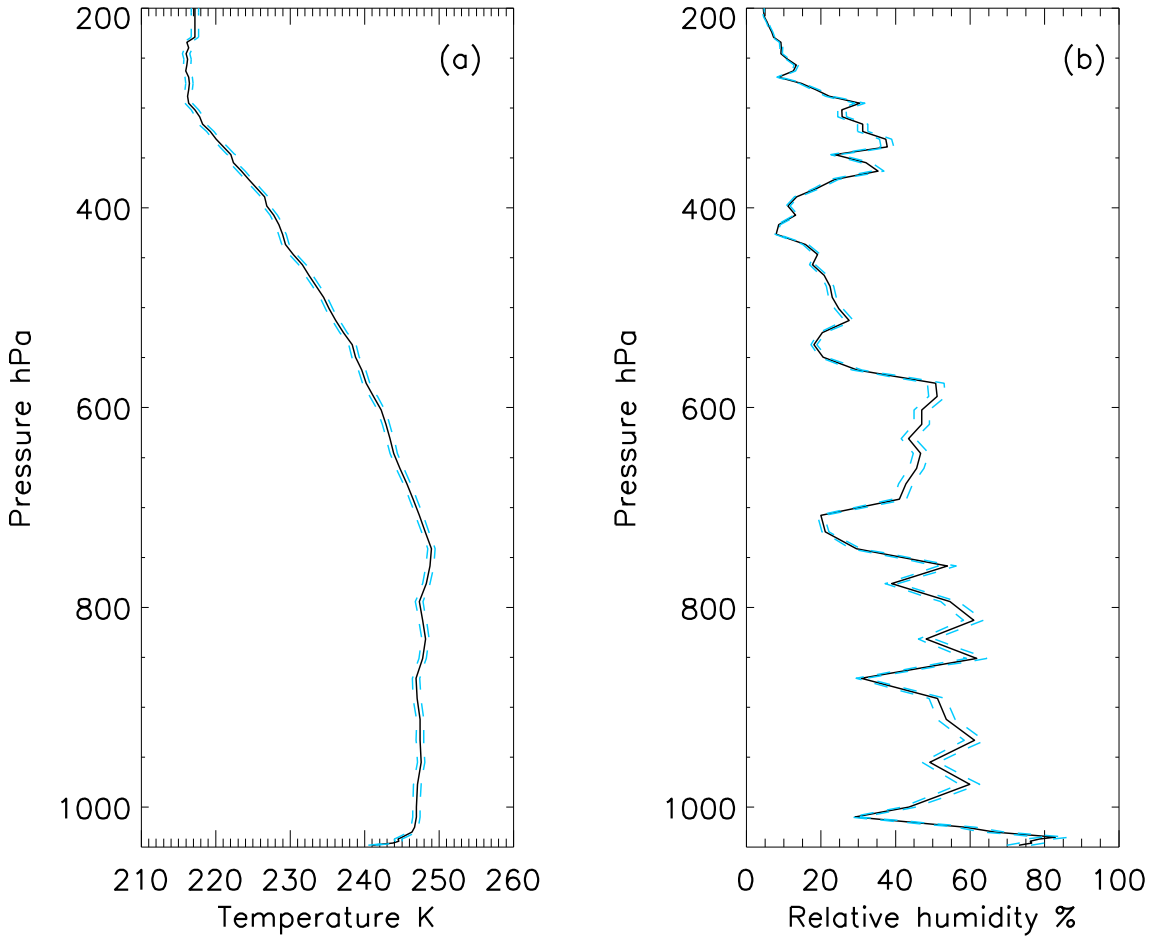


Figure 5.4: *The final composite temperature (a) and relative humidity (b) atmospheric profiles used in the analysis, with the combined uncertainty values shown in blue.*

Simulated radiances are calculated from the profile information using LBLRTM v12.2 with the AER v3.2 line database and MT-CKD 2.5.2 continuum parameterization [*Clough et al.*, 2005; *Mlawer et al.*, 2012]. The LBLRTM line parameters are based on the HITRAN 2008 [*Rothman et al.*, 2009] spectroscopic database, which includes the updated air-broadened half-widths of FIR water-vapour absorption lines reported in Delamere et al. [2010]. A full record of recent revisions can be found on the Atmospheric and Environmental Research Inc. (AER) website (http://rtweb.aer.com/). The MT-CKD 2.5.2 foreign-broadened water vapour continuum coefficients in the simulated measurement region are based on the Delamere et al. [2010] study of RHUBC AERI-ER observations. As it has already been shown in §5.3 that the TAFTS and AERI-ER observations from the single case analysed here are generally consistent, it would be expected that there would be agreement between the TAFTS observations and the LBLRTM simulations.

5.4.2 Comparison of observed and simulated radiances

The calibrated TAFTS FIR radiances shown in Figure 5.5 (a) were recorded co-incidentally with the duration of the 1333 UTC radiosonde launch, from which the simulation profile was constructed. The corresponding LBLRTM simulation for these data is shown in the same panel. The micro-window regions, where continuum absorption is seen, are indicated in purple. Figure 5.5 (a) shows that the observed radiances have general agreement with those calculated by LBLRTM, giving confidence that the model can accurately simulate case studies such as this one. The structure of the differences seen between the TAFTS radiances and simulations is mainly attributable to uncertainties in the line strengths and widths. Better agreement is seen in the window regions, where the signal from the foreign-broadened continuum is better isolated.

The residual (observed minus simulated radiances) is shown in Figure 5.5 (b) along with the combined radiance uncertainties. These uncertainties are a cumulative value calculated from several individual sources, each of which are shown in Figure 5.6, alongside the same residual as plotted in Figure 5.5 (b). Figure 5.6 (a) shows the equivalent radiance uncertainty from the profile used for the LBLRTM simulation (combined RH and T uncertainties), and Figure 5.6 (b) shows the TAFTS calibration uncertainty. In order to assess the effect of the uncertainties in the simulation due to the line parameters (such as the large adjustments to H_2O line widths suggested by Delamere et al. [2010]), simulations have been performed where the intensity and width of water vapour lines given in AER v3.2 have been perturbed by 5%. The original minus perturbed simulation for the line strengths and widths are shown in Figure 5.6 (c) and (d) respectively. The residuals between the original and perturbed simulations show the sensitivity of the calculated radiances to the uncertainties in the line strengths and widths.

By comparing the magnitude of the residual between the TAFTS observations and the LBLTRM simulation in Figure 5.5 (b) with the combined uncertainty value, those features which lie outside the uncertainty range can be identified. The model continuum coefficients were adjusted until values were identified that best fitted the TAFTS observations within the microwindows. The magnitude of the residual between the simulation using these altered continuum values, and the simulation using the original continuum values, is shown by the red stars in Figure 5.5 (b). As the majority of the red stars lie within the range of the uncertainties (blue lines), these suggested adjustments in model continuum coefficients are ultimately indistinguishable from uncertainty in the instrumental measurements.

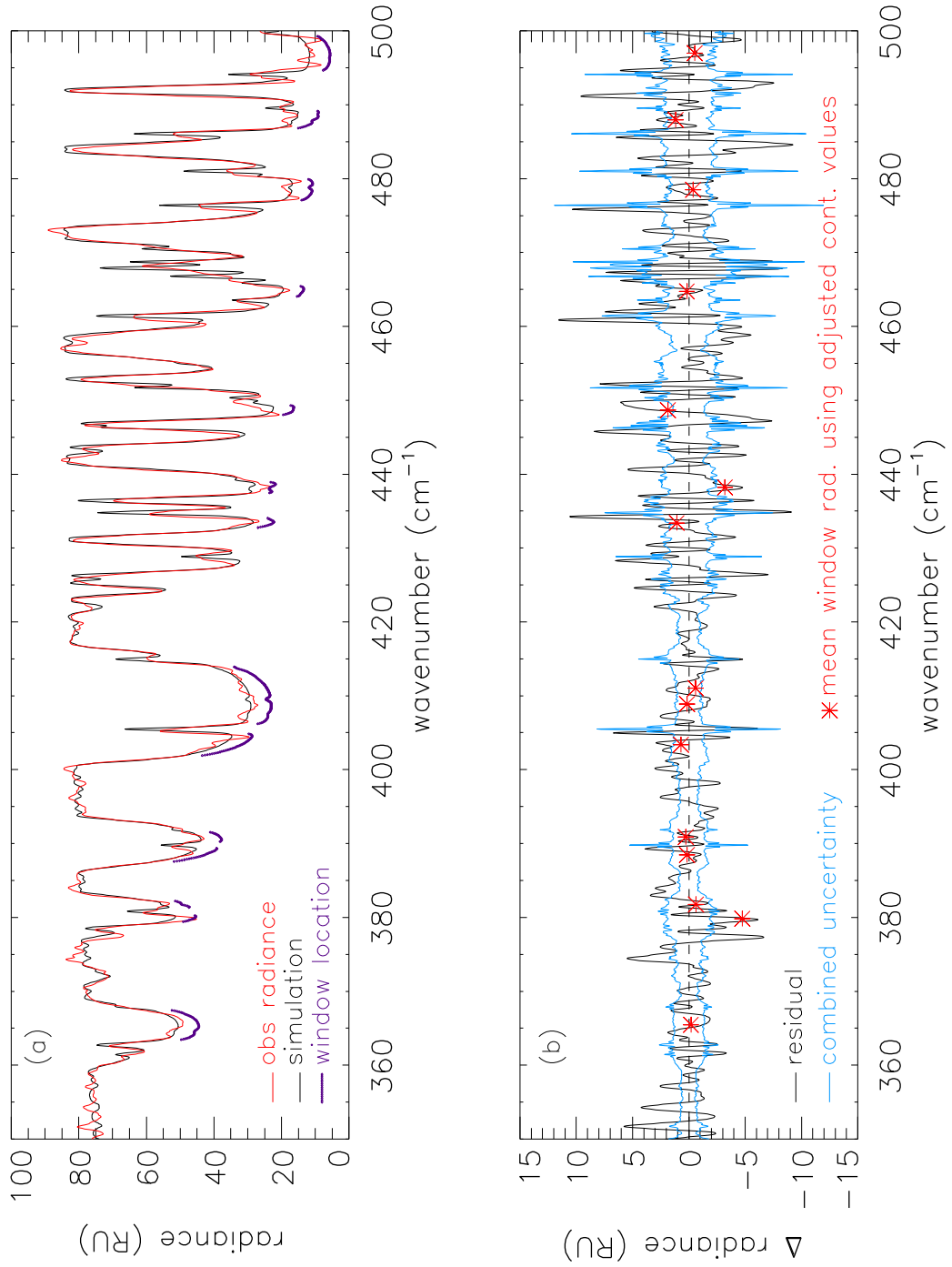


Figure 5.5: *Comparison of the TAFTS and simulated radiances. (a) A section of the TAFTS data measured during the 1333 radiosonde launch (black), with the corresponding simulated radiance (red). The window regions are indicated in purple. (b) Observation - simulation residual (black), cumulative uncertainties (blue). The red stars in each microwindow are the magnitude of the residual between the simulation when using adjusted model continuum coefficients, and the original simulation.*

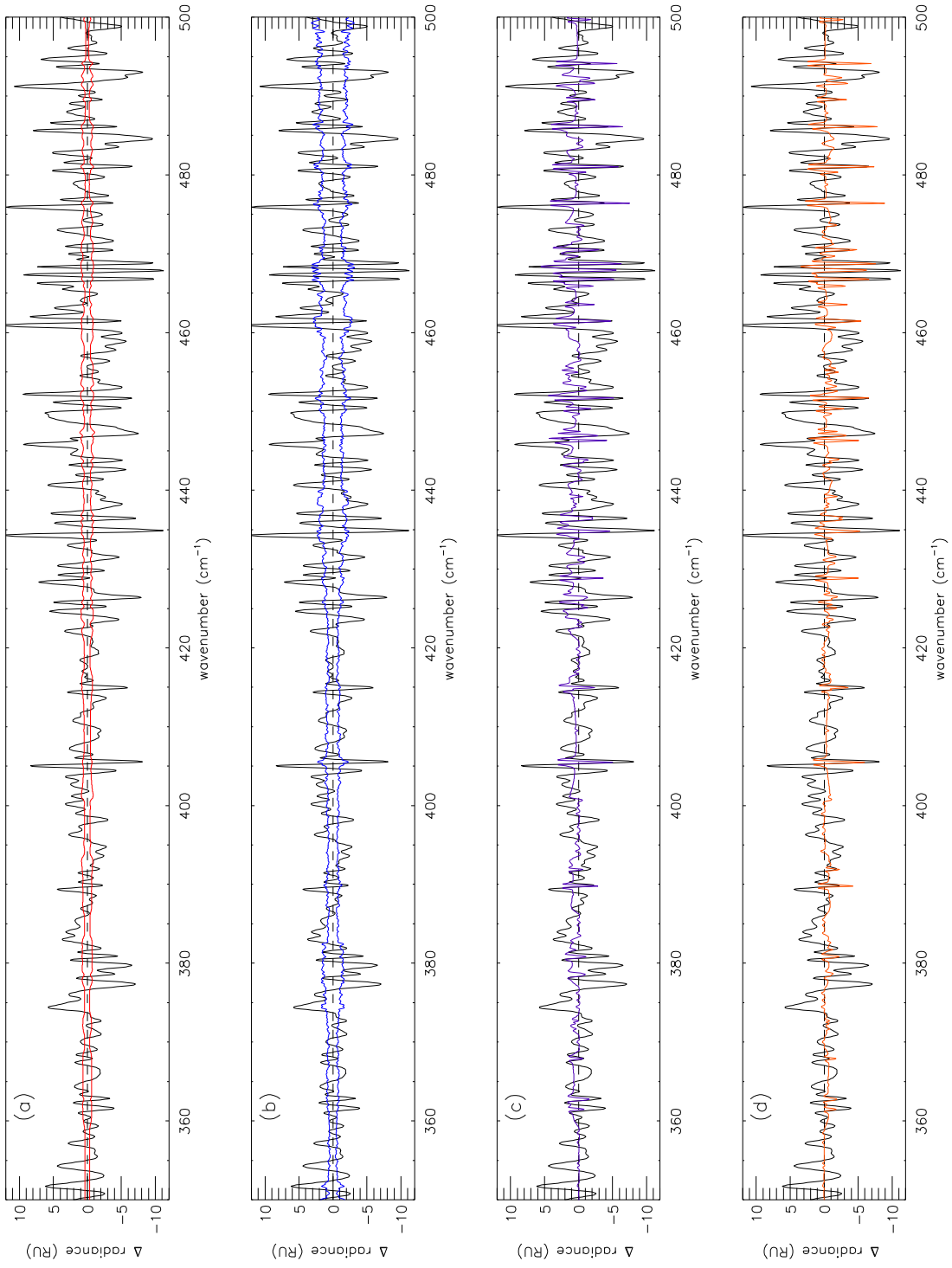


Figure 5.6: *Sources of uncertainty in the radiance simulation. All panels; the observed-simulated residual (black). (a) The equivalent radiance uncertainty due to the T and RH uncertainties in the LBLRTM profile (red). (b) The TAFTS radiometric calibration uncertainty (blue). (c) and (d) Uncertainty due to a 5% perturbation in the AER v3.2 water vapour line intensity and width respectively, where the coloured lines represent the original simulation minus the perturbed simulation.*

5.4.3 Discussion and comparison with previous studies

Table 5.1 summarizes the values of continuum absorption strength in each microwindow as suggested by the measured TAFTS radiances, given as a percentage change of the current continuum model, and also in units of spectral density function C_f ($cm^2\ mol^{-1}(cm^{-1})^{-1}$). This data is plotted in Figure 5.7, where the dashed red line represents a weighted linear fit to the data. Here the error bars represent the combined uncertainty from the TAFTS calibration and simulation profile. Figure 5.7 indicates that the suggested continuum from the calibrated TAFTS radiances has good agreement with the MT-CKD continuum, with almost all of the values lying within their uncertainty of the zero line. However the TAFTS measurements do suggest a steady rise in percentage continuum adjustment from -2.3 % at 350 cm^{-1} to +12.6 % at 500 cm^{-1}. The standard deviation of the suggested percentage continuum adjustment values is 13.4 %, meaning that all the suggested changes are within one standard deviation from 0 % adjustment. Thus it can be concluded that the results from this case study presented are in agreement with the current MT-CKD 2.5 foreign-broadened continuum values.

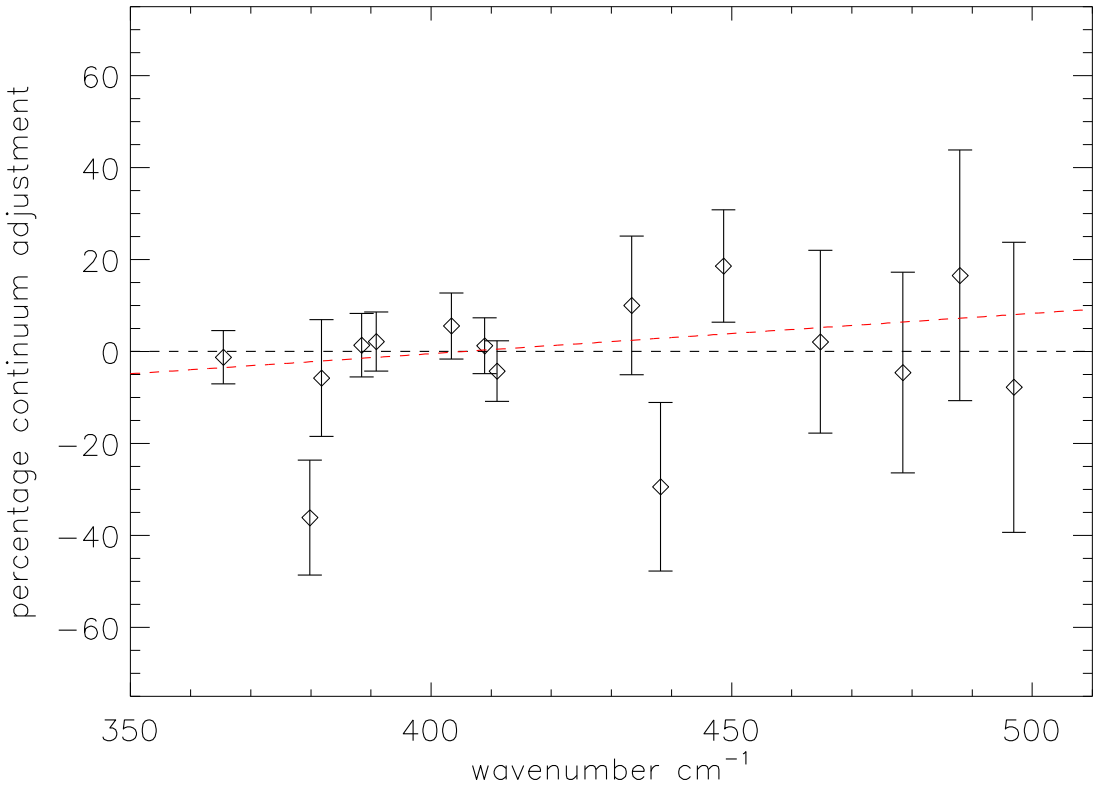


Figure 5.7: *Percentage adjustments to the continuum model as calculated from TAFTS radiances recorded during the 1333 UTC radiosonde launch. The dashed red line through these points is a linear fit to these data, weighted for the uncertainties.*

Table 5.1: *Continuum strengths for each micro-window alongside the associated uncertainty as derived in this study*

Microwindow centre wavenumber cm^{-1}	**Suggested change in continuum absorption strength %**	**Suggested continuum absorption strength** Cf $(cm^2\ mol^{-1}(cm^{-1})^{-1})\times 10^{-24}$
365.4	-1 ± 7	0.457 ± 0.030
379.8	-35 ± 20	0.233 ± 0.046
381.8	-5 ± 14	0.326 ± 0.045
388.5	+2 ± 8	0.301 ± 0.023
390.9	+3 ± 7	0.288 ± 0.020
403.4	+6 ± 7	0.241 ± 0.017
408.9	+1 ± 6	0.207 ± 0.013
411.0	-4 ± 7	0.189 ± 0.014
433.4	+12 ± 14	0.152 ± 0.021
438.2	-29 ± 26	0.090 ± 0.024
448.7	+19 ± 11	0.127 ± 0.013
464.8	+3 ± 19	0.085 ± 0.016
478.5	-4 ± 23	0.066 ± 0.015
488.0	+17 ± 23	0.069 ± 0.016
497.0	-7 ± 34	0.048 ± 0.016

In Figure 5.8, the continuum strengths determined from these measurements are presented alongside studies by Green et al. [2012] and Liuzzi et al. [2014]. The MT-CKD 2.5 [*Mlawer et al.*, 2012], which is based on the study by Delamere et al. [2010], is also shown for comparison. Figure 5.8 shows that this study is in general agreement with MT-CKD 2.5 (and therefore with Delamere et al. [2010]) within uncertainties, with only the points at 380 and 438 cm^{-1} having error bars outside of the MT-CKD line. A possible explanation for this is the higher resolution of the TAFTS instrument resolving the microwindows to a greater depth, and that this mismatch is caused by an error in a spectroscopic parameter (i.e. width) of a line near these locations. However it must also be considered that this study is based only on a single case, and therefore has uncertainties due to the limited averaging that is possible. An error in the line parameterisation would be evident in other studies with different

thermodynamic conditions, and requires further study to unequivocally determine the source of the residuals seen.

Green et al. [2012] used measurements recorded by TAFTS and concluded that for the region above 300 cm^{-1}, the current MT-CKD 2.5 parameterization was correct. The results presented here corroborate this where the wavenumber range overlaps (360-420 cm^{-1}), but includes measurements at greater wavenumbers, thus extending the wavenumber range at which MT-CKD 2.5 has been studied by TAFTS to 500 cm^{-1}. It can be seen that in the window at 380 cm^{-1}, the study by Green et al. agrees with this study in indicating a lower radiance than MT-CKD 2.5, thus increasing the possibility that the TAFTS instrument is resolving this microwindow to a greater depth and highlighting a line width parameterisation error. The work by Liuzzi et al. [2014] was recorded by the Radiation Explorer in the Far InfraRed – Prototype for Applications and Development (REFIR-PAD) instrument [*Bianchini and Palchetti*, 2008] during deployment in Antarctica, and consists of three sets of continuum coefficient retrievals; two using LBLRTM 12.2, AER 3.2 and MT-CKD 2.5.2 (named REFIR-L, summer and winter conditions) and one using a different water vapour line compilation from HITRAN 2012 [*Rothman et al.*, 2013] (named REFIR-H). The version of continuum coefficients shown in Figure 5.8 is the winter REFIR-L, as this provides the most similar atmospheric conditions to those at RHUBC, and also has been performed using the same simulation models as this study. It should be noted that the TAFTS data is plotted only for the microwindow regions, whereas the REFIR-L values are at more regular wavenumber intervals and thus take into account both line and continuum absorption contributions. The conclusions of Liuzzi et al. [2014] validated the current MT-CKD 2.5 model in the region 350-590 cm^{-1}, and justified the adjustment [*Delamere et al.*, 2010] of the water vapour line widths in the region 350-600 cm^{-1}, which have been implemented in AER 3.2. The results of this study are in agreement with those of Liuzzi et al., and thus provide a further verification of MT-CKD 2.5 in this spectral region.

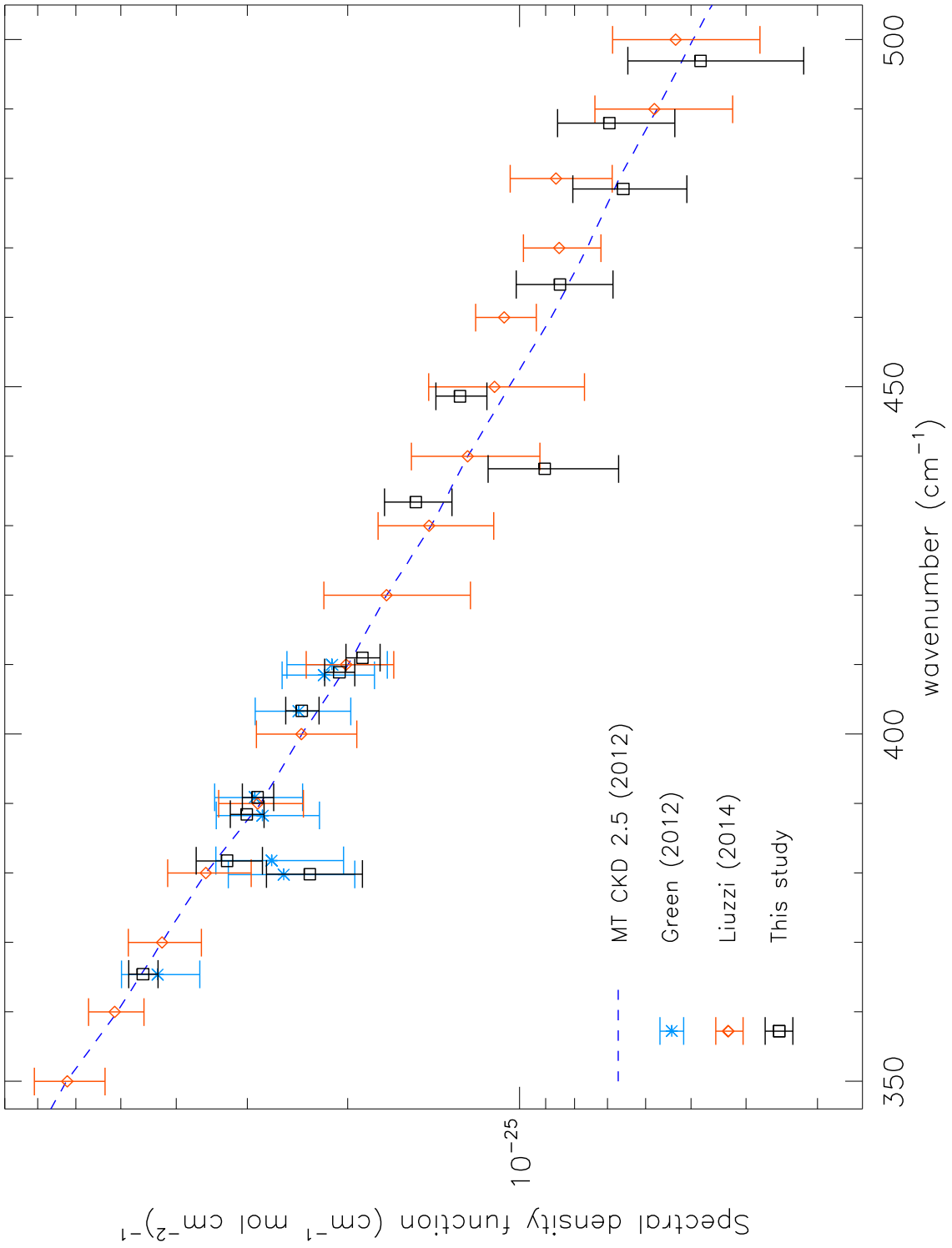


Figure 5.8: *A comparison of the MT-CKD continuum model with the results of studies by Green et al. [2012], Liuzzi et al. 2014] and this study.*

5.5 Summary and conclusions

This chapter has described the analysis of TAFTS data recorded during the RHUBC campaign in March 2007. During RHUBC, high resolution far-infrared spectra were measured simultaneously and independently by two different spectrometers - the TAFTS and AERI-ER instruments. Co-incidental spectra were compared and the two instruments were found to show good agreement within the overlap (400-550 cm^{-1}) in their measurement ranges. This allows a greater confidence in future results from both instruments.

Also presented is a case study of far-infrared atmospheric radiances measured by the TAFTS instrument during RHUBC. Using these, together with recorded atmospheric profiles, the current parameterization of the water vapour continuum, MT-CKD 2.5, has been tested at wavenumbers between 350 and 500 cm^{-1}. Derived continuum coefficients from the measured TAFTS radiances show agreement with both simulated spectra and previous studies, including that upon which the current MT-CKD parameterization is based [*Delamere et al.*, 2010]. This study thus demonstrates that the current MT-CKD 2.5 model continuum values can be used to accurately simulate radiances at wavenumbers 350-500 cm^{-1}, and adds to validation in this region from other locations [*Green et al.*, 2012; *Liuzzi et al.*, 2014].

6 Studies of the sensitivity of cirrus scattering models to changes in cloud properties

As described in §4.4, in order to perform simulations of radiative transfer in a cloudy atmosphere, a database of single scattering parameters must be used to account for the scattering and absorption of radiation by the ice particles within the cloud. The ability of the radiative transfer model to accurately simulate cloud radiances relies heavily upon the scattering database used. In this work, the scattering databases used are those developed by Baum et al. [2014] (described fully in §4.6).

In §7 of this thesis, these scattering databases are used to simulate cloudy radiances which are then compared to airborne radiation observations taken above cirrus. Variations between observed and simulated radiances are likely to be caused by changes in the underlying cloud properties, which are used as an input to the model. Thus, in order to assess the sensitivity to changes in the microphysical properties across the MIR and FIR spectral regions, this chapter describes simulations performed using the LBLDIS radiative transfer code, incorporating the Baum et al. scattering databases, at varying values of both effective radius and cloud optical thickness. These simulations are performed in the MIR and FIR spectral regions, corresponding to the ARIES and TAFTS LW and SW channels.

As well as investigating the effect of changing particle size and cloud optical depth, the simulations were performed using the three different Baum scattering parameter databases (General Habit Mix GHM, Aggregated Solid Columns ASC, and Single Columns only SC) in order to assess to sensitivity to particle habit.

For all simulations, the cloud height, cloud geometric thickness, and observer height were fixed. For the simulations of varying optical thickness, the particle effective diameter was held at a value of 35 μm, and for the simulations of varying particle effective diameter the optical thickness was held at a value of 4 (for a wavelength of 355 nm).

The results of these simulations are shown in Figure 6.1 (ARIES LW channel, varying optical thickness), Figure 6.2 (ARIES LW channel, varying particle effective diameter), Figure 6.3 (ARIES SW channel, varying optical thickness), Figure 6.4 (ARIES SW channel, varying particle effective diameter), Figure 6.5 (TAFTS LW channel, varying optical thickness), Figure 6.6 (TAFTS LW channel, varying particle effective diameter), Figure 6.7

(TAFTS SW channel, varying optical thickness), and Figure 6.8 (TAFTS SW channel, varying particle effective diameter).

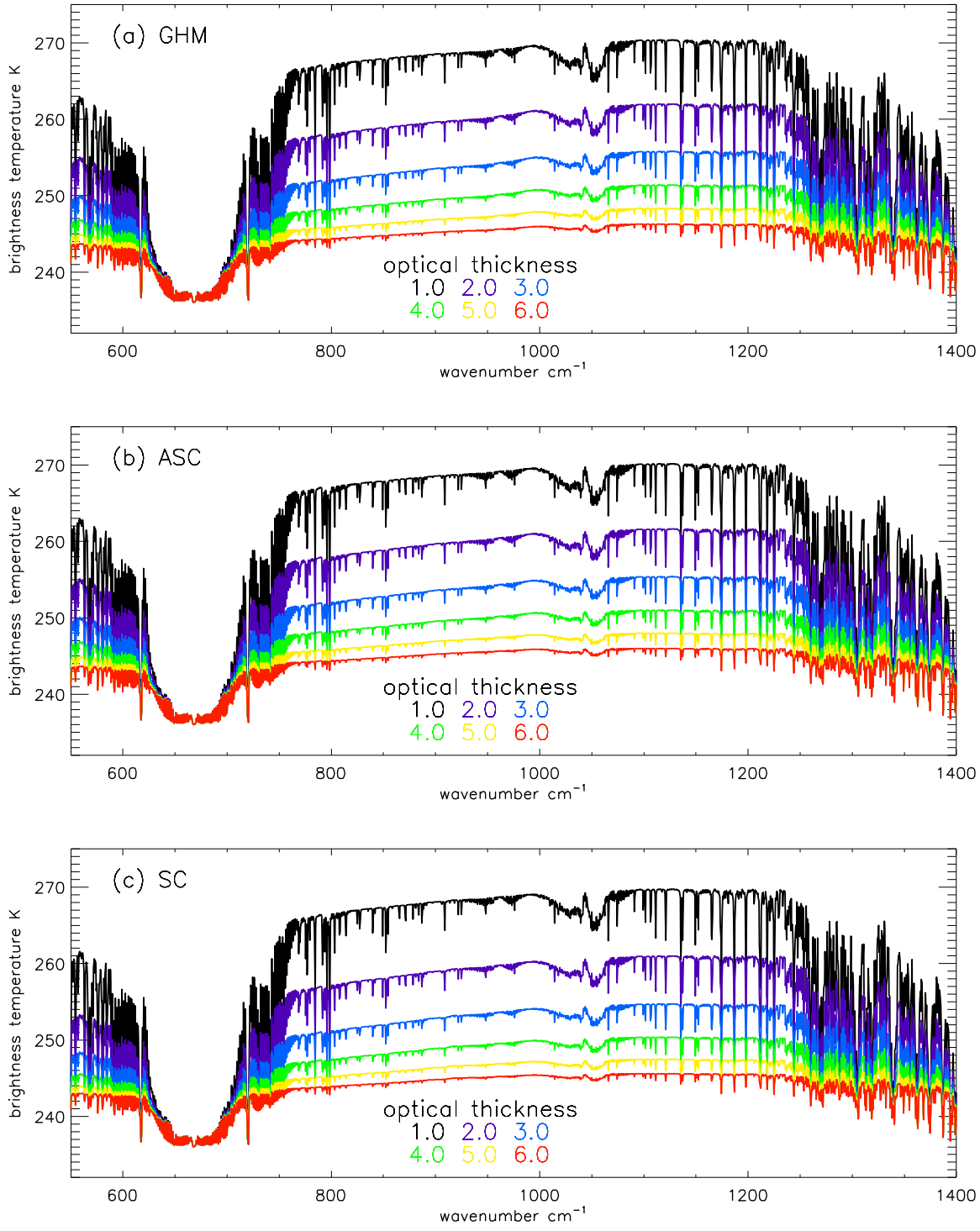


Figure 6.1: *ARIES LW channel simulations of varying cloud optical thickness performed using the (a) GHM; (b) ASC; (c) SC scattering database. The cloud particle effective radius is held fixed at 35 μm for all simulations.*

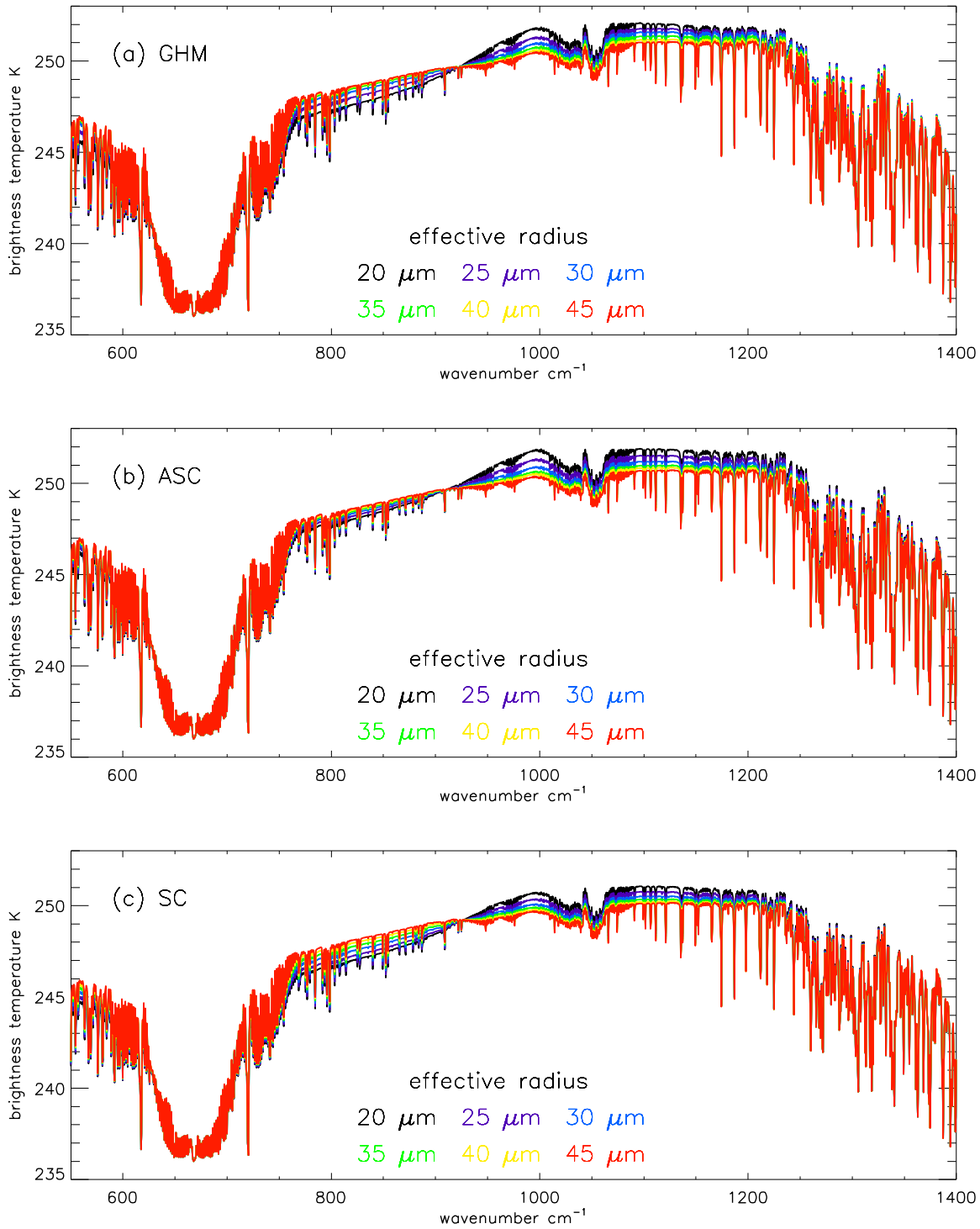


Figure 6.2: *ARIES LW channel simulations of varying cloud particle effective radius performed using the (a) GHM; (b) ASC; (c) SC scattering database. The cloud optical thickness is held fixed at 4 for all simulations.*

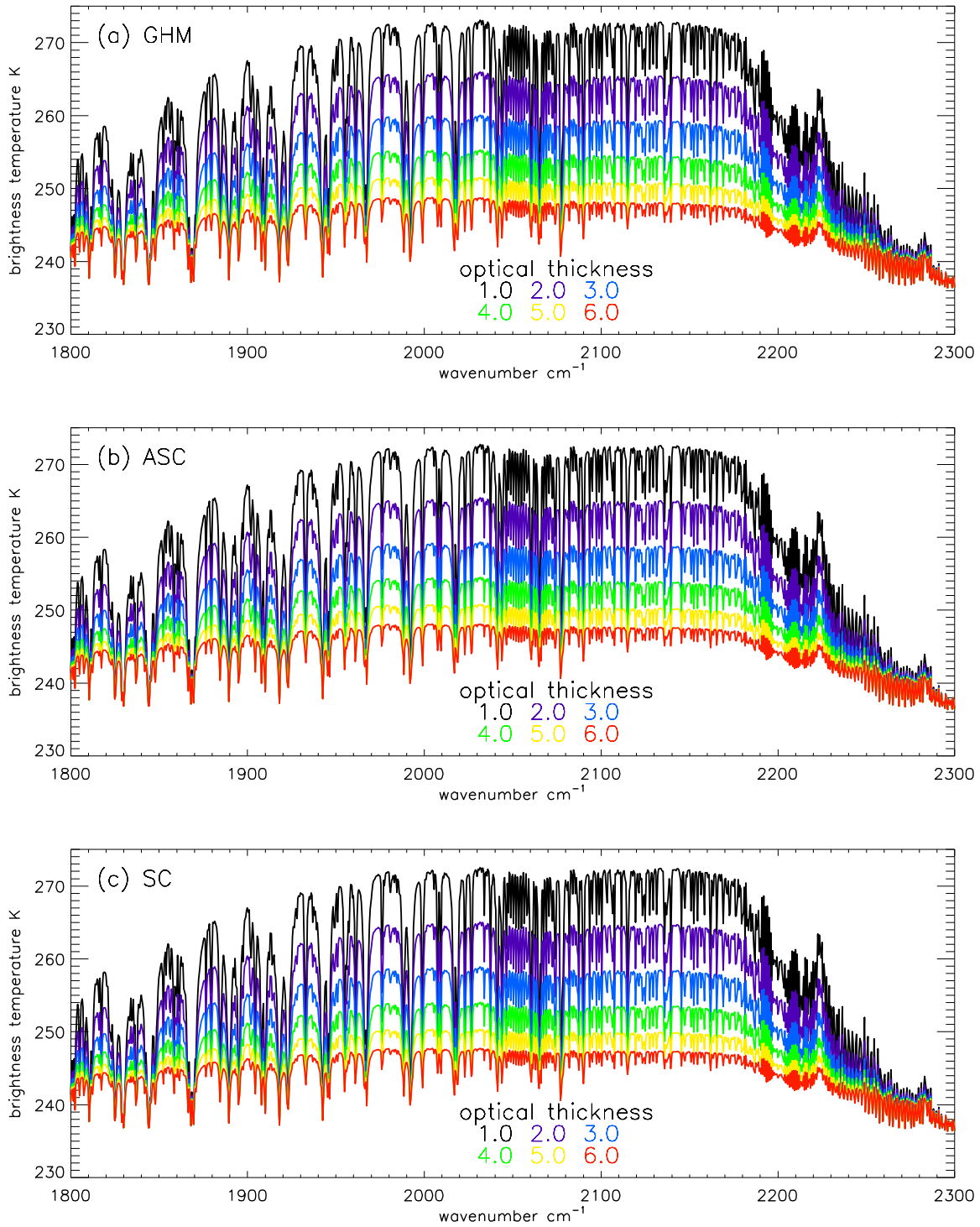


Figure 6.3: *ARIES SW channel simulations of varying cloud optical thickness performed using the (a) GHM; (b) ASC; (c) SC scattering database. The cloud particle effective radius is held fixed at 35 μm for all simulations.*

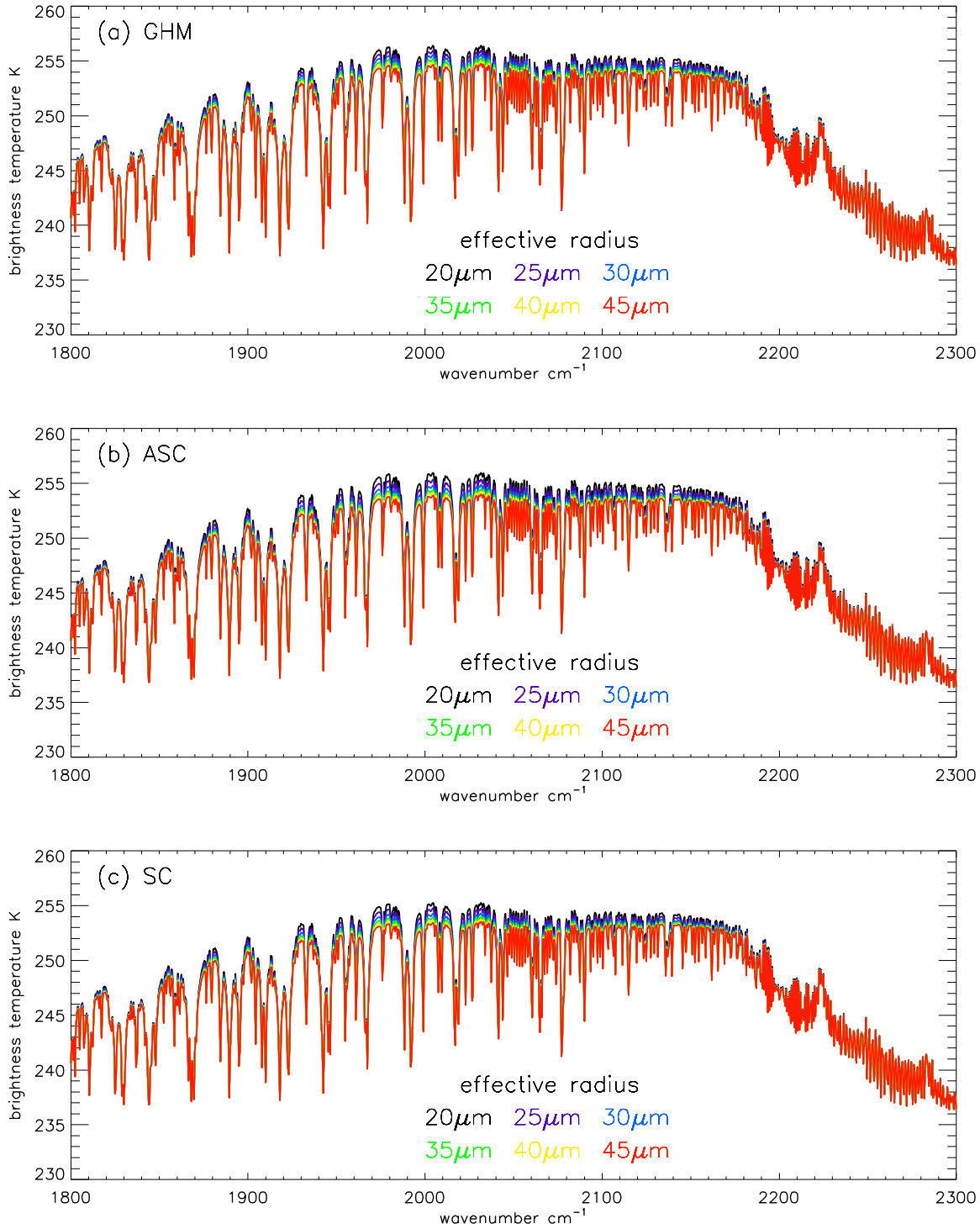


Figure 6.4: *ARIES SW channel simulations of varying cloud particle effective radius performed using the (a) GHM; (b) ASC; (c) SC scattering database. The cloud optical thickness is held fixed at 4 for all simulations.*

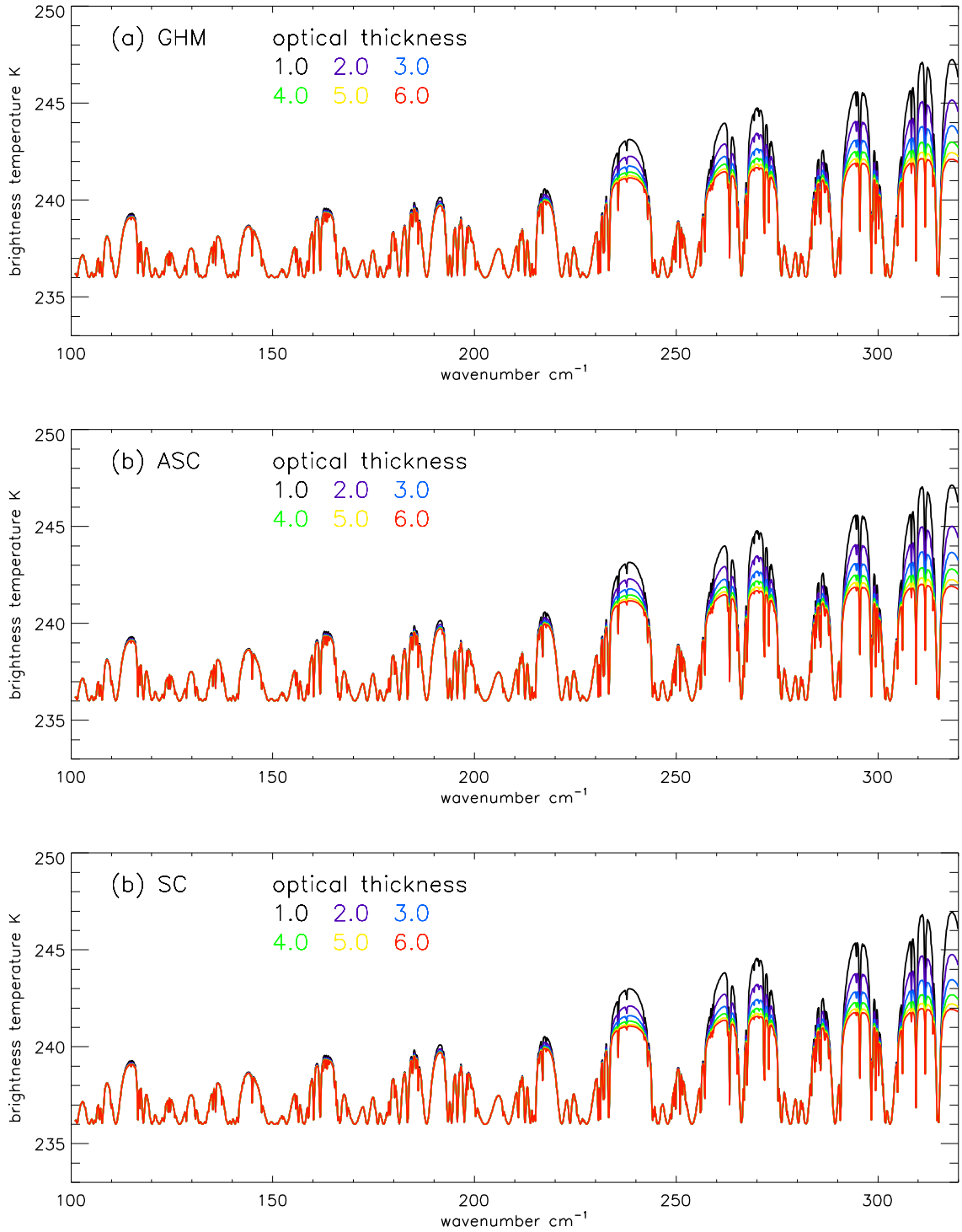


Figure 6.5: *TAFTS LW channel simulations of varying cloud optical thickness performed using the (a) GHM; (b) ASC; (c) SC scattering database. The cloud particle effective radius is held fixed at 35 μm for all simulations.*

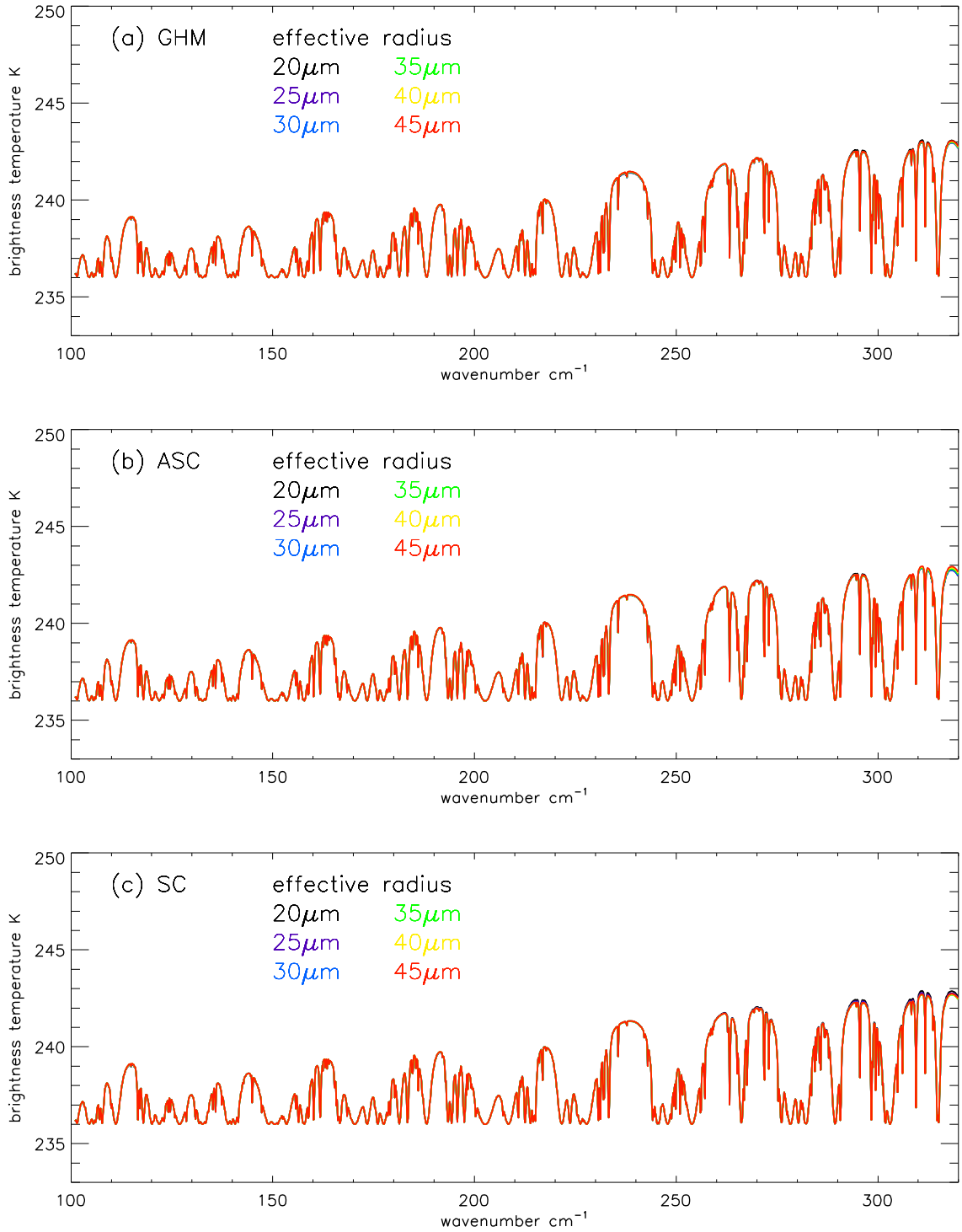


Figure 6.6: *TAFTS LW channel simulations of varying cloud particle effective radius performed using the (a) GHM; (b) ASC; (c) SC scattering database. The cloud optical thickness is held fixed at 4 for all simulations.*

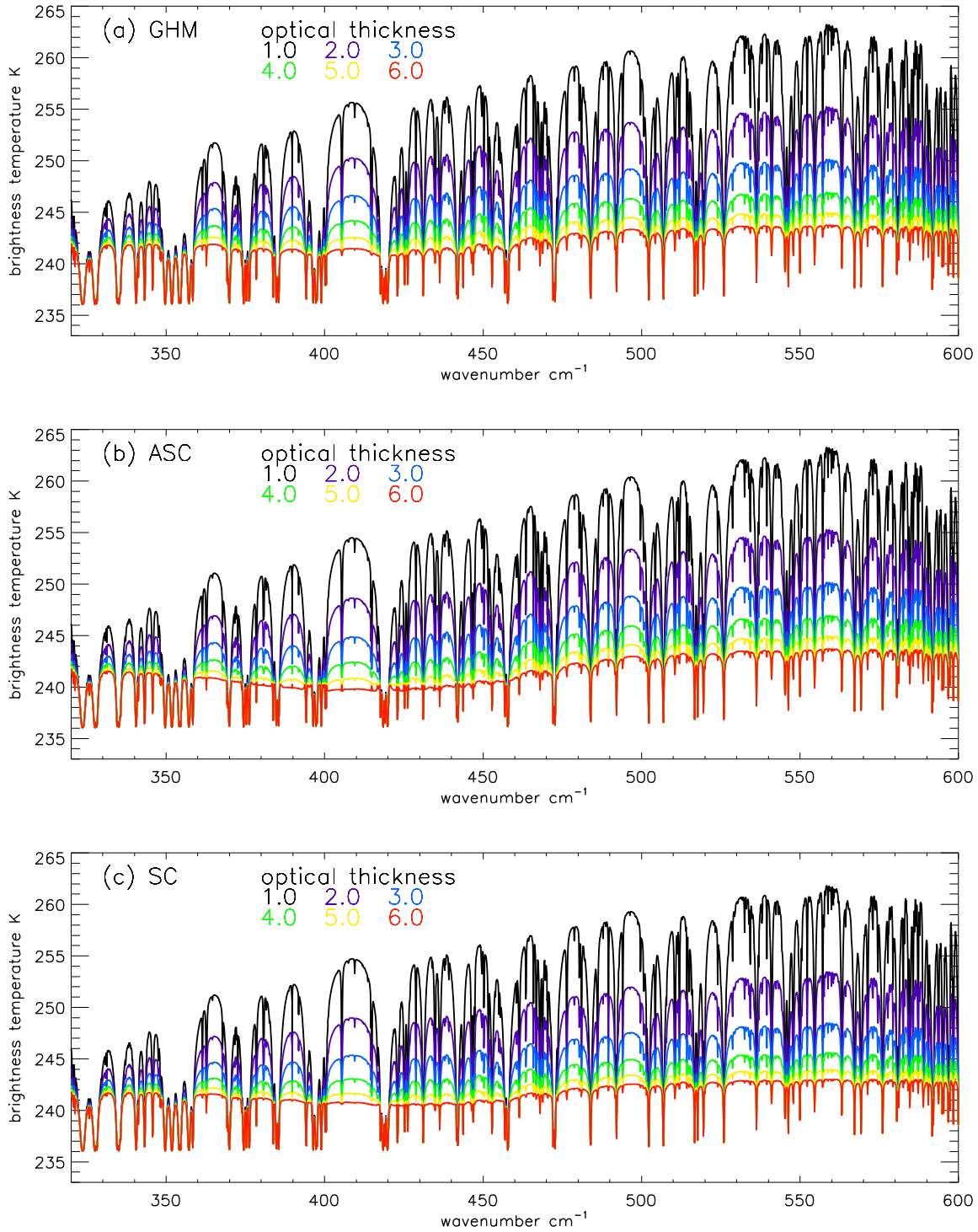


Figure 6.7: *TAFTS SW channel simulations of varying cloud optical thickness performed using the (a) GHM; (b) ASC; (c) SC scattering database. The cloud particle effective radius is held fixed at 35 μm for all simulations.*

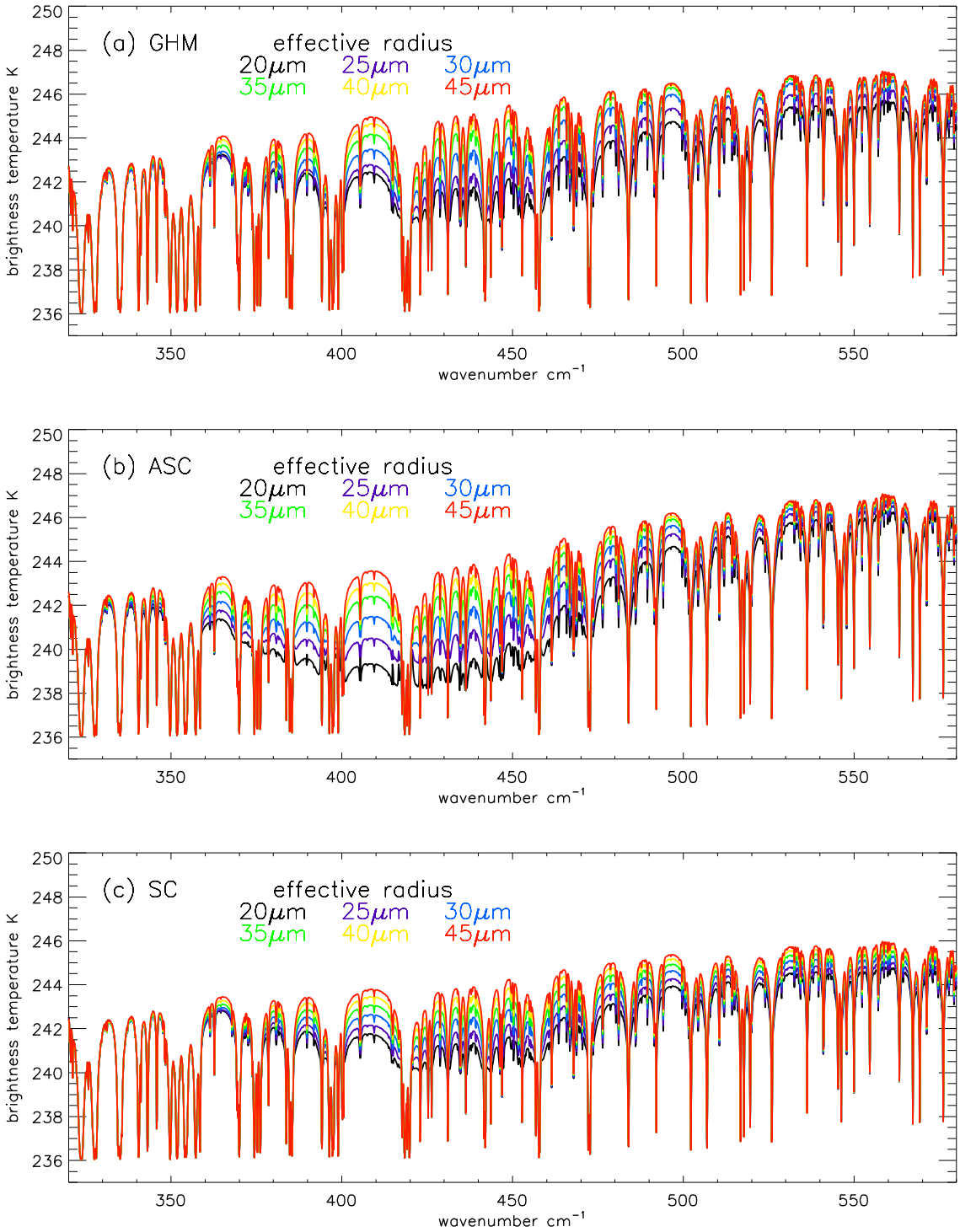


Figure 6.8: *TAFTS SW channel simulations of varying cloud particle effective radius performed using the (a) GHM; (b) ASC; (c) SC scattering database. The cloud optical thickness is held fixed at 4 for all simulations.*

The results of the sensitivity studies will be discussed for each wavenumber region in turn.

6.1.1 ARIES LW channel (550-1400 cm^{-1})

The effect of increasing the cloud optical thickness in this region is to lower the brightness temperature of the spectra, except in the CO_2 band centred at 667 cm^{-1}. Changing the scattering database does not have any effect on the simulated spectra.

Altering the cloud particle effective radius produces an effect in the window region 750-1250 cm^{-1}. Between 1000-1250 cm^{-1} the effect is to lower the brightness temperature as the particle size is increased. However in the region 750 – 950 cm^{-1}, changes in particle size affect the angle of the slope of the window. This is a well-known effect, with smaller particles causing a sharper slope than larger particles [*Bantges et al.*, 1999; *Chung et al.*, 2000], and is due to a greater absorption of radiation at 750 cm^{-1} by smaller particles than by larger ones.

There is sensitivity to the choice of habit database in this region, as the three databases vary in the angle of the BT slope in the window region. This is due to the varying shapes of the ice crystals in each database which have different scattering and absorption properties.

6.1.2 ARIES SW channel (1800-2300 cm^{-1})

As in the ARIES LW region, increasing the cloud optical depth lowers the brightness temperature over the entire spectral region. There is no observable sensitivity to scattering database.

Increasing the particle effective radius results in a slightly lower brightness temperature within the microwindows in the region. There is no observable sensitivity to scattering database.

6.1.3 TAFTS LW channel (100-320 cm^{-1})

Increasing the cloud optical thickness lowers the brightness temperature in the microwindows between spectral lines in the TAFTS LW channel region. However, this effect is not seen at the lowest wavenumbers, only becoming visible at 140 cm^{-1} and then having an increasing effect at increasing wavenumbers. Changing the scattering database does not have any effect.

The TAFTS LW channel does not exhibit any sensitivity to the particle effective radius, as in this region the simulations are all overlying each other. There is also no sensitivity to scattering database.

The lack of sensitivity to changes in cloud properties in this region is likely to be caused by the strong absorption by water vapour at these wavenumbers, which has the effect of saturating the brightness temperature.

6.1.4 TAFTS SW channel (320-580 cm^{-1})

The TAFTS SW region shows a similar sensitivity to changing optical thickness as the other regions, i.e. increasing the optical thickness lowers the brightness temperature of the simulated spectra in the microwindow regions. However in this region the choice of scattering database does have an effect. For all databases, the suppression of the brightness temperature increases in the region 350-500 cm^{-1}, with the lowest values at wavenumbers around 400 cm^{-1}, but this effect is seen the most when using the ASC database, with the GHM database having the smallest effect.

Similarly, although decreasing the particle effective radius results in a lowering of the brightness temperature in all of the microwindow regions, the effect increases in the region 350-500 cm^{-1}, with the lowest values at wavenumbers around 400 cm^{-1}. Again, this effect is seen most strongly in simulations using the ASC database, and the least when using the GHM database.

These results suggest that at wavenumbers from 300-550 cm^{-1}, the scattering parameters used in the Baum databases are exhibiting interesting behaviour and that this occurs most strongly in the ASC database. This can be investigated by plotting the scattering parameters in this region for varying values of particle effective radius to see how they change. Figure 6.9 shows the variation of the asymmetry parameter g with wavenumber for the (a) GHM; (c) ASC; and (e) SC databases, and the variation of the single scattering albedo ω_0 with wavenumber for the (b) GHM; (d) ASC; and (f) SC databases. Figure 6.9 shows that around the wavenumber region of interest centred approximately at 400 cm^{-1}, the scattering parameters show a pattern of reducing asymmetry parameter and increasing single scattering albedo as the effective particle size decreases.

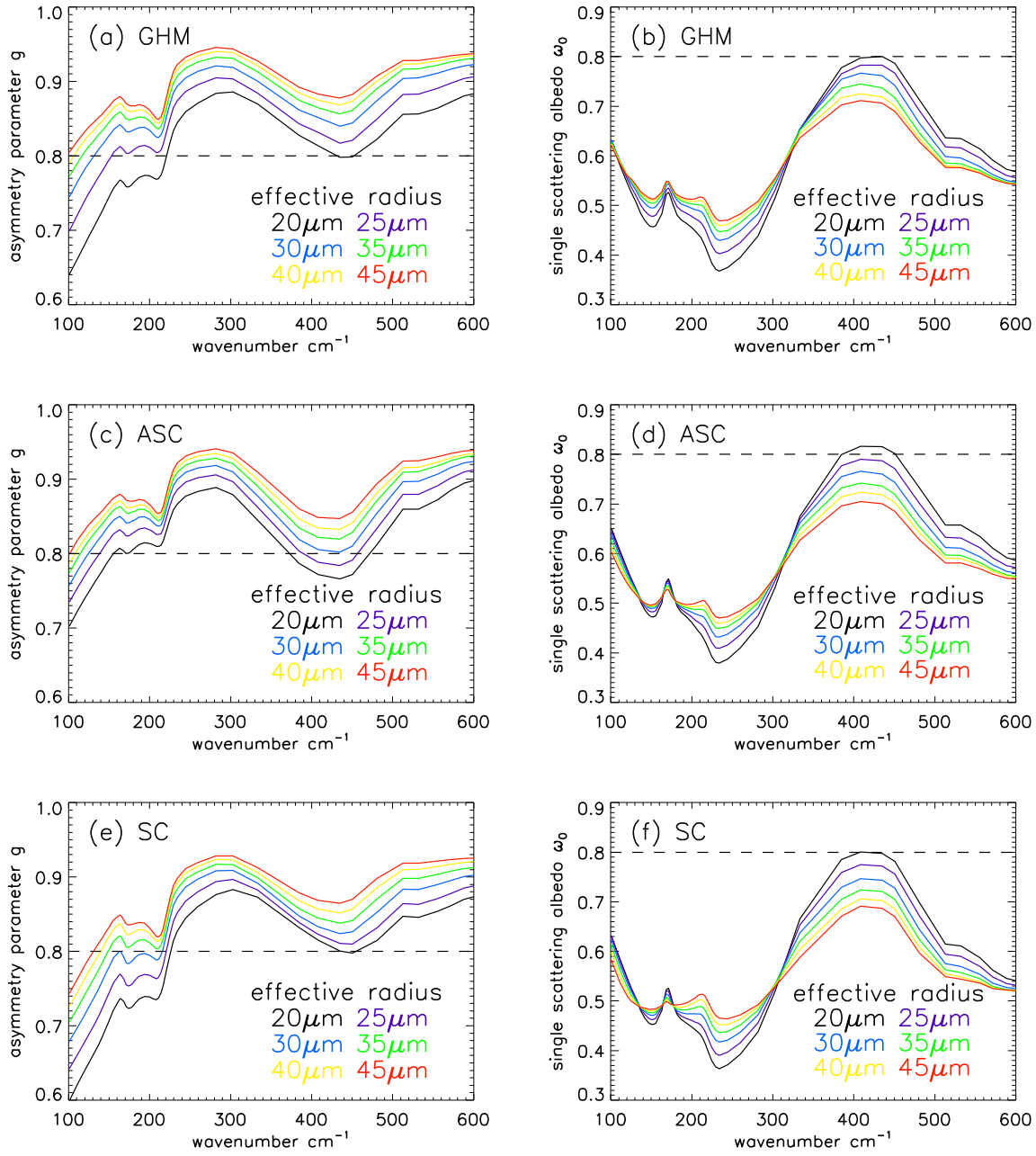


Figure 6.9: *The variation of the asymmetry parameter g with wavenumber for the (a) GHM; (c) ASC; and (e) SC databases, and the variation of the single scattering albedo* ω_0 *with wavenumber for the (b) GHM; (d) ASC; and (f) SC databases. The dashed line is to allow easier comparison.*

The increase in single scattering albedo can be explained by the decrease in ice absorption in this region (see Figure 7.6), as single scattering albedo is equal to the ratio of the scattering and extinction cross sections, and thus would increase as absorption decreases. This effect is stronger with smaller particles as smaller particles absorb more strongly than larger particles.

The asymmetry parameter defines the amount of radiation that is scattered in the forward direction i.e. for $g = 1$ all radiation is scattered forwards, for $g = -1$ all radiation is back-scattered, and for $g = 0$, the radiation is scattered isotropically. The reduction in g around 400 cm^{-1} would result in less radiation being forward scattered i.e. towards the detectors of a nadir facing instrument. This would cause the reduction in brightness temperature observed in the sensitivity studies shown in Figure 6.8, especially given the greater contribution of scattering shown by the increase in ω_0. The dashed lines plotted on Figure 6.9 allow easier comparison between the scattering databases, and show that these effects are stronger in the ASC database, which is consistent with the changes shown in Figure 6.8.

6.2 Summary and conclusions

Studies were performed to assess the sensitivity of the various spectral regions to changes in the cirrus properties. It was found that the optical thickness of the cloud affected the brightness temperature observed in the window regions across the spectrum, with the least changes seen in the TAFTS LW channel. An increase in the cloud particle size generally resulted in lower brightness temperatures within the window regions, with the most noticeable effect in the window 750 – 950 cm^{-1}, where changes in particle size affect the angle of the slope of the window. The TAFTS LW channel did not exhibit any sensitivity to changes in the particle size, and was only sensitive to changes in cloud optical thickness at wavenumbers above 200 cm^{-1}. This may be due to the high water vapour absorption in the FIR saturating the brightness temperature at these longer wavelengths. The TAFTS SW channel showed the most sensitivity to changes in particle effective radius, with all databases giving a lowering of the brightness temperature with decreasing particle size, especially in the region 350-500 cm^{-1}, with the lowest values at wavenumbers around 400 cm^{-1}. This effect is seen most strongly in simulations using the ASC database, and the least when using the GHM database. Thus the underlying single scattering parameters for the three databases were examined in this region, and it was found that the suppression of the brightness temperature is likely to be caused by a decrease in the asymmetry parameter in this wavenumber region, and that this decrease is greatest in the ASC scattering database.

7 Aircraft-based observations of cirrus mid- and far-infrared radiative signatures during CIRCCREX-I

This chapter reports the results of a case study using TAFTS to take FIR spectral radiance measurements in the presence of cirrus. These measurements were recorded during the first phase of the Cirrus Coupled Cloud-Radiation Experiment (CIRCCREX), which was an aircraft campaign based out of Prestwick, Scotland, in November 2013. The author, along with J. E. Murray of Imperial College London, was directly responsible for pre-flight preparation and in-flight operation of the TAFTS instrument during CIRCCREX. This chapter begins with an introduction to the campaign and its aims, and the particular flight which was used for analysis of cirrus radiative signatures. The different instrumentation and their data are then described, and this data is then applied to several studies. Firstly a method of using ARIES spectra to retrieve the properties of the cirrus is described and compared with a method of obtaining properties from cloud probe in-situ measurements. Simultaneous MIR and FIR spectral observations are then used to test the performance of state-of-the-art ice crystal scattering models, and to validate their consistency across the infrared region.

7.1 Introduction

As discussed in §2.3, the net radiative effect of cirrus, whether it warms or cools the Earth's surface, depends on its microphysical properties, vertical position and extent, and geographical location. Key microphysical parameters include ice crystal habit, crystal size distribution [*Zhang et al.*, 1999] and morphology such as aggregation, roughness and concavity [*Baran*, 2012; *Yang et al.*, 2012; *Baum et al.*, 2014]. However, these parameters are extremely variable in both time and space, and are dependent on the changes in temperature, RH and meteorological environment the cloud experiences [*Yang et al.*, 2012]. If this relationship between radiative and microphysical properties is to be exploited in GCM and NWP models, it is vital that the radiative effect of cirrus can be accurately predicted – this is reliant on knowledge of cirrus optical properties which are currently poorly constrained [*Baran*, 2012]. Several cirrus bulk scattering and absorption models have been developed using in-situ observations and databases of ice single scattering properties (SSPs), which aim to include realistic physical representations of the ice crystals found in nature, including

habit, aggregation and roughness e.g. [*Yang et al.*, 2008, 2012; *Baran et al.*, 2014; *Baum et al.*, 2014].

These cirrus models require validation across the electromagnetic spectrum by comparing modelled spectra with observations, and studies of model consistency in the solar and MIR [*Baran and Francis*, 2004; *Baum et al.*, 2014] have shown good agreement in these regions. However, studies have indicated that information concerning cirrus optical properties may theoretically be derived from FIR observations [*Maestri and Rizzi*, 2003; *Baran*, 2005, 2007] because of the sensitivity of radiation to ice crystal optical properties in this region. This FIR sensitivity results from the substantial variation of the real and imaginary refractive indices of water and ice in the FIR [*Downing and Williams*, 1975; *Warren*, 1984; *Warren and Brandt*, 2008], and suggests that SSPs that are valid for the MIR may not be correct for the FIR.

Cox et al. [2010] presented aircraft observations of MIR and FIR spectra in the presence of cirrus, and concluded that simulations are not able to consistently reproduce observed spectral radiances across the infrared, and are particularly poor in the region 330-600 cm^{-1}. This study did not have an in-situ cloud probe capable of measuring small (< 100 μm) ice crystals, and so the contribution from small crystals in the cirrus PSD was estimated iteratively [*Cox et al.*, 2010]. Studies of FIR spectral radiance observations of tropical cirrus reported by Humpage [2010] during the EMERALD-II campaign also found that small ice crystals were not being correctly counted during in-situ measurements and that in order to gain the best agreement between observations and simulations, the small crystal concentrations in the measured PSD needed to be reduced by 66%. This was due to shattering effects on the in-situ probes artificially increasing the number of counted small ice crystals [*Humpage*, 2010]. These results suggest that the problem of accurately measuring the number of in-situ small ice crystals is of great importance in the simulation of cirrus radiative signatures.

Work by Maestri et al. [2014] analysed downwelling FIR spectral radiances in the presence of cirrus recorded by the REFIR-PAD instrument at a ground-based site. They used retrieved cloud properties to simulate radiances in the region 250-1100 cm^{-1} and found excellent observation-simulation agreement in the mid-infrared window, but large residuals in the FIR. This study demonstrated that a 'view-from-above' (satellite or aircraft) experimental configuration would be of great advantage to the study of FIR cirrus optical properties [*Maestri et al.*, 2014], and indeed, aircraft campaigns are ideal for performing model

validation exercises as the radiative signature of the clouds can be recorded closely in time with the cloud microphysics, allowing them to be directly linked [*Baran and Francis*, 2004; *Maestri*, 2005].

Presented here is an analysis of coincident upwelling radiation recorded above cirrus in both the FIR and MIR spectral regions during the first stage of the Cirrus Coupled Cloud-Radiation Experiment (CIRCCREX), a flight campaign out of Prestwick airport, Scotland, during November and December 2013. For CIRCCREX, the UK Facility for Airborne Atmospheric Measurements (FAAM) BAe-146 aircraft was fitted with a suite of atmospheric temperature and relative humidity (T and RH) measurement instruments, state-of-the-art cloud probes and radiometers. The radiative measurements were made by the Imperial College Tropospheric Airborne Fourier Transform Spectrometer (TAFTS, [*Canas et al.*, 1997]) in the FIR, and the UK Met Office Airborne Research Interferometer Evaluation System (ARIES, [*Wilson et al.*, 1999]) in the MIR, both flying aboard FAAM. This first phase of CIRCCREX was intended as preparation for the second phase which was due to take place in Goose Bay, Canada, in March 2014 (this phase was later postponed). Hence, many of the flights from this first phase did not produce any useful data, due to issues with performance of instruments and a lack of suitable cirrus flying conditions. The best case study flight, B818, which is analysed here, took place on the 29th November 2013. Flight B818 was located over the sea to the west of Scotland, and measurements of both the radiative signature of cirrus, and in-situ cirrus properties such as ice particle size distribution were recorded. This work uses the B818 case study to simulate FIR TAFTS and MIR ARIES spectra and assess the performance of the bulk cirrus scattering and absorption models developed by Baum et al. [2014] at reproducing radiance observations across the infrared spectral region.

The flight plan of B818 was designed to include characterisation of the atmospheric profile below the cirrus layer, in-situ cirrus microphysics measurements within the cloud, and radiative observations below and above the cirrus layer. Thus it comprised several horizontal runs, vertical aircraft profiles and dropsonde releases, as shown in the flight track in Figure 7.1. The main issue with this case study was the rapidly evolving weather system present. The flight was planned with reference to the cloud forecast model provided by the UKMO 36 hours beforehand, which indicated that a band of high cirrus cloud was advancing towards the flight area from the north-west (see Figure 7.2). However during the flight, it was found that the weather system was moving much more rapidly than expected, and the cirrus was

quite tenuous and patchy. Figure 7.3 shows images from the SEVIRI satellite instrument taken at 1130, 1145, 1200 and 1215 UTC, which highlight the speed of the changing conditions, and show that the band of cirrus has already moved south-east compared to the cloud forecast for 1200 UTC (Figure 7.2). The red dot in Figure 7.3 indicates the location of the aircraft. Figure 7.4 shows an image from the MODIS instrument onboard the NASA Terra satellite, which overflew the scene at 1200 UTC. This image clearly shows the tenuous and patchy nature of the cirrus in the observation area, whereas the more uniform cirrus has already moved south-east. Figure 7.5 shows measurements from the Lidar onboard the aircraft, which was used to identify layers of cirrus below the flight level. The Lidar observations show that the cirrus is not homogeneous and that there is low cloud present beneath the cirrus, which adds to the complexity of the case. Despite these difficulties, this flight proved to be a useful study of the cirrus radiative signature across the infrared due to the simultaneous observations made by the TAFTS and ARIES instruments.

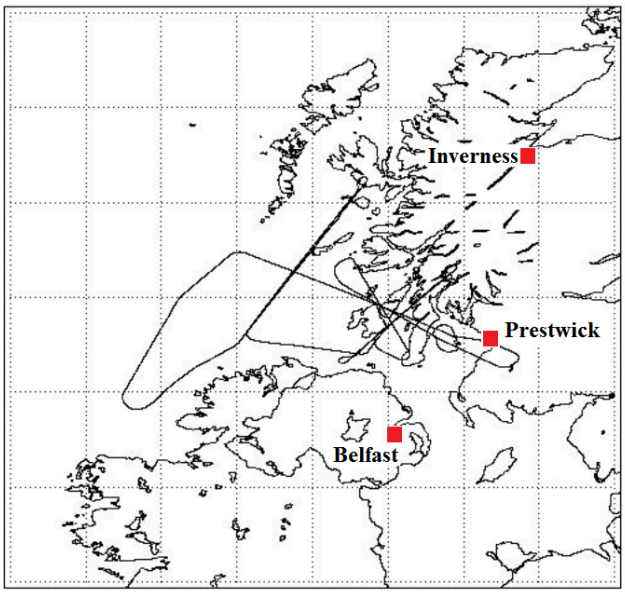


Figure 7.1: *A plot of the flight track of the FAAM aircraft during B818 on the 29th November*

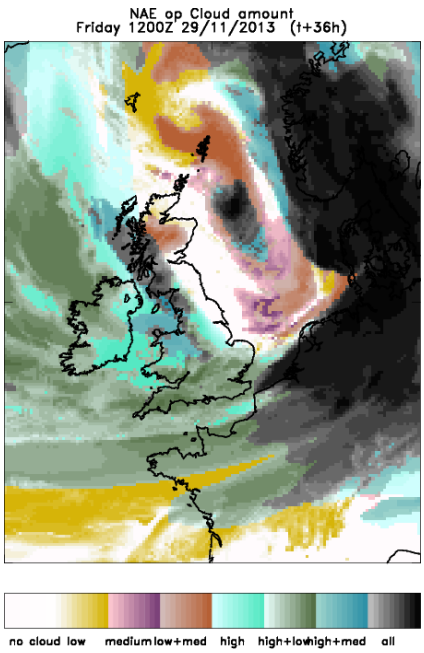


Figure 7.2: *UKMO cloud forecast model for 1200 UTC on the 29th November 2013. Cirrus is indicated in turquoise, and cirrus with underlying low cloud in green. Image courtesy UKMO.*

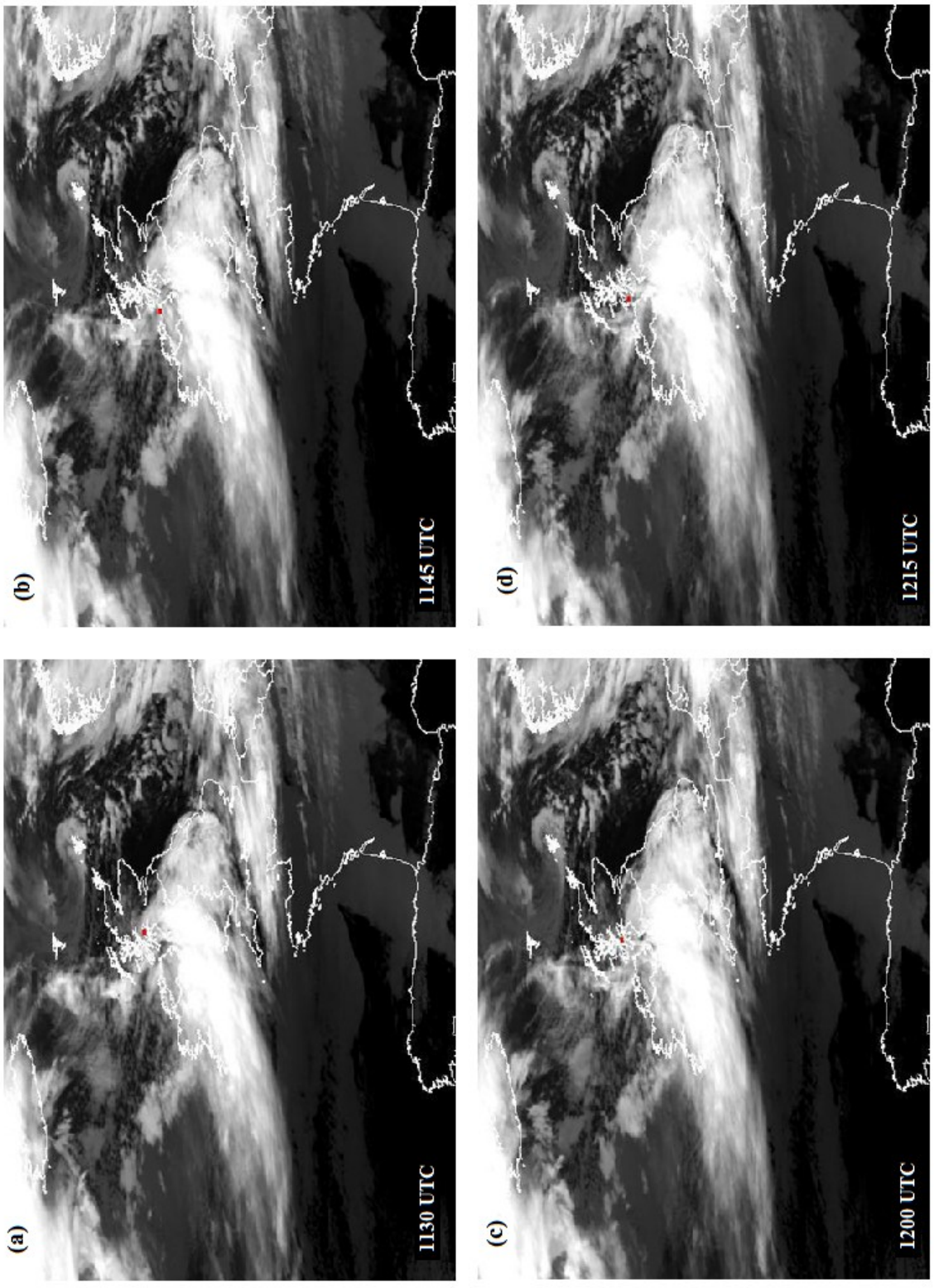


Figure 7.3: *10.8 μm inverted BT scale images from SEVIRI taken at (a) 1130 UTC; (b) 1145 UTC; (c) 1200 UTC; (d) 1215 UTC showing the band of cirrus cloud that was sampled during flight B818. The red dot shows the location of the aircraft in each image.*

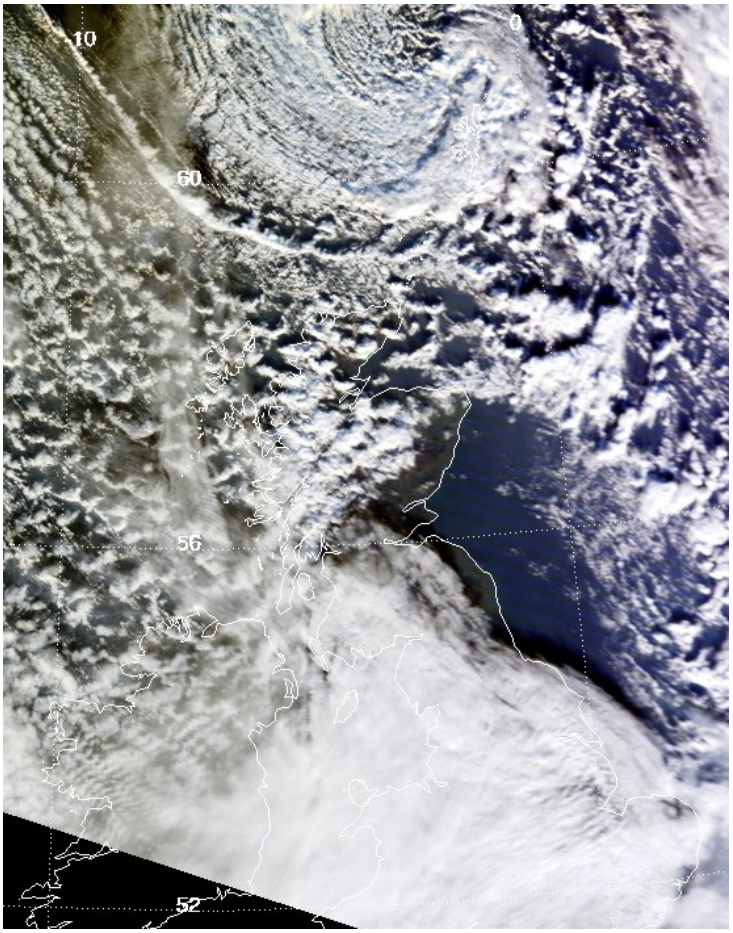


Figure 7.4: *MODIS level 1b scene from the MODIS Terra overpass, 1200 UTC, 29/11/13, showing the cirrus conditions in the measurement area. Source: NASA* [2014].

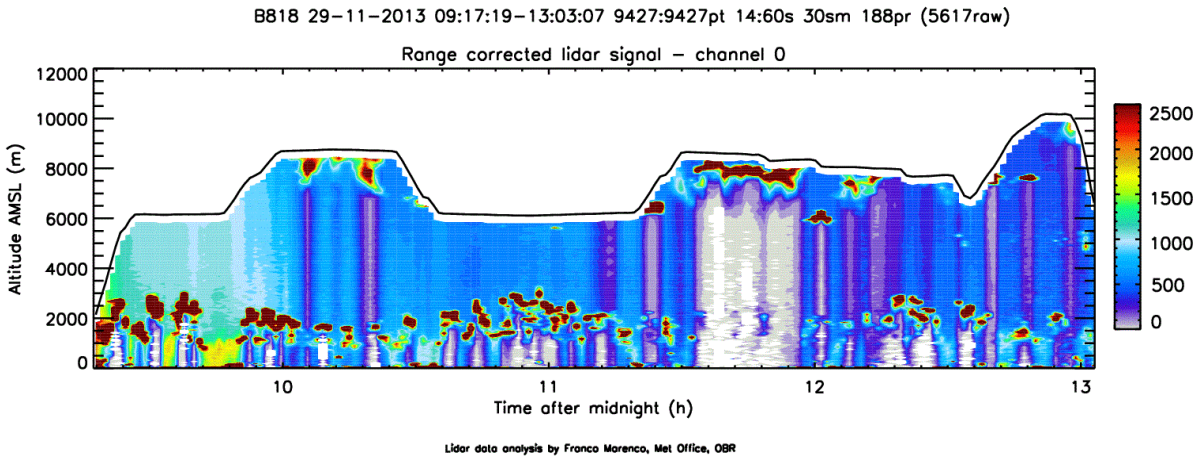


Figure 7.5: *The Lidar observations for the B818 flight, showing the position of clouds. Cirrus can be seen above approx. 7000m, with underlying low cloud at around 2000m. Image courtesy F. Marenco, UKMO.*

7.2 Spectral radiance measurements

The analysis presented in this chapter focuses on the radiance measurements taken with the TAFTS and ARIES instruments (see §3.2 and §3.4). Firstly, a method of determining the presence of cirrus using the ARIES brightness temperature differences is shown, followed by a comparison of recorded spectra to radiances simulated using the LBLDIS model and the scattering databases described in §4.6.3. The ARIES data used in this work was provided by the UK Met Office.

7.2.1 Tri-spectral algorithm analysis of ARIES spectra

In order to accurately assess the radiative effect of cirrus, it must be ascertained that the measured spectra are indeed from a scene including cirrus. As the cirrus present in B818 was patchy, and the initial Lidar data was integrated over 1 minute time periods, it was difficult to be sure of the presence of cirrus in each individual radiometer scan. A methodology taking advantage of the spectral signature of cirrus can be used to check for evidence of cirrus in the recorded spectra. This method is the TriSpectral infrared band Algorithm (TSA) suggested by Ackerman et al. [1990] and Strabala et al. [1994]. The TSA relies on the difference in the scattering properties of ice and water droplets, and is thus able to discriminate between clouds composed of water or of ice.

Single scattering properties of cloud particles are determined by the complex index of refraction ($m = m_r - i\, m_i$), along with the distribution of particle sizes and shapes. The imaginary part of this index of refraction is related to the absorption coefficient κ and the wavelength of the absorbed radiation by equation 7.1, which indicates that the magnitude of the absorption at each wavelength can be estimated by the value of m_i. The real and imaginary parts of m for ice and water are shown in Figure 7.6 for wavelengths between 7-200 μm (50-1500 cm^{-1}), where the values for water are taken from Downing and Williams [1975], and the values for ice are taken from Warren [1984] with IR updates from Warren and Brandt [2008].

$$\kappa = \frac{4\pi\, m_i}{\lambda} \qquad 7.1$$

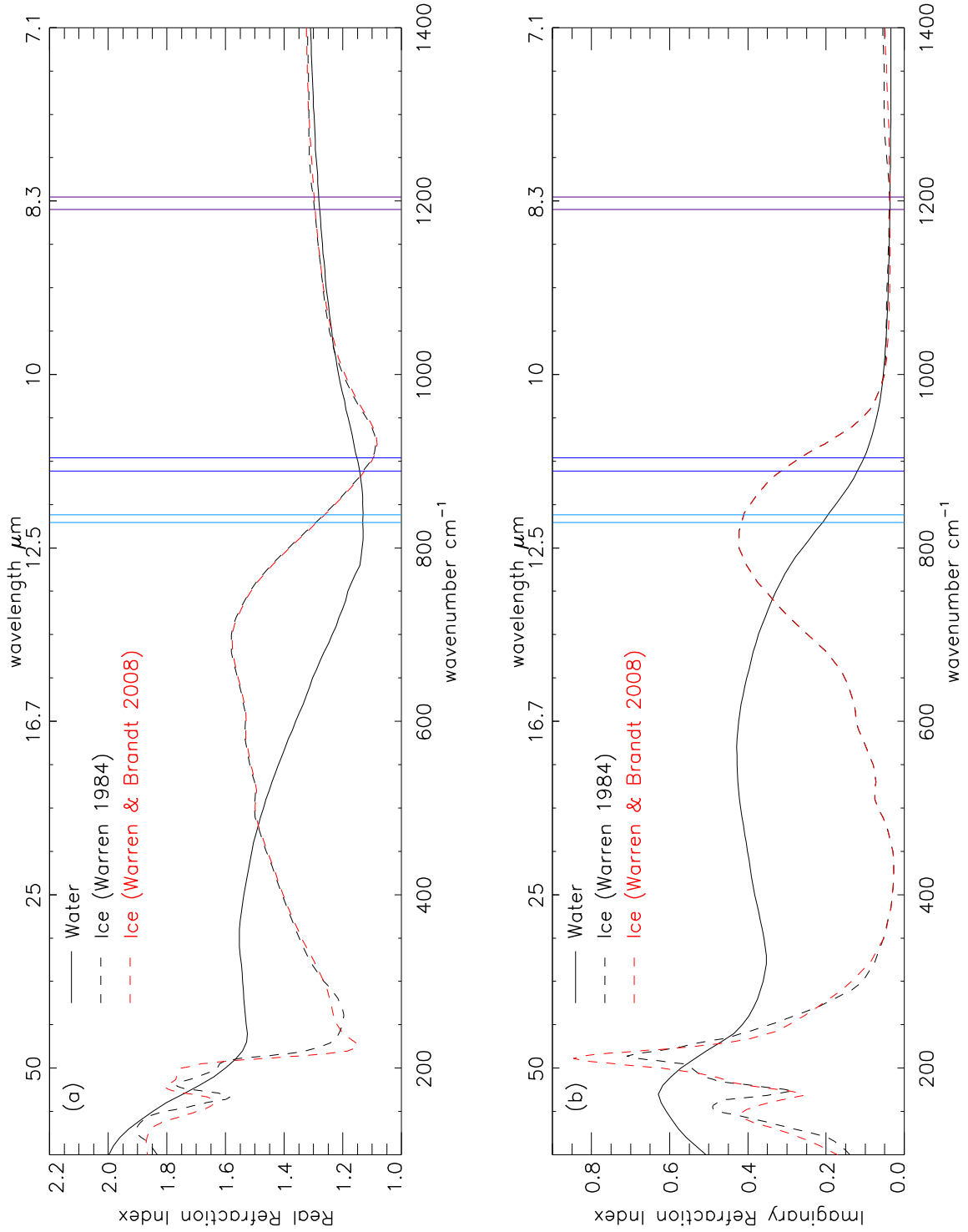


Figure 7.6: *The (a) real; and (b) imaginary component of the complex index of refraction for ice and water. The windows used in the tri-spectral analysis are indicated by blue and purple lines.*

From Figure 7.6 (b) it can be seen that the magnitude of m_i for water and ice are comparable between 7 and 10 μm, but then diverge at longer wavelengths, with ice having a higher value between 10 and 13 μm. This means that if an ice cloud and a water cloud were to have the same temperature, with similar particle size and shape distributions, the two clouds would have similar radiances at 8.3 μm (1200 cm^{-1}), but different radiances at 11 and 12 μm, as the ice cloud would absorb more radiation. It is this difference in absorption that forms the basis of the TSA to infer cloud thermodynamic phase. Strabala et al. [1994] demonstrated that a plot of Brightness Temperature Differences (BTD) between 8.3 and 11 μm [BTD(8.3-11μm)] against BTD between 11 and 12 μm [BTD(11-12μm)] would show a separation between the radiances of ice and water clouds. Ice clouds tend to have greater values of BTD(8.3-11μm) than BTD(11-12μm), whereas for water clouds the inverse tend to be true. This results in a distinctive 'slope' in BT across the window 10-13 μm that is indicative of the presence of cirrus (see e.g. Figure 7.9, Figure 7.10).

This analysis was performed on the individual ARIES LW UW spectra recorded during CIRCCREX flight B818 in order to identify those scenes which contained cirrus. The resulting TSA plot is shown in Figure 7.7, where each cross represents the tri-spectral differences for one individual spectrum.

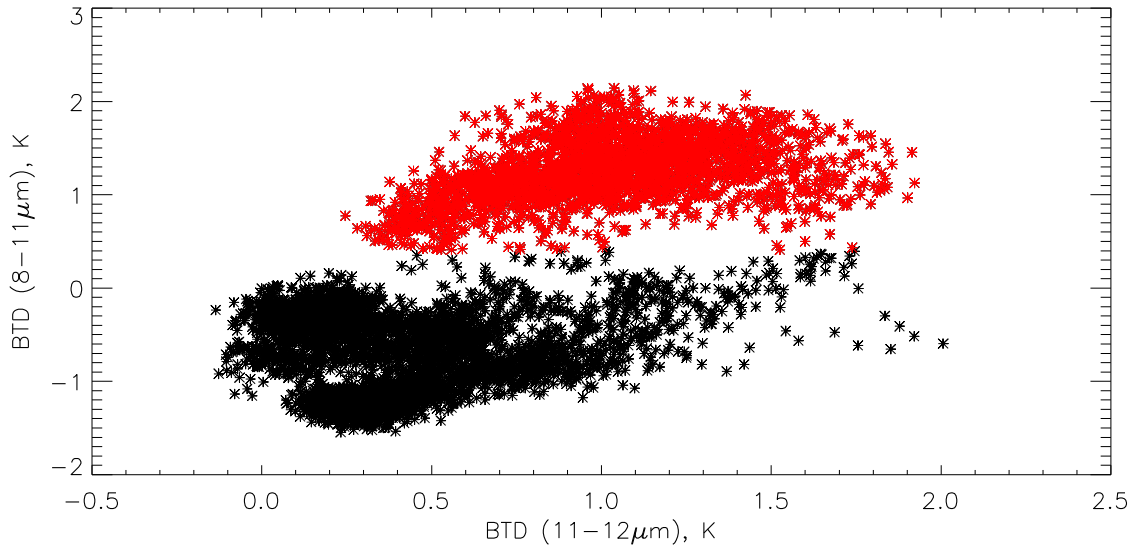


Figure 7.7: *B818 ARIES UW tri-spectral differences. Points that meet the cirrus threshold of BTD(8.3-11μm) > 0.4K are shown in red.*

Figure 7.7 shows two distinct clusters of points. Following the analysis of Strabala et al. [1994], it was proposed that any points with a BTD(8.3-11μm) greater than a threshold of 0.4 K (indicated in red in Figure 7.7) were assumed to be from views containing cirrus. This threshold will vary from instrument to instrument, however 0.4 K is an adequate threshold to use in this work, as the points in Figure 7.7 clearly separate into two groupings above and below this value. Thus, the spectra which meet this threshold were selected for further analysis.

Figure 7.8 shows a plot of BTD(8.3-11μm) against time for B818, again with spectra which meet the 0.4 K threshold indicated in red. Superimposed on the plot is the flight Outside Air Temperature (OAT), which can be used as a proxy for aircraft altitude i.e. a lower temperature would correspond to a higher altitude. Figure 7.8 shows that cirrus was observed at high aircraft altitudes in three sections of the flight, with the largest section of observed cirrus between 11:34:03 and 11:52:43 UTC. This can be compared with the Lidar measurements for the flight (shown in Figure 7.5), which indicate the presence of high cloud at the time suggested by the TSA, thus adding confidence that this section was indeed viewing cirrus. The following analysis concentrates on the section 11:34:03 and 11:52:43 UTC of the flight, hereafter referred to as the 'cirrus section'.

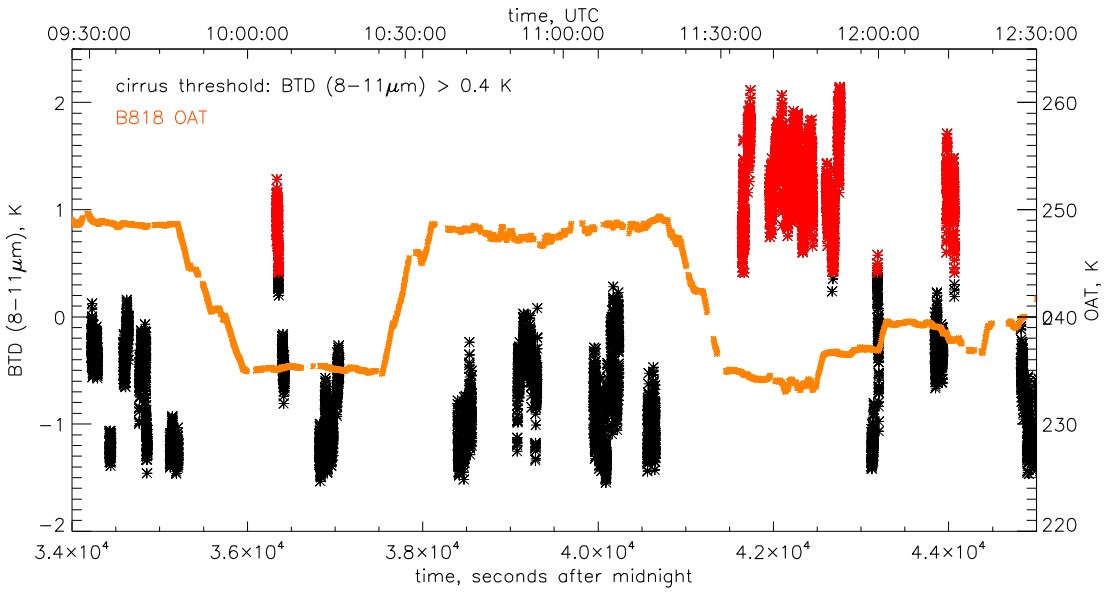


Figure 7.8: *B818 BTD(8.3-11μm) against time, showing where in the flight cirrus was encountered. Points meeting the cirrus threshold are shown in red. The aircraft OAT is overplotted in orange*

7.2.2 MIR and FIR spectra recorded in the presence of cirrus

Once the scenes where cirrus was present had been identified, the radiance measurements from these times were selected for analysis. As mentioned earlier, TAFTS and ARIES are both capable of viewing both nadir and zenith scenes. However, as TAFTS and ARIES are operated independently, their views do not always coincide. Thus, radiance spectra were selected for optical coincidence of the radiometers, which reduced the data available for analysis to only three sets of coincident TAFTS/ARIES views. The individual ARIES LW spectra from these three times are shown in Figure 7.9, where the relative scan number is denoted by a colour bar which varies temporally from black to red. Figure 7.9 shows that the spectra are variable over all of the measurement time periods, but in the time 11:39:13-11:39:50 UTC (shown in panel (a) of Figure 7.9), the variation shown is a smooth increase in brightness temperature with time in the window region 750-1200 cm^{-1}, implying that the changes in cloud properties are changing more uniformly in time, allowing an easier analysis of how these changes affect the radiative signature. Additionally, the other two datasets shown in panel (b) and (c) of Figure 7.9 were recorded during the aircraft orbits, where the increased vibration affected the TAFTS data (see §3.2.5). Ultimately, only the dataset consisting of coincident TAFTS and ARIES nadir view scans above cirrus, recorded over the time period 11:39:16-11:39:45 UTC, was selected for calibration and analysis.

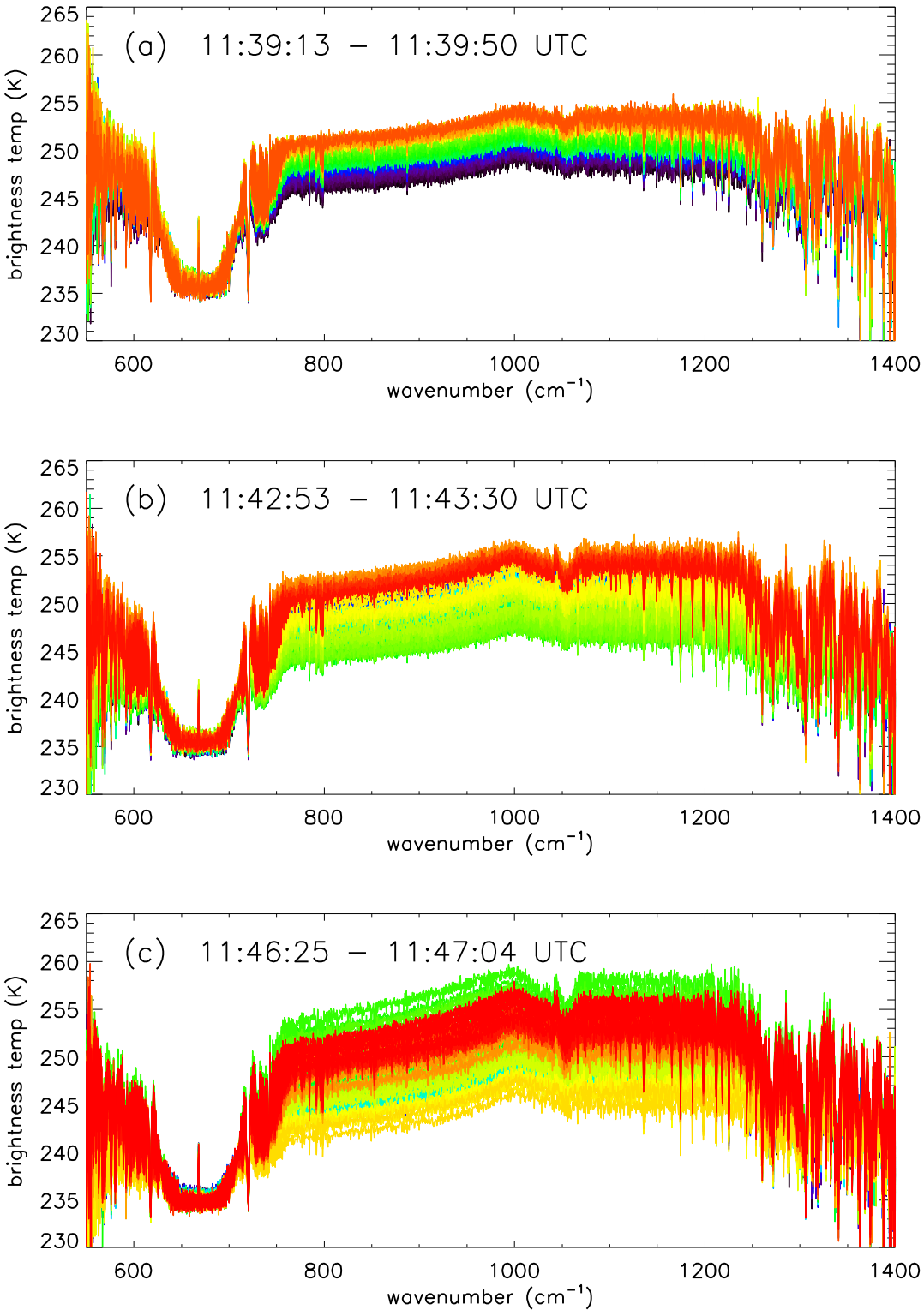


Figure 7.9: *ARIES LW individual spectra recorded during the three time periods of coincidental TAFTS and ARIES views, showing the variation in brightness temperatures over the measurement time.*

Over the chosen measurement time 11:39:16-11:39:45 UTC, the brightness temperature of the observed ARIES spectra increases. This increase may be caused by a change in cloud top height and/or changes in the underlying cloud microphysical properties. In order to more easily analyse these changes in cloud properties, and allow a reasonable sensitivity to changes, the ARIES spectra from this time period have been averaged across BT 2K bins in the window region 8.3-8.4 μm / 1190-1205 cm^{-1}, resulting in three sets of averaged spectra, called ARIES_0, ARIES_1 and ARIES_2, which are plotted for the LW and SW channels in Figure 7.10. A breakdown of the ARIES scans included in each average is given in Table 7.1, where the averages ARIES_0, ARIES_1, and ARIES_2 correspond to the black, blue and orange lines respectively in Figure 7.10.

Table 7.1**:** *Information on the spectra included in each ARIES 2K average*

Average	**BT bin range (K)**	**Number of averaged ARIES spectra**	**Measurement time (UTC) of averaged ARIES spectra**
ARIES_0	$248 \leq T < 250$	12	11:39:16 - 11:39:21
ARIES_1	$250 \leq T < 252$	33	11:39:21 - 11:39:36
ARIES_2	$252 \leq T < 254$	15	11:39:36 - 11:39:45

The corresponding TAFTS spectra (called TAFTS_0, TAFTS_1, and TAFTS_2), were recorded at the same times as the measurements shown in Table 7.1. These are plotted for the LW and SW channels in Figure 7.11, where again TAFTS_0, TAFTS_1, and TAFTS_2 correspond to the black, blue and orange lines respectively. The number of TAFTS spectra was significantly reduced during the calibration process, and ultimately only 5 individual spectra were of high enough quality to include in the analysis. Thus TAFTS_0 and TAFTS_2 are each averages of two spectra, and TAFTS_1 is an individual spectrum.

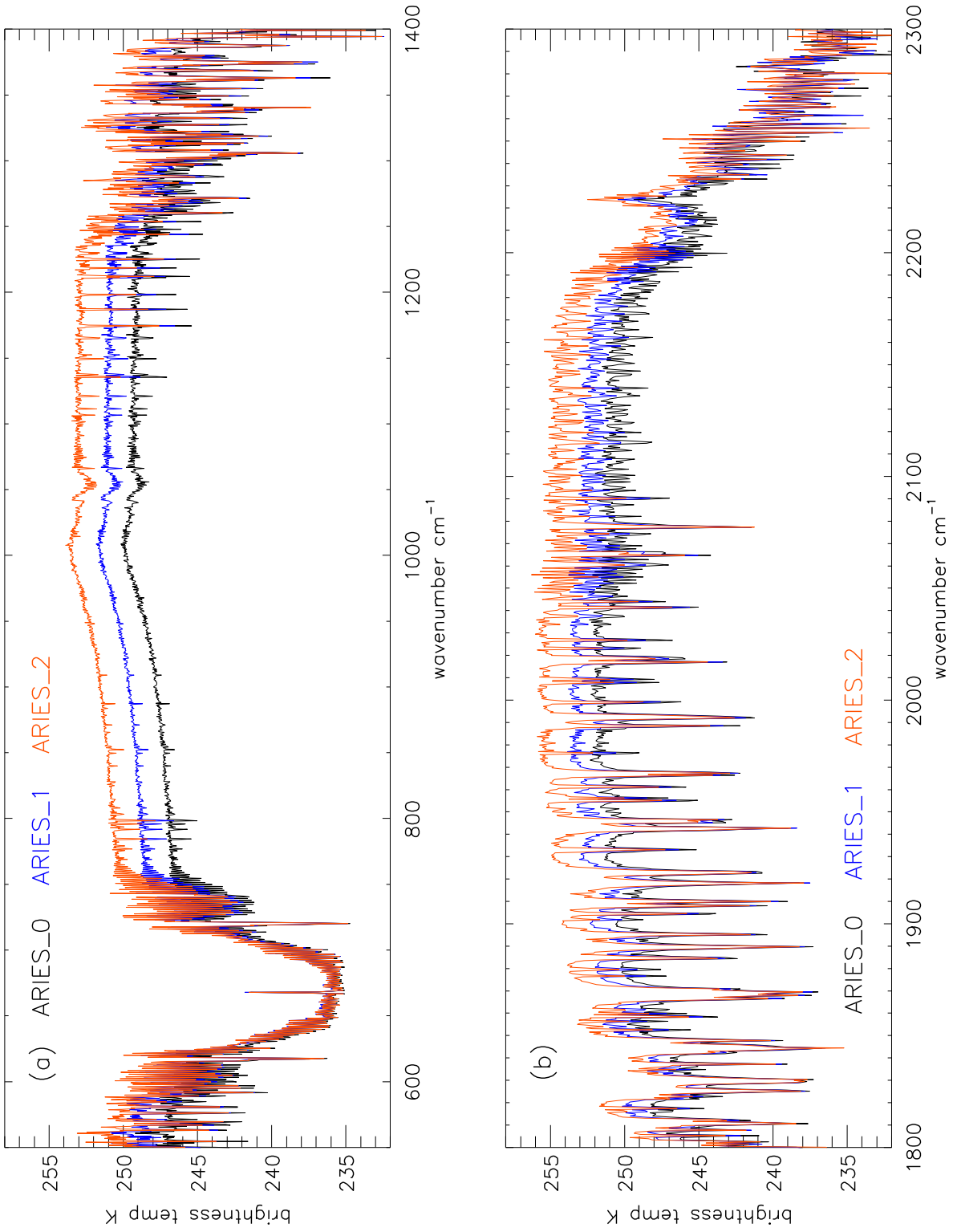


Figure 7.10: *The measured B818 ARIES (a) LW and (b) SW spectra for time 11:39:16-11:39:45 UTC. The spectra are averaged over 2K brightness temperature bins in the window region 8.3-8.4 μm / 1190-1205 cm^{-1}*

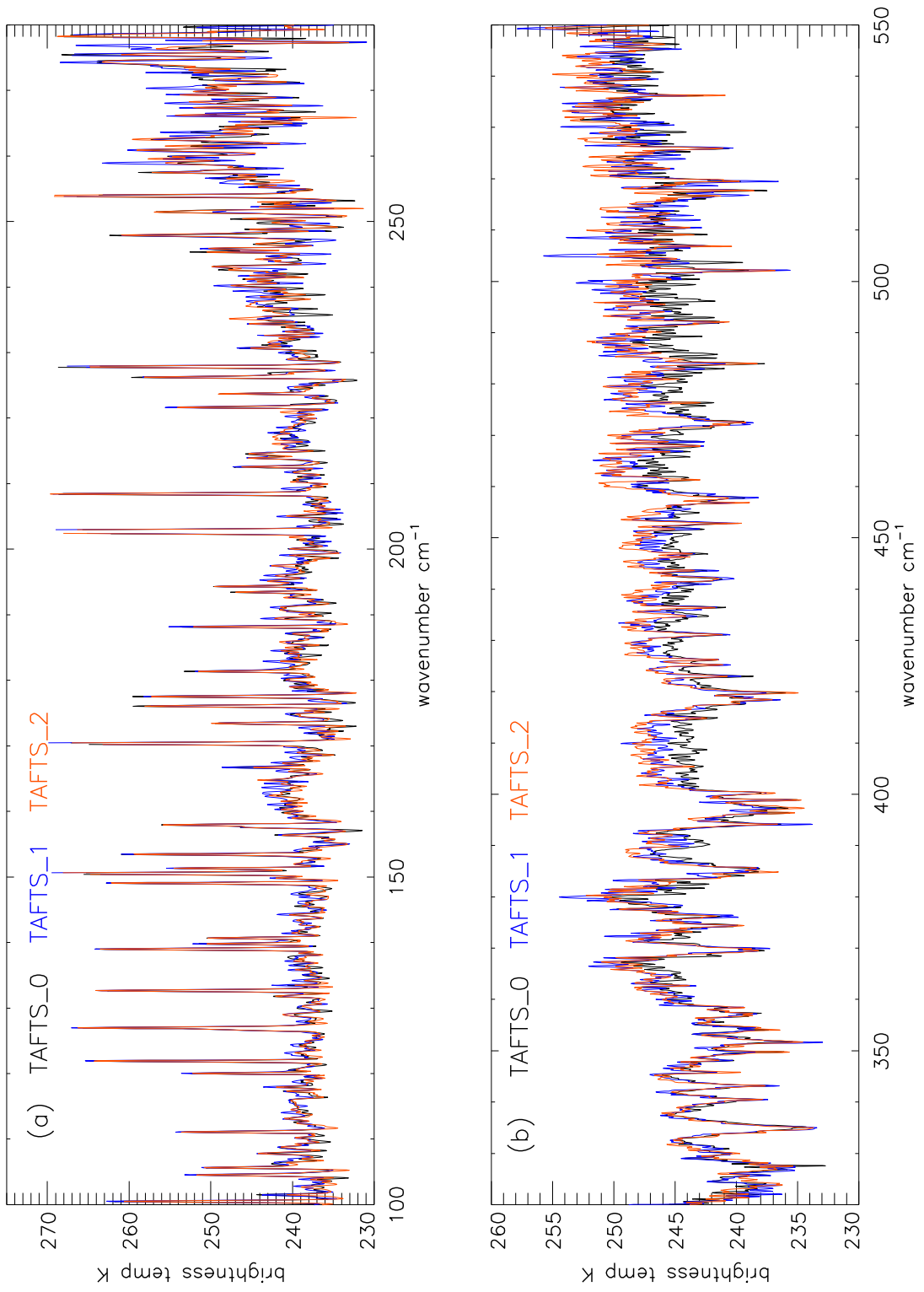


Figure 7.11: *The measured B818 TAFTS (a) LW and (b) SW spectra, that coincide with the 2K averaged ARIES spectra plotted in Figure 7.10*

Inspection of Figure 7.11 (a) suggests that the TAFTS LW channel is not sensitive to the changes in cloud properties for this case study, as the three sets of spectra are overlying. The LW channel also exhibits large spikes in the water vapour lines – this is caused by water vapour inside the pointing optics box of the instrument. Figure 7.11 (b) shows that the TAFTS SW channel exhibits sensitivity to changes in cloud properties within the spectral microwindows; however it does not always follow the same pattern as in the ARIES spectra. For example, in general the ARIES LW and SW spectra increase in brightness temperature sequentially in the window regions, with ARIES_0 having the lowest temperature and ARIES_2 the highest. This pattern is observed in the TAFTS SW spectra in the microwindow centred around 410 cm^{-1}, however, in the microwindows between 350 and 400 cm^{-1}, TAFTS_1 appears to have the highest brightness temperature. This may suggest something about the behaviour of the underlying microphysical cloud properties in the FIR spectral region; however it could be attributed to the noise level due to limited averaging of spectra.

7.3 Auxiliary measurements

This section presents the measurements recorded by instruments onboard the aircraft other than the radiometers, and outlines how they are used to constrain the atmospheric state and the properties of the cirrus.

7.3.1 Atmospheric profiling

An accurate picture of the atmospheric state is vital for radiative closure experiments such as CIRCCREX in order to obtain a reliable simulation [*Cox et al.*, 2010; *Green et al.*, 2012]. The FAAM aircraft measures T and RH using the Rosemount Temperature Sensor [*Stickney et al.*, 1994] and the General Eastern Hygrometer [*General Eastern Instruments*, 1987]. Also onboard is a Lidar [*Marenco*, 2010], which can be used to map the cloud extent and boundary variation, as well as independently constrain the cloud optical thickness. Profiling through and below the cloud is performed using dropsondes and the onboard Airborne Vertical Atmospheric Profiling System (AVAPS) [*Vaisala*, 1999].

A composite atmospheric profile was constructed for use in the radiance simulation; a baseline profile of T, RH, and ozone concentration was obtained from the 1200 UTC European Centre for Medium-range Weather Forecasts (ECMWF) analysis, which provides profile information in the upper atmosphere beyond the range of in situ measurements. Superimposed on the ECMWF profile, where measurements were available, is the temperature and humidity data from the dropsonde released at 1101 UTC; this dropsonde was

the closest temporally to the cirrus measurements. The atmospheric measurements recorded by the Rosemount temperature probe and General Eastern Hygrometer as the plane made a profile ascent through the cirrus (called pro6) make up the profile nearest to the flight level. The profile sources, and a composite profile where the sources have been combined and smoothed, are shown in Figure 7.12.

The dropsondes used during CIRCCREX are the Vaisala RD-94, which have a temperature and relative humidity measurement uncertainty of ±0.2 °C and ±2 %RH respectively [*Vaisala*, 2010a]. The Rosemount temperature probe has a calibration uncertainty of ±0.3 K [*Stickney et al.*, 1994] , and the General Eastern Hygrometer measures frost point temperature with an uncertainty of ±0.4 °C [*General Eastern Instruments*, 1987], from which the Volume Mixing Ratio (vmr) is calculated using measurements of pressure and OAT. This gives an uncertainty in vmr of ±0.2 %.

Additionally, the variation of the atmosphere must be considered as a source of uncertainty on the profile. As the dropsonde measurements used in the composite profile were recorded approximately 40 minutes prior to the radiative measurements, an uncertainty has been assumed based on the variation between this 1101 UTC dropsonde and the previous one, released at 1006 UTC. It is reasonable to assume that the variation between these two dropsondes is similar to that between the 1101 sonde and the atmosphere at the time of the radiative measurements. The use of the profile uncertainties to calculate an equivalent radiance simulation uncertainty is discussed in §7.5.

The concentration of atmospheric carbon dioxide was set to the value recorded at the Mauna Loa Observatory, Hawaii, which for November 2013 was 395.11 ppm. Concentrations of other atmospheric gases were taken from the standard MLW atmosphere [*McClatchey et al.*, 1972].

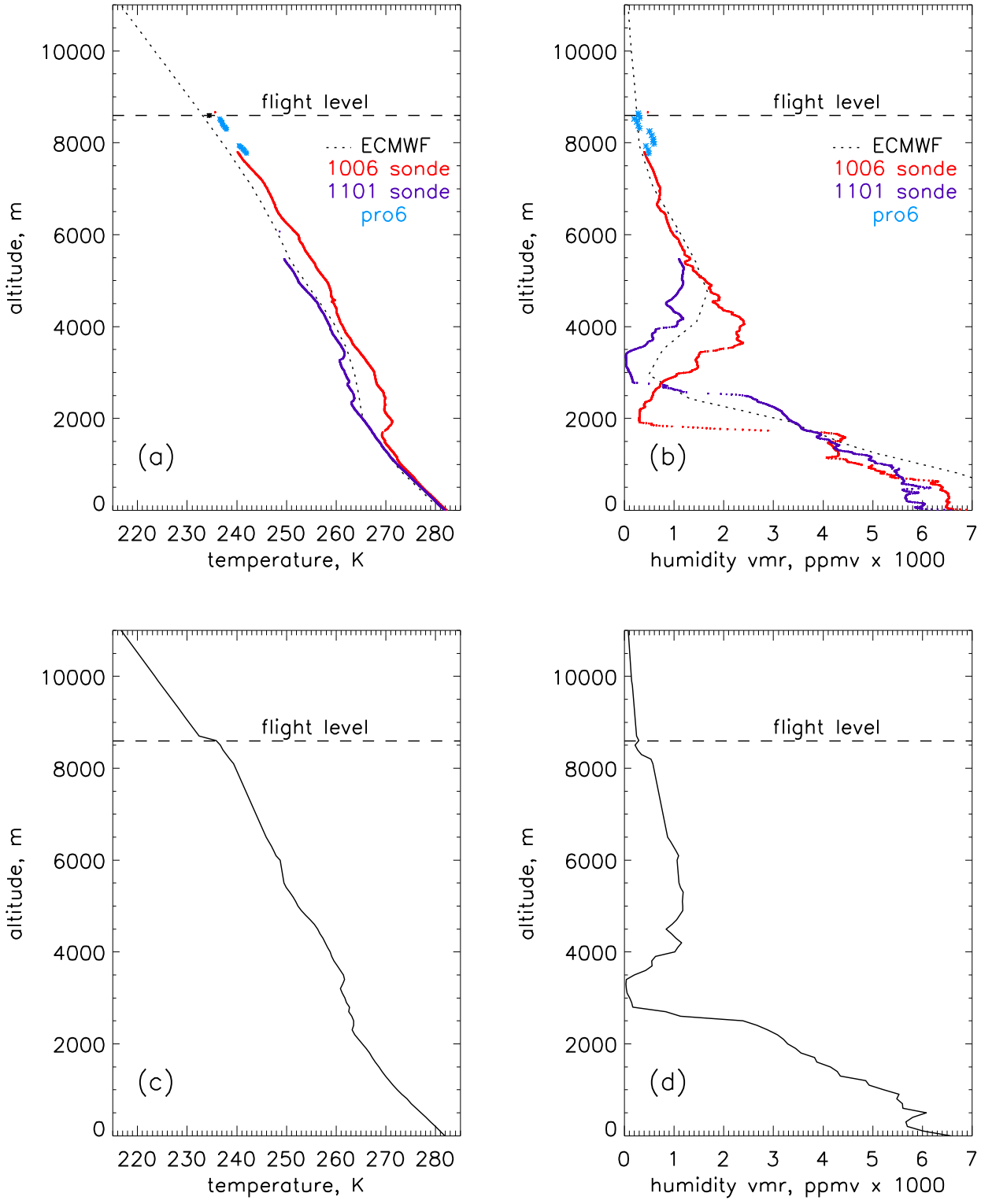


Figure 7.12: *Sources of the atmospheric (a) temperature and (b) humidity profile used for simulating flight B818 atmospheric radiances; the final composite (c) temperature and (d) humidity profiles. The uncertainties on the composite temperature and humidity profiles are ±0.3 K and ±2 % respectively from the instrumentation.*

7.3.2 Cloud physics

Several cloud physics instruments were flown during the CIRCCREX flight B818. This was to ensure that an accurate in-situ PSD could be calculated by measuring particles at as wide a size range as possible. The cloud probe instruments used to construct the PSD for flight B818 were the FAAM 2-Dimensional Particle Size Spectrometer (2DC, [*Knollenberg*, 1970; *Baumgardner and Korolev*, 1997]), the University of Manchester 2-Dimensional Stereo Probe (2DS, [*Lawson et al.*, 2006]) and the University of Hertfordshire Small Ice Detector 2 (SID2 [*Cotton et al.*, 2010]). The cloud physics instruments are mounted in pylons attached to the underside of the aircraft wings, as shown in Figure 7.13. As the aircraft moves forward, cloud particles are swept into the probe inlets where they are measured and analysed.



Figure 7.13: *A view of the cloud probe pylons attached to the underside of the aircraft wings*

The determination of the contribution of small ice particles to the PSD has been a large uncertainty in previous studies of cirrus radiative properties [*Cox et al.*, 2010; *Humpage*, 2010]. A major issue for most optical cloud probes is the effect of ice crystals shattering on the inlet as they are swept into the probe. This results in an over-counting of small particles and under-counting of larger particles, as the larger crystals get broken up into a number of smaller ones. This leads to large errors by both artificially increasing the variability of and skewing the form of the derived PSD [*Field et al.*, 2006]. Work by Korolev et al. [2011] demonstrated that modifying the tips of the cloud probes can significantly reduce shattering

effects and therefore mitigate the level of PSD contamination by artificial small particles. The probes that were used in CIRCCREX were therefore fitted with anti-shattering 'Korolev tips' [*Korolev*, 2009], shown in Figure 7.14. In addition, post-processing of the data from the probes utilises an algorithm that identifies spurious particles using the interarrival times of the crystals and corrects the size distributions accordingly [*Field et al.*, 2006].

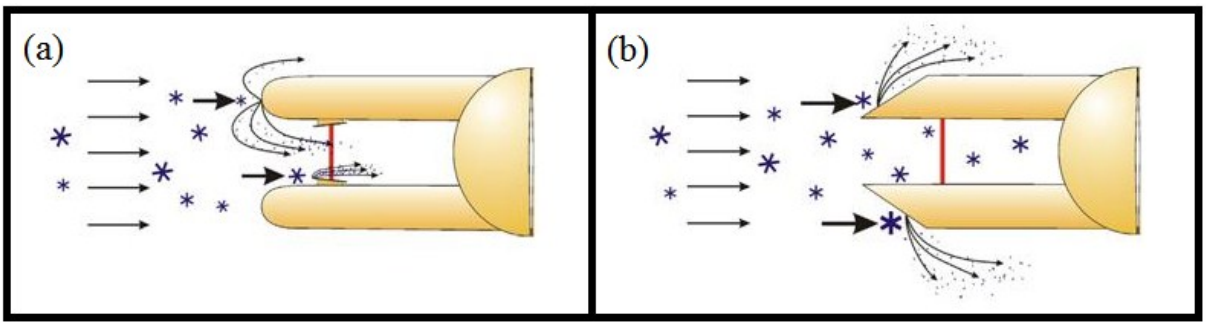


Figure 7.14: *(a) Original CIP tip design, showing how particles can shatter and 'bounce' into the sample volume; (b) Modified 'Korolev tips' which deflect shattered fragments away from the sample volume. Image credit: Droplet Measurement Technologies [2014].*

7.4 Determination of cirrus properties

In order to simulate radiances in the presence of cirrus using the scattering models described in §4.6, key physical properties of the cirrus need to be sampled. These are the particle size distribution (PSD) of the ice crystals making up the cloud, the geometric cloud height and thickness, and the cloud optical thickness. The PSD was measured using the cloud probes 2DS, 2DC and SID2 as the aircraft flew in-situ through the cloud, and the height, thickness and optical thickness were determined using the onboard lidar. However, as the cirrus system was advecting and changing form rapidly, these microphysical measurements are not directly aligned with the radiative measurements, and thus may not exactly represent the scene viewed by the radiometers. Thus a secondary method of determining the cirrus properties was used; a bispectral retrieval technique using the ARIES spectra. This is valid for this work, as the spectra from which the properties are retrieved are from the well-studied MIR window region. By fixing the cirrus properties in the MIR, the consistency of the cirrus model can be tested when it is extended into the less well-understood FIR region. This also allows a useful comparison of the in-situ measurements to the retrieved properties, indicating the ability of the cloud probes to correctly measure small ice particles, which has been identified as a problematic area in previous studies e.g. [*Cox et al.*, 2010; *Humpage*, 2010]. The cirrus properties deduced from both methods are described and compared below.

7.4.1 In-situ measurements of properties

During the radiance measurements of the cirrus, the cloud probes did not register any cloud particles, as the plane was in clear sky above the cloud. However, the plane passed through the cirrus during three level runs after the radiance measurements, and the microphysics measurements from these are used to construct three PSDs for the cirrus at altitudes of 8336m, 8018m and 7708m (these were during level runs 9, 10, and 11 respectively). Measurements from the SID2, 2DS and 2DC instruments are used to construct a composite PSD for each cirrus level by interpolating within their measurement ranges, as described more fully below. The uncertainty on the cloud probe measurements of particle counts are ±25 % for the SID2 [*Cotton et al.*, 2010], and a standard cloud probe uncertainty level of ±20% was assumed for the 2DS and 2DC [I. Crawford and M. Gallagher, UoM, personal communication June 2014]. This was taken as an uncorrelated error on the particle count, which was then carried forwards into the calculations for the particle effective radius and IWC.

Particle size measurements from the 2DC are considered unreliable for particles less than 100 μm in diameter, as laboratory measurements [*Korolev et al.*, 1998; *Strapp et al.*, 2001] have shown that large counting and sizing errors occur when particles pass outside the focal depth of field. In addition, counting and sizing errors occur due to the relatively slow time response of the 2DC, resulting from the finite time response of the photodiode array and first-stage amplifier [*Lawson et al.*, 2006].

The 2DS probe is also prone to errors in characterizing small particles (<100 μm) due to its large photodetector widths (10 μm) [*Cotton et al.*, 2010]. Measurements from the 2DS of particles smaller than 100 μm are classified as 'small' particles i.e. they may be ice crystals or water droplets, although given the temperatures recorded for the in-situ sampling in this work, and evidence from other instrumentation, it is reasonable to assume that these particles are indeed ice crystals.

The SID2 instrument is a higher resolution instrument specifically designed to address these small particle issues: it has a measurement range of 3-140 μm, and can also discriminate between supercooled liquid drops and small ice particles [*Cotton et al.*, 2010].

Initially the composite PSD bin widths are set to 20 μm over a range of 0-550 μm. For particles larger than 140 μm, the composite PSD is set to the average of the 2DC and 2DS values. This is reasonable as these two instruments show good agreement within uncertainties for this measurement range. For particles smaller than 140 μm the composite PSD value is set

to the average of the 2DS and SID2 instruments. These two instruments show good agreement for this range. During Run 11, the SID2 instrument encountered a fault; hence the number of SID2 measurements for this run are reduced. However, as the PSDs from the other two runs show that the SID2 instrument has reasonable agreement with the 2DS instrument, it can be assumed that the 2DS instrument is providing accurate values for the smaller particles. The PSDs recorded by each instrument, along with the composite PSD, are shown for each altitude level in Figure 7.15.

The mean effective radius R_e of the ice particles at each level was calculated from the PSDs using Equation 7.2 where $V(D_m)$, $\langle A(D_m)\rangle$ and $n(D_m)$ are the volume, average cross-sectional area and number concentration of ice particles at each maximum dimension D_m respectively [*Baran*, 2005].

$$R_e = \frac{3}{4}\,\frac{\int V(D_m)\, n(D_m)\, dD_m}{\int \langle A(D_m)\rangle\, n(D_m)\, dD_m} \qquad 7.2$$

The measured PSDs can also be used to calculate the IWC for each layer using Equation 7.3, where the density of ice ρ_{ice} = 0.917 g cm^{-3} [*Baum et al.*, 2014]. Information on the in-situ data from each measurement height, including the instrument uncertainty, is summarised in Table 7.2

$$IWC = \rho_{ice} \int V(D_m)\, n(D_m)\, dD_m \qquad 7.3$$

Table 7.2: *Cloud characterisation at each in-situ measurement height*

Run	Mean altitude (m)	Mean OAT (K)	Effective Radius (µm)	IWC (g cm^{-3})
9	8336	236.8 ± 0.03	38 ± 10	3.4 ± 0.9
10	8018	238.7 ± 0.03	25 ± 6	3.0 ± 0.8
11	7708	240.2 ± 0.03	22 ± 6	4.3 ± 1.1

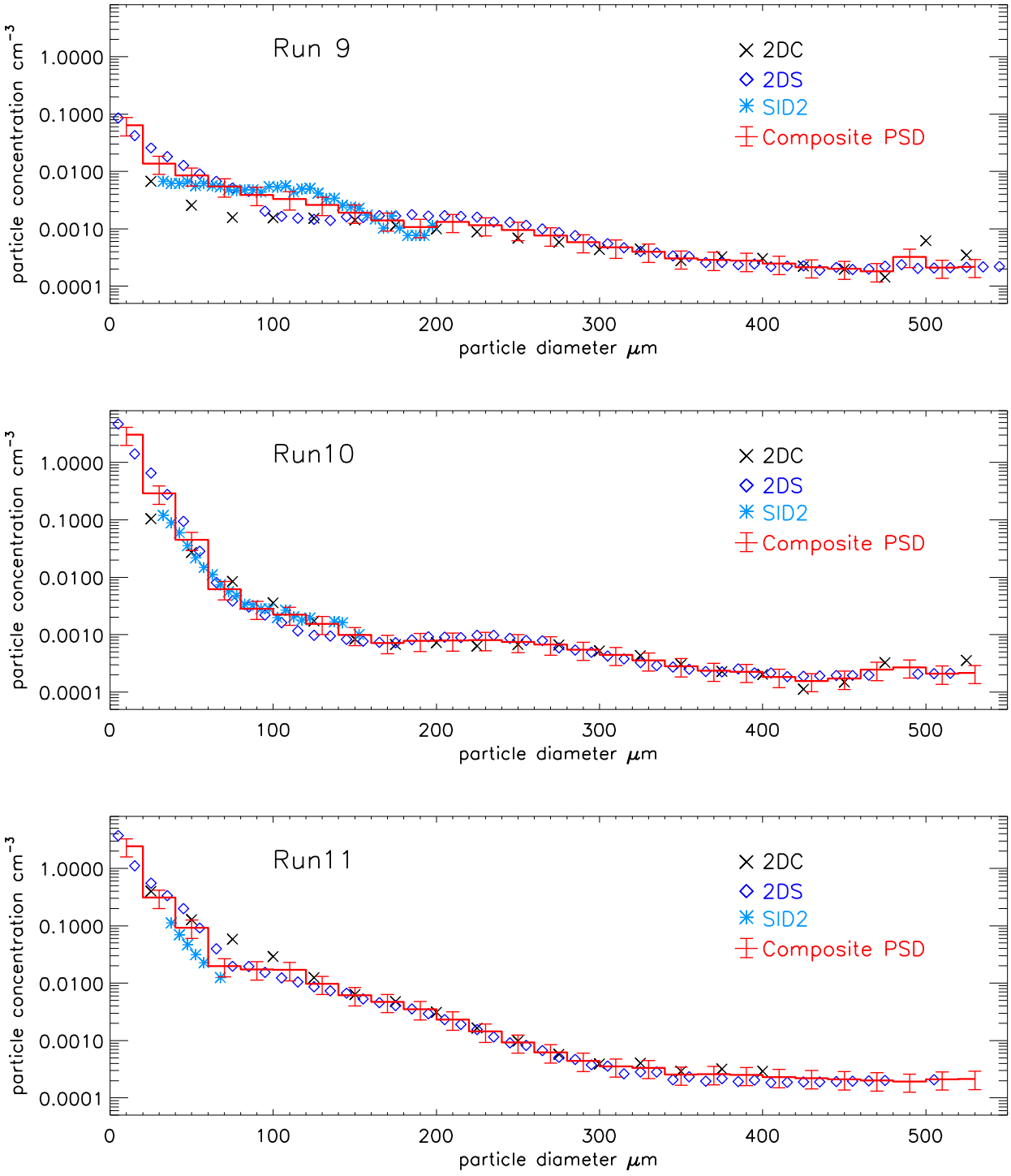


Figure 7.15: *PSDs of ice particles observed by the SID2, 2DC, and 2DS instruments, along with a composite PSD constructed by interpolation throughout the three instruments measurement ranges. Measurements were averaged along three level runs within the cirrus. The uncertainties shown on the composite profile are calculated from the uncertainties on the individual cloud probes.*

The cloud height and geometric thickness can be estimated using the measurements from the nadir-viewing 355 nm Lidar onboard the aircraft. The Lidar allows the identification of different atmospheric layers below the aircraft (clear air, aerosols, clouds) and uses a depolarization channel to indicate the presence of non-spherical particles such as ice or volcanic ash [*Marenco et al.*, 2011]. Figure 7.16 shows the Lidar observations from the B818 cirrus section, with 2 second temporal resolution [*Marenco and Hogan*, 2011; *Marenco et al.*, 2011].

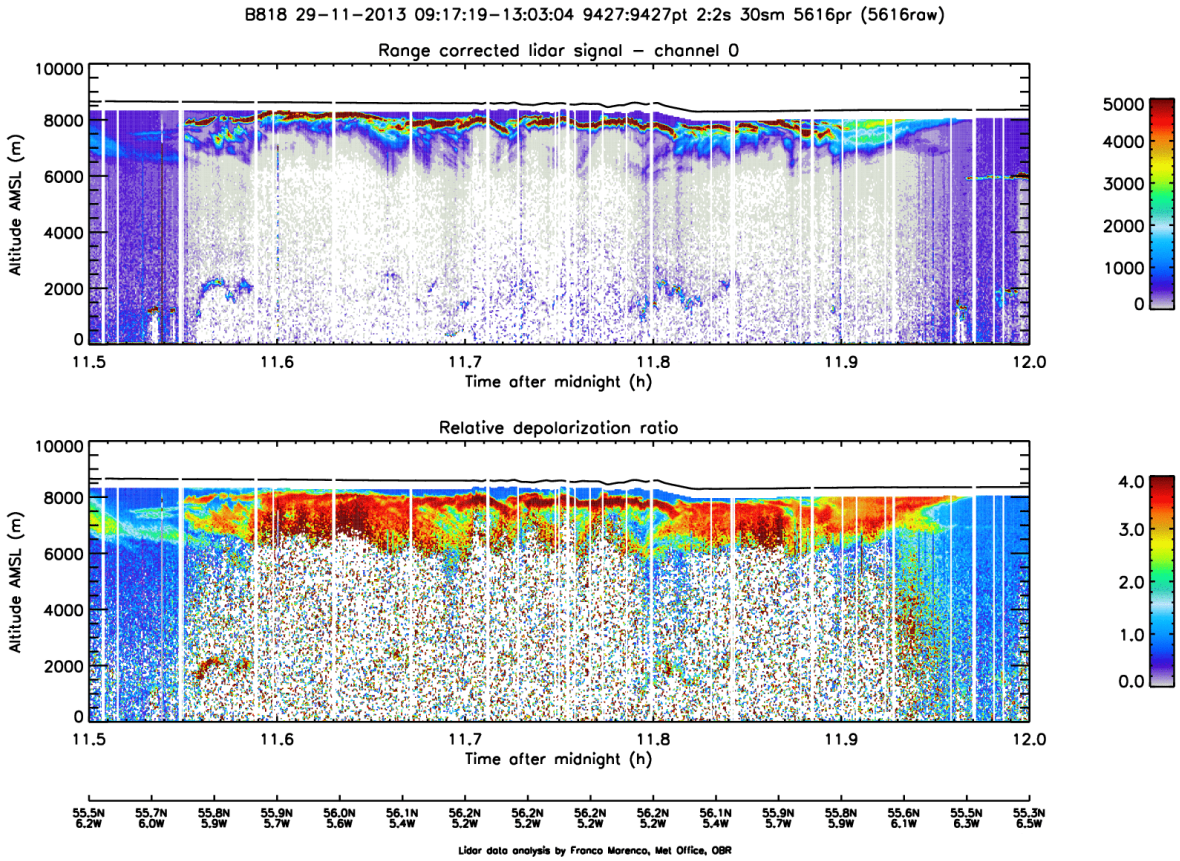


Figure 7.16: *Lidar backscatter signal (top panel) and relative depolarisation ratio (lower panel) for the B818 cirrus section.*

Figure 7.16 shows that the cirrus was patchy and variable in thickness. As ice crystals are non-spherical, the depolarized channel is more suitable for retrieval of the cloud geometric thickness (F. Marenco, UKMO, personal communication). For the time of the radiance measurements being analysed, the cloud top is at approximately 8000±100 m, and the base at approximately 6500±100 m.

7.4.2 Retrieval of properties from ARIES spectra

As the conditions during the flight were changing rapidly, recording both radiative and in-situ measurements of the same patch of cirrus was next to impossible. However, a method that has been previously used in studies to characterise cirrus is to retrieve the cloud properties from observed MIR spectra using a radiative transfer model [*Yang*, 2003; *Garrett et al.*, 2009; *Wang et al.*, 2011; *Baum et al.*, 2014]. The method uses a bispectral technique developed by Nakajima and King [1990], and relies on the differences in brightness temperature in two spectral bands, one of which is sensitive to cloud optical thickness and the other to effective particle size. For ice clouds, the spectral region 750 - 1100 cm^{-1} (10.0 - 13.3 μm) has been shown to be sensitive to particle size [*Bantges et al.*, 1999; *Chung et al.*, 2000], and that the angle of the slope of this region, along with values from the wavelength band 1070 – 1135 cm^{-1} (8.8 – 9.3 μm) can be used to infer optical thickness [*Wei et al.*, 2004]. Studies utilising this technique have been performed using spectral measurements from the Atmospheric Infrared Sounder (AIRS) [*Li et al.*, 2005], the High-Resolution Interferometer Sounder (HIS) [*Huang et al.*, 2004], the MODIS Airborne Simulator (MAS) [*Baum et al.*, 2000], and the MODIS satellite instrument [*Garrett et al.*, 2009]. Here, this bispectral method is applied to the ARIES LW channel observations using the brightness temperatures at bands centred on 8.3 and 11 μm (shown in Figure 7.6).

Following the method outlined by Garrett et al. [2009], simulations were performed using the LBLDIS model and the three ice scattering databases from Baum et al. [2014] (described in §4.6) using varying values of particle effective radius (10-30 μm) and cloud optical thickness (τ = 5-7). This indicates how the bispectral differences vary as the cloud properties are changed, as well as differences between the three habit databases. The cloud geometric extent was fixed at 6500 - 8000 m as observed by the Lidar, and the optical thickness is defined at the wavelength of the Lidar, 355 nm. Bispectral plots for the three scattering databases are shown in Figure 7.17 with the ARIES B818 bispectral values overplotted as stars, where the colours black-red denote sequential spectra, and correspond to those spectra plotted in Figure 7.9 (a). The B818 ARIES averaged spectra are overplotted as red triangles, and correspond to those spectra plotted in Figure 7.10 (a). As shown in Figure 7.10, the observed brightness temperature at 11μm increases with time for the individual spectra, and this corresponds to a decrease in optical thickness. The spread of values of effective radius stays relatively constant over the measurement time.

In Figure 7.17, the three plots show different bispectral values for the range of cloud optical thickness and particle effective radius, thus indicating that the three scattering databases give variations in brightness temperature for the same cloud properties. In order to identify those values of cloud properties that gave a simulated spectrum that best matched the three observed B818 ARIES spectral averages, the values for the cloud properties used in the simulation were varied in steps of 1μm for effective radius, and 0.1 for optical depth, until the residuals between the simulation and observations in the 8.3 and 11 μm brightness temperature bands were minimised. This was repeated for each of the three scattering databases. These retrieved properties are summarised in Table 7.3. The retrieved effective radius values are in general smaller than the measured in-situ values (which ranged from 22-38 μm, with uncertainties up to ±10 μm), however they are within the range of the uncertainties. Differences are likely to be due to the fact that the in-situ measurements took place within a different section of the cirrus to that above which the radiance measurements were taken. This general agreement between in-situ and retrieved particle sizes may indicate that the cloud probes are accurately measuring the PSD, and the problem of undercounting small particles is reduced.

Table 7.3: *Cirrus properties from the three B818 ARIES spectral averages, retrieved using a RT model and the three different scattering databases of Baum et al.* [2014]

ARIES_0		
Scattering database	**Effective radius (μm)**	**Optical Depth**
GHM	14	6.1
ASC	10	6.4
SC	12	5.8

ARIES_1		
Scattering database	**Effective radius (μm)**	**Optical Depth**
GHM	28	5.0
ASC	18	5.1
SC	22	4.7

ARIES_2		
Scattering database	**Effective radius (μm)**	**Optical Depth**
GHM	33	4.2
ASC	24	4.2
SC	27	3.9

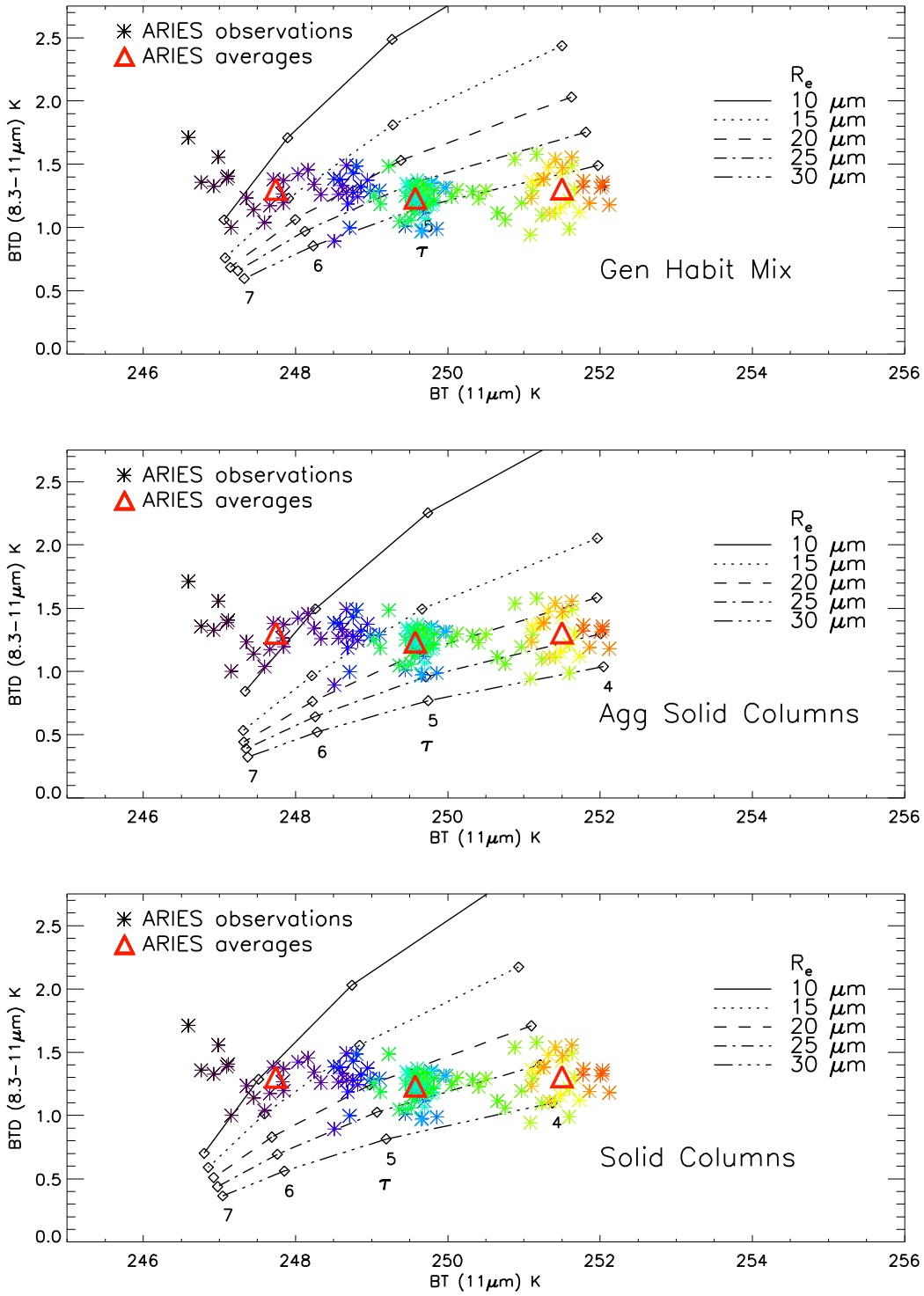


Figure 7.17: *Bi-spectral plots for the three Baum scattering databases showing how BTD vary with varying particle effective radius (r_eff) and cloud optical depth (τ). The bispectral values of the individual B818 ARIES spectra are overplotted as stars, where the colour black-red denotes sequential scans (as in Figure 7.9 (a)) The 2K averaged ARIES spectra are overplotted as red triangles.*

A further check of the in-situ measured and the retrieved properties can be performed using data from the MODIS instrument on the Terra platform, which overpassed the flight area at 1200 UTC, around 20 minutes after the ARIES radiance measurements were performed. MODIS level 2 cloud products [King et al., 2003; Platnick et al., 2003] are shown in Figure 7.18 (a) particle effective radius and (b) cloud optical thickness. These two figures show that effective radius was very variable, with values from around 20 – 40 μm, and that visible optical thickness was mostly < 10, with patches of underlying thicker cloud.

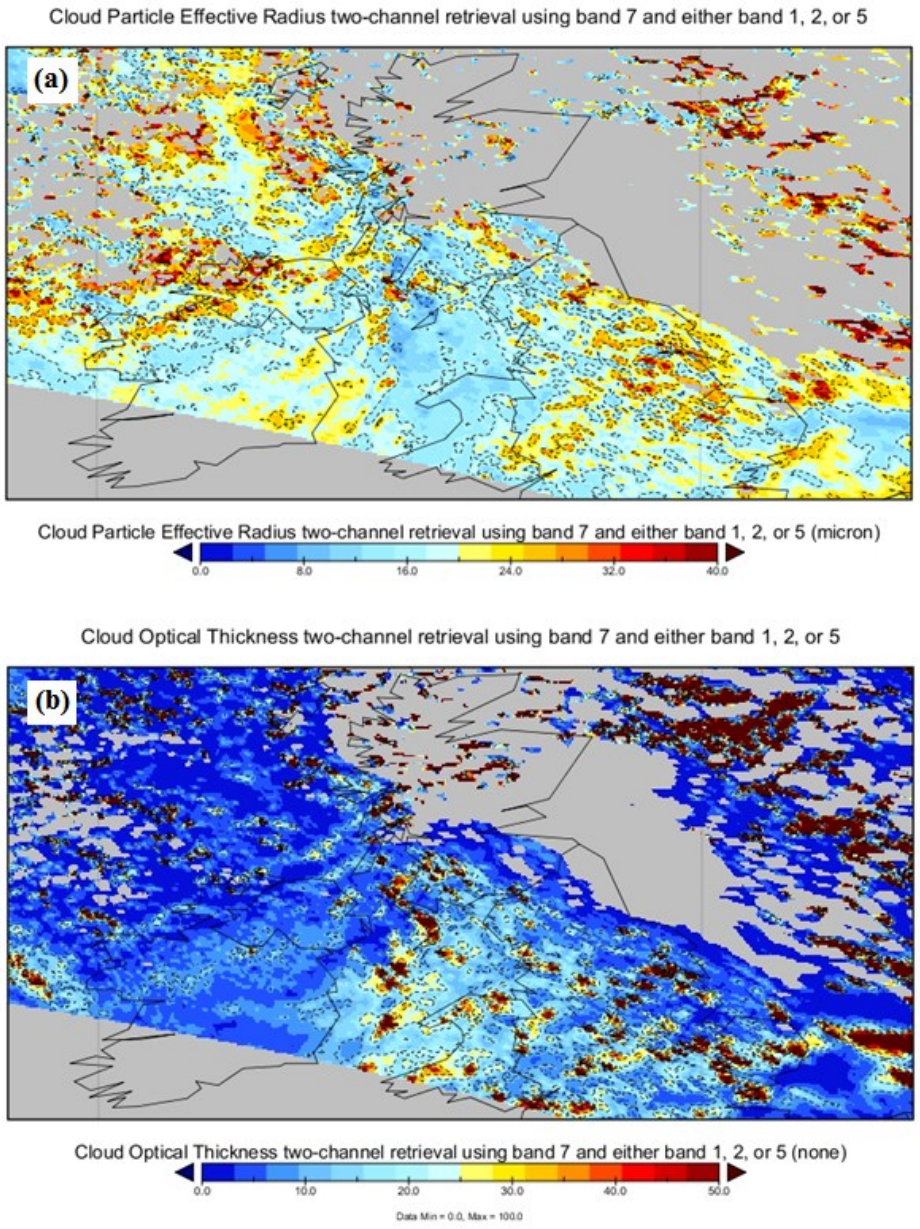


Figure 7.18: *MODIS Level 2 cloud product – (a) particle effective radius and (b) cloud optical thickness, from the MODIS Terra overpass, 1200 UTC, 29/11/13. Source: NASA* [2014].

7.5 Results of modelling across the MIR and FIR

The retrieved cirrus properties given in Table 7.3 were used to simulate the brightness temperature spectra in the other spectral regions for which we have observations – the TAFTS LW and SW channels, and the ARIES SW channel. This allows a test of whether the models are spectrally coherent i.e. are the models able to accurately simulate the changes observed in the BT across all observed spectral regions if the same cloud properties are used for all simulations.

The simulations were performed using the Line by Line Radiative Transfer Model (LBLRTM, [*Clough et al.*, 2005]) and the Line by Line Discrete Ordinates Radiative Transfer Model (LBLDIS, [*Turner*, 2005]), which were described in §4.3 and §4.5 respectively. As described earlier, LBLDIS requires an input parameter file giving details of the cloud height, thickness, particle effective radius, and optical thickness. The model then computes the scattering of the radiation as it passes through the cloud layer using a database of Single Scattering Parameters (SSPs). The databases used in this study are those developed by Baum et al. at the Space Science and Engineering Center of the University of Wisconsin-Madison [*Baum et al.*, 2014], described fully in §4.6. They consist of sets of single scattering properties (SSPs), including the single scattering albedo ω_0, extinction coefficient β_v, and scattering phase function $P(\theta)$ for a wide wavelength range spanning the ultraviolet (UV) to the FIR.

The uncertainties in the instrument measurements, as well as in the simulations, will now be considered. The uncertainties associated with the TAFTS and ARIES spectra due to the calibration, instrument noise and the standard deviation of the averaged spectra have been combined into a single instrument uncertainty.

The uncertainties in the simulation come from several sources. Firstly, the errors on the measurements that were used to construct the atmospheric profile used in the radiative transfer modelling can be considered. For the dropsondes, temperature and relative humidity uncertainties are ±0.2 °C and ±2 %RH respectively [*Vaisala*, 2010a]. The aircraft Rosemount temperature probe has a calibration uncertainty of ±0.3 K [*Stickney et al.*, 1994] , and the General Eastern Hygrometer gives a vmr measurement with an uncertainty of ±0.2 % [*General Eastern Instruments*, 1987]. However, a larger uncertainty in the profile comes from the variation of the atmosphere between the time of the dropsonde and the time of the radiance measurements. As discussed in §7.3.1, these were estimated to be similar to the

changes in the atmosphere between the dropsonde at 1006 UTC and 1101 UTC. In order to obtain the equivalent uncertainty in brightness temperature, simulations were performed at the maximum uncertainty levels of the profile, and the difference between this perturbed simulation and the original simulation taken as the brightness temperature uncertainty.

The observed and simulated spectra for the averages ARIES_0 and TAFTS_0, for each of the three Baum scattering databases are shown in Figure 7.19– Figure 7.22. For brevity; the observed and simulated spectra for the other two averages are not discussed here as results are very similar for all three averages.

For each of Figure 7.19– Figure 7.22, the observed spectra from the ARIES LW (Figure 7.19), ARIES SW (Figure 7.20), TAFTS LW (Figure 7.21), and TAFTS SW (Figure 7.22), for averages ARIES_0 and TAFTS_0 are plotted in black. Overplotted in dark blue, light blue, and green are the simulations using the GHM, ASC, and SC databases respectively, and the cloud properties in Table 7.3. Also overplotted are the observation-simulation residuals for each channel and database, alongside the radiance uncertainties from the measurements and the simulations. The instrument uncertainty is plotted in orange, and the simulation uncertainty in purple.

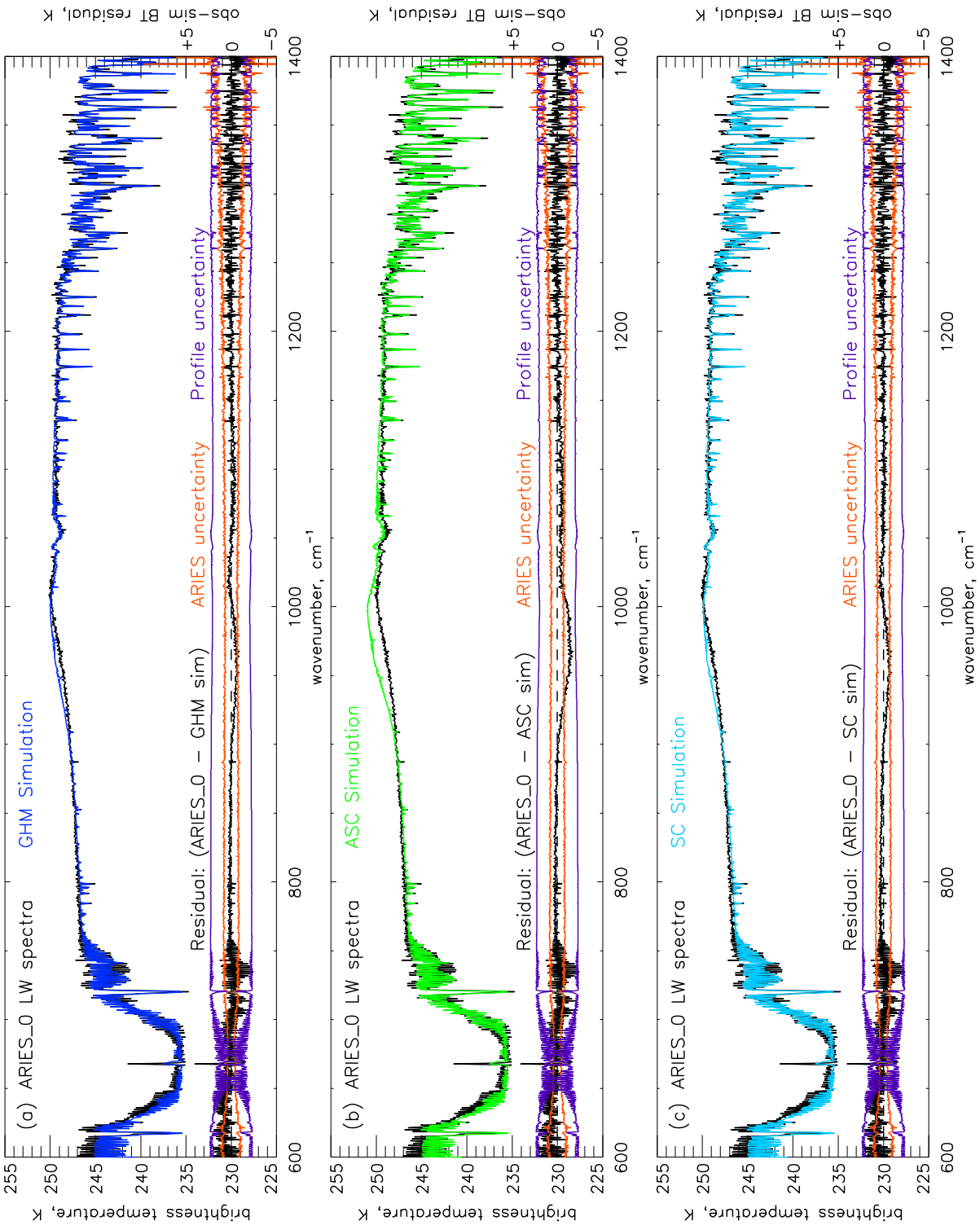


Figure 7.19: *The B818 spectral average ARIES_0 LW spectra (black), alongside simulations using the three scattering databases GHM, ASC, and SC (coloured lines). Also plotted are the observation-simulation residuals and the uncertainties due to the instrumentation (orange) and the atmospheric profile used in the simulation (purple).*

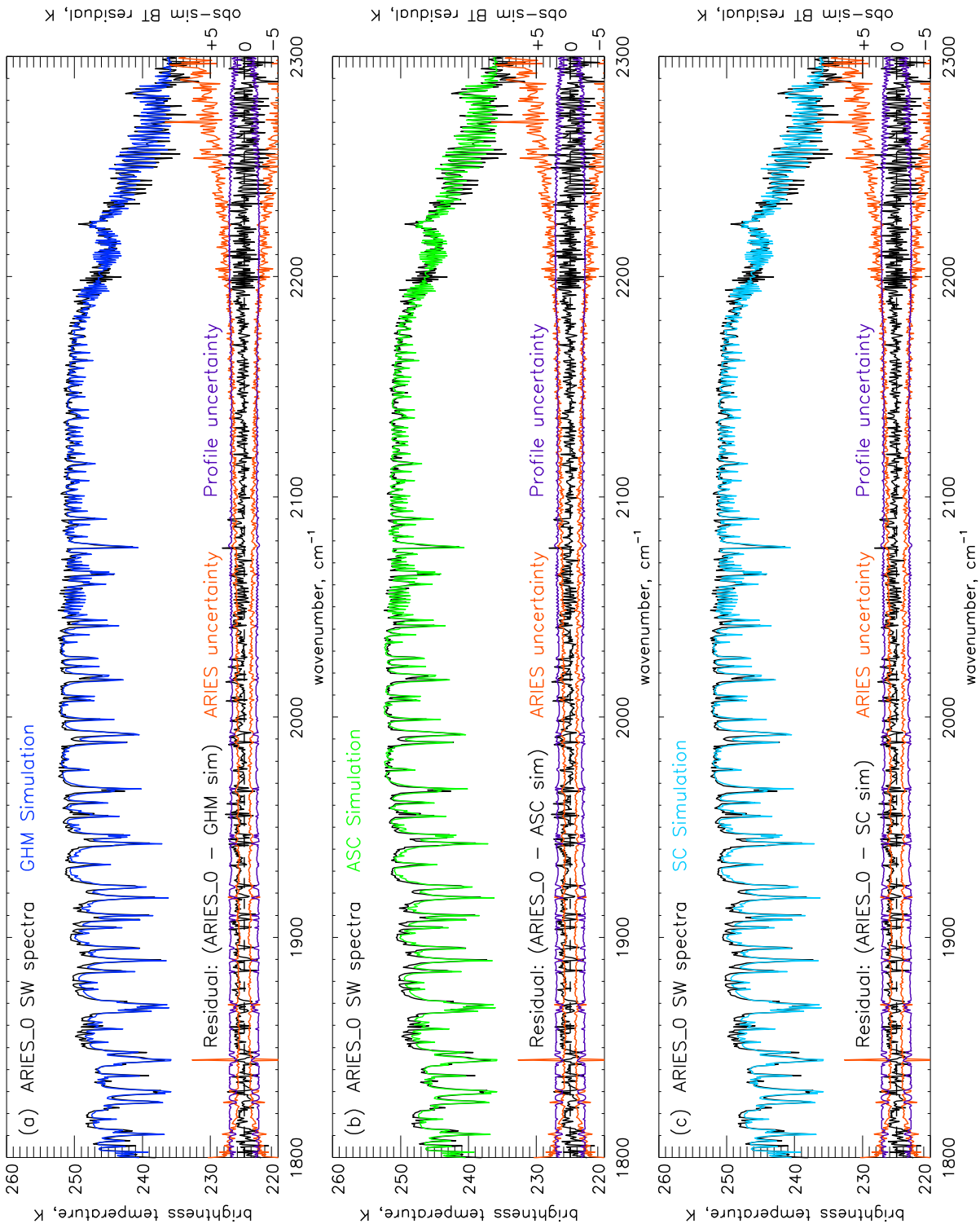


Figure 7.20: *The B818 spectral average ARIES_0 SW spectra (black), alongside simulations using the three scattering databases GHM, ASC, and SC (coloured lines). Also plotted are the observation-simulation residuals and the uncertainties due to the instrumentation (orange) and the atmospheric profile used in the simulation (purple).*

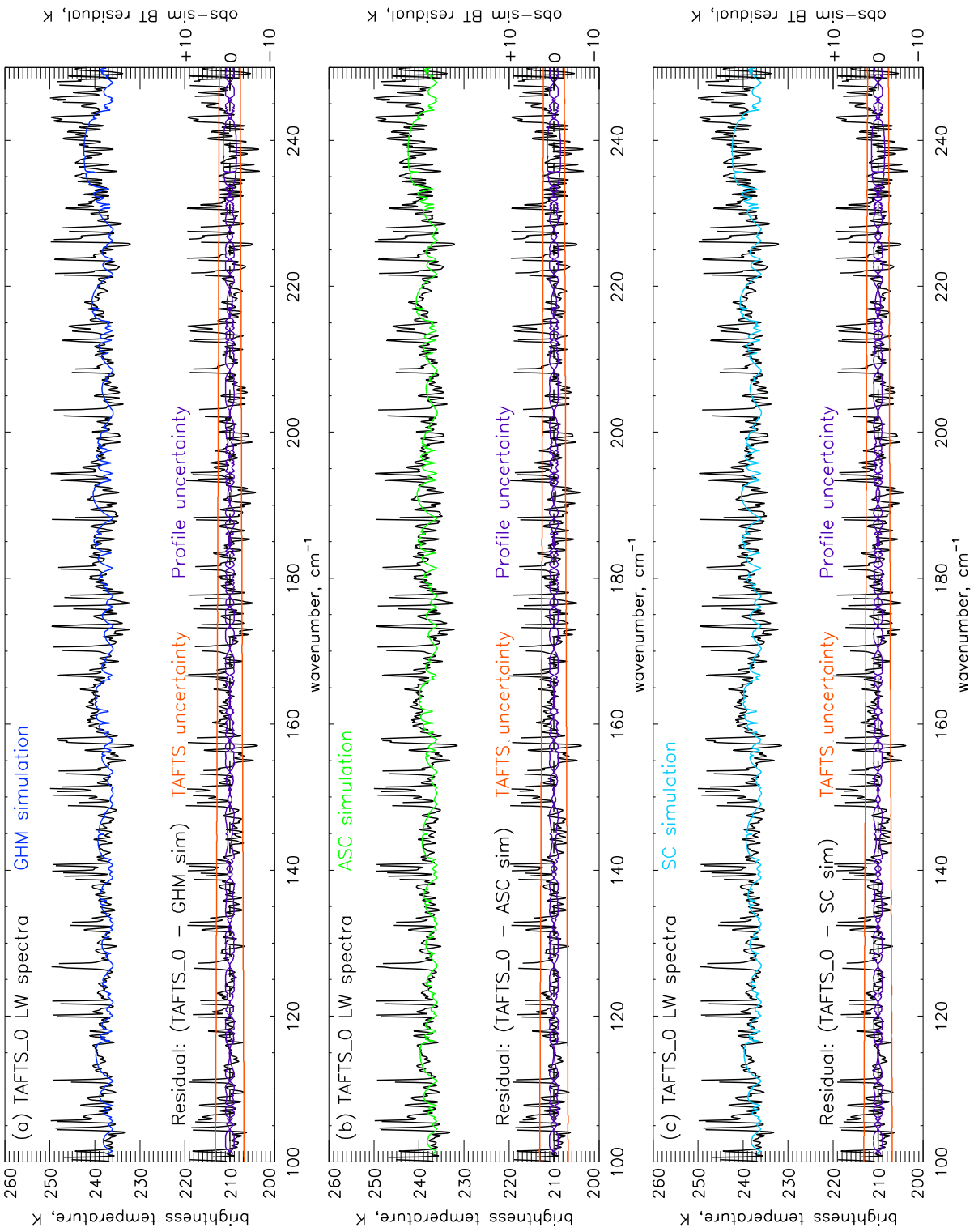


Figure 7.21: *The B818 spectral average TAFTS_0 LW spectra (black), alongside simulations using the three scattering databases GHM, ASC, and SC (coloured lines). Also plotted are the observation-simulation residuals, and the uncertainties due to the instrumentation (orange) and the atmospheric profile used in the simulation (purple).*

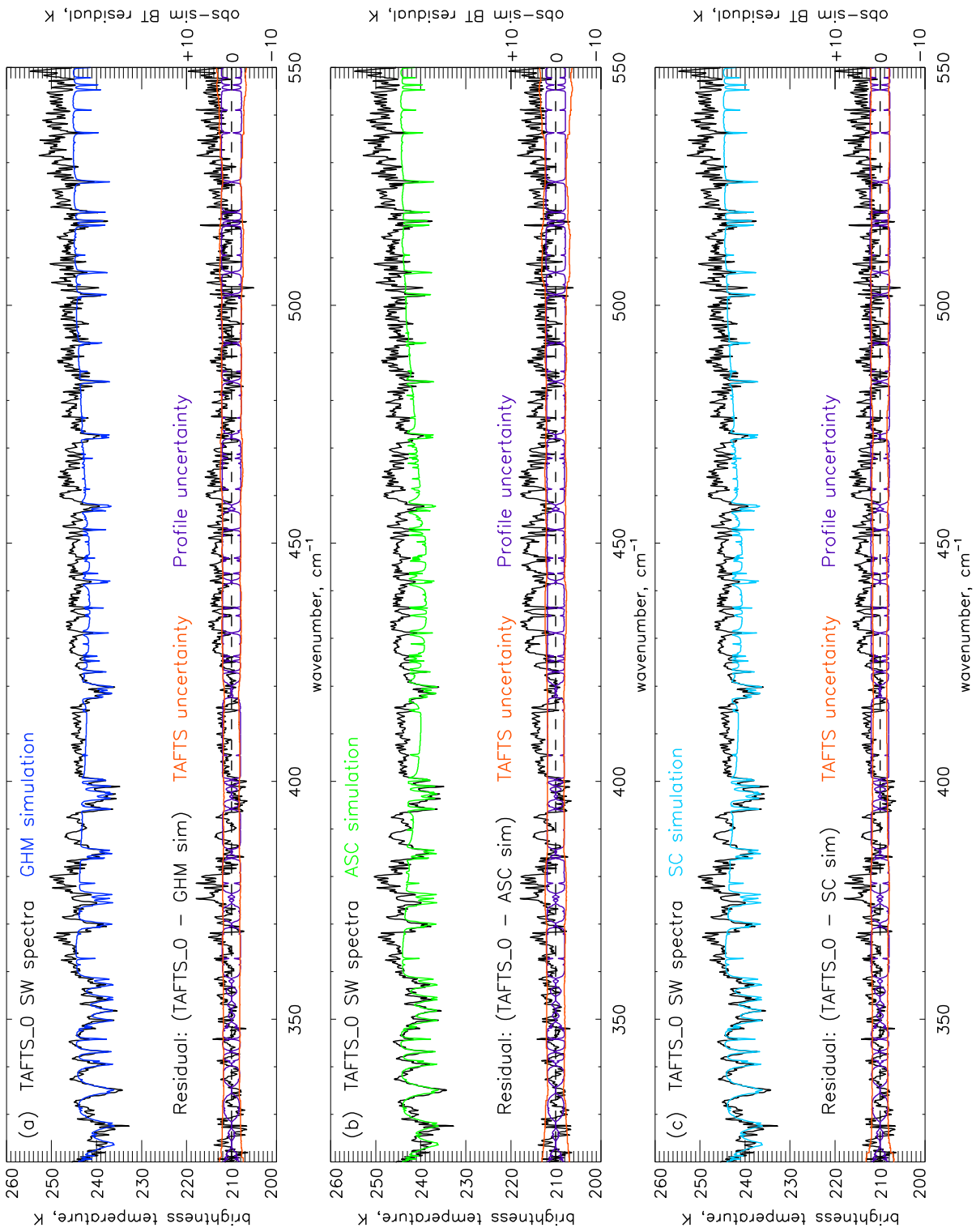


Figure 7.22: *The B818 spectral average TAFTS_0 SW spectra (black), alongside simulations using the three scattering databases GHM, ASC, and SC (coloured lines). Also plotted are the observation-simulation residuals, and the uncertainties due to the instrumentation (orange) and the atmospheric profile used in the simulation (purple).*

First considering the ARIES LW channel (Figure 7.19), while all three models reproduce the observations well (although it should be noted that the cloud properties used in the simulation were selected to give a best match), the GHM and SC models better fit the shape of the curve in the window region 750 – 950 cm^{-1} than the ASC model. Notable observation-simulation differences are seen in the region 900-1050 cm^{-1}, particularly in the ASC model. Referring to the sensitivity studies shown in §6, these differences can be attributed to the modelled effective radius being too small. As the retrieved value of the ASC effective radius is smaller than for the other two databases, it is to be expected that the differences would be greatest when using this model. Most of the residuals for the ARIES LW channel lie within the instrument and profile uncertainties. This is not surprising, as it was this region that was used to retrieve the cloud properties used in the simulation.

In the ARIES SW channel (Figure 7.20), all of the models reproduce the observations well, with only small observation-simulation differences seen in the microwindows in the region 1800-2000 cm^{-1}. The residuals for this channel lie within the levels of the uncertainties, so this observation-simulation discrepancy may be due to an error in the atmospheric profile, or uncertainty in the measurements. Thus it can be concluded that the models are representing this MIR region accurately.

In the TAFTS LW channel (Figure 7.21), the observations show absorption lines that are caused by water vapour inside the optics box of the instrument. In order to show results more clearly, this effect has been minimised by truncating the line spikes in both the observations and the residual (the original spectrum without truncating is shown in Figure 7.11). Hence only the underlying microwindows are considered, and in these regions all three models perform equally well at reproducing the spectra. This suggests that sensitivity to the cloud properties is low in this region; this is in agreement with the sensitivity studies in §6. The residuals, (again disregarding the absorption spikes caused by water vapour inside the instrument), mostly fall within the instrument uncertainty level.

In the TAFTS SW channel (Figure 7.22), the models consistently predict brightness temperatures that are between 2 and 10 K lower than those measured by the instrument. Residuals for all databases are outside of the limits of the uncertainties. The ASC database in particular gives suppressed brightness temperatures in the window regions of the TAFTS SW channel. This suppression was seen in the sensitivity studies presented in §6, where it was shown to be caused by the underlying single scattering properties, and increased as the

effective radius was decreased. The retrieved effective radius for the ASC databases was lower than for the other two databases, thus it is logical that the brightness temperature suppression is seen to be greater in those simulations using ASC. As this effect is not reproduced in the observations, these results suggest that the simulation is not reproducing this spectral region particularly well.

7.6 Summary & conclusions

This chapter presented three sets of averaged TAFTS FIR and ARIES MIR upwelling brightness temperature spectra, measured simultaneously above cirrus. The properties of this cirrus are determined through two methods; in-situ measurements of ice particles by cloud probe instruments, and retrievals from the ARIES spectra using a bispectral method. Good agreement was found for the particle effective radius from both methods, given the varying scene evolution. This suggests that the use of the SID2 probe in conjunction with the 2DS and 2DC may have somewhat alleviated those problems of measuring small particles reported in Cox et al. [2010] and Humpage [2010].

The observed spectra were simulated using the retrieved cirrus properties and the SSP databases of Baum et al. [2014], as inputs to the LBLRTM and LBLDIS radiative transfer models. This allowed a study of the consistency of the scattering databases across the infrared spectral region, by fixing the cloud properties to those retrieved in the MIR, and expanding the simulation into the underexplored FIR region. The simulations differed from the observations in the FIR TAFTS SW channel, with residuals in brightness temperature of up to 10K, indicating that the models are not accurately representing the observations from this case study. With respect to the three habit databases, the retrieved cloud properties from the ASC database result in simulations which show a signal of an under-estimated effective radius, with this effect seen to a lesser extent when using the other databases. Differences between retrieved properties were small, and within the uncertainties of the measured in-situ properties. Further investigation of in-situ ice particle habits would allow a more meaningful analysis of the best scattering database to use in the simulations.

The inability to simultaneously reconcile observations and simulations across the entire FIR spectral range implies that the radiative effect of cirrus in this region is still not clearly understood. Further observations are required to unequivocally determine the cirrus radiative signature, in order that the SSP databases used in this work can be improved, and ultimately the effect of cirrus be correctly represented in GCMs and NWP models.

8 Conclusions and future work

In this thesis, original far-infrared high-resolution spectra recorded using the Tropospheric Airborne Fourier Transform Spectrometer (TAFTS) instrument have been presented and analysed. Comparisons have been made between spectra observed by TAFTS and simulations from radiative transfer models, under both clear sky and cirrus conditions, from both ground- and aircraft based platforms. These comparisons are then used to validate state-of-the-art models of atmospheric processes in the crucial and under-studied far-infrared spectral region. The results of two main studies were reported, one of the water vapour absorption continuum in the Arctic, and the second of airborne observations of cirrus radiative signatures. A summary of the main results found by the author during this work, and their significance, is given in the first part of this chapter. The results presented indicate the potential for more extensive use of far-infrared spectral radiance measurements for studies of cirrus, and also for other applications. Some possibilities of furthering and developing the work presented here are therefore discussed in the second part of this chapter.

8.1 Summary of results from ground-based arctic study

8.1.1 MT-CKD v2.5 validation

Clear sky observations of downwelling radiance were made by TAFTS when based in Alaska during the RHUBC campaign. This campaign was the first time that TAFTS had performed ground-based measurements, as the extremely dry conditions during the Arctic winter allowed the atmosphere to become more transparent to infrared radiation, due to reduced absorption by the water vapour pure rotation band. This allowed a study of the FIR water vapour continuum absorption. TAFTS spectra were compared to those simulated using a measured atmospheric profile and LBLRTM [*Clough et al.*, 2005], and continuum coefficients derived from the measured TAFTS radiances were found to agree with both the simulation and with previous studies. Thus this study concludes that the current MT-CKD 2.5 model continuum values can be used to accurately simulate radiances at wavenumbers 350-500 cm^{-1}, and adds to validation in the >400 cm^{-1} region from other locations.

8.1.2 TAFTS/AERI-ER comparison

A cross-comparison study between two infrared spectrometers was presented, comparing simultaneous measurements from the AERI-ER and TAFTS instruments during RHUBC. This represents the first time that the AERI-ER has been compared to a different design of

interferometer such as TAFTS. The study showed a good agreement between the two instruments within the overlap in their measurement ranges, with 68% of the residual lying within the uncertainty boundaries, and the maximum residual within three standard deviations of the average uncertainty. This agreement between the TAFTS and AERI-ER measurements gives confidence in the ability of both instruments to accurately measure the far-infrared down-welling radiances, given their differences in interferometer and detector design.

8.2 Results of sensitivity studies to changes in cloud properties

Studies were performed to assess the sensitivity of the various spectral regions to changes in the cirrus properties. It was found that the optical thickness of the cloud affected the brightness temperature observed in the window region across the spectrum, with the least changes seen in the TAFTS LW channel. An increase in the cloud particle size generally resulted in lower brightness temperatures within the window regions, with the most noticeable effect in the window 750 – 950 cm^{-1}, where changes in particle size affect the angle of the slope of the window. The TAFTS LW channel did not exhibit any sensitivity to changes in the particle size, and was only sensitive to changes in cloud optical thickness at wavenumbers above 200 cm^{-1}. Sensitivity to the choice of scattering database was observable in the TAFTS SW channel, where the brightness temperatures were suppressed in the region 350-500 cm^{-1}, with the most suppression seen when using the ASC database, and the GHM database having the smallest effect. This was investigated through examination of the underlying SSPs in each of the databases. It was found that the ASC database had a decrease in asymmetry parameter in the region 350-500 cm^{-1}, which would result in less radiation being scattered towards an instrument detector. This would account for the lower brightness temperatures observed in the sensitivity studies.

8.3 Summary of results from airborne cirrus study

8.3.1 Simultaneous FIR and MIR spectra recorded above cirrus

Coincidental observations of upwelling radiances measured above cirrus were recorded by the FIR TAFTS and MIR ARIES instruments during the CIRCCREX campaign. Although the number of spectra available for analysis was significantly reduced, this is nonetheless an important study as it allows the effect of cirrus across the infrared spectrum to be investigated. Previously, models of the scattering of radiation by cirrus were based on observations made in the MIR only, and then extrapolated into the FIR. The deployment of the TAFTS instrument gives a unique insight into the under-explored FIR, as there are

currently no other aircraft-based instruments capable of making measurements in this longer wavelength region.

8.3.2 Determination of cirrus properties

The properties of the sampled cirrus (particle effective radius and cloud optical thickness) were determined through two methods; in-situ measurements of ice particles by cloud probe instruments, and retrievals from the ARIES spectra using a bispectral method. Good agreement was found for the particle effective radius from both methods, suggesting that the use of the SID2 probe may have alleviated those problems of misrepresenting small particles reported in previous studies. Previously, the measured PSDs were modified by adding or subtracting small ice crystals in order to fit the observations in the infrared window. As this was not needed in the work presented here, this signifies an improvement in the study of cirrus particles <100 μm, and increases confidence that properties retrieved from MIR spectra are correctly representing the in-situ PSD of the ice crystal particles.

8.3.3 First test of Baum scattering models in FIR region

The observed TAFTS and ARIES spectra were simulated using the retrieved cirrus properties and the SSP databases of Baum et al. [2014], as inputs to the LBLRTM and LBLDIS radiative transfer models. This allowed a study of the consistency of the scattering databases across the infrared spectral region, by fixing the cloud properties to those retrieved in the MIR, and expanding the simulation into the underexplored FIR region. This was the first time that these models had been compared to cirrus radiative observations spanning the entire infrared region. The simulations were able to reproduce the observations in the MIR within uncertainties, but differed from the observations in the FIR TAFTS SW channel, with residuals in brightness temperature of up to 10K. This suggests that models may not be accurately representing this spectral region, and that further work is required.

8.4 Future Work

8.4.1 Improved and extended cirrus datasets

A limitation of the work presented in Chapter 7 of this thesis is the limited number of spectral scans available for analysis. The main reasons for this were a low occurrence of suitable cirrus conditions, lack of coincidental views between TAFTS and ARIES, and high levels of vibration affecting the quality of some of the TAFTS data. The second phase of the CIRCCREX campaign (in which the author participated) took place out of Prestwick, Scotland, in March 2015. Much of the knowledge gained from the analysis of data recorded

during CIRCCREX-I was applied during these new flights in order to obtain better and more extensive measurements, as will now be explained.

If the bispectral method of retrieving cloud properties is to be used for model validation, it is vital that TAFTS and ARIES have coincidental views. This is straight-forward to achieve, as TAFTS can be pre-programmed to cycle through a set patterns of viewing configurations, and the ARIES view direction can be changed by the operator during flight. Hence, TAFTS can be set to record a set of nadir scans when above the cirrus, and this can be communicated to the ARIES operator, who can then set ARIES to the nadir view. This was implemented successfully during CIRCCREX-II and has resulted in a much larger dataset available for analysis, which will be a great improvement in terms of signal-to-noise as many more scans can be averaged.

The problematic noise on some of the TAFTS spectra was caused by excessive vibration as the aircraft performed orbits. Unfortunate timing meant that this happened during the time the aircraft was above cirrus. Better planning of flight sorties during CIRCCREX-II prevented this from occurring, and the greater number of TAFTS/ARIES coincidental views will allow a much larger dataset from which scans with minimum noise can be selected.

The occurrence of cirrus is unfortunately out of our control. However there have been successful cirrus flights out of the UK in the past and the CIRCCREX-II campaign was scheduled for a time when cirrus conditions are climatologically likely (C. Harlow, UKMO, personal communication Jan 2015). At the time of writing, several successful flights were undertaken which included both radiative and in-situ measurements of cirrus. This will hopefully allow the characterisation of the cirrus properties, and their link with the radiative signature, to be ascertained correctly.

8.4.2 Testing and validation of alternative cirrus scattering models

In addition to those scattering databases developed by Baum et al. [2014] described in §4.6 and used in the analysis in §7, there are also new SSP databases developed at the UK Met Office by Baran et al. [*Baran and Labonnote*, 2007; *Baran et al.*, 2014]. Time has not allowed the inclusion of these databases in this thesis, but the performance of these models in the FIR region will be validated in future, using both the data presented here, and the data recorded during CIRCCREX-II. This will allow an interesting comparison study between the two sets of databases from Baum et al. and Baran et al., which has not previously been investigated.

8.4.3 Measurements of FIR surface emissivity

A recent paper by Feldman et al. [2014] highlighted the importance of FIR (15-100 μm) observations of the Earth's surface emissivity to climate, and the current lack of any such measurements. FIR surface emissivity has a direct impact on OLR and infrared cooling rates in regions of very low PWV i.e. high altitude and high latitude locations, and as such is important to correctly constrain for use in climate models. TAFTS would be an ideal instrument for such studies, as its measurement range covers the entire FIR region, and its ability to be operated from an aircraft platform means that upwelling surface radiances could be observed in-situ. This would be a new direction of study for TAFTS, and indeed for any FIR instrument, as such observations of surface emissivity have not yet been carried out. During CIRCCREX-II, flights were undertaken over the Greenland ice sheet, and first-look analysis suggests that TAFTS data from these flights could be used to investigate the emissivity of a snow-covered surface.

8.4.4 FIR space-based observations

Although field campaigns such as those described in this thesis are very useful in providing observations of FIR radiative processes in the atmosphere, greater insights could be made into this crucial spectral region through the development of a space-based instrument with the ability to make FIR measurements. The proposed NASA Climate Absolute Radiance and Refractivity Observatory (CLARREO, [*Wielicki et al.*, 2013]) mission is one such instrument, and comprises a polar-orbiting nadir view interferometer that can observe radiances down to 200 cm^{-1} at a resolution of 0.5 cm^{-1}. The global coverage from this proposed mission would enable studies of the FIR radiative energy budget for all atmospheric conditions, rather than the specific local conditions encountered during field campaigns.

8.4.5 Implications for GCMs and NWP

The cirrus radiative effect in GCMs and NWP models is usually parameterised with respect to a diagnosed variable such as the ice particle effect radius. For example, the cirrus parameterisation [*Edwards et al.*, 2007] in the current UK Met Office Unified Model GCM [*Collins et al.*, 2011] uses an ice aggregate model [*Yang and Liou*, 1998] combined with a database of SSPs [*Baran and Francis*, 2004]. However these parameterisations are known to have inherent problems due to their reliance on PSDs now known to be affected by ice probe shattering effects and resultant uncertainties [*Korolev et al.*, 2011]. Studies show that large errors in the cirrus radiative effect can result from the use of inadequate cirrus scattering models and parameterizations, based on, for example, skewed PSDs [*Mitchell et al.*, 2010].

Similarly, flux errors in excess of 100 Wm^{-2} can result when assumptions are made for crystal effective size, and consideration of roughness can alter up and downward fluxes by 10-15 Wm^{-2} [*Yang et al.*, 2012]. A study comparing the calculated TOA OLR using the UKMO Unified Model with its current ice aggregate model and with the proposed ensemble model of Baran [*Baran and Labonnote*, 2007; *Baran et al.*, 2014] show differences in the 10 year total global area average radiative forcing of -6 Wm^{-2} (SW) and 5 Wm^{-2} (LW). This reinforces the need for a thorough validation of the performance of cirrus scattering models throughout the electromagnetic spectrum.

The measurements and resultant findings of the CIRCCREX campaign will be used to correct SSPs and also improve bulk scattering models in order to gain consistency over the 0.3-125μm wavelength range. Observations will also be reproduced using the high-resolution (1.0 km) version of the UKMO Unified Model, in the relevant location, to simulate the SW, LW fluxes and cloud cooling rate. These will then be compared against aircraft and satellite derived cooling rates [CIRCCREX Case for Support, 2012].

References

Ackerman, S. A., W. L. Smith, J. D. Spinhirne, and H. E. Revercomb (1990), The 27-28 October 1986 FIRE IFO Cirrus Case Study: Spectral Properties of Cirrus Clouds in the 8-12 μm Window, *Mon. Weather Rev.*, *118*, 2377–2388.

Andrews, D. G. (2010), *An Introduction to Atmospheric Physics*, 2nd ed., Cambridge University Press, Cambridge.

Aumann, H. H. et al. (2003), AIRS/AMSU/HSB on the aqua mission: design, science objectives, data products, and processing systems, *IEEE Trans. Geosci. Remote Sens.*, *41*(2), 253–264, doi:10.1109/TGRS.2002.808356.

Bantges, R. J., J. E. Russell, and J. D. Haigh (1999), Cirrus cloud top-of-atmosphere radiance spectra in the thermal infrared, *J. Quant. Spectrosc. Radiat. Transf.*, *63*(2-6), 487–498, doi:10.1016/S0022-4073(99)00034-5.

Baran, A. J. (2005), The dependence of cirrus infrared radiative properties on ice crystal geometry and shape of the size-distribution function, *Q. J. R. Meteorol. Soc.*, *131*(607), 1129–1142, doi:10.1256/qj.04.91.

Baran, A. J. (2007), The impact of cirrus microphysical and macrophysical properties on upwelling far-infrared spectra, *Q. J. R. Meteorol. Soc.*, *133*, 1425–1437, doi:10.1002/qj.132.

Baran, A. J. (2012), From the single-scattering properties of ice crystals to climate prediction: A way forward, *Atmos. Res.*, *112*, 45–69, doi:10.1016/j.atmosres.2012.04.010.

Baran, A. J., and P. N. Francis (2004), On the radiative properties of cirrus cloud at solar and thermal wavelengths: A test of model consistency using high-resolution airborne radiance measurements, *Q. J. R. Meteorol. Soc.*, *130*(598), 763–778, doi:10.1256/qj.03.151.

Baran, A. J., and L. C. Labonnote (2007), A self-consistent scattering model for cirrus . I : The solar region †, *Q. J. R. Meteorol. Soc.*, *1912*(October), 1899–1912, doi:10.1002/qj.

Baran, A. J., R. Cotton, K. Furtado, S. Havemann, L.-C. Labonnote, F. Marenco, A. Smith, and J.-C. Thelen (2014), A self-consistent scattering model for cirrus. II: The high and low frequencies, *Q. J. R. Meteorol. Soc.*, *140*(680), 1039–1057, doi:10.1002/qj.2193.

Baranov, Y. I., and W. J. Lafferty (2012), The water vapour self- and water-nitrogen continuum absorption in the 1000 and 2500 cm^{-1} atmospheric windows., *Philos. Trans. A. Math. Phys. Eng. Sci.*, *370*(1968), 2578–89, doi:10.1098/rsta.2011.0234.

Baum, B. A., P. F. Soulen, K. I. Strabala, M. D. King, S. A. Ackerman, W. P. Menzel, and P. Yang (2000), Remote sensing of cloud properties using MODIS airborne simulator imagery during SUCCESS 2. Cloud thermodynamic phase, *J. Geophys. Res.*, *105*(D9), 11781–11792.

Baum, B. A., A. J. Heymsfield, P. Yang, and S. T. Bedka (2005a), Bulk Scattering Properties for the Remote Sensing of Ice Clouds. Part I: Microphysical Data and Models, *J. Appl. Meteorol.*, *44*(12), 1885–1895.

Baum, B. A., P. Yang, A. J. Heymsfield, S. Platnick, M. D. King, Y. X. Hu, and S. T. Bedka (2005b), Bulk Scattering Properties for the Remote Sensing of Ice Clouds. Part II: Narrowband Models, *J. Appl. Meteorol.*, *44*(12), 1896–1911.

Baum, B. A., P. Yang, S. Nasiri, A. K. Heidinger, A. Heymsfield, and J. Li (2007), Bulk Scattering Properties for the Remote Sensing of Ice Clouds. Part III: High-Resolution Spectral Models from 100 to 3250 cm $^{-1}$, *J. Appl. Meteorol. Climatol.*, *46*(4), 423–434, doi:10.1175/JAM2473.1.

Baum, B. A., P. Yang, A. J. Heymsfield, C. G. Schmitt, Y. Xie, A. Bansemer, Y.-X. Hu, and Z. Zhang (2011), Improvements in Shortwave Bulk Scattering and Absorption Models for the Remote Sensing of Ice Clouds, *J. Appl. Meteorol. Climatol.*, *50*(5), 1037–1056, doi:10.1175/2010JAMC2608.1.

Baum, B. A., P. Yang, A. J. Heymsfield, A. Bansemer, B. H. Cole, A. Merrelli, C. Schmitt, and C. Wang (2014), Ice cloud single-scattering property models with the full phase matrix at wavelengths from 0.2 to 100μm, *J. Quant. Spectrosc. Radiat. Transf.*, *146*, 123–139, doi:10.1016/j.jqsrt.2014.02.029.

Baumgardner, D., and A. Korolev (1997), Airspeed Corrections for Optical Array Probe Sample Volumes, *J. Atmos. Ocean. Technol.*, *14*, 1224–1229.

Bianchini, G., and L. Palchetti (2008), Technical Note : REFIR-PAD level 1 data analysis and performance characterization, *Atmos. Chem. Phys. Discuss.*, *8*(1), 367–401, doi:10.5194/acpd-8-367-2008.

Blumstein, D. et al. (2004), IASI instrument: Technical overview and measured performances, *Infrared Spaceborne Remote Sens. Xii.*, *5543*, 196–207.

Brault, J. W. (1996), New approach to high-precision Fourier transform spectrometer design., *Appl. Opt.*, *35*(16), 2891–6.

Brindley, H. E., and J. E. Harries (1998), The impact of far IR absorption on clear sky greenhouse forcing: sensitivity studies at high spectral resolution, *J. Quant. Spectrosc. Radiat. Transf.*, *60*(2), 151–180, doi:10.1016/S0022-4073(97)00152-0.

Cadeddu, M. P., J. C. Liljegren, and A. L. Pazmany (2007), Measurements and Retrievals From a New 183-GHz Water-Vapor Radiometer in the Arctic, *IEEE Trans. Geosci. Remote Sens.*, *45*(7), 2207–2215, doi:10.1109/TGRS.2006.888970.

Cady-Pereira, K. E., M. W. Shephard, D. D. Turner, E. J. Mlawer, S. A. Clough, and T. J. Wagner (2008), Improved Daytime Column-Integrated Precipitable Water Vapor from Vaisala Radiosonde Humidity Sensors, *J. Atmos. Ocean. Technol.*, *25*(6), 873–883, doi:10.1175/2007JTECHA1027.1.

Cageao, R. P., J. A. Alford, D. G. Johnson, D. P. Kratz, and M. G. Mlynczak (2010), Far-IR Measurements at Cerro Toco, Chile: FIRST, REFIR, and AERI, in *Proc. SPIE 7808, Infrared Remote Sensing and Instrumentation XVIII*, vol. 7808, edited by M. Strojnik and G. Paez.

Canas, A., J. E. Murray, and J. E. Harries (1997), The Tropospheric Airborne Fourier Transform Spectrometer (TAFTS), in *Proc. SPIE 3220, Satellite Remote Sensing of Clouds and the Atmosphere II*, pp. 91–102.

Chamberlain, J. E. (1979), *The Principles of Interferometric Spectroscopy*, edited by G. W. Chantry and N. W. B. Stone, Wiley, Bath.

Choi, Y.-S., and C.-H. Ho (2006), Radiative effect of cirrus with different optical properties over the tropics in MODIS and CERES observations, *Geophys. Res. Lett.*, *33*(21), L21811, doi:10.1029/2006GL027403.

Chung, S., S. Ackerman, and P. F. van Delst (2000), Model Calculations and Interferometer Measurements of Ice-Cloud Characteristics, *J. Appl. Meteorol. Climatol.*, *39*(5), 634–644.

Cimini, D., F. Nasir, E. R. Westwater, V. H. Payne, D. D. Turner, E. J. Mlawer, M. L. Exner, and M. P. Cadeddu (2009), Comparison of Ground-Based Millimeter-Wave Observations and Simulations in the Arctic Winter, *IEEE Trans. Geosci. Remote Sens.*, *47*(9), 3098–3106, doi:10.1109/TGRS.2009.2020743.

Clough, S. A., F. X. Kneizys, and R. W. Davies (1989), Line Shape and the Water Vapor Continuum, *Atmos. Res.*, *23*(3-4), 229–241.

Clough, S. A., M. J. Iacono, and J.-L. Moncet (1992), Line-by-line calculations of atmospheric fluxes and cooling rates: Application to water vapor, *J. Geophys. Res. Atmos.*, *97*(D14), 15761–15785.

Clough, S. A., M. W. Shephard, E. J. Mlawer, J. S. Delamere, M. J. Iacono, K. Cady-Pereira, S. Boukabara, and P. D. Brown (2005), Atmospheric radiative transfer modeling: a summary of the AER codes, *J. Quant. Spectrosc. Radiat. Transf.*, *91*(2), 233–244, doi:10.1016/j.jqsrt.2004.05.058.

Cole, B. H., P. Yang, B. A. Baum, J. Riedi, L. C.-Labonnote, F. Thieuleux, and S. Platnick (2013), Comparison of PARASOL Observations with Polarized Reflectances Simulated Using Different Ice Habit Mixtures, *J. Appl. Meteorol. Climatol.*, *52*(1), 186–196, doi:10.1175/JAMC-D-12-097.1.

Collins, W. J. et al. (2011), Development and evaluation of an Earth-System model – HadGEM2, *Geosci. Model Dev.*, *4*(4), 1051–1075, doi:10.5194/gmd-4-1051-2011.

Cotton, R., S. Osborne, Z. Ulanowski, E. Hirst, P. H. Kaye, and R. S. Greenaway (2010), The Ability of the Small Ice Detector (SID-2) to Characterize Cloud Particle and Aerosol Morphologies Obtained during Flights of the FAAM BAe-146 Research Aircraft, *J. Atmos. Ocean. Technol.*, *27*(2), 290–303, doi:10.1175/2009JTECHA1282.1.

Cotton, R. J., P. R. Field, Z. Ulanowski, P. H. Kaye, E. Hirst, R. S. Greenaway, I. Crawford, J. Crosier, and J. Dorsey (2013), The effective density of small ice particles obtained from in situ aircraft observations of mid-latitude cirrus, *Q. J. R. Meteorol. Soc.*, *139*(676), 1923–1934, doi:10.1002/qj.2058.

Cox, C. V., J. E. Harries, J. P. Taylor, P. D. Green, A. J. Baran, J. C. Pickering, A. E. Last, and J. E. Murray (2010), Measurement and simulation of mid- and far-infrared spectra in the presence of cirrus, *Q. J. R. Meteorol. Soc.*, *136*(648), 718–739, doi:10.1002/qj.596.

Davis, S. P., M. C. Abrams, and J. W. Brault (2001), *Fourier Transform Spectroscopy*, Academic Press.

Delamere, J. S., S. A. Clough, V. H. Payne, E. J. Mlawer, D. D. Turner, and R. R. Gamache (2010), A far-infrared radiative closure study in the Arctic: Application to water vapor, *J. Geophys. Res.*, *115*(D17), 1–17, doi:10.1029/2009JD012968.

Dirac, P. (1958), *Principles of quantum mechanics*, 4th ed., Clarendon Press, Oxford.

Dowling, D. R., and L. F. Radke (1990), A Summary of the Physical-Properties of Cirrus Clouds, *J. Appl. Meteorol.*, *29*(9), 970–978.

Downing, H. D., and D. Williams (1975), Optical Constants of Water in the Infrared, *J. Geophys. Res.*, *80*(12), 1656–1661.

Edwards, D. P. (1992), *A General Line-by-Line Atmospheric Transmittance and Radiance Model Version 3 . 0 Description and Users Guide*, Boulder, CO.

Edwards, J., and A. Slingo (1996), Studies with a flexible new radiation code .1. Choosing a configuration for a large-scale model, *Q. J. R. Meteorol. Soc.*, *122*(531), 689–719.

Edwards, J. M., S. Havemann, J. C. Thelen, and A. J. Baran (2007), A new parametrization for the radiative properties of ice crystals: Comparison with existing schemes and impact in a GCM, *Atmos. Res.*, *83*(1), 19–35, doi:10.1016/j.atmosres.2006.03.002.

Elasser, W. M. (1938), Mean absorption and equivalent absorption coefficient of a band spectrum, *Phys. Rev.*, *54*, 126–129.

Eliasson, S., S. A. Buehler, M. Milz, P. Eriksson, and V. O. John (2011), Assessing observed and modelled spatial distributions of ice water path using satellite data, *Atmos. Chem. Phys.*, *11*(1), 375–391, doi:10.5194/acp-11-375-2011.

Elsasser, W. . (1938a), New values for the infrared absorption coefficient of atmospheric water vapor, *Mon. Weather Rev.*, *66*, 175–178.

Elsasser, W. M. (1938b), Note on atmospheric absorption caused by the rotational water band, *Phys. Rev.*, *53*(768).

Emersic, C. (2012), Light scattering by ice crystals,

Feldman, D. R., W. D. Collins, R. Pincus, X. Huang, and X. Chen (2014), Far-infrared surface emissivity and climate., *Proc. Natl. Acad. Sci. U. S. A.*, *111*(46), 16297–302, doi:10.1073/pnas.1413640111.

Field, P. R., R. J. Hogan, P. R. A. Brown, A. J. Illingworth, T. W. Choularton, and R. J. Cotton (2005), Parametrization of ice particle size distributions for mid-latitude stratiform cloud, *Q. J. R. Meteorol. Soc.*, *131*(609), 1997–2017.

Field, P. R., A. J. Heymsfield, and A. Bansemer (2006), Shattering and Particle Interarrival Times Measured by Optical Array Probes in Ice Clouds, *J. Atmos. Ocean. Technol.*, *23*(10), 1357–1371.

Field, P. R., A. J. Heymsfield, and A. Bansemer (2007), Snow Size Distribution Parameterization for Midlatitude and Tropical Ice Clouds, *J. Atmos. Sci.*, *64*(12), 4346–4365, doi:10.1175/2007JAS2344.1.

Fox, C., P. D. Green, J. C. Pickering, and N. Humpage (2015), Analysis of far-infrared spectral radiance observations of the water vapor continuum in the Arctic, *J. Quant. Spectrosc. Radiat. Transf.*, *155*, 57–65, doi:10.1016/j.jqsrt.2015.01.001.

Fu, Q. (2007), A New Parameterization of an Asymmetry Factor of Cirrus Clouds for Climate Models, *J. Atmos. Sci.*, *64*(11), 4140–4150, doi:10.1175/2007JAS2289.1.

Garrett, K. J., P. Yang, S. L. Nasiri, C. R. Yost, and B. A. Baum (2009), Influence of Cloud-Top Height and Geometric Thickness on a MODIS Infrared-Based Ice Cloud Retrieval, *J. Appl. Meteorol. Climatol.*, *48*(4), 818–832, doi:10.1175/2008JAMC1915.1.

Garrett, T. J. (2003), Small, highly reflective ice crystals in low-latitude cirrus, *Geophys. Res. Lett.*, *30*(21), 2132, doi:10.1029/2003GL018153.

Garrett, T. J., P. V Hobbs, and H. Gerber (2001), Shortwave, single-scattering properties of arctic ice clouds, *J. Geophys. Res.*, *106*, 155–172.

General Eastern Instruments (1987), *Model 1011B Dew Point Hygrometer For Aircraft: Preliminary Operating Manual.*

Goody, R. M., and Y. L. Yung (1989), *Atmospheric radiation: Theoretical basis*, 2nd ed., Oxford University Press.

Gordon, I. E., L. S. Rothman, R. R. Gamache, D. Jacquemart, C. Boone, P. F. Bernath, M. W. Shephard, J. S. Delamere, and S. A. Clough (2007), Current updates of the water-vapor line list in HITRAN: A new "Diet" for air-broadened half-widths, *J. Quant. Spectrosc. Radiat. Transf.*, *108*(3), 389–402, doi:10.1016/j.jqsrt.2007.06.009.

Green, P. D. (2003), The development of a Fourier transform spectrometer to measure far IR fluxes in the upper troposphere, University of London.

Green, P. D., S. M. Newman, R. J. Beeby, J. E. Murray, J. C. Pickering, and J. E. Harries (2012), Recent advances in measurement of the water vapour continuum in the far-

infrared spectral region., *Philos. Trans. A. Math. Phys. Eng. Sci.*, *370*(1968), 2637–55, doi:10.1098/rsta.2011.0263.

Gu, Y., K. N. Liou, S. C. Ou, and R. Fovell (2011), Cirrus cloud simulations using WRF with improved radiation parameterization and increased vertical resolution, *J. Geophys. Res.*, *116*(D6), D06119, doi:10.1029/2010JD014574.

Guignard, A., C. J. Stubenrauch, A. J. Baran, and R. Armante (2012), Bulk microphysical properties of semi-transparent cirrus from AIRS: a six year global climatology and statistical analysis in synergy with geometrical profiling data from CloudSat-CALIPSO, *Atmos. Chem. Phys.*, *12*, 503–525.

Harries, J., B. Carli, R. Rizzi, C. Serio, M. Mlynczak, L. Palchetti, T. Maestri, H. Brindley, and G. Masiello (2008), The Far-Infrared Earth, *Rev. Geophys.*, *46*(4), doi:10.1029/2007RG000233.

Harries, J. E. (1996), The greenhouse Earth: A view from space, *Q. J. R. Meteorol. Soc.*, *122*(532), 799–818.

Harries, J. E. (2000), Physics of the Earth's radiative energy balance, *Contemp. Phys.*, *41*(5), 309–322.

Heidinger, A. K., and M. J. Pavolonis (2005), Global Daytime Distribution of Overlapping Cirrus Cloud from NOAA's Advanced Very High Resolution Radiometer, *J. Clim.*, *18*(22), 4772–4784.

Held, I. M., and B. J. Soden (2000), Water vapor feedback and global warming, *Annu. Rev. Energy Environ.*, *25*, 441–475.

Heymsfield, A. J., and L. M. Miloshevich (2003), Parameterizations for the Cross-Sectional Area and Extinction of Cirrus and Stratiform Ice Cloud Particles, *J. Atmos. Sci.*, *60*(7), 936–956, doi:10.1175/1520-0469(2003)060<0936:PFTCSA>2.0.CO;2.

Heymsfield, A. J., and C. M. R. Platt (1984), A Parameterization of the Particle-Size Spectrum of Ice Clouds in Terms of the Ambient-Temperature and the Ice Water-Content, *J. Atmos. Sci.*, *41*(5), 846–855.

Heymsfield, A. J., K. M. Miller, and J. D. Spinhirne (1990), The 27-28 October 1986 Fire Ifo Cirrus Case-Study - Cloud Microstructure, *Mon. Weather Rev.*, *118*(11), 2313–2328.

Heymsfield, A. J., A. Bansemer, P. R. Field, S. L. Durden, J. L. Stith, J. E. Dye, W. Hall, and C. A. Grainger (2002), Observations and Parameterizations of Particle Size Distributions in Deep Tropical Cirrus and Stratiform Precipitating Clouds : Results from In Situ Observations in TRMM Field Campaigns, *J. Atmos. Sci.*, *59*(24), 3457–3491.

Huang, H.-L., P. Yang, H. Wei, B. A. Baum, Y. Hu, P. Antonelli, and S. A. Ackerman (2004), Inference of ice cloud properties from high spectral resolution infrared observations, *IEEE Trans. Geosci. Remote Sens.*, *42*(4), 842–853, doi:10.1109/TGRS.2003.822752.

Humpage, N. (2010), Observing and modelling the impact of arctic and tropical cirrus clouds on far-infrared radiance spectra, Imperial College London.

Hunt, W. H., D. M. Winker, M. a. Vaughan, K. a. Powell, P. L. Lucker, and C. Weimer (2009), CALIPSO Lidar Description and Performance Assessment, *J. Atmos. Ocean. Technol.*, *26*(7), 1214–1228, doi:10.1175/2009JTECHA1223.1.

IPCC (2007), *Climate Change 2007: The Physical Science Basis. Contribution of Working Group I to the Fourth Assessment Report of the Intergovernmental Panel on Climate Change. Summary for Policymakers*, edited by S. Solomon, D. Qin, M. Manning, Z. Chen, M. Marquis, K. B. Averyt, M. Tignor, and H. L. Miller, Cambridge University Press, Cambridge, United Kingdom and New York, NY, USA.

IPCC (2013), *Climate Change 2013 - The Physical Science Basis: Working Group I Contribution to the Fifth Assessment Report of the Intergovernmental Panel on Climate Change*, edited by T. F. Stocker, D. Qin, G.-K. Plattner, M. Tignor, S. K. Allen, J. Boschung, A. Nauels, Y. Xia, V. Bex, and P. M. Midgley, Cambridge University Press, Cambridge, United Kingdom and New York, NY, USA.

Jensen, E. J., O. B. Toon, D. L. Westphal, and A. J. Heymsfield (1994), Microphysical modeling of cirrus: 2. Sensitivity studies, *J. Geophys. Res. Atmos.*, *99*(D5), 10443–10454.

Kiehl, J. T., and K. E. Trenberth (1997), Earth's Annual Global Mean Energy Budget, *Bull. Am. Meteorol. Soc.*, *78*(2), 197–208.

Knollenberg, R. G. (1970), The Optical Array: An Alternative to Scattering or Extinction for Airborne Particle Size Determination, *J. Appl. Meteorol.*, *9*(1), 86–103.

Knuteson, R. O. et al. (2004a), Atmospheric Emitted Radiance Interferometer . Part I : Instrument Design, *J. Atmos. Ocean. Technol.*, *21*(12), 1763–1776.

Knuteson, R. O. et al. (2004b), Atmospheric Emitted Radiance Interferometer. Part II: Instrument Performance, *J. Atmos. Ocean. Technol.*, *21*(12), 1777–1789.

Korolev, A. V. (2009), Probe tips for airborne instruments used to measure cloud microphysical parameters. U.S. Patent Application No. 12/415,314; Canadian Patent Application No. 2660753,

Korolev, A. V., J. W. Strapp, and G. A. Isaac (1998), Evaluation of the Accuracy of PMS Optical Array Probes, *J. Atmos. Ocean. Technol.*, *15*(3), 708–720.

Korolev, A. V., E. F. Emery, J. W. Strapp, S. G. Cober, G. A. Isaac, M. Wasey, and D. Marcotte (2011), Small Ice Particles in Tropospheric Clouds: Fact or Artifact? Airborne Icing Instrumentation Evaluation Experiment, *Bull. Am. Meteorol. Soc.*, *92*(8), 967–973, doi:10.1175/2010BAMS3141.1.

Lawson, R. P., D. O'Connor, P. Zmarzly, K. Weaver, B. Baker, and Q. Mo (2006), The 2D-S (Stereo) Probe : Design and Preliminary Tests of a New Airborne, High-Speed, High-Resolution Particle Imaging Probe, *J. Atmos. Ocean. Technol.*, *23*(1997), 1462–1477.

Lee, J., P. Yang, A. E. Dessler, B.-C. Gao, and S. Platnick (2009), Distribution and Radiative Forcing of Tropical Thin Cirrus Clouds, *J. Atmos. Sci.*, *66*(12), 3721–3731, doi:10.1175/2009JAS3183.1.

Li, J., H.-L. Huang, C.-Y. Liu, P. Yang, T. J. Schmit, H. Wei, E. Weisz, L. Guan, and W. P. Menzel (2005), Retrieval of Cloud Microphysical Properties from MODIS and AIRS, *J. Appl. Meteorol.*, *44*(10), 1526–1543, doi:10.1175/JAM2281.1.

Liou, K. N. (2002), *An Introduction to Atmospheric Radiation*, 2nd ed., Academic Press, San Diego, California, USA.

Liuzzi, G., G. Masiello, C. Serio, L. Palchetti, and G. Bianchini (2014), Validation of H2O continuum absorption models in the wave number range 180–600 cm^{-1} with atmospheric emitted spectral radiance measured at the Antarctica Dome-C site, *Opt. Express*, *22*(14), 16784, doi:10.1364/OE.22.016784.

Lynch, D. K., K. Sassen, D. O. Starr, and G. Stephens (2002), *Cirrus*, Oxford University Press, New York, USA.

Maestri, T. (2005), Spectral infrared analysis of a cirrus cloud based on Airborne Research Interferometer Evaluation System (ARIES) measurements, *J. Geophys. Res.*, *110*(D6), D06111, doi:10.1029/2004JD005098.

Maestri, T., and R. Rizzi (2003), A study of infrared diabatic forcing of ice clouds in the tropical atmosphere, *J. Geophys. Res.*, *108*(D4), 4139, doi:10.1029/2002JD002146.

Maestri, T., R. Rizzi, E. Tosi, P. Veglio, L. Palchetti, G. Bianchini, P. Di Girolamo, G. Masiello, C. Serio, and D. Summa (2014), Analysis of cirrus cloud spectral signatures in the far infrared, *J. Quant. Spectrosc. Radiat. Transf.*, *141*, 49–64, doi:10.1016/j.jqsrt.2014.02.030.

Magono, C., and C. V. Lee (1966), Meteorological classification of natural snow crystals, *J. Fac. Sci. Univ. Hokkaido*, *2*(4), 321–362.

Marenco, F. (2010), *Capabilities and operation of the FAAM EZlidar*.

Marenco, F., and R. J. Hogan (2011), Determining the contribution of volcanic ash and boundary layer aerosol in backscatter lidar returns: A three-component atmosphere approach, *J. Geophys. Res.*, *116*, D00U06, doi:10.1029/2010JD015415.

Marenco, F., B. Johnson, K. Turnbull, S. Newman, J. Haywood, H. Webster, and H. Ricketts (2011), Airborne lidar observations of the 2010 Eyjafjallajökull volcanic ash plume, *J. Geophys. Res.*, *116*, D00U05, doi:10.1029/2011JD016396.

Martin, D. H., and E. Puplett (1969), Polarised Interferometric Spectrometry for the Millimetre and Submillimetre Spectrum, *Infrared Phys.*, *10*(2), 105–109.

McClatchey, R. A., R. W. Fenn, J. E. A. Selby, F. E. Volz, and J. S. Garing (1972), Optical Properties of the Atmosphere, in *Environmental Research Papers*, vol. 411, AFCRL-72-0497, Hanscom AFB, Bedford, Massachusetts.

Meador, W. E., and W. R. Weaver (1980), Two-Stream Approximations to Radiative Transfer in Planetary Atmospheres: A Unified Description of Existing Methods and a New Improvement, *J. Atmos. Sci.*, *37*(3), 630–643.

Michelson, A. A. (1890), A simple Interference Experiment, *Am. J. Sci.*, *39*(231), 216–218.

Miloshevich, L. M., H. Vömel, D. N. Whiteman, and T. Leblanc (2009), Accuracy assessment and correction of Vaisala RS92 radiosonde water vapor measurements, *J. Geophys. Res.*, *114*(D11), D11305, doi:10.1029/2008JD011565.

Mitchell, D. L., R. P. d'Entremont, and R. P. Lawson (2010), Inferring Cirrus Size Distributions through Satellite Remote Sensing and Microphysical Databases, *J. Atmos. Sci.*, *67*(4), 1106–1125, doi:10.1175/2009JAS3150.1.

Mlawer, E. J., S. A. Clough, and D. C. Tobin (2003), A new water vapor continuum model: MT CKD 1.0., in *13th ARM Science Team Meeting*, Dept. of Energy, Broomfield, CO,US.

Mlawer, E. J., V. H. Payne, J.-L. Moncet, J. S. Delamere, M. J. Alvarado, and D. C. Tobin (2012), Development and recent evaluation of the MT_CKD model of continuum absorption., *Philos. Trans. A. Math. Phys. Eng. Sci.*, *370*(1968), 2520–56, doi:10.1098/rsta.2011.0295.

Mlynczak, M. G. et al. (2006), First light from the Far-Infrared Spectroscopy of the Troposphere (FIRST) instrument, *Geophys. Res. Lett.*, *33*(7), L07704, doi:10.1029/2005GL025114.

Nakajima, T., and M. D. King (1990), Determination of the Optical Thickness and Effective Particle Radius of Clouds from Reflected Solar Radiation Meaurements. Part I: Theory, *J. Atmos. Sci.*, *47*(15), 1878–1983.

NASA (2014), MODIS Atmosphere data products, Available from: http://modis-atmos.gsfc.nasa.gov

Nazaryan, H., M. P. McCormick, and W. P. Menzel (2008), Global characterization of cirrus clouds using CALIPSO data, *J. Geophys. Res.*, *113*(D16), D16211, doi:10.1029/2007JD009481.

Ou, S. C. S., and K. N. Liou (1984), A Two-Dimensional Radiation-Turbulence Climate Model. I: Sensitivity to Cirrus Radiative Properties, *J. Atmos. Sci.*, *41*(15), 2289–2309.

Palchetti, L., G. Bianchini, F. Castagnoli, B. Carli, C. Serio, F. Esposito, V. Cuomo, R. Rizzi, and T. Maestri (2005), Breadboard of a Fourier-transform spectrometer for the radiation explorer in the far infrared atmospheric mission., *Appl. Opt.*, *44*(14), 2870–8.

Penner, S. S., and P. J. Varanasi (1967), Spectral absorption coefficients in the pure rotation spectrum of water vapor, *J. Quant. Spectrosc. Radiat. Transf.*, *7*(4), 687–690.

Platnick, S., M. D. King, S. A. Ackerman, W. P. Menzel, B. A. Baum, J. C. Riédi, and R. A. Frey (2003), The MODIS Cloud Products: Algorithms and Examples From Terra, *IEEE Trans. Geosci. Remote Sens.*, *41*(2), 459–473.

Ptashnik, I. V. (2008), Evidence for the contribution of water dimers to the near-IR water vapour self-continuum, *J. Quant. Spectrosc. Radiat. Transf.*, *109*(5), 831–852, doi:10.1016/j.jqsrt.2007.09.004.

Revercomb, H. E., H. Buijs, H. B. Howell, D. D. Laporte, W. L. Smith, and L. A. Sromovsky (1988), Radiometric calibration of IR Fourier transform spectrometers: solution to a problem with the High-Resolution Interferometer Sounder., *Appl. Opt.*, *27*(15), 3210–3218.

Ringer, M. A. et al. (2006), Global mean cloud feedbacks in idealized climate change experiments, *Geophys. Res. Lett.*, *33*(7), L07718, doi:10.1029/2005GL025370.

Rolland, P., K. N. Liou, M. D. King, S. C. Tsay, and M. Validation (2000), Remote sensing of optical and microphysical properties of cirrus clouds using Moderate-Resolution Imaging Spectroradiometer channels : Methodology and sensitivity to physical assumptions, *J. Geophys. Res.*, *105*(D9), 11721 –11738.

Rossow, W. B., and R. a. Schiffer (1999), Advances in Understanding Clouds from ISCCP, *Bull. Am. Meteorol. Soc.*, *80*(11), 2261–2287, doi:10.1175/1520-0477(1999)080<2261:AIUCFI>2.0.CO;2.

Rothman, L. S. et al. (2009), The HITRAN 2008 molecular spectroscopic database, *J. Quant. Spectrosc. Radiat. Transf.*, *110*(9-10), 533–572, doi:10.1016/j.jqsrt.2009.02.013.

Rothman, L. S. et al. (2013), The HITRAN 2012 molecular spectroscopic database, *J. Quant. Spectrosc. Radiat. Transf.*, *130*, 4–50, doi:10.1016/j.jqsrt.2013.07.002.

Rowe, P. M., and V. P. Walden (2009), Improved measurements of the foreign-broadened continuum of water vapor in the 6.3 micron band at -30 degrees C., *Appl. Opt.*, *48*(7), 1358–65.

Shine, K. P., I. V. Ptashnik, and G. Rädel (2012), The Water Vapour Continuum: Brief History and Recent Developments, *Surv. Geophys.*, *33*(3-4), 535–555, doi:10.1007/s10712-011-9170-y.

Sinha, A., and J. E. Harries (1995), Water vapour and greenhouse trapping: The role of far infra- red absorption, *Geophys. Res. Lett.*, *22*(16), 2147–2150.

Stamnes, K., S. C. Tsay, W. Wiscombe, and K. Jayaweera (1988), Numerically stable algorithm for discrete-ordinate-method radiative transfer in multiple scattering and emitting layered media., *Appl. Opt.*, *27*(12), 2502–9.

Stephens, G. L., S.-C. Tsay, P. W. Stackhouse, and P. J. Flatau (1990), The Relevance of the Microphysical and Radiative Properties of Cirrus Clouds to Climate and Climatic Feedback, *J. Atmos. Sci.*, *47*(14), 1742–1754.

Stephens, G. L. et al. (2008), CloudSat mission: Performance and early science after the first year of operation, *J. Geophys. Res.*, *113*(D8), doi:10.1029/2008JD009982.

Stickney, T. M., M. W. Shedlov, and D. I. Thompson (1994), *Total Temperature Sensors Technical Report 5755*.

Strabala, K. I., S. A. Ackerman, and W. P. Menzel (1994), Cloud Properties Inferred from 8-12μm Data, *J. Appl. Meteorol.*, *33*, 212–229.

Strapp, J. W., F. Albers, A. Reuter, a. V. Korolev, U. Maixner, E. Rashke, and Z. Vukovic (2001), Laboratory Measurements of the Response of a PMS OAP-2DC, *J. Atmos. Ocean. Technol.*, *18*(7), 1150–1170, doi:10.1175/1520-0426(2001)018<1150:LMOTRO>2.0.CO;2.

Stubenrauch, C. J., A. Chédin, G. Rädel, N. A. Scott, and S. Serrar (2006), Cloud Properties and Their Seasonal and Diurnal Variability from TOVS Path-B, *J. Clim.*, *19*(21), 5531–5553.

Taylor, J. P., S. M. Newman, T. J. Hewison, and A. McGrath (2003), Water vapour line and continuum absorption in the thermal infrared—reconciling models and observations, *Q. J. R. Meteorol. Soc.*, *129*(594), 2949–2969, doi:10.1256/qj.03.08.

Thorne, A. P. (1988), *Spectrophysics*, Chapman & Hall Ltd.

Tobin, D. et al. (1999), Downwelling spectral radiance observations at the SHEBA ice station: Water vapor continuum measurements from 17 to 26μm, *J. Geophys. Res.*, *104*(D2), 2081–2092.

Turner, D. et al. (2004a), The QME AERI LBLRTM : A Closure Experiment for Downwelling High Spectral Resolution Infrared Radiance, *J. Atmos. Sci.*, *61*(22), 2657–2675.

Turner, D. D. (2003), Microphysical properties of single and mixed-phase arctic clouds derived from ground-based AERI observations., University of Wisconsin - Madison.

Turner, D. D. (2005), Arctic Mixed-Phase Cloud Properties from AERI Lidar Observations : Algorithm and Results from SHEBA, *J. Appl. Meteorol.*, *44*(4), 427–444.

Turner, D. D., and E. J. Mlawer (2010), The Radiative Heating in Underexplored Bands Campaigns, *Bull. Am. Meteorol. Soc.*, *91*(7), 911–923, doi:10.1175/2010BAMS2904.1.

Turner, D. D., H. E. Revercomb, R. O. Knuteson, R. G. Dedecker, and W. F. Feltz (2004b), An Evaluation of the Nonlinearity Correction Applied to Atmospheric Emitted Radiance Interferometer (AERI) Data Collected by the Atmospheric Radiation Measurement Program, *Tech. Rep.*, *ARM TR-013*(September).

Turner, D. D., R. O. Knuteson, H. E. Revercomb, C. Lo, and R. G. Dedecker (2006), Noise Reduction of Atmospheric Emitted Radiance Interferometer (AERI) Observations Using Principal Component Analysis, *J. Atmos. Ocean. Technol.*, *23*(9), 1223–1238.

Tyndal, J. (1861), On the absorption and radiation of heat by gases and vapours, and on the physical connexion of radiation, absorption, and conduction, *Philos. Mag.*, *22*, 169–194.

Ulanowski, Z., E. Hesse, P. H. Kaye, and A. J. Baran (2006), Light scattering by complex ice-analogue crystals, *J. Quant. Spectrosc. Radiat. Transf.*, *100*(1-3), 382–392, doi:10.1016/j.jqsrt.2005.11.052.

Ulanowski, Z., P. H. Kaye, E. Hirst, R. S. Greenaway, R. J. Cotton, E. Hesse, and C. T. Collier (2014), Incidence of rough and irregular atmospheric ice particles from Small Ice Detector 3 measurements, *Atmos. Chem. Phys.*, *14*(3), 1649–1662, doi:10.5194/acp-14-1649-2014.

Vaisala (1999), *Advanced AVAPS System for Airborne Weather Research*.

Vaisala (2010a), *Vaisala Dropsonde RD94 Technical Datasheet*.

Vaisala (2010b), *Vaisala Radiosonde RS92 Technical Datasheet*.

Viktorova, A. A., and S. A. Zhevakin (1967), Absorption of micro-radiowaves in air by water vapor dimers, *Sov. Phys. Dokl.*, *11*, 1059–1062.

Wang, C., P. Yang, B. a. Baum, S. Platnick, A. K. Heidinger, Y. Hu, and R. E. Holz (2011), Retrieval of Ice Cloud Optical Thickness and Effective Particle Size Using a Fast Infrared Radiative Transfer Model, *J. Appl. Meteorol. Climatol.*, *50*(11), 2283–2297, doi:10.1175/JAMC-D-11-067.1.

Warren, S. G. (1984), Optical constants of ice from the ultraviolet to the microwave., *Appl. Opt.*, *23*(8), 1206–1225.

Warren, S. G., and R. E. Brandt (2008), Optical constants of ice from the ultraviolet to the microwave: A revised compilation, *J. Geophys. Res.*, *113*(D14), D14220, doi:10.1029/2007JD009744.

Wei, H., P. Yang, J. Li, B. A. Baum, H.-L. Huang, S. Platnick, Y. Hu, and L. Strow (2004), Retrieval of semitransparent ice cloud optical thickness from atmospheric infrared sounder (AIRS) measurements, *IEEE Trans. Geosci. Remote Sens.*, *42*(10), 2254–2267, doi:10.1109/TGRS.2004.833780.

Wetherald, R. T., and S. Manabe (1988), Cloud Feedback Processes in a General Circulation Model, *J. Atmos. Sci.*, *45*(8), 1397–1416.

Wielicki, B. a. et al. (2013), Achieving Climate Change Absolute Accuracy in Orbit, *Bull. Am. Meteorol. Soc.*, *94*(10), 1519–1539, doi:10.1175/BAMS-D-12-00149.1.

Wilson, S. H. S., N. C. Atkinson, and J. A. Smith (1999), The Development of an Airborne Infrared Interferometer for Meteorological Sounding Studies, *J. Atmos. Ocean. Technol.*, *16*(12), 1912–1927.

Wylie, D. P., W. P. Menzel, H. M. Woolf, and K. I. Strabala (1994), 4 Years of Global Cirrus Cloud Statistics using Hirs, *J. Clim.*, *7*(12), 1972–1986.

Yang, H., S. Dobbie, R. Herbert, P. Connolly, M. Gallagher, S. Ghosh, S. M. R. K. Al-Jumur, and J. Clayton (2012), The effect of observed vertical structure, habits, and size distributions on the solar radiative properties and cloud evolution of cirrus clouds, *Q. J. R. Meteorol. Soc.*, *138*(666), 1221–1232, doi:10.1002/qj.973.

Yang, P. (2003), Spectral signature of ice clouds in the far-infrared region: Single-scattering calculations and radiative sensitivity study, *J. Geophys. Res.*, *108*(D18), 4569, doi:10.1029/2002JD003291.

Yang, P., and K. N. Liou (1998), Single-Scattering Properties of Complex Ice Crystals in Terrestrial Atmosphere, *Contr. Atmos. Phys.*, *71*(2), 223.

Yang, P., B.-C. Gao, B. A. Baum, Y. X. Hu, W. J. Wiscombe, S.-C. Tsay, D. M. Winker, and S. L. Nasiri (2001), Radiative properties of cirrus clouds in the infrared (8–13 μm) spectral region, *J. Quant. Spectrosc. Radiat. Transf.*, *70*, 473–504.

Yang, P., G. W. Kattawar, G. Hong, P. Minnis, and Y.-X. Hu (2008), Uncertainties Associated With the Surface Texture of Ice Particles in Satellite-Based Retrieval of Cirrus Clouds—Part I: Single-Scattering Properties of Ice Crystals With Surface Roughness, *IEEE Trans. Geosci. Remote Sens.*, *46*(7), 1940–1947, doi:10.1109/TGRS.2008.916471.

Zhang, Y., A. Macke, and F. Albers (1999), Effect of crystal size spectrum and crystal shape on stratiform cirrus radiative forcing, *Atmos. Res.*, *52*(1-2), 59–75, doi:10.1016/S0169-8095(99)00026-5.